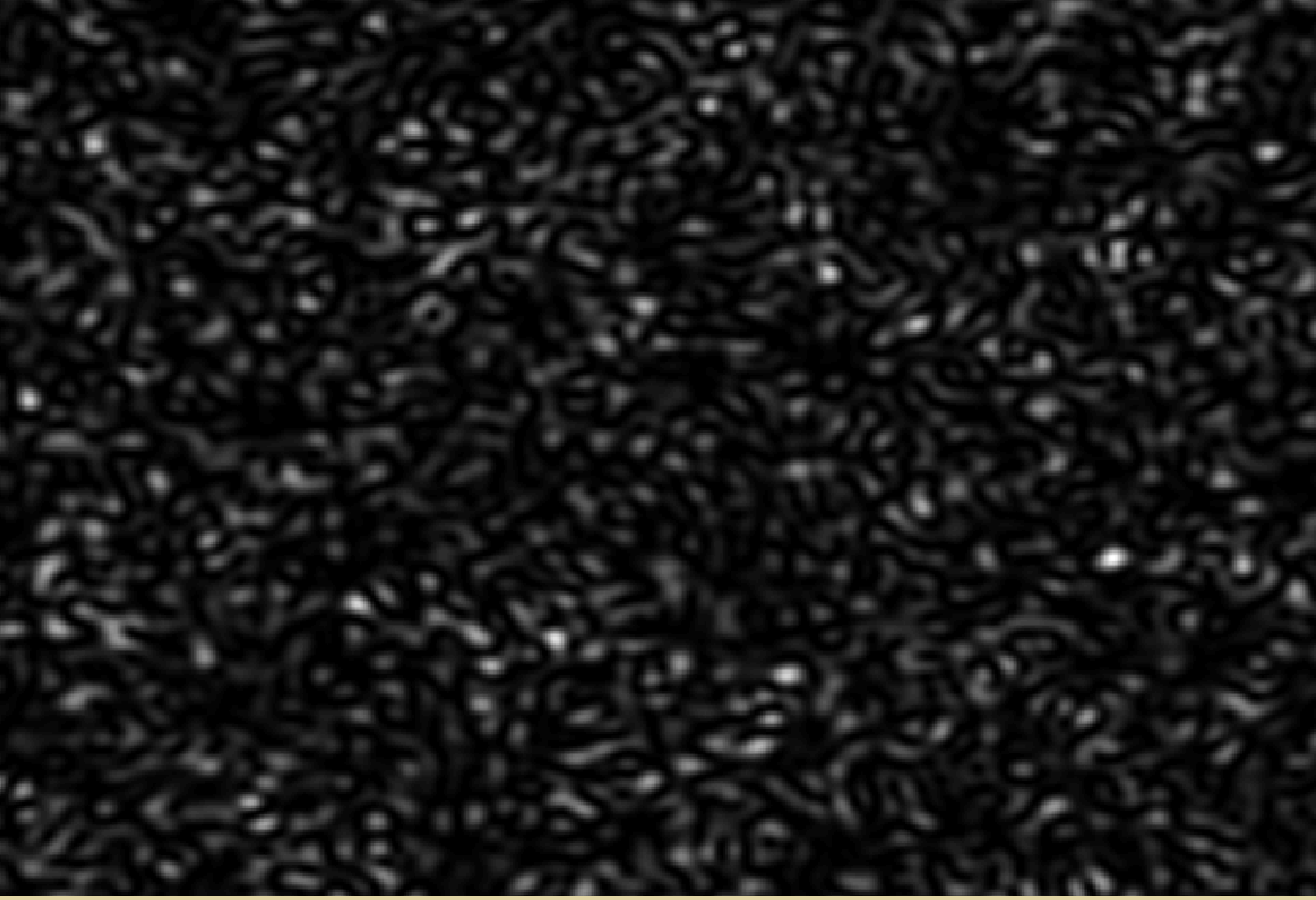

Pedro Guilherme da Cunha Leitão Dias Vaz

METHODS FOR HEMODYNAMIC PARAMETERS MEASUREMENT USING THE LASER SPECKLE EFFECT IN MACRO AND MICROCIRCULATION

PhD thesis in Biomedical Engineering, in co-supervision (co-tutelle) regime between the University of Coimbra (UC) - Portugal and the University of Angers (UA) - France, under the supervision of Dr. João Manuel Rendeiro Cardoso (UC) and Professor Anne Humeau-Heurtier (UA), submitted to the Faculty of Sciences and Technology of the University of Coimbra.

September 2016

· U C ·

Universidade de Coimbra

UNIVERSITY OF COIMBRA
AND
UNIVERSITY OF ANGERS

PHD THESIS

PROGRAMA DOUTORAL EM ENGENHARIA BIOMÉDICA (UC)
AND
DOCTORAT EN TRAITEMENT DU SIGNAL ET DE L'IMAGE (UA)

Methods for hemodynamic parameters measurement using the laser speckle effect in macro and microcirculation.

Author:
Pedro Guilherme da Cunha Leitão Dias VAZ
Supervisors:
Dr. João Rendeiro CARDOSO
(University of Coimbra)
Prof. Anne HUMEAU-HEURTIER
(University of Angers)

2016

The research reported in this thesis was performed with financial support of the following institutions/programs:

- PhD scholarship number SFRH/BD/89585/2012 granted by the Fundação para a Ciência e Tecnologia.
- PESSOA/Hubert Curien travelling program granted by the Fundação para a Ciência e Tecnologia and by the CAMPUS FRANCE.
- Ações integradas Luso Francesas/PAUILF granted by Conselho de Reitores das Universidades Portuguesas (CRUP) and Conférence des Présidents d'Université (CPU).

Resumo

O laser speckle corresponde a um efeito de interferometria que foi muitas vezes considerado como uma grande limitação do uso de fontes de luz coerente. No entanto, para um conjunto específico de aplicações, este efeito pode ser usado como fonte de informação. Entre estas aplicações podemos encontrar várias no âmbito da biomedicina. Esta técnica tem vindo a ser utilizada durante décadas para avaliar a perfusão sanguínea mas, apenas agora, começa a despertar interesse como meio de avaliar também a macrocirculação. Este trabalho pretende demonstrar que o efeito de laser speckle pode ser usado, também, para extrair informação importante relativa à condição cardiovascular, nomeadamente da macrocirculação, com boa fiabilidade e usando métodos semelhantes aos já aplicados na avaliação da microcirculação. O facto de serem usados os mesmo métodos poderá levar a uma rápida inclusão deste tipo de análise nos dispositivos já existentes. No campo do uso de laser speckle para avaliação da microcirculação, uma das questões mais importantes está relacionada com o efeito dos dispersores estáticos. A quantidade de dispersores estáticos influencia fortemente o sinal de laser speckle, levando a interpretações incorretas dos dados. Este é um dos fatores que impede a existência de dispositivos laser speckle com capacidade de quantificar o fluxo sanguíneo. Devido a isto, o estudo do efeito de diferentes concentrações de dispersores estáticos nos sinais de contraste e correlação speckle é também um dos objetivos deste trabalho.

Esta tese apresenta os estudos realizados com o objetivo de testar a possibilidade de usar o efeito de laser speckle para avaliação de parâmetros hemodinâmicos da microcirculação e o trabalho experimental realizado no âmbito do efeito dos dispersores estáticos. Antes do trabalho experimental, esta tese começa por descrever os princípios básicos da teoria de laser speckle. Nesta secção é realizada uma análise crítica da literatura disponível e são identificados os desafios futuros desta técnica. Algumas ideias inovadoras são também propostas como métodos para lidar com alguns dos problemas atuais da técnica de laser speckle. Os trabalhos desenvolvidos na área da macrocirculação demonstraram que o efeito de laser speckle pode ser usado para extrair a forma de onda de pulso. Um estudo com fontes de luz de diferentes comprimentos de onda foi efetuado para determinar qual destes comprimentos de onda apresenta melhores resultados. Os comprimentos de onda mais curtos (luz verde) conseguiram atingir os melhores resultados na identificação do ritmo cardíaco. Num segundo teste, usando os mesmo métodos já usados para a avaliação da microcirculação, o efeito de laser speckle foi capaz de reconstruir a onda de pulso e identificar pontos característicos como o pico sistólico e o nó dicrótico. Para alem disto, este mesmo sistema foi usado num teste piloto para segmentar alvos bidimensionais com movimentos longitudinais. Um algoritmo baseado no cálculo da entropia foi usado com sucesso para distinguir dois alvos idênticos, onde apenas um apresentava movimento. Para além disto, este método permitiu segmentar o alvo em movimento sem nenhuma informação antecipada sobre a movimentação dos alvos ou a disposição da cena.

Relativamente ao campo da microcirculação, um teste experimental foi desenvolvido para estudar o efeito dos dispersores estáticos no sinal de laser speckle. Este teste consistiu na avaliação de um fantoma constituído por um micro-canal e diferentes camadas de dispersores. Este fantoma foi usado para simular a perfusão sanguínea em vasos de pequeno calibre. Os dados recolhidos foram processados em termos de contraste e correlação. Os resultados indicaram que a correlação entre duas imagens consecutivas é capaz de identificar a quantidade relativa de dispersores estáticos/dinâmicos e deve ser usada como meio para atingir uma técnica completamente quantitativa. A correlação de speckle demonstrou também ser independente da velocidade dos dispersores dinâmicos. Em relação ao contraste de speckle, o algoritmo temporal apresentou uma boa independência em termos de concentração de dispersores estáticos. O algoritmo espaço-temporal demonstrou ser aquele que apresenta uma melhor coerência com a teoria do efeito laser speckle.

Concluindo, o efeito de laser speckle é uma ferramenta altamente versátil e provou ser capaz de extrair parâmetros hemodinâmicos relacionados com a macrocirculação. Este trabalho também demonstrou que a correlação de laser speckle permite estimar o rácio entre a quantidade de dispersores estáticos/dinâmicos com boa fiabilidade.

Palavras-chave: Laser speckle, forma de onda de pulso, dispersores estáticos, macrocirculação, microcirculação.

Resumé

Le speckle laser est un effet d'interférence longtemps considéré comme néfaste lors de l'utilisation de sources de lumière cohérente. Cependant, pour certaines applications, cet effet peut être bénéfique et utilisé comme source d'information. C'est le cas du domaine biomédical. Ainsi, le speckle laser est utilisé depuis des décennies pour la surveillance du flux sanguin microvasculaire. Il commence à être considéré aussi pour l'extraction de paramètres de la macrocirculation sanguine. Ce travail vise donc tout d'abord à démontrer que le speckle laser permet d'évaluer les paramètres hémodynamiques de la macrocirculation avec fiabilité et à partir d'une technique identique à celle employée dans l'étude de la microcirculation. Ceci conduira à une intégration rapide du dispositif dans les instruments existants. Par ailleurs, l'un des problèmes les plus importants du speckle laser, empêchant l'obtention d'une analyse totalement quantitative, est l'effet des diffuseurs statiques. Ce type de diffuseurs influence fortement le contraste de speckle, conduisant à une mauvaise interprétation des données. Le second objectif de ce travail est donc d'étudier l'effet des diffuseurs statiques sur la corrélation et le contraste du speckle laser.

Afin d'atteindre ces objectifs, nous commençons ce travail par une introduction à la théorie de base du speckle laser. Une analyse critique de la littérature sur ce phénomène est proposée. Nous suggérons également des défis à lever pour les futures applications du speckle laser. Par la suite, nos travaux réalisés dans le domaine de macrocirculation sont exposés. Nous montrons que le speckle laser peut être utilisé pour extraire l'onde de pouls. En outre, une étude multi-longueur d'onde a été menée afin de déterminer quelle longueur d'onde serait la plus appropriée pour l'analyse de la macrocirculation. Les longueurs d'onde plus courtes ont permis d'aboutir à de meilleurs résultats dans l'identification de la fréquence cardiaque. Par ailleurs, nous observons que l'utilisation des mêmes méthodes de traitement du signal que celles employées dans les dispositifs actuels (étude de la microcirculation) permet de reconstituer l'onde de pouls et d'identifier ses points caractéristiques comme le pic systolique et l'encoche dicrote. Par ailleurs, le même dispositif expérimental a été utilisé pour effectuer une segmentation en deux dimensions de cibles avec mouvements longitudinaux. Un algorithme basé sur l'entropie a été appliqué aux données du speckle laser afin de discerner deux cibles identiques, dont une seule est en mouvement. Cette méthode a permis d'effectuer une segmentation en deux dimensions sans connaissances *a priori* sur la scène ou le mouvement de la cible.

En ce qui concerne le domaine de la microcirculation, un test expérimental a été réalisé pour étudier l'effet des diffuseurs statiques sur le signal de speckle laser. Le test expérimental a consisté en un dispositif à micro-canaux, utilisé pour simuler l'écoulement de sang dans les petits vaisseaux sanguins. Cet appareil a été couplé à un ensemble de couches de diffuseurs statiques. Les enregistrements ont été analysés en termes de corrélation et de contraste. Les résultats montrent que la corrélation entre deux images consécutives permet de déterminer la proportion des diffuseurs statique/dynamique et pourrait être utilisée dans des études quantitatives. La corrélation du speckle laser s'est également avérée être indépendante de la vitesse des diffuseurs dynamiques. En ce qui concerne le contraste du speckle laser, l'algorithme de calcul temporel du contraste présente une bonne indépendance vis-à-vis de la variation de la concentration des diffuseurs statiques. Par ailleurs, nous notons que l'algorithme de calcul spatio-temporel présente une meilleure cohérence avec la théorie du speckle laser.

En guise de conclusion, ce travail a permis de montrer que le speckle laser est un effet très polyvalent qui s'avère utile pour extraire les paramètres hémodynamiques de la macrocirculation. Nous démontrons également que la corrélation du speckle laser conduit à une estimation du rapport entre diffuseurs statiques/dynamiques avec une bonne fiabilité. En outre, le calcul temporel du contraste permet d'obtenir de très bonnes performances pour discerner des diffuseurs dynamiques avec des vitesses différentes.

Mots-clés: Laser speckle, onde de pression artérielle, diffuseur statique, macrocirculation, microcirculation.

Abstract

Laser speckle is an interference effect that has been considered as a main drawback in the use of coherent light sources. However, for a specific set of applications, this effect is used as source of information. Among these applications we can find the biomedical ones. Laser speckle has been used for decades for microvascular blood flow monitoring but only now starts to be considered as a method that can also be used for macrocirculation parameters extraction. This work aims at demonstrating that the laser speckle can be used for macrocirculation assessment with good reliability, using the same technique as the ones used in microcirculation assessment. The use of the same methods could lead to a rapid inclusion of this new evaluation in the existing devices. One of the most important laser speckle issues, that prevents a fully quantitative analysis, is the effect of static scatterers. This type of scatterers strongly influences the measurement of speckle contrast, leading to a wrong interpretation of the data. The other objective of this work is to study the effect of static scatterers on the laser speckle correlation and contrast which are used to quantify the blood flow.

This thesis presents the studies conducted to explore the possibility of using the speckle effect for hemodynamic parameters measurement in macrocirculation and the experimental work performed on the effect of static scatterers in microcirculation. Before the experimental work, the thesis begins by an introduction to the basic laser speckle theory. A critical analysis of the available literature is performed in addition to the identification of the future laser speckle challenges. Several ideas are also proposed to deal with the most common issues. The work developed in the macrocirculation field shows that the laser speckle effect can be used to reliably extract the pulse pressure waveform. A multi-wavelength study was also conducted to determine which light wavelength is better for laser speckle macrocirculation analysis. Shorter wavelengths achieved the best results in identifying the heart rate. In a second test, using the same processing methods as the ones that are used in the current devices, speckle effect was able to reconstruct the pulse pressure waveform and identify feature points like the systolic peak and dicrotic notch. Moreover, the same system has been used to perform a two-dimensional segmentation of targets with longitudinal movements. An entropy-based algorithm was applied to the laser speckle data in order to discern between two identical targets where only one is moving. This method was able to perform a two-dimensional segmentation without any *a priori* knowledge on the scene or the target movement.

Regarding the microcirculation field, an experimental test was performed to study the effect of static scatterers on the laser speckle signal. The experimental test consisted of a micro-channel device, used to simulate the blood flow inside small blood vessels, coupled with a set of different static scatterers layers. The recorded laser speckle data were analyzed in terms of correlation and contrast. The results show that the correlation between two consecutive images can identify the proportion of statics/dynamic scatterers and should be used in order to achieve a quantitative laser speckle technique. The speckle correlation also proved to be independent from the dynamic scatterers velocity. Regarding the laser speckle contrast, the temporal algorithm presents a good independence on the variation of static scatterers concentration. The spatio-temporal algorithm should be used because it presents a better concordance with laser speckle theory.

To conclude, laser speckle is a highly versatile tool and proved to be able to extract hemodynamic parameters in macrocirculation. This work also demonstrates that the laser speckle correlation is able to estimate the ratio between static/dynamic scatterers with good reliability. Moreover, the temporal speckle contrast achieved a very good performance in discerning dynamic scatterers with different velocities.

Keywords: Laser speckle, pulse pressure waveform, static scatterer, macrocirculation, microcirculation.

Acknowledgments

First of all I would like to thank my supervisors for their tireless work during the past 4 years. To Dr. João Rendeiro Cardoso who has been available at all the hours, which gave me many useful ideas and advices, which always helped me solving the difficult problems and, most importantly, who has been and will always be a friend. To Professor Anne Humeau-Heurtier who has been tireless in helping me on co-tutelage agreement issues, who always helped me with an enormous celerity in correcting my work and pointing the right direction giving me her unconditional support. To Dr. Edite Figueiras who has always been available to find me solutions for difficult situations, who has left me an outstanding background work and know-how that provide the foundation of this work.

I would like to express my gratitude to Professor Luís Requicha Ferreira who was my first PhD advisor for teaching me a rigorous professional conduct, for encouraging me to do my best all the time and never neglect my work no matter how small it was. I would like to express my special thanks to Professor Carlos Correia, head of the Lab, who has been present during most part of my academic path in the University of Coimbra, for giving me important technical knowledge and instilling me creative thinking.

My sincere thanks also goes to Dr. Joose Kruetzer for providing a microchannel device without which it would not have been possible to perform this work. I would like to thank to Dr. Elisabete Ferreiro, Dr. Paulo Pinheiro and Eng. Carolina Costa for giving me access and help in the laboratory works. I would like to thank my master students Diana Capela, André Carvalheira, Sara Oliveira and Helga Fonseca who gave me continuous challenges and with whom I have learn how to guide and teach. To my lab collegues Tiago Marçal and Miguel Cecílio and former collegues Tânia Pereira, Vânia Almeida and Catarina Pereira who have been part of my daily work always willing to help.

Gostaria de deixar um grande agradecimento aos meus pais e à minha família pelo apoio durante toda a minha vida, por não se terem oposto às minhas decisões e por fazerem sempre o seu melhor por mim. Gostaria de agradecer aos meus amigos Anastácio Sousa, João Dias, Tobias Correia, Danilo Jesus e Pedro Santos por estarem sempre perto mesmo quando estão longe. Por último, mas de modo algum menos importante, quero deixar um muito especial agradecimento à Margarida Martins que me tem acompanhado todos os dias bons e todos os dias maus e tornando a minha vida mais preenchida.

Without all these people this work would not have been possible.

Contents

List of Acronyms

AC Accuracy

AUC Area Under the Curve

AV Atrioventricular

bpm beats per minute

CBF Cerebral Blood Flow

FFT Fast Fourier Transform

FN False Negatives

FOV Field Of View

FP False Positives

fps frames per second

Hb Hemoglobin

HR Heart Rate

LASCA Laser Speckle Contrast Analysis

LDF laser Doppler flowmetry

LDI Laser Doppler Imaging

LSCI Laser Speckle Contrast Imaging

LSF Laser Speckle Flowmetry

LSFG Laser Speckle Flowgraphy

LSI Laser Speckle Imaging

LSPI Laser Speckle Perfusion Imaging

MAP Mean Arterial pulse Pressure

MCC Matthews Correlation Coefficient

MESI Multi-Exposure Speckle Imaging

MPE Maximum Permissible Exposure

NIR Near-Infrared

NPV Negative Predictive Value

OPS Orthogonal Polarization Spectral

pdf probability density function

PPG Photoplethysmograph

PPV Positive Predictive Value

PPW Pulse Pressure Waveform

PSD Power Spectral Density

PTT Pulse Transit Time

PWV Pulse Wave Velocity

RBC Red Blood Cells

RMS Root Mean Square error

ROC Receiver Operating Curve

ROI Region Of Interest

SDF Sidestream Darkfield

SE Sensitivity

SI Similarity Index

SNR Signal-to-Noise Ratio

SP Specificity

SVM Support Vector Machine

SVR Systemic Vascular Resistance

TiVi Tissue Viability

TN True Negatives

TP True Positives

UV Ultraviolet

VC Video Camera

List of Figures

List of Tables

Chapter 1

Introduction

Aristotle (384 BC - 322 BC) was the father of comparative anatomy. He was the first to use the term aorta, from the Greek, $\dot{\alpha}\epsilon\acute{\iota}\rho\omega$*, meaning "to hang".*

This document gather the relevant information arising from the work developed in order to obtain the academic degree of Ph.D. in biomedical Engineering (University of Coimbra) and in Image and Signal Processing (University of Angers). This work has been conducted in a co-tutelage agreement between the University of Angers and the University of Coimbra.

1.1 Background

Speckle is an interference phenomenon that results from the interaction of multiple coherent, acoustic or electromagnetic, waves. Speckle effect is characterized by the visualization of a spatial pattern of light and dark spots called speckles. This phenomenon occurs often in medical ultrasonic devices, because the information carrier is a coherent acoustic wave, and in applications where laser light is used.

Laser speckle effect has been, historically, considered to be a big drawback of the use of coherent light sources. This interference limits the spatial resolution and decreases the Signal-to-Noise Ratio (SNR). Several methods have been developed in order to remove the speckles in applications such as optical coherent tomography [1], holography [2], laser projection systems [3] and synthetic aperture radar imagery [4].

Nevertheless, many useful applications of this effect can be found. Laser speckle proved to be a very powerful metrology technique for applications that range from material characterization [5–7] and velocity determination [8] to biomedical applications [9], or even speech reconstruction [10].

Regarding biomedical applications, laser speckle effect is traditionally used for microcirculation imaging in highly vascularized tissues, for example in the retina and cerebrum. Apart from this tissues, laser speckle has been used in the forearm and hand in order to study the tissue perfusion during external stimulus or artery occlusion. For the macrocirculation case, the development of a large distance fully non-contact method to determine a subject heart rate, could be very important during catastrophes. During natural catastrophes or war scenarios, the possibility to determine, from a large distance, if a subject is alive is of vital importance. This information could lead to a more effective use of the rescue teams.

The speckle effect encodes information about the micro-circulatory system originated in the interaction between the laser light and the moving Red Blood Cells (RBC), *i.e.*, moving scatterers. The most important characteristic of speckle based systems is their ability to produce two-dimensional blood perfusion images, with high temporal resolution, at a fair cost, making them very attractive for clinical use.

The assessment of moderately vascularized tissues represents a major challenge for laser speckle methods. The lack of vascularization means that less useful information is available. A higher presence of static scatterers, which happens in tissues like the hand or forearm, mean a decreasing of the SNR. However, the assessment of this type of tissue is very important in the control and monitorization of diseases like systemic sclerosis and Raynaud's phenomenon. The main investigation line of this thesis is focused on the application of laser speckle in this type of tissues.

Systemic sclerosis is a disease characterized by injuries of the small arteries and by the accumulation of collagen which leads to skin thickening. The systemic sclerosis prevalence in Europe, considering studies that uses data beyond the year 2000, range from 88 to 341 cases per million, depending on the analysed geography and time interval [11]. On the other hand, Raynaud's phenomenon is not an uncommon condition and prevalences of thousands of cases per million can be found [12]. This disease is characterized by vasospastic attacks in the body extremities, mainly in fingers, toes and ears. Both conditions are caused by degeneration or deficient control of the microcirculation system and cause incapacity and discomfort.

The main contribution of this work is to introduce laser speckle techniques for evaluation of hemodynamics in a macrocirculation scale. As stated before, laser speckle is widely used for microcirculation assessment but, by its nature, it can also be used to extract information from macrocirculation. Moreover, the effect of static scatterers is a major issue in the assessment of moderately vascularized tissues because prevent quantitative results. A major experimental work has been conduct in order to study the effect of static scatterers on laser speckle contrast and laser speckle correlation.

1.2 Goals

The goal of this work is to study laser speckle imaging methods in order to improve its usability in moderately vascularized tissues. To achieve this goal, several bench tests and processing algorithms were developed. In some case, *in vivo* pilot experiments were performed. This work can be subdivided in two major contributions, one for macrocirculation assessment and other for microcirculation applications.

1.2.1 Macrocirculation assessment

The first part of this thesis is focused on the presentation of a novel approach for laser speckle use, in order to extract the pulse pressure waveform. This devices could be used as long distance (several meters) heart rate meter, depending only on the used instrumentation. The combination of this novel information with the perfusion map, already extracted from laser speckle, could also lead to a technical improvement of the existing microcirculation assessment devices. Both information sources can be combined in order to extract novel assessment parameters that will help improve medical diagnosis.

An investigation about which light wavelength can achieve better performances has been conducted. Moreover, an experimental set-up was developed to test several processing techniques in order to reconstruct the movement of a silicone membrane. The vibration frequency of the membrane was also identified. The silicone membrane was used as a model of the skin in terms of optical properties. After that, these methods were applied *in vivo* in order to extract the pulse pressure waveform and complete the proof of concept.

1.2.2 Microcirculation assessment

The second part of this thesis is focused on the effect of static scatterers in the quality and reliability of laser speckle signals. This issue is particularly important in the assessment of moderately vascularized tissues because almost all the laser speckle tuning studies are performed in highly vascularized tissues.

To achieve this goal, a bench test was developed by using a microcirculation phantom and multiple static scatterers layers. These layers present different scatterers concentrations. The developed laser speckle imaging prototype allows the user to fully control experimental parameters like exposure time, image resolution, and speckle size. The data extracted from this bench test has been processed using the state of the art laser speckle algorithms. The influence of statics scatterers in speckle correlation and contrast has been determined and discussed.

1.3 Thesis overview

This thesis is divided into 6 chapters:

- Chapter 1 - Introduction: The first chapter presents a generalized overview of the laser speckle phenomenon and the goals of this work. Finally, the scientific contribution is detailed.

- Chapter 2 - Cardiovascular system: The second chapter presents a short overview of medical concepts that are important to understand this work. Issues like the blood components and the heart operation cycle are discussed.

- Chapter 3 - Laser speckle imaging: This chapter presents an extensive review of the laser speckle imaging theory and literature. Moreover, new hypothesis for the resolution of several laser speckle imaging problems are also presented.
- Chapter 4 - Methods: The fourth chapter introduces, in detail, the methods and experiments that have been developed. This chapter is subdivided in three main sections that separate the methods used in the macrocirculation and microcirculation studies, and an algorithm optimization test.
- Chapter 5 - Results: This chapter presents the major results and contributions of this work. Once again, it is divided in three main sections, two to present the results obtained in the microcirculation and macrocirculation studies, and other to show the algorithm optimization test evidences.
- Chapter 6 - Conclusions: The final remarks are presented in this chapter. The limitations of the studies are presented and ideas to correct them are proposed. Finally, the possibilities for future work are explored.

1.4 Scientific contributions

The scientific contributions resulting from this thesis are cited in table 1.1. International journal paper number 3 and conference paper number 3 were result of work developed in the academic part of the Ph.D. in biomedical engineering. All the other were result of the scientific investigation.

1.5 Research Team

This work was only possible due to the dedication and effort of an excellent team of professors and investigators. This work has been conducted from 2012 to 2016 in the former Electronics and Instrumentation Group (GEI), currently LIBPhys (University of Coimbra), and in the Laboratoire Angevin de Recherche en Ingénierie des Systèmes (LARIS - University of Angers). Table 1.2 presents the research team members and their position.

Table 1.1: Reference of scientific contributions.

#	International journal papers	Ref.
1	P. Vaz, A. Humeau-Heurtier, E. Figueiras, C. Correia, J. Cardoso, Laser speckle imaging to monitor microvascular blood flow: a Review, IEEE Reviews in Biomedical Engineering, vol.PP, no.99, pp.1-1 doi: 10.1109/RBME.2016.2532598	[13]
2	P. Vaz, T. Pereira, E. Figueiras, C. Correia, A. Humeau-Heurtier, J. Cardoso, Which wavelength is the best for arterial pulse waveform extraction using laser speckle imaging?, Biomedical Signal Processing and Control, Volume 25, March 2016, Pages 188-195, ISSN 1746-8094, http://dx.doi.org/10.1016/j.bspc.2015.11.013.	[14]
3	P. Vaz, V. Almeida, L.R. Ferreira, C. Correia, J. Cardoso, Signal (Stream) synchronization with White noise sources, in biomedical applications, Biomedical Signal Processing and Control, Volume 18, April 2015, Pages 394-400, ISSN 1746-8094, http://dx.doi.org/10.1016/j.bspc.2015.02.015.	[15]
	International conference proceedings papers	
1	P. Vaz, P. Santos, E. Figueiras, C. Correia, A. Humeau-Heurtier, J. Cardoso, Laser speckle contrast analysis for pulse waveform extraction. Proc. SPIE 9540, European Conferences on Biomedical Optics, Novel Biophotonics Techniques and Applications III, 954007 (July 17, 2015); doi:10.1117/12.2183293.	[16]
2	P. Vaz, D. Capela, T. Pereira, C. Correia, R. Ferreira, A. Humeau-Heurtier, J. Cardoso, Use of laser speckle and entropy computation to segment images of diffuse objects with longitudinal motion. Proc. SPIE 9286, Second International Conference on Applications of Optics and Photonics, 92861H (August 22, 2014), doi:10.1117/12.2060845.	[17]
3	P. Vaz, R. Couceiro, P. Carvalho, J. Henriques, An Automatic method for motion artifacts detection in photoplethysmographic signals referenced with electrocardiography data, in 7th International Conference on Biomedical Engineering and Informatics (BMEI), (pp. 704–708), IEEE, (2014).	[18]

Table 1.2: Composition of the research team.

Position	Name	Research Group
Supervisor	PhD João Rendeiro Cardoso	LIBPhys
Supervisor	Professor Anne Humeau-Heurtier	LARIS
Scientific Advisor	PhD Edite Areias Figueiras	UBNP
Head of the lab	Professor Carlos Manuel Correia	LIBPhys
Technical advisor	Emeritus Professor Luís Requicha Ferreira	LIBPhys
MSc student	MSc Diana Filipa Capela	LIBPhys

Chapter 2

Cardiovascular system

Galen of Pergamum (130 – 200) was a gladiator surgeon. He was the first one to prove that arteries contain blood instead of air.

The main components of the cardiovascular system are the heart, the arteries, the veins, and the capillaries. The cardiovascular system has the function of transport the blood, which carries vital substances, from the heart to the body tissues and *vice versa*. To understand the chemical and physical behaviours of the cardiovascular system it is important to know the structure and function of each of its component. This chapter presents an overview of the cardiovascular system with a focus on arteries and capillaries. These two components are the main information sources for the application of the laser speckle methodologies.

2.1 Blood

The blood is a non-Newtonian fluid, considered as a connective tissue, that mainly contains red blood cells (erythrocytes) suspended in a matrix called plasma [19]. In large arteries, *i.e.* macrocirculation, the blood can be considered as a Newtonian fluid [20]. Contrary, in small arteries, due to the proximity between cell size and vessel diameter, the blood behave like an non-Newtonian emulsion [21, 22].

In a 70 kg man, the total blood volume is about 5.6 litres [23]. The blood density can vary from 1040 to 1050 grams per litre [24] and its viscosity is around 3.55 mPa s [25].

The blood has many vital functions in the organism. It is the transportation vehicle that carries vital substances to the organs, like glucose and oxygen, and transport metabolism waste products, like carbon dioxide, to the disposal sites. The regulative hormones are also transported by the blood from productions sites to specific targets. Moreover, the blood has a major role in the immunologic system because it carries the leukocytes (white blood cells) to the infection sites [26].

The main component of the blood is the plasma (55%), which is composed by water, ions and proteins with defensive and regulative function. The cellular elements of blood correspond to 45% of the total blood volume [27]. The blood viscosity is mainly controlled

Table 2.1: Major components of blood [26,28].

Phase	Constituent	Quantity (* / litre)
Plasma	Sodium	144 mmol
	Chloride	105 mmol
	Hydrogen ion	40 nmol
	Glucose	4.5 mmol
	Cholestrol	5.2 mmol
	Albumin	0.7 mmol
Blood cells	Erythrocytes	5×10^{12} cells
	Leukocytes	5×10^{9} cells
	Platelets	3×10^{11} cells

by the percentage of haematocrit (percentage of erythrocytes) [23]. The major blood constituents and their concentrations are presented in table 2.1.

2.1.1 Plasma

The plasma components can be divided into ions, glucids, proteins and lipids. The water content of plasma represents 92% of the total volume, making it an almost Newtonian fluid [19]. The remaining 8% are composed by ions (blood electrolytes), proteins, lipids, glucids and gas [28]. The ions presented in plasma, and some proteins like albumin, play a major role in maintaining the osmotic balance of the blood and act like a buffer to maintain a pH of approximately 7.4 [27].

The glucids, which are the primary energy source of the human body, are also transported in plasma to the target sites. The blood plasma transport not only glucose, the compound used in cellular respiration, but also other types of monosaccharides and polysaccharides like fructose and glycogen [28]. The blood glucose concentration is often referred as glycemia and it is an important control parameter in diseases like diabetes [29]. The plasma is also the carrier of several hormones, for example insulin and glucagon which stabilize the glycemia. The blood plasma viscosity is usually between 1.1-1.3 mPa s at $37°C$ [30].

2.1.2 Blood cells

Erythrocytes The most numerous blood cells in humans are the erythrocytes, also called red blood cells. Their main function is to transport oxygen (O_2). The RBC are non-nucleated and they are a biconcave disk shape with a diameter of 7.7 μm, thinner in the centre (1.4 μm) and thicker in the boundaries (2.8 μm) [28]. They are produced in the bone marrow and have a lifespan of only 120 days. For that reason, RBC must be renewed continuously by a process called hematopoiesis [26,31].

Their shape promotes the oxygen diffusion due to the large surface/volume ratio [27]. These small cells, with a volume of 90 μm^3 can achieve surface areas of 140 μm^2 leading to a surface/volume ratio of 1.56 [28]. As an example, a perfect sphere with a diameter equal to the RBC has a surface/volume radio of ≈ 0.78, half of the erythrocytes. Another characteristic of the RBC is that they can flow inside very thin capillaries. These small blood vessels can go down to 5 μm of diameter which are smaller than the RBC. In fact, the RBC are very flexible and can deform into a parachute shape to reduce their diameter, and flow through the capillaries [28].

The absence of nucleus in the RBC leave space for a globular protein made of four subunits called Hemoglobin (Hb) [23]. This iron-containing protein is responsible for the transport of O_2 and gives the red colour to erythrocytes. Each RBC contains approximately 280×10^6 Hb molecules, each one with 4 Fe^{++} ions inside a co-factor called heme [28]. The oxygen molecule creates a reversible binding with the Fe^{++} ion. The O_2 molecule oxidizes the iron ion to Fe^{+++} while it transforms into a superoxide (O_2^-) creating a covalently reversible binding. The RBC does not have mitochondria so they can only produce energy by anaerobic metabolism. This is another important characteristic to increase the efficiency of the erythrocytes, otherwise they will consume part of the carried oxygen [27].

Leukocytes The white blood cells, or leukocytes, are the cells in charge of the human body defence against infections. The leukocytes can be classified into granulocytes (70%), monocytes (5%) and lymphocytes (25%). The formers are characterized by the possession of granules and constitute the primary mechanism of the immune system. Some granulocytes are phagocytes which can destroy, and digest, other bacteria while others produce and excrete substances, in order to help the immunological response [26].

Platelets Platelets, also called thrombocytes, are very small cell fragments with a lifespan of approximately 10 days. Their function is to prevent bleeding in case of vascular damage [26].

RBC are the dominant components of blood and the Laser Speckle Imaging (LSI) signal is mainly dependent on their movement. The other blood molecules, like leukocytes, also produce a laser speckle interference signal [32] but their influence in LSI signal is not well studied.

2.2 Human heart

The heart is a strong muscle composed by four chambers which are subdivided into two atria (left and right) and two ventricles (left and right). Figure 2.1 shows an illustration of the human heart labelled with the four chambers and the inflow and outflow vessels. The heart receives the blood by its atria and expels it by the ventricles. The right atrium receives the blood from the systemic circulation (deoxygenated blood) and acts like an holding chamber to prevent the blood flow to stanch. The right atrium pumps the blood

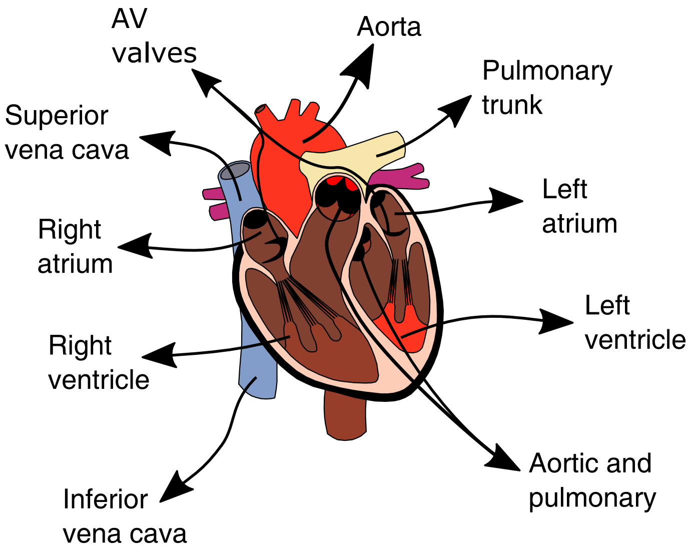

Figure 2.1: The human heart representation. Adapted from a public domain image.

into the right ventricle, which in turn pumps the blood to the pulmonary circulation to be oxygenated in the lungs [33].

The oxygenated blood returns to the heart through the left atrium. Its function is similar to the right atrium. The left ventricle is the strongest chamber of the heart and it pumps the blood throughout the body. The oxygenated blood travels through the arteries carrying oxygen and nutrients. When it reaches the capillary system (very thin blood vessels) nutrients and gases exchanges occur between the tissues and the blood. After that, the deoxygenated blood is collected in the venous system and returns to the heart [34]. The complete set of events that occurs in the heart, from the beginning of an heart beat to the beginning of the next one, is called a cardiac cycle.

2.2.1 Cardiac cycle

The cardiac cycle is divided into two main phases, the diastole and the systole which can be subdivided into six stages: two in systole and four in diastole [35]. The end of the diastole, which is, by convention, the beginning of the cardiac cycle, corresponds to a situation where the ventricles are filled with blood and the pulmonary and aortic valves are closed. After that, the systole begins with the Atrioventricular (AV) valves closure and the isovolumetric contraction of the ventricles which causes a rapid pressure increase (stage S1). The next stage starts with the opening of the aortic valve and pulmonary valve which occurs when the ventricular pressures are higher than the blood vessel pressures. The valves opening cause the blood ejection to systemic and pulmonary circulation (stage S2) [36].

The diastole begins when the pressure inside the ventricles is lower than the pressure in aorta and pulmonary artery. These pressure gradient, caused by the isovolumetric ventricular relaxation, induces the closure of the valves (D1). This phase ends when the ventricles pressure is lower than the atria pressure, inducing the opening of AV valves

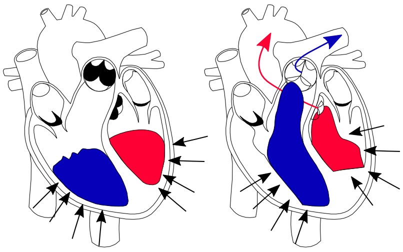

(a) S1 - S2

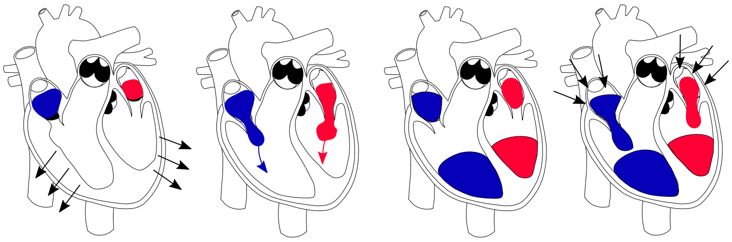

(b) D1 - D2 - D3 - D4

Figure 2.2: Schematic representation of the heart cycle stages. Blue areas represent venous blood and red areas represent arterial blood. Black valves represent closed paths and white valves represent open paths. Black arrows represent forces and coloured arrows fluxes. The image is not to scale. Adapted from public domain image.

and starting a passive, but rapid, ventricle blood filling (D2). The blood flow into the ventricles equalizes the atria and ventricle pressures until the blood flow halts (D3). The final diastole stage is the active atria contraction (D4), atrial systole, which causes an additional 20% ventricle filling [37].

Figure 2.2(a) represents the two stages of systole, S1 and S2, from left to right. The systole is characterized by the ejection of blood into the systemic and pulmonary circulation as a result of the ventricles contraction, first isovolumetrically and finally with volume change. The diastole stages are represented in figure 2.2(b), from left to right. The diastole is generally characterized by the ventricles relaxation and blood filling. The detailed pressure and volume changes, in the left ventricle, during the cardiac cycle are represented in figure 2.3.

2.2.2 Heart rate, stroke volume, and cardiac output

The intrinsic nature of the heart, like a peristaltic pump, leads to a cyclic operation (cardiac cycle), with a period of ejection (systole) and a period of filling (diastole). As all periodic signals, this cycle can be expressed in terms of frequency and amplitude. The frequency of the cardiac cycle is usually called Heart Rate (HR) and its strength, *i.e.* the blood volume ejected by each cycle, is called stroke volume.

The HR is expressed as a frequency unit ($[T^{-1}]$) and, for an adult individual without any cardiac pathologies, is around 70 beats per minute (bpm). Systole and diastole correspond to different durations. The systole lasts approximately 40% of the cardiac cycle and the diastole lasts approximately 60% [34]. The stroke volume is expressed in volume units

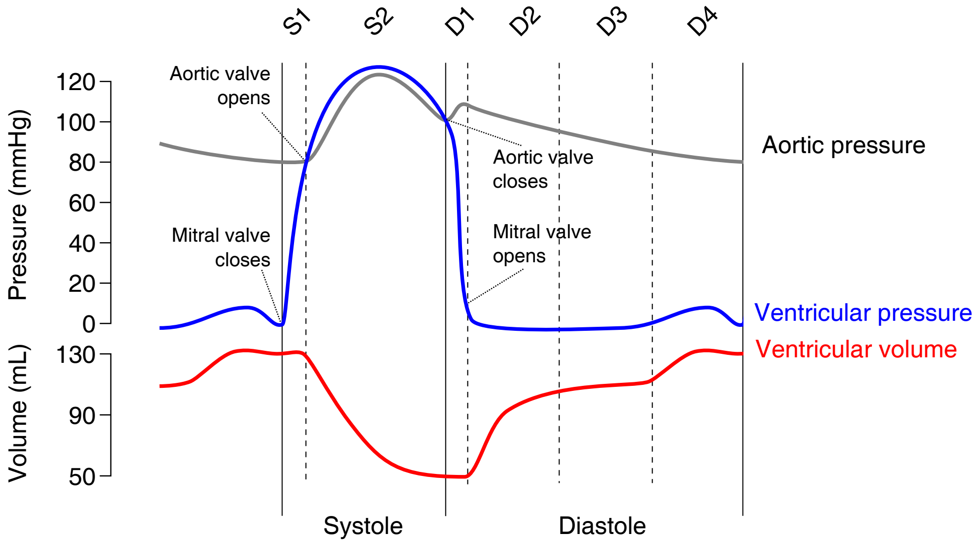

Figure 2.3: Adapted Wiggers diagram [34].

($[V]$) and is about 70 mL in a resting situation and for an average individual male [36].

The capacity of the heart to pump blood is highly dependent from the HR and from the stroke volume. These two parameters can be multiplied to compute the cardiac output (volume of blood ejected by unit of time) [33]. This measurement of the mean blood flow ($\phi = [V] \cdot [T^{-1}]$) is usually expressed in litres per minute and, using the standard values described earlier, for an average individual is approximately 4.9 L/min (0.07 L × 70 bpm). These parameters have been related to the Mean Arterial pulse Pressure (MAP), Pulse Pressure Waveform (PPW) and Systemic Vascular Resistance (SVR) by several studies [38–42].

2.3 Macrocirculation

The macrocirculation corresponds to the blood circulation in large arteries and veins. These vessels are characterized by their multi cell layer morphology and elasticity. Their function is to transport the blood from the heart to all body tissues and to attenuate the effect of the pulsatile pressure gradient generated by the heart. The elastic nature of these blood vessels is also of very important for the maintenance of a minimum blood pressure in the circulatory system [43]. The architectural organization of the arteries is often called arterial tree, because of its branching pattern which is similar to a tree.

2.3.1 Arteries

The arteries receive the blood pumped from the heart and transport it to all the body tissues. Most part of the arteries transport oxygenated blood but, in the pulmonary circulation, they also transport deoxygenated blood. The arteries, and also veins, can be defined as tubes with a biological tissue wall and an inner cavity called lumen which contains blood.

The arterial walls of large vessels are composed by multiple layers with different components. From outside to inside we can find the tunica externa, the tunica media and tunica intima [34]. The outer layer (tunica externa) is mainly composed of connective tissue (collagen) which gives tensile strength to the vessel. Between the externa and the media there is the external elastic lamina which is composed by elastic fibers (elastin). The tunica media, mainly composed by smooth muscle cells, is responsible for the vasodilation and vasoconstriction mechanisms. Between the media and the intima there is another elastic layer (internal elastic lamina). The inner layer, tunica intima, is composed of the basal lamina and the endothelium. The endothelium consist of a single layer of epithelial cells which have a smooth surface to minimize blood flow resistance [27, 44].

Blood vessels are not rigid and they distend when the pressure increases. This arterial property is called compliance ($C = \Delta V/\Delta P$). The elastic properties of the vessels allow a continuous blood flow even during the diastole. When the pressure inside the vessels decreases, the arterial wall shrinks and causes a forward force to push the blood and maintain the flow uninterrupted [37].

The morphological architecture of the arteries is often called arterial tree. This architecture is a complex system that starts in the aorta and ends in the capillarity bed. The arteries diameter changes along the arterial tree, being the aorta the thickest vessel and the capillaries the thinnest ones. The arterial diameter reduction is followed by an increase in the number of vessels and an increase in the total cross-section area of the arterial tree. In each division, the resultant branches have a total cross-section area that varies from approximately 1.2 to 1.7 times the parent cross-section area [45].

Figure 2.4 illustrates the vessel diameter changes along the arterial tree. Vessels diameters are expressed in millimeters and are drawn to scale [46]. Moreover, the layers that constitute the arterial vessels are also illustrated, but, not to scale. The red arrow indicates the blood flow direction. The arterial pressure wave and the total cross-section area along the arterial tree are presented in the graphic of figure 2.4. The total cross-section rises exponentially in the micro-circulatory region (capillaries).

2.3.2 Pulse pressure propagation

The pulse pressure that is generated in the left ventricle produces a pressure gradient with higher pressures in the heart than in the peripheral vessels. This gradient causes the blood ejection and produces a flow away from the heart and in the direction of the body tissues. The pressure gradient between an artery and the correspondent vein that drains its flow is called perfusion pressure [34]. This pressure is propagated through the arterial tree as a DC value with pulsatile component.

The arterial branching results in a reduction of the MAP through the arterial system. Moreover, the pulse pressure waveform also changes along the transmission path because the pressure oscillations, produced by the heart, are attenuated [27] (Fig. 2.4 - red line). This wave distortion is caused by the change in vessels wall morphology, diameter and

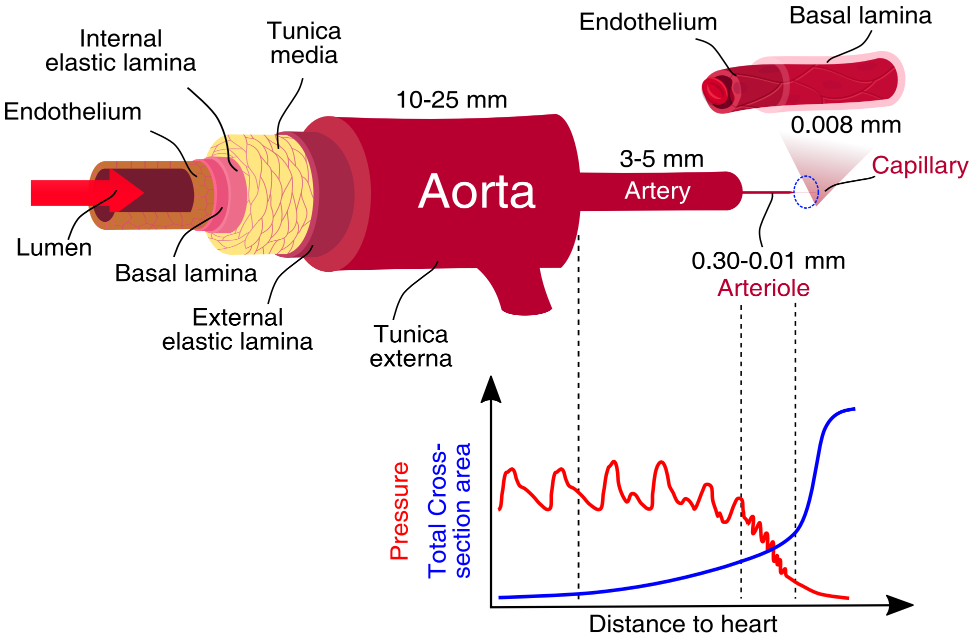

Figure 2.4: Illustration of the arteries morphology. Layer thickness not to scale. Vessels diameter drawn to scale apart from the capillary detail. Adapted from public domain image [47] and [34, 46].

impedance [20].

The pulse wave propagation is neither instantaneous nor constant. Its velocity depends on the pressure gradient generated by the heart and the mechanical properties of the vessels. Moens and Korteweg described the Pulse Wave Velocity (PWV) as [48]:

$$PWV = \sqrt{\frac{E_v h}{d \rho_b}} \quad [m/s] \, , \tag{2.1}$$

where E_v is the vessel Young's module, h is the vessel wall thickness, d is the vessel diameter and ρ_b is the blood density.

The PWV is highly related with the vessels wall mechanical properties which are considered in the Young's module (E_v) and in the blood vessels compliance. These parameters accounts for the arterial elasticity by relating the lumen volume with the transmural pressure. A hypertension situation causes the arteries to have higher Young's modules, *i.e.* less elasticity, because E_v depends on the lumen pressure. Moreover, the stiffening of the arterial tree also causes an increase in the Young's module. Increased PWV has been related with arterial stiffness by several studies [49–52] and corresponds to a marker of cardiovascular risk. All these factors make the PWV the "gold standard" measure of arterial stiffness [43].

The PWV is usually assessed, non-invasively, by computing the Pulse Transit Time (PTT) using the PPW measurement taken at two different sites of the arterial tree [49, 53]. The distance between these two sites is divided by the time gap between the passage of the pulse pressure (PTT). The PWV is usually assessed regionally (carotid-femoral [54, 55], brachial-ankle [56]) but novel assessment techniques can produce local values of PWV by reducing the distance between two sensors whether they are acoustic [57], mechanic [58] or optic [59, 60].

Additionally, the vessels composition is not uniform along the arterial tree. Larger vessels contain more elastin and less smooth muscle. These structural changes also increase the stiffness of blood vessels along the arterial tree making important the assessment of the PWV locally [61].

2.3.3 Aortic pulse pressure waveform

The aorta is the segment of blood vessel that receives the blood right after its ejection from the left ventricle. Not only this interface but also the complete arterial tree have a mechanical impedance which resists to blood flow. The entry of blood in the arteries causes their walls to distend and to increase the pressure inside the vessels, for a healthy subject, to approximately 120 mmHg (systolic pressure) [34]. The arterial pressure and its waveform are a function of the cardiac work, the physical properties of the blood, like viscosity, and the arterial tree impedance [62]. After the end of systole, the pressure decreases slowly due to the blood vessel compliance, maintaining a considerable minimum blood pressure in the vascular system, around 80 mmHg (diastolic pressure). The stiffening of the arterial tree, which is expressed by an increase of the SVR, increases the amount of needed cardiac work to pump the same quantity of blood [63].

Figure 2.5 represents a typical aortic pressure waveform. The strong rise in the aortic pressure happens right after the aortic valve opening which marks the end of the isovolumetric ventricle contraction (S1) and the beginning of blood ejection (S2). The feature point of the waveform, where the maximum pressure is reached, is called systolic peak. After the systolic peak the pressure starts to fall. The aortic valve closure produces a distinctive feature in the waveform (dichrotic notch) which is caused by a short period of backflow [37]. Thereafter, the blood pressure continues to fall until the next cycle, reaching its minimum pressure in the end of the stage S1.

Lastly, an important phenomenon that must be taken into account is the reflected wave. The forward pressure wave produced by the ventricle ejection is reflected in any site of vascular mismatch impedance. Rapid changes in vascular impedance occur mainly in sites of transition between compliant and muscular blood vessels and branching points with large lumen diameter changes [43].

The reflected pressure waves travel back to the aorta and, when PWV is high [64], they arrive during the systolic phase. This phenomenon cause an increase of the systolic pressure and thus a decrease of the blood flow [65, 66]. This reflected wave is visible in figure 2.5 and corresponds to a pathological situation. In healthy and young subjects, where the PWV is low, the reflected wave is summed in peripheral arteries pressure instead of aortic pressure wave. This phenomenon is called pulse pressure amplification and leads to the presence of higher pressures in the systemic arteries than in central arteries [43].

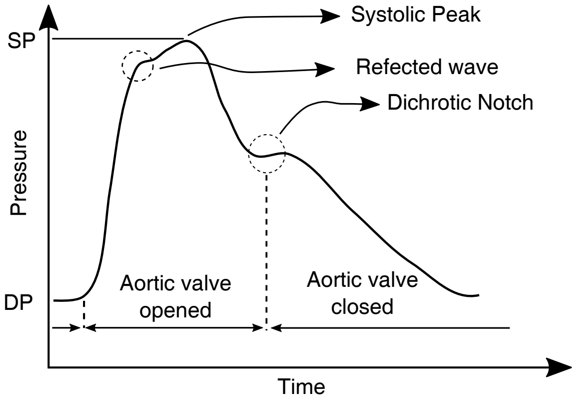

Figure 2.5: Aortic pressure waveform. SP - Systolic pressure. DP - Diastolic pressure. Adapted from [67].

2.3.4 Blood flow *versus* blood speed

The blood flow is often confused with blood speed but these terms represent different quantities. The flow indicates the motion of a blood volume in a certain amount of time (volumetric flow rate). Contrary, the blood speed represents the velocity of blood particles. The blood velocity is usually expressed as the mean value of the blood particles.

When a fluid flows through a closed tube it must obey to the conservation of mass, *i.e.*, the tube inlet mass must be equal to the outlet mass. The mass inlet, or outlet, per time unity, for incompressible fluids, can be expressed as:

$$\frac{dm}{dt} = \rho_f v_f A \ [kg/s] \, , \tag{2.2}$$

where ρ_f is the fluid density, v_f is the fluid velocity and A the tube cross-section area. The definition of volumetric flow (Q) is simply:

$$Q = \frac{dV}{dt} = \frac{1}{\rho_f}\frac{dm}{dt} = v_f A \ [m^3/s] \, . \tag{2.3}$$

The volumetric flow depends on the fluid velocity and on the tube cross-section area. By considering blood flowing through a blood vessel with different inlet and outlet calibres we obtain the continuity equation:

$$Q_b = Q'_b \equiv v_b A = v'_b A' \, , \tag{2.4}$$

where Q_b is the inlet volumetric flow, Q'_b is the outlet volumetric flow, v_b is the blood velocity at the input vessel with a cross-section area A and v'_b is the blood velocity at the output vessel with a cross-section area A'. This equation is illustrated in figure 2.6. The blood volumes represented in blue (V_1 and V_2) are equal. The cross-section A_1 is smaller than A_2 therefore, by the continuity equation, the velocity of the particles in V_1 is higher than the velocity of the particles in V_2.

The human circulatory system is a closed system, *i.e.* the amount of blood is ap-

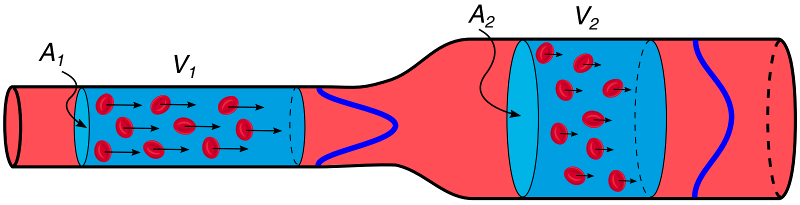

Figure 2.6: Illustration of the continuity equation.

proximately constant in time. In accordance to the principle of mass conservation, the volumetric flow must be constant along the circulatory system. However, to maintain the volumetric flow constant, the blood velocity must change because the total cross-section area of the arterial tree increases with the distance to the heart.

The increasing of the total cross-section area, as in the arterial tree, results in a blood speed decrease. In fact, the blood speed is approximately 48 cm/s in aorta and only 0.1 cm/s in capillaries [27]. Moreover, the blood velocity is not uniform along the vessel transversal cross-section. Near the vessel's walls the particles have lower velocities compared to the core particles. This effect is due to the friction between the blood and the vessel's walls [20]. The blue curves of figure 2.6 represent the magnitude of the velocity in each vessel.

The blood volumetric flow rate can also be expressed by the application of the Ohm's law to fluid mechanics [68]:

$$Q_b = \frac{\Delta P}{R} \quad [m^3/s], \tag{2.5}$$

where ΔP is the pressure gradient between the vessel extremities, and R the vessel resistance. Jean Poiseuille performed many works regarding the vascular system that resulted in the definition of the Poiseuille's law [69]. This law corresponds to a more complete analysis that determines how the vessels morphology influences the blood flow [34]:

$$Q_b = \frac{\Delta P \pi r^4}{8\eta_b l} \quad [m^3/s], \tag{2.6}$$

where r is the vessel radius, l the vessel length and η_b the blood viscosity. By combining equations (2.5) and (2.6) we can obtain the flow resistance in terms of the blood viscosity and vessel geometry as [23]:

$$R = \frac{8\eta_b l}{\pi r^4} \quad [Pa.s.m^{-3}]. \tag{2.7}$$

This conclusion proves that the flow resistance in a blood vessels is proportional to the blood viscosity and the vessel length. However, it is also inversely proportional to the vessel diameter fourth power, making this parameter crucial in the flow resistance determination. The Poiseuille law is only applicable for a rigid tube, *i.e.* zero compliance, and laminar flow. In healthy subjects, the aorta is the only blood vessel without laminar flow (turbulent flow) [34] and capillaries meet these requirements because they have very low compliance and the blood flow is laminar [70].

According to the Poiseuille's law, the thinner the vessel the higher resistance it presents. However, the arterioles are the blood vessels with the highest blood flow resistance [34]. These blood vessels have the ability to control the blood inflow in the capillarity bed by increasing or decreasing the flow resistance [71]. A more detailed analysis on arterioles will be performed in section 2.4.

2.3.5 Veins

After the capillarity bed (see section 2.4.2), the blood is collected by the veins. These blood vessels transport the deoxygenated blood back to the heart. The veins are similar to the arteries in size and structure but their walls are thinner than the arterial walls [72]. Most part of the blood is stored in veins (75%) because of their large total cross-section area [33]. The veins have a very important function by controlling the blood availability. Their walls can constrict or expand in order to store more or less blood, making it available for the arterial circulation according to the body needs [73].

The pressure inside veins is also much smaller than in arteries. This fact causes the veins to collapse easily when an external pressure is applied. Moreover, veins are much more compliant than the arteries. To allow the blood to reach the heart, against the gravity force, and since the pressure inside veins is low, they need to have valves that prevent blood backflow [72].

2.3.6 Non-invasive assessment techniques

The central aortic blood pressure is an excellent predictor of cardiovascular risk. However, the assessment of the central pressure requires the use of invasive methods like cardiac catheterization. Alternative non-invasive methods were developed recently in order to estimate the central pulse pressure by recording the peripheral pulse pressure waveform.

As discussed in section 2.3.3 the peripheral pulse pressure is higher than the central pressure due to the amplification effect. Moreover, its waveform is also different due to the vascular attenuation and reflection phenomenons. To estimate the central pressures and waveform, mathematical methods, like transfer functions, can be applied to the peripheral waveform. These methods are usually applied in the common carotid artery, radial artery and brachial artery [74].

Traditional techniques, to record the peripheral pulse pressure wave, comprise oscillometry and applanation tonometry methods. Modifications of these techniques are commercially available in order to estimate the central pressure waveform and analyze its feature points. Tonometric based systems record the pulse pressure waveform by applying a pressure sensor on the top of a major superficial artery (radial or femoral). The application of these methods, in order to record arterial pressure changes, requires the compression of the artery into a solid base (usually bone) [75].

Contrary, oscillometric methods use high sensitive cuff sensors operating above the

Table 2.2: Commercial devices available for pulse waveform analysis.

Device	Method	Measuring sites	Sensor	Central pressure	PWV	Ref
SphygmoCor®	Tonometry	Radial; Femoral	Millar tonometer	Yes^1	Regionally	[75]
Arteriograph®	Oscillometry	Brachial	Cuff	Yes^2	Regionally	[76]
Complior Analyse®	Vibrometry	Carotid; Femoral	Piezo-electric	Yes^3	Regionally	[77]
Omron HEM-9000AI ®	Tonometry	Radial	Tonometer array	Yes^4	No	[78]

[1] Method based on the application of transfer function to the peripheral waveform.

[2] Method based on the application of a cuff pressure above the systolic pressure.

[3] Method based on the assumption that carotid pressure is equivalent to central pressure.

[4] Method based on the identification of the early and late systolic blood pressure.

systolic pressure. The artery occlusion forms a small diaphragm which is sensitive to the pressure changes produced in the heart, like the human ear is sensitive to sound. These "beats" are detected by pressure sensors in the cuff pneumatic circuit. The advantage of cuff based system is that they do not need external calibrations. By its nature, oscillometric systems are able to determine the systolic and diastolic blood pressures [76].

Several commercial devices are available to record and analyze the pulse pressure waveform, some of them with capability to estimate the central pressure waveform. Additionally, devices with multiple sensors are able to determine the PWV, which is also an important marker of the cardiovascular risk. The most used commercial devices are detailed in table 2.2.

Beyond these commercial devices, the techniques previously referenced in subsection 2.3.2 for local PWV determination have the capability to assess and analyze the peripheral pulse pressure waveform. For example, the optical techniques developed by Pereira *et al.* [59, 79] are based on the emission of coherent or non-coherent light, being a truly non-contact system. The light reflected from the artery, which is amplitude modulated (non-coherent case) or frequency modulated (coherent case), is recorded by a photodiode. The registered profile corresponds to the artery distension wave which is extremely related with the pulse pressure waveform. Moreover, bio-electric impedance techniques were also developed to extract parameters related with the arterial stiffness and PWV [80].

2.4 Microcirculation

To the system composed of small vessels (less then 300 μm [43]) is often called microcirculation and its function is to deliver the nutrients and gases to the body tissues. The microcirculation comprises the arterioles, capillaries, venules, and terminal lymphatic vessels. It is characterized by low blood velocity and short distances between the vessel and the body tissues [71]. Our analysis will be exclusively dedicated to the blood carrier vessels.

Figure 2.7 represents the microvasculature organization. The arterioles derive in metar-

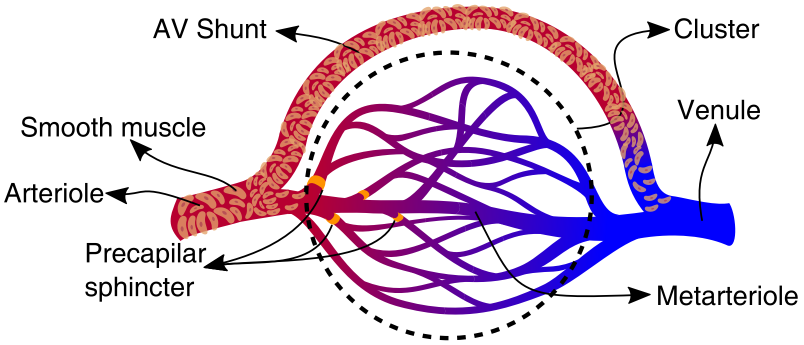

Figure 2.7: Schematic of a capillary cluster. Adapted from public domain image [47].

terioles which in turn branch into the capillary bed. The vessels are then gathered in a venule. During the passage of the blood in the capillary bed, the blood loses oxygen and gains carbon dioxide. Nutrients are also delivered to the surrounding tissues and metabolic waste (like ammonia) is collected [33].

2.4.1 Arterioles

As stated before, the arterioles are the most resistive vessels in the vascular system. They conduct the blood to the capillaries and have an important role in blood flow control. Their diameters range from 20 to 50 μm and they have a strong muscular layer which is responsible for the control of the lumen diameter and therefore the blood flow resistance (Eq. (2.7)) [23, 81].

Each metarteriole gives origin to a capillarity group called cluster (Fig. 2.7) [34]. The metarteriole sizes range from 10 to 15 μm. This type of blood vessels can contain a smooth muscle precapillary sphincter in the transition between metarteriole and capillary. This sphincter acts in response to local concentration of molecules which can cause the closing of a region of capillaries. When they are open, the vessel diameter is just enough to able a single cell to passes through, forming an inline of blood cells [23].

2.4.2 Capillaries

The capillaries constitute the smallest vessels of the circulatory system with a diameter between 5 and 8 μm and a length up to 1 mm [34]. They have the effective function of delivering nutrients and oxygen to the surrounding tissues and collect waste from metabolism. The large vessels, arteries and veins, are just the transportation vehicle for the blood to reach tissues farther from the heart and return to it.

The capillaries have an endothelium formed with a single cell layer and no smooth muscle [33]. This very thin wall promote the diffusion of substances (nutrients and gases) to and from the body tissues but did not allow for blood flow regulation. The transfer of substances between capillaries and body tissues is passive and, from the solute perspective, can be expressed by the diffusion coefficient and by the concentration gradient of each substance. The capillarity wall area and relative permeability are also parameters that affect the diffusion [34].

The total cross-section of the capillaries is about 25 times larger than the arterioles, reducing considerably the blood velocity in this zone [34]. Besides the constant low pressures and low velocity present in capillaries, the blood does not flow continuously [81]. This phenomenon is called vasomotion and results from a cyclical contraction of the metarterioles and precapillary sphincters.

2.4.3 Arteriovenous shunts

The arteriovenous shunts (AV shunts) correspond to direct connections between the arterioles and venules without passing through the capillary bed (Fig. 2.7). When these passages are open, a great quantity of blood flows through it, decreasing the total peripheral resistance and thus increasing the cardiac output [82].

A deficient control of the AV shunts could lead to output cardiac failure. A too low peripheral resistance will cause an increase in the blood venous return that overloads the heart, making it work at full power. When a person tries to perform physical exercises with this condition, the heart will not be able to increase its cardiac output anymore. Because a great quantity of blood is passing in the AV shunts, the body tissues will be poor perfused, causing a cardiac failure. This condition is called high-output failure [83].

The microcirculation organization is highly dependent on the analysed tissue. In this thesis, more attention will be given on cutaneous microcirculation.

2.4.4 Cutaneous microcirculation

The skin is the largest body organ with an exterior contact surface that can achieve values up to 2 m^2 [84]. Besides the large extension of skin, the cutaneous microcirculation is much greater than it should be for its nutrition [85]. The skin is the adequate organ to regulate the temperature of the human body because of its large extension and proximity to exterior. The function of cutaneous microcirulation is then, apart from nutrition, thermoregulation [86].

The skin is constituted by the epidermis, a superficial layer, the dermis, a deep layer, and by the hypodermis (Fig. 2.8). The epidermis is a non perfused layer with a thickness of approximately 400 μm. The dermis has a thickness of approximately 1.5 mm and is highly perfused. The deeper layer, the hypodermis, is mainly composed by fat tissue.

The cutaneous microcirculation is organized in two horizontal plexus, the nutritive layer and the thermoregulatory layer [87]. The superficial plexus is situated in the papillary dermis which is right above the epidermis (nutritive layer). Between the dermis and the hypodermis is the deep plexus, named sub-papillary plexus (thermoregulatory layer) [87,88].

The nutritive plexus comprises the capillarity loops and forms most of the skin microvasculature [85]. Approximately 10 % of the blood flow is in the nutritional layer [87].

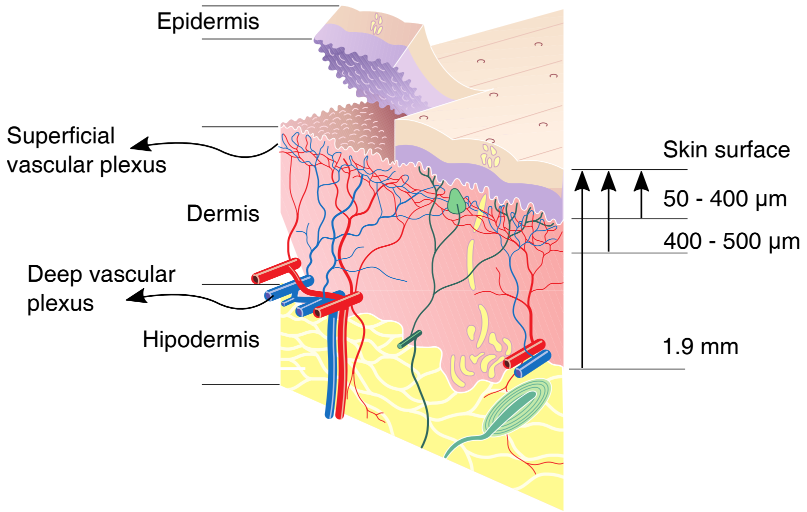

Figure 2.8: Skin layers and their thinness. Adapted from public domain image [90] and [87].

The blood vessels present in this plexus are made of small arterioles, metarterioles, capillaries, and postcapillary venules with diameters up to 25 μm [85].

Vertical blood vessels connect the deep plexus with the superficial plexus and deliver nutrients to the core dermis. The thermoregulatory plexus contains approximately 90% of the blood flow of skin microvasculature [87] and is an important reservoir of blood [86]. The blood vessels in this deeper layer can achieve diameters of 50 μm [85]. It is in this region that the AV shunts can be found, mainly in the body extremities, *e.g.* fingers and nose [89]. These structures are extremely important in thermal control since they can reduce or increase of the blood flow from 1 to 150 mL/100g of skin [86]. The more blood flow in superficial plexus, the more heat is transferred to the exterior medium.

2.4.5 Cutaneous optical properties

The assessment of blood flow at different depths is important to understand the different control mechanisms that are associated with the nutritive and thermoregulatory layers [85, 87, 88]. When considering the use of optical techniques to assess microcirculation, the optical properties of the skin are an important parameter [91–93].

The epidermis is mainly composed by keratin, which is a tough and fibrous protein, and by melanin which is a yellow-brown pigment that is responsible of the absorption of the Ultraviolet (UV) radiation. Contrary, the dremis is composed by connective tissue containing collagen and elastin [94]. Moreover, since the blood is the subject of study, it is important to take into account the optical properties of the RBC which are mainly composed by haemoglobin.

Assuming that the sample is thick enough to prevent transmission, the combination of both absorbed and scattered light is equal to the incident light. In this case, the optical proprieties of a predetermined sample are usually defined by its absorption and scattering

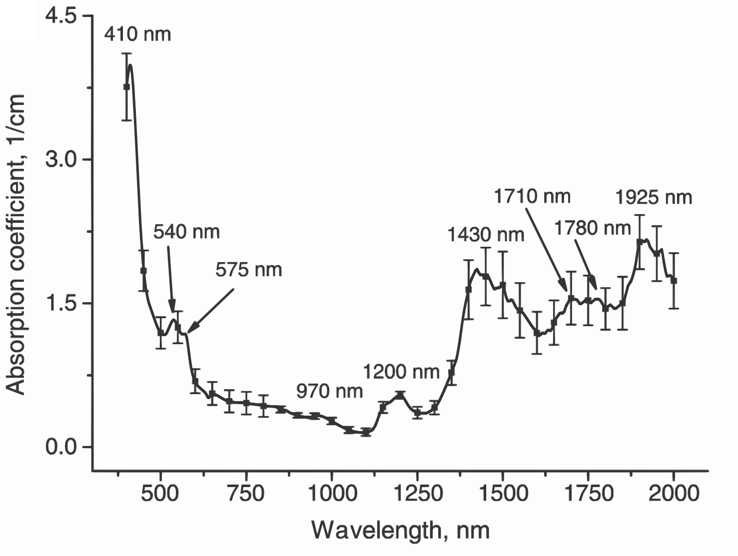

Figure 2.9: Absorption coefficient of the skin as function of the light wavelength. Adapted from [92].

coefficients. The oxyhaemoglobin reaches its maximal absorption coefficient values at the wavelengths of 410, 540, and 575 nm [92]. Moreover, in the spectral band between 600 nm and 1100 nm the absorption coefficient of the skin is lower than in the other frequencies and decreases with the increase of the wavelength [95].

With this information, one can conclude that Near-Infrared (NIR) light (from 800 to 1000 nm) penetrates more in the skin [92] than visible light (Fig. 2.9). In the other hand, from UV to green light (up to 550 nm) the skin penetrations is low. In the red band, the light penetration increases exponential due to the strong decrease in the oxyhaemoglobin absorption coefficient [95].

2.4.6 Non-invasive assessment techniques

Non-invasive assessing techniques are used not only to monitor cardiovascular diseases but also in pharmacological tests and post-occlusive reactive hyperaemia. This type of functional studies are often performed using optical techniques [96]. Since this work is related with these techniques, an overview of optical methods to assess microcirculation will be performed in this subsection.

Optical assessment techniques can record blood perfusion data in single-point or two-dimensional images and are based on different methodologies. Among all the assessment techniques, we can highlight laser Doppler flowmetry (LDF), laser speckle imaging (LSI), Orthogonal Polarization Spectral (OPS) imaging, Sidestream Darkfield (SDF) imaging, and Tissue Viability (TiVi).

Both OPS and SDF correspond to video-microscopic techniques which are based on the ancestral method of direct capillary observation. The OPS imaging working principle is very simple and consists on the tissue illumination using polarized light. Moreover, a video camera, coupled with a microscopy lens and a polarizer, is used to acquire the tissue image. The incident light polarization orientation is orthogonal to the video camera polarizer. This orientation blocks the light reflect from superficial boundaries because only the light reflected from inner tissues change its polarization. The key factor in OPS and SDF is the used light wavelength (548 nm or 530 nm). This green light is strongly absorbed by RBC making them to appear dark in a grey matrix [96]. The SDF imaging consists in simple improvements of OPS. For example, by illuminating the tissue outside the field of view, this technique excludes the use of polarized light. Moreover, by synchronizing the illumination and image acquisition, the image blurring is reduced.

The TiVi is another imaging technique, similar with the OPS but using polarized white light and wide-field imaging. The images obtained by TiVi are colour isolated and then the values of the green channel are subtracted from the red channel [97]. This signal processing is applied in order to remove the background contribution which is low and equal for the three channels [98]. The obtained images represent the concentration of RBC.

Laser Doppler flowmetry is a well established technique to monitor microcirculation [99]. This technique is based on the analysis of the light frequency change when coherent light is reflected from moving RBC [100]. The Doppler effect is characterized by a light frequency shift proportional to the scatterers velocity. These techniques provide blood flow indexes which are qualitative. Traditional LDF methods are single-point acquisition systems, *i.e.* they assess a small tissue volume (1 mm^2) [101]. Recent developments in LDF led to the introduction of depth discrimination capabilities [99] and self-mixing mode [102]. The depth discrimination feature is achieved by using multiple light source wavelengths and multiple source-detector separations.

A two-dimensional image technique called Laser Doppler Imaging (LDI) is also available. The first devices used a scanning laser to record multiple single-point signals. This process is time consuming because the perfusion image is obtained as a group of single measurements [96], leading to a strong reduction of the method temporal resolution. Full-frame Doppler imaging prototypes are also available by using an expanded laser beam and high frame rate video cameras. However, this is a very expensive technique due to the requirement of a video camera with frame rates of approximately 20k frames per second [103].

Some of the commercial devices for microcirculation assessment are detailed in table 2.3. Laser speckle techniques and applications will be discussed in chapter 3 and, for that reason, no information is given here except the one available in table 2.3.

2.5 Cardiovascular conditions

As stated in section 2.3 the pulse waveform and PWV are biological markers of the arterial stiffness. Similarly, the arterial stiffness is highly related with hypertension, being an independent marker of cardiovascular mortality [109, 110]. Techniques to assess and

Table 2.3: Commercial devices available for perfusion blood flow assessment.

Device	Method	Measuring site	Depth variation	2-D	Ref
Periflux 5000	Doppler	Skin	Yes [5]	No	[104]
moorVMS-LDF	Doppler	Skin; Endo sites; Cerebrum	Yes [6]	No	[105]
moorLDI2-HIR	Doppler	Skin	No	Yes[7]	[106]
PeriCam PSI	Speckle	Skin; Cerebrum	No	Yes	[107]
moorFLPI-2	Speckle	Skin; Cerebrum	No	Yes	[108]

[5] Method based in multiple source-detector separations.

[6] Using needle probes to assess deeper tissues.

[7] Method based in laser beam scanning.

analyze the pulse waveform provide important information to predict and control hypertension [61, 111].

For example, arteriosclerosis produces a stiffening of the arteries, causing an increase in PWV and an early return of the reflected wave. Hypertension can enhance the arterial degradation that occurs with ageing, making the pulse waveform of younger individuals similar to elder ones. Moreover, diabetes is also an arterial stiffening disease [64].

Regarding the microcirculation, the assessment of blood perfusion is also important because several diseases can manifest on multiple levels. Arterial stiffness cause an hypoperfusion. Non-related cardiac diseases, like diabetes and Alzheimer, can also cause vascular malfunctions [100]. Moreover, diseases like Raynaud phenomenon and systemic sclerosis cause severe vasoconstriction of blood vessels [112].

Chapter 3

Laser speckle imaging

William Herschel (1738 – 1822), in 1800, discovered the first non-visible radiation (infra-red) while he was moving a thermometer through the light diffracted by a prism.

The designation LSI is associated with a two-dimensional assessment technique used in many research fields and for many applications such as object's velocity measurements [8, 113], surface roughness evaluation [114–116], laser vibrometry [117–119] and speech detection [10]. This chapter presents an overview of the laser speckle theory and practical concepts that can be found in literature as well as a critical analysis.

A *compendium* about the methods that have been used since the last 35 years is missing [120] and could facilitate the work of actual and future researchers in this field. To understand the laser speckle nature and the methods used in laser speckle biomedical applications, concepts like speckle contrast, decorrelation time, and Multi-Exposure Speckle Imaging (MESI) will be explored.

3.1 Speckle contrast: an overview

Laser speckle is a random scattering phenomenon which can only be described statistically [121]. The laser speckle effect occurs when coherent light is reflected by a rough surface, on the scale of the used optical wavelength. This effect is characterized by a visualization of a granularity pattern composed by dark and bright spots.

The intensity registered in the observation plane ($I(t)$), at a specific point, is the coherent sum of many photon electric fields ($E(t)$) scattered from different points in the surface (or medium). Since each scattered wave travels different optical paths, they arrive to the observation plane with phase differences leading to constructive or destructive interferences [122].

In perfect conditions, *i.e.* using a complete coherent and polarized light source and assessing a static medium, the speckle pattern resulting from the sample illumination is fully developed, which means that its speckles are perfectly defined. An example of an ideal speckle pattern is presented in figure 3.1.

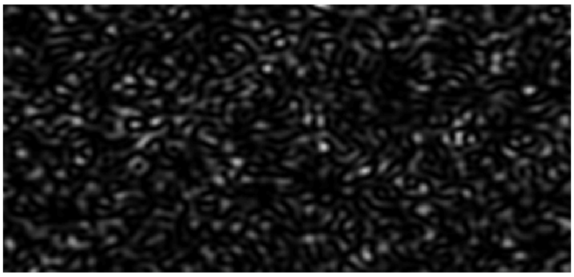

Figure 3.1: Fully developed speckle pattern (digitally simulated).

3.1.1 Contrast

It has been shown by Goodman [123] (appendix A) that, for a fully developed speckle pattern, there is an equality between its spatial standard deviation (σ_s) and its spatial mean intensity ($\langle I \rangle$). This is an extremely useful property of the speckle interference effect that is crucial to its application in the biomedical field [124].

Following this idea, the contrast (K) is typically defined as the quotient between the standard deviation and the mean intensity [125]:

$$K = \frac{\sigma_s}{\langle I \rangle} = \frac{\sqrt{\langle (I - \langle I \rangle)^2 \rangle}}{\langle I \rangle} \,. \tag{3.1}$$

Considering the statistical equality between σ_s and $\langle I \rangle$ of a fully developed speckle pattern, we can easily conclude that the contrast of an ideal speckle pattern is 1. In fact, under real conditions, the contrast is always lower than 1 and follows the condition [126]:

$$0 \leq K \leq 1 \,. \tag{3.2}$$

In practice, the speckle pattern that is observed depends on the used coherent light source, on the illuminated medium and on the image plane. The speckle pattern will remain unchanged if all of these elements are static (static speckle pattern). On the contrary, a time-change in one of these components cause a modification of the interference pattern (dynamic speckle pattern) [127].

The temporal changes in the interference pattern contain information about the motion of scattering particles inside the medium, for example the red blood cells flowing inside the blood vessels or the artery walls vibration during the cardiac cycle. The interference patterns can acquired using imaging systems with finite exposure times. These systems perform an integration of all the light that reaches the sensor during the exposure time. If the speckle pattern changes during this integration time, the areas where the particles are moving become blurred [128].

It is clear that, by using an imaging system, it is the intensity ($I(t)$) of the speckle pattern that is recorded. By having this intensity spatial distribution (2D image) we can compute the speckle contrast (K) easily. But, what is the relation of the measured contrast with the scatterers motion?

3.1.2 Autocorrelation functions

Following the analysis performed by Boas and Yodh [129] we can deduce that the time fluctuations on the intensity of speckles contain information on the dynamic properties of the medium. These intensity fluctuations are provoked by electric field changes caused by the light scattered by moving particles. A good way to analyze these fluctuations is by using the normalized temporal autocorrelation function of the electric field which, for complex functions ($E(t) \in \mathbb{C}$), is expressed as [130]:

$$g_1(\tau) = \frac{\langle E(t) \cdot E^*(t+\tau) \rangle}{\langle E(t) \cdot E^*(t) \rangle} \, , \tag{3.3}$$

where $E(t)$ is the electric field at a time t, E^* denotes the complex conjugate of the electric field, τ the autocorrelation delay time and $\langle \, \rangle$ the time average.

The conventional imaging systems are not sensitive to the light electric field. They are indeed sensitive to intensity fluctuations so it is convenient to analyze the signal information as the normalized temporal autocorrelation function of the intensity [131]. Since the intensity is a real function ($I(t) \in \mathbb{R}$), its autocorrelation is simply:

$$g_2(\tau) = \frac{\langle I(t) \cdot I(t+\tau) \rangle}{\langle I(t)^2 \rangle} \, . \tag{3.4}$$

The Siegert relation relates the second-order autocorrelation function (Eq. (3.4)) with the first-order autocorrelation function (Eq. (3.3) [122, 132]):

$$g_2(\tau) = 1 + \beta \, |g_1(\tau)|^2 \, , \tag{3.5}$$

where $\beta \leq 1$ is a normalization constant that accounts for the system imperfections, namely the absence of light stability and the speckle averaging due to spatial aliasing in the image detector [125, 133, 134]. In perfect conditions this constant equals 1 and in the preliminary speckle studies it has been omitted [126, 135]. The quadratic factor in equation (3.5) occurs because of the relation between amplitude and intensity [136].

It has been proved by Bandyopadhyay *et al.* [122] that the reduced variance of the intensity across the pixels is related with $g_1(\tau)$. This relation falls from the idea that the variance of the intensity levels of the speckle pattern is greater when the scatterers motion is slow compared to the imaging system exposure time. The following equation states the relationship between speckle contrast and the autocorrelation function in terms of the imaging system exposure time:

$$K(T)^2 = \frac{2\beta}{T} \int_0^T |g_1(\tau)|^2 \left(1 - \frac{\tau}{T}\right) d\tau \, , \tag{3.6}$$

where $K(T)$ is the speckle contrast as function of the exposure time T. The second term in this expression $(1 - \tau/T)$ was not used in the original expression of Briers and Webster [124] but several authors claim that this is the correct expression and must be used to obtain accurate results [9, 133, 137–139]. This term falls from the transformation of the covariance into the correlation where a triangular weighting must be multiplied to the autocorrelation function [122].

3.1.3 Motion distributions

Two major types of motions can be considered for dynamic scatterers, the ordered flow of the scatterers (ordered motion) and its disordered motion due to the effect of temperature (Brownian motion) [125]. The rotation of the molecules is often neglected in speckle analysis [131].

The dynamic scatterers motion was historically considered to be close to Brownian motion [121, 125, 135, 137, 139–141] and with single scattering contribution [142] with the argument that the blood circulation is dense and turbulent [139]. These arguments support the approximation of the velocity distribution to a Lorentzian profile which leads to the autocorrelation function:

$$g_1^L(\tau) = e^{-\tau/\tau_{cl}} \,, \tag{3.7}$$

where τ_{cl} is the Lorentzian decorrelation time. The decorrelation time (τ_c) quantifies the dynamics of the scatterers [133], where lower values of τ_c are associated with light scattered from scatterers with faster movements. Mathematically, this factor represents the autocorrelation function width by determining the delay where the function falls from 1 to $1/e$ [124]. If we substitute the autocorrelation function by a Lorentzian profile in equation (3.6) gives:

$$K^L(T)^2 = \beta \left[\frac{\tau_{cl}}{T} + \frac{\tau_{cl}^2}{2T^2} \left(e^{-2T/\tau_{cl}} - 1 \right) \right] \,. \tag{3.8}$$

The issue with this model is that, in fact, there are several motions present in blood flow [125, 143] and the ideal model can be explained as a combination of both Brownian (Lorentzian distribution) and ordered motion (Gaussian distribution). The autocorrelation function for a Gaussian velocity distribution, which is the correct one for ordered flow, has been proposed as [125]:

$$g_1^G(\tau) = e^{-(\tau/\tau_{cg})^2} \,, \tag{3.9}$$

where τ_{cg} is the Gaussian decorrelation time. A different equation was suggested by Ramirez-San-Juan *et al.* [143] as the correct one to model a Gaussian velocity distribution:

$$g_1^G(\tau) = e^{-\frac{\pi}{2}(\tau/\tau_{cg})^2} \,. \tag{3.10}$$

Their choice of the Gaussian model is based on the Mandel's definition of decorrelation time which states that:

$$\tau_c = \int_{-\infty}^{\infty} |g_1^G(\tau)^2| \,. \tag{3.11}$$

In fact, equation (3.10), does not satisfies our original definition of the decorrelation time (falling from 1 to $1/e$ in τ_c). Contrary, the equation (3.9) does meet this requirement and, additionally, it is most referred in literature to model a Gaussian velocity distribution. Having this into account, we assume that it is the most correct one.

By substituting the autocorrelation function for a Gaussian velocity profile, Eq. (3.9), in equation (3.6) yields to:

$$K^G(T)^2 = \beta \left[\frac{\tau_{cg}}{T} \sqrt{\frac{\pi}{2}}\, erf(\sqrt{2}\ T/\tau_{cg}) + \frac{\tau_{cg}^2}{2T^2} \left(e^{-2T^2/\tau_{cg}^2} - 1 \right) \right] . \tag{3.12}$$

It is important to retain that the autocorrelation functions, equations (3.7) and (3.9) are valid only for an approximation of single dynamic scattering regime, however it was shown that they present a good agreement with the experimental results [142].

Some recent works [125,131,140] claim that biological tissues are complex systems with multiple sources of decorrelation, *i.e.* multiple phenomenons that cause speckle pattern time changes. For this reason, an autocorrelation function that uses both Lorentzian and Gaussian distributions was proposed as the more accurate model [131]:

$$|g_1(\tau)|^2 \approx |g_1^L(\tau)|^2 \times |g_1^G(\tau)|^2 \, . \tag{3.13}$$

Although, even in the definition of the combined velocity distribution there are some misunderstandings because other authors [125] describe the model as a convolution between the two distributions yielding to a Voigt profile:

$$g_1^V(\tau) = g_1^L(\tau) * g_1^G(\tau) \, , \tag{3.14}$$

where $g_1^V(\tau)$ represents the Voigt autocorrelation function.

The model that should be used for the autocorrelation function is still a major investigation field in laser speckle contrast imaging [121]. Some authors say that a combined Lorentzian and Gaussian distribution improves the accuracy of the extracted scatterers velocities [125, 131].

Despite all these works, the Lorentzian model is still the most used in laser speckle studies [137, 141, 144–146] because the ordered flow is approximated by a Lorentzian distribution when scattering is random and uncorrelated [147]. Although, several authors [125,148,149] claim that the Gaussian distribution should be used.

Figure 3.2 shows the difference in the obtained contrast when the function parameters (T and τ_c) are fixed for both Lorentzian and Gaussian distributions. In can be seen that large differences are present when the exposure time is equal to the laser speckle decorrelation time ($T \approx \tau_c$). This is equivalent to say that, using the Lorentzian distribution to analyse ordered flows yields to larger errors when $\tau_c/T \approx 1$. This is particularly important because the sensitivity of speckle contrast in relation to the decorrelation time ($|dK/d(1/\tau_c)|$) is maximum when $\tau_c/T = 1$ [9, 128].

Equations (3.8) and (3.12) are, theoretically, the most correct ones, but some authors

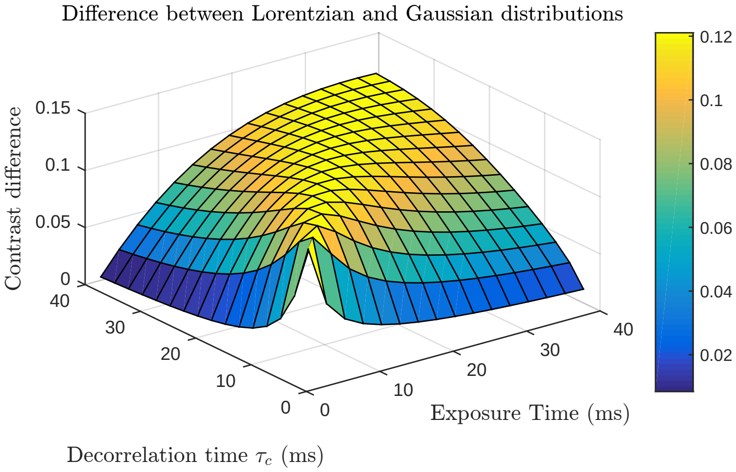

Figure 3.2: Error in contrast between the use of Lorentzian and Gaussian distribution as function of the exposure time and decorrelation time.

pointed that the use of the triangular weighting, Eq. (3.6) - second term, does not improve the results for biomedical applications when long exposure times ($T >> \tau_c$) are used [9, 125, 150].

Smausz *et al.* [151] showed that, the curve obtain by using the equation (3.6) without the triangular weighting can be approximated to the theoretically correct one by substituting the variable T/τ_c for $\approx 0.57\, T/\tau_c$ in the case of a Lorentzian distribution.

The steps to find this multiplier constant ($C_s = 0.57$) were not detailed in their work, but the visual inspection of the two curves (triangular weighting vs variable substitution) show only small differences between them (Fig. 3 of [151]). The issue with this approach is that the window selected to show the curves ($0.001 \le \tau_c/T \le 10$) has great influence in the multiplier constant that seems to better adjust both curves.

In our opinion, a more numerical approach should be performed. A simulation was done in order to find which is the proper C_s for both Lorentzian and Gaussian distributions. The C_s was swapped between 0.1 and 0.9 and the resultant function was compared with the theoretically correct ones (Eqs. (3.8) and (3.12)). The comparison was performed by computing the Root Mean Square error (RMS) between the two functions within a window of interest ($0.001 \le \tau_c/T \le 2$) because in real applications the exposure time is always higher than the scatterers decorrelation time. Decorrelation times of microseconds have been reported elsewhere [133, 152].

The results of the simulation revealed that the constant that minimize the RMS error are $C_s = 0.61$ for Lorentzian distribution with an error of 0.96% and $C_s = 0.62$ for Gaussian distribution with an error of 1.6%. The approximated equations correspondent to equations (3.8) and (3.12) can be expressed as:

$$K^L(T)^2 \approx \frac{\beta}{2}\,\frac{\tau_{cl}}{0.61T} \times (1 - e^{-2\times 0.61T/\tau_{cl}})\,, \tag{3.15}$$

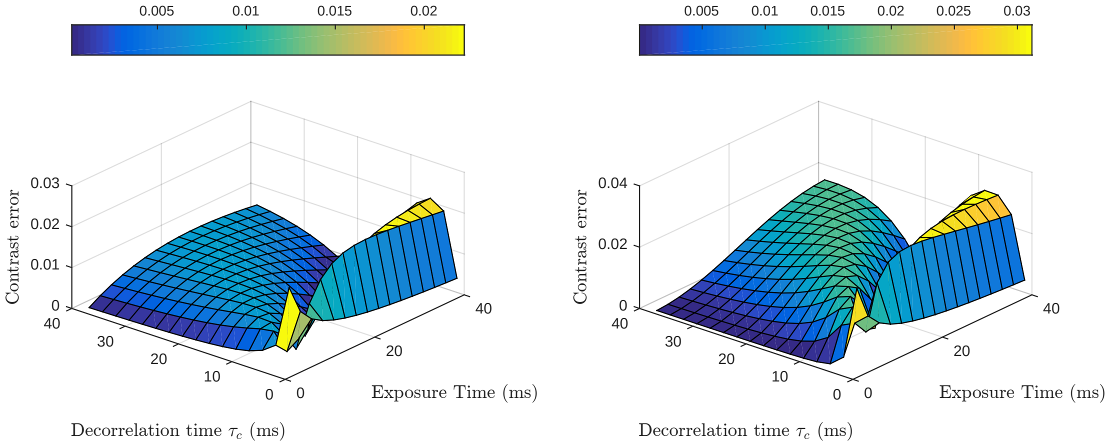

(a) Lorentzian Distribution (b) Gaussian Distribution

Figure 3.3: Errors between the theoretical speckle visibility equations (Eq. (3.8) and eq. (3.12)) and the shifted approximate equations (Eqs. (3.15) and (3.16)).

for a Lorentzian distribution and:

$$K^G(T)^2 \approx \frac{\beta}{2}\,\frac{\tau_{cg}}{0.62T}\sqrt{\frac{\pi}{2}} \times erf(\sqrt{2} \times 0.62T/\tau_{cg})\,, \tag{3.16}$$

for a Gaussian distribution. The differences between the theoretical equations and the approximate equations can be seen in figure 3.3. These figures show that the maximum error in the contrast determination is low for all the combination of values of exposure time and decorrelation time. The maximum error in contrast for Lorentzian distribution is 0.022 and for Gaussian distribution is 0.031 which makes this approximation a much more valid than the application of a Lorentzian distribution to ordered flow (Fig. 3.2).

Our suggestion is that approximated equations, like (3.15) and (3.16), could be used when faster processing is required. This equations are much simpler and do not have any quadratic terms which reduces the computation time to evaluate them. The online processing in multi-exposure speckle contrast techniques takes long time because it is necessary to fit the data to the selected equation for every single pixel in the contrast image.

3.1.4 Normalization constant

The normalization constant (β) is related with the experimental apparatus and needs to be computed for each individual system. The normalization constant can be computed as $\beta = \lim_{T\to 0} K(T)$ [153]. As stated in section 3.1.2, β is a constant that accounts for the system light source instability, the system vibrations, non perfect polarization of the laser light and, principally, the spatial averaging that can occur when the speckle size is smaller than two times the imaging system pixel size (Nyquist limit) [131]. Other authors [134, 153] propose a different normalization constant in which the normalization constant is $\beta_m = 1/K_{max}$. This is equivalent to say that β_m is the maximum contrast admissible by the experimental system. Then, this constant is multiplied by the measured contrast and not by the right side of equation (3.6). This definition does not contradict the original definition [129, 154] which states that $\beta \leq 1$. Although β_m is always greater than 1 ($K_{max} < 1$), it is multiplied in the opposite side of the equation (left side of Eq. (3.6)).

Thompson *et al.* [134] also showed, by simulation and experiment, that the normalization constant β_m produces good result to correct for both spacial averaging and external illumination. In practice, since the normalization constant should be to "normalize" the contrast curve ($K(T)$), this second definition could be more useful and easier to determine experimentally.

Other type of normalization constant can also be used, in addition to β. The constant ν is often defined as a quantification of the noise presented in the system [133] and its expressed by an additive term in equation (3.6). This term is propagated through the speckle contrast analysis which leads to its inclusion in all the equations that relate contrast, decorrelation time and exposure time. In this work, the authors decide to omitted this term in the theoretical analysis. Its influence will be discussed during the analysis of static scatterers (subsection 3.1.5) and other practical concepts (subsection 3.2.3).

3.1.5 Effect of static scatterers

The presented models are based on a set of approximations that does not account for the presence of static scatterers in the assessed medium. However, static scatterers produce a speckle contrast component that remains constant when the imaging system exposure time increases. The light that is scattered by this type of elements cause an underestimation of the system dynamics, in other words, it increases the speckle contrast [9]. The static scatterers issue has been neglected in the past [122, 150, 155] but nowadays it is often take into account [137, 142]. The existence of static scatterers has been addressed by Parthasarathy *et al.* [133] and Zakharov *et al.* [156] who presented a new method to compute accurate values of τ_c.

The effective electrical field function that reaches the imaging system is a sum of photons scattered by static particles and photons scattered by dynamic particles:

$$E(t) = E_d(t) + E_s \,, \tag{3.17}$$

where $E_d(t)$ is the light electrical field scattered by dynamic particles and E_s the light electrical field scattered by static particles which, since its contribution is static, does not variate in time [129, 132]. The new intensity autocorrelation function can be expressed as:

$$g_2(\tau) = 1 + \beta[(1-\rho)^2|g_{1d}(\tau)|^2 + 2\rho(1-\rho)|g_{1d}(\tau)| + \rho^2] \,, \tag{3.18}$$

where $g_{1d}(\tau)$ is the field autocorrelation function of the fluctuating electric fields and ρ

is the fraction of light that is scattered by static particles, $\rho = \langle I_s \rangle / (\langle I_s \rangle + \langle I_d \rangle)$. When using the constant ρ one should be very careful about its definition. Inverse definitions can be founded in literature. For example, several author define ρ as the dynamic fraction of scattered light [9, 128, 131, 148] instead of the definition mentioned above.

The intensity autocorrelation function depends on the autocorrelation function of the dynamic component but does not depend on the autocorrelation function of the static component. This result is expected because, since the static electric field is constant, its autocorrelation function is approximately 1 for all the delay values (τ) [129].

By applying the Siegert relation (Eq. (3.5)) to the intensity autocorrelation function yields to the new field autocorrelation function [132]:

$$g_1(\tau) = (1-\rho)|g_{1d}(\tau)| + \rho\,. \tag{3.19}$$

By substituting the modified field autocorrelation function, equation (3.19), in the integral of equation (3.6) yields to:

$$\begin{aligned} K^2(T) &= \frac{2\beta}{T}\int_0^T [(1-\rho)^2|g_{1d}(\tau)| + \rho]^2 (1-\frac{\tau}{T})d\tau = \\ &= \frac{2\beta}{T}\left[(1-\rho)^2\int_0^T |g_{1d}(\tau)|^2(1-\frac{\tau}{T})d\tau + 2\rho(1-\rho)\int_0^T |g_{1d}(\tau)|(1-\frac{\tau}{T})d\tau + \right. \\ &\qquad \left. + \int_0^T \rho^2(1-\frac{\tau}{T})d\tau\right]. \end{aligned} \tag{3.20}$$

The first integral is equivalent to equation (3.6). The modified speckle contrast relation shares a common part with the original relation in the same way that the autocorrelation function is a weight-average of the static and dynamic components. The analytical result for the integral of the equation (3.20), if we consider the autocorrelation function of the dynamic component as an exponential decay (Lorentzian distribution), is [9]:

$$K(T)^2 = \beta\left[(1-\rho)^2\frac{e^{-2x}-1+2x}{2x^2} + 4\rho(1-\rho)\frac{e^{-x}-1+x}{x^2} + \rho^2\right], \tag{3.21}$$

where $x = T/\tau_c$. Using the same method, the speckle contrast for an autocorrelation function with Gaussian distribution is [131]:

$$\begin{aligned} K(T)^2 = \beta\Bigg[&(1-\rho)^2\frac{e^{-2x^2}-1+\sqrt{2\pi}x\,\mathrm{erf}(\sqrt{2}x)}{2x^2} + \\ &+ 2\rho(1-\rho)\frac{e^{-x^2}-1+\sqrt{\pi x}\,\mathrm{erf}(x)}{x^2} + \rho^2\Bigg]. \end{aligned} \tag{3.22}$$

Several authors [128,131,133,134], include in the equations (3.21) and (3.22) an additive term that accounts for the noise presented in the system (ν_{noise} or C_{noise} or K_0). In practice, this term accounts for the minimum contrast that the system can achieve. This term is mainly used in analysis that take in account the presence of static scatterers but it can also be applied in more studies.

In our opinion, these two last equations, equations (3.21) and (3.22) also known as speckle visibility expressions [142], are the most complete equation to analyze laser speckle contrast data because they take in account the imperfections of the imaging systems, the non-complete light coherence and the presence of static scatterers in the medium.

Simpler results to deal with the system imperfections and static scatterers can also be found in literature [151, 153] like the equation:

$$K(T)^2 = \frac{1}{T} \int_0^T P_1^2 |g_1(\tau)|^2 \left(1 - \frac{\tau}{T}\right) + P_2^2 \, d\tau \, . \tag{3.23}$$

This methods includes two constants (P_1 and P_2) in equation (3.6) that normalize the experimentally obtained speckle contrast between 0 and 1. These constants account for both the static scatterers and speckle spatial averaging, and can be determined by fitting this equation to the laser speckle data [153].

Even if this is a promising method and very simple to apply, current researcher still prefer to use the methods described by Zakharov *et al.* and Parthasarathy *et al.*, Eq. (3.20), because of its better transcription of the laws of physics.

3.1.6 Scatterers velocity determination

Laser speckle contrast analysis starts with the computation of the imaging contrast and wants to determine the decorrelation time. The more accurate is the decorrelation time determination, the more accurate will be the scatterers velocity estimation. This is why so many different methods and analyzes have been used during the last years to improve the estimation of τ_c. The most used relationship between scatterers velocity and decorrelation time, used in laser speckle contrast analysis, can be expressed as [124]:

$$V = \frac{\lambda}{2\pi \, \tau_c} \, , \tag{3.24}$$

where V is the scatterers velocity and λ is the laser light wavelength. This relation is not physics-based and is purely speculative [125] but it is the most used expression to relate the decorrelation time with the scatterers velocity. This simple relation is based on the intuitive notion that the velocity is inversely proportional to the decorrelation time $V \propto 1/\tau_c$.

A different method, with a concrete physical meaning, which relates the scatterers velocity with the decorrelation time can be found in the literature [125, 140]:

$$V = PSF/\tau_c \, , \tag{3.25}$$

where PSF is the point-spread function [140]. The PSF describes the response of an imaging system to a point source. From the knowledge of the authors, this velocity determination model has not been used in laser speckle contrast studies possibly due to the difficulty in determine the PSF.

A correct determination of the decorrelation time and its relation with the velocity of the scatterers are the key factors to achieve a quantitative laser speckle analysis instead of a qualitative analysis, which is performed in most of the cases [9]. In laser speckle studies, arbitrary perfusion units are more used than velocity values because laser speckle does not proved yet to be a quantitate tool for complex systems [121, 125, 138, 139, 157, 158]. This is in fact, one of the most discussed topics in laser speckle contrast imaging research. However, if the decorrelation time is computed with an high accuracy, controlled phantoms or external methods can be used to calibrate the laser speckle data [131, 142].

3.2 Practical considerations

The theoretical considerations discussed in the previous section represent the basis of laser speckle contrast analysis for biomedical applications. However, researchers and engineers have to face another type of problems when performing experimental work or build laser speckle devices such as: How to maximize the speckle contrast? How to increase the SNR? What are the values for β and ρ?

3.2.1 Speckle size

One of the most important point to consider when designing a laser speckle system is the size of each individual speckle. When a digital imaging system is used, *e.g.* CCD or CMOS sensors, their pixels have a finite size. When the size of each speckle, produced in the imaging sensor, is smaller than its pixel size, a spatial averaging occurs. In other words, more than one speckle are imaged by the same pixel which cause a decrease in contrast [120].

The speckle size in the imaging sensor depends on the used wavelength (λ) and also, and mainly, on the optical components used to image that pattern. The minimum resolvable speckle size, for a system using an imaging lens, is often expressed by [159]:

$$d_{min} \approx 1.2(1 + M)\lambda\, f/\# \,, \tag{3.26}$$

where d_{min} is the minimum speckle diameter in the same units as the used wavelength, M is the imaging system magnification, and $f/\#$ is the imaging lens f-number. From this expression, it is clear that the easiest parameter to control is the f-number which can be changed by using the iris diaphragm.

Several authors [134, 160] use equation (3.26) to compute an estimative of the speckle size, but others [9, 139] use a different one ($d_{min} \approx 2.4(1 + M)\lambda\, f/\#$). The older reference mentioning the size of speckle, in the knowledge of the author, can be found in Ennos's work [159] which states that the minimum diameter of a speckle, viewed by an imaging system, is given by equation (3.26). This expression is valid for the so-called “subjective” speckle [159]. The “subjective” speckle is obtained with imaging systems that use a lens to project the speckle pattern in the imaging sensor [161]. This type is the most common in biomedical applications.

It is also possible to obtain a different type of speckle pattern, the “objective” speckle [159]. This type of speckle is obtained as a projection of the speckle pattern in the imaging sensor without any lens. In fact, the speckle pattern is a tri-dimensional field through the space and the position of the imaging sensor in “objective” speckle will influence the observed pattern [162, 163].

An experimental method to determine the speckle size has also been presented by Khaksari and Kirkpatrick [164]. This method is important to estimate the real speckle size of the image and it is implemented by computing the image two dimensional Power Spectral Density (PSD). Using this structure, the minimum speckle size can be determined by:

$$d_{min} = 2\,\frac{l_{PSD}}{d_{energy}}\,, \tag{3.27}$$

where l_{PSD} is the power spectral density width, in pixels and d_{energy} is the diameter of the energy band.

Several authors have studied the influence of having different speckles sizes on the contrast values [134, 165, 166]. All the studies agree in the definition of speckle size as the number of pixels that a single speckle occupy in the imaging sensor (pixels/speckle), but different optimal speckle sizes can be found in literature.

The first works in LSI tried to maximize the system spatial resolution by forcing a speckle size equal to the sensor pixel size. Also several recent papers [160, 167] continue to use 1 pixel/speckle which could be a reckless decision.

The work of Kirkpatrick *et al.* [166] showed, by simulation and *in vitro* tests, that this size is under the Nyquist limit, leading to spatial aliasing and resulting in a reduction of up to 30% in the global contrast. They conclude that a minimum size of 2 pixels/speckle should be used for the speckle size but, in the opinion of the author, their results show that the contrast is still increasing for larger speckle sizes (up to 4 pixels/speckle). The increasing of the speckle size has the disadvantage of lowering the spatial resolution because, since each speckle is the source of information, there are fewer speckles in the same area.

The simulations performed by Thompson *et al.* [134] showed that with 2 pixels/speckle there is also a significant decrease in the contrast (10% lower than theoretically maximum contrast value). However, their most important conclusion regarding speckle size, in the opinion of the author, is that the optimal speckle size is influenced by the size of the window used to compute the contrast.

Ramirez-San-Juan *et al.* [165] also address this issue and concluded that the speckle size has no strong influence in the determination of τ_c, mainly when the temporal con-

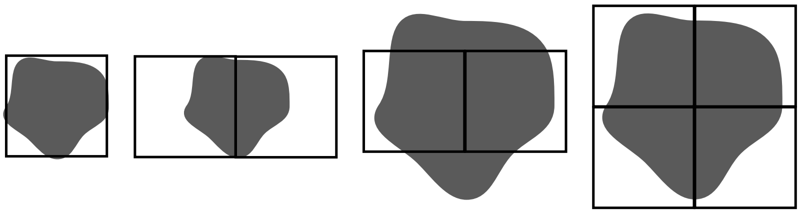

Figure 3.4: Spatial sampling of speckles with different sizes.

trast analysis is used (see section 3.4). However, this conclusion is only valid for relative measurements of τ_c in an homogeneous phantom. Their work is based on simplifications that are not valid in real cases, like the absence of static scatterers. Therefore, this result should be use carefully.

Contrary conclusions have also been reported. For example, Qiu *et al.* [168] suggested that speckle sizes under the pixel size can improve the SNR and the spatial resolution. This paper also shows that β can correct the speckle contrast even when the speckle size is under the pixel size. However, the metric used to analyze the SNR should be taken with caution ($SNR \equiv \mu_K / \sigma_K$). It is clear that when the speckle size is smaller than the pixel size a spatial averaging occurs acting like a general 2D low-pass filter. This filter produces an intensity increase in darker zones and an intensity decreasing in brighter zones. The intensity average is maintained but its standard deviation is reduced, leading to a reduction in the mean contrast and, more important, to an uniformization of the contrast values. This uniformizatinon causes a reduction in the contrast standard deviation which results in an increase of the SNR in the proposed metric.

The size defined by 2 pixels/speckle is also ambiguous since it is expected that each speckle has a round shape. Figure 3.4 illustrates the spatial sampling of speckles. Both images from the left side show a speckle with diameter equals to one pixel. The two images from the right side show a speckle with a diameter of 2 pixels/speckle. This illustration shows that it is necessary to have 4 pixels to sample a speckle with 2 pixels of diameter. In the opinion of the author, considering a spatial contrast computation (see section 3.4), the speckle size should be maintained above the Nyquist limit for both dimensions (x and y). To ensure a correct sampling of a two-dimensional structure, at least two points should be sampled in each dimension.

In line with this idea, in a very recent work, Braga and Gonzáles-Peña [169] studied the influence of laser speckle size in bio-speckles *in vitro*. They tested sizes from 1.31 to 5.23 pixels/speckle and found that the size of 3.6 pixels/speckle ensure the best results for both time and frequency domains.

As it was mentioned before, the increase in speckle size leads to a strong decrease in spatial-resolution. First, less speckles are present in the same region and, second, larger processing windows must be used to ensure enough statistical relevance in the computation of the contrast. On the other hand, nowadays, the current imaging systems are very powerful and can have dozens of Megapixels which balance the reduction of the resolution that happens due to the processing method.

3.2.2 Light polarization

The photons produced by light amplification by stimulated emission of radiation (LASER) are coherent and, usually, linearly polarized. When light penetrates in a boundary between two media with distinct refractive indexes (n) some fraction of the light is reflected while the other fraction is transmitted. The amount of light that is reflected and transmitted depends on the angle of incidence of the photons, on its polarization, and on the media refractive indexes. This light behaviour is described by the Fresnel equations [170].

The light that is reflected in this process is partially polarized in the orientation perpendicular to the plane of incidence (s-polarized). Most of laser speckle contrast systems uses a polarizer in front of the imaging system to cut this light because it does not contain any information about moving scatterers inside the tissue [160].

However, by the Fresnel equation it is possible to prove that, if the incident light is polarized parallel to the plane of incidence (p-polarized), there is an angle in which all the light is transmitted through the medium. This angle is the so-called Brewster's angle [171] and can be expressed as [170]:

$$\tan(\theta_B) = n_2/n_1 \ , \tag{3.28}$$

where θ_B is the Brewster angle in radians, n_1 is the refractive index of the initial medium, and n_2 is the refractive index of the final medium. Figure 3.5 shows the case of a p-polarized light beam that reaches a media boundary with the Brewster's angle. There is no reflected beam because, as stated early, the reflected beam should be s-polarized but this component is not present in the incident beam.

From the knowledge of the author, the Brewster's angle has not been explored in laser speckle contrast systems for biomedical application. However, some authors [147] have used an illumination angle between 30-40 degrees but with no estimation of the exact Brewster's angle.

The use of this penetration angle could prevent the reflection of light in the first tissue layer, increasing the penetration depth and avoiding the use of the imaging system polarizer. Another advantage of this approach is that it can allow the reduction of the laser power because more light is transmitted to the tissue and interacts in the inner moving scatterers. Even so, the exact Brewster's Angle is difficult to define because the optical refractive index of biological tissues is difficult to estimate. Moreover, since the samples are not usually flat, it is difficult to select an illumination angle very close to Brewster's Angle which reduces the efficiency of this method. Anyway, more studies should be performed in order to confirm or refute this hypothesis.

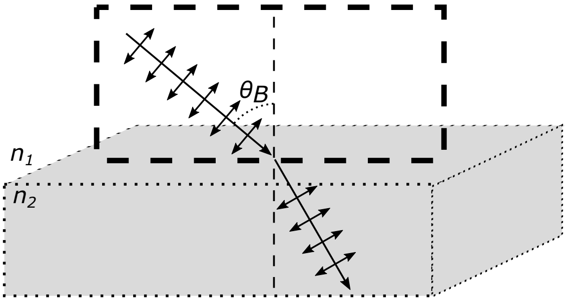

Figure 3.5: Schematic representation of the Brewer's angle. n_1 and n_2 represent the refractive index of each medium and θ_B the Brewster's angle. The plane of incidence is represented by the thick-dashed rectangle.

3.2.3 Measuring beta (β)

The normalization constant (β) is the variable in laser speckle contrast theory to account for the spatial averaging and partial light polarization. The primary and the precise way to compute β is to use the limit $\beta = \lim_{T \to 0} K(T)$. To compute this limit, it is necessary to take a set of contrast images with different exposure times (T), from an exclusive dynamic sample ($\rho = 0$), and apply a fitting process to the obtained contrast [133]. The y-intercep value obtained by the fitting process is equal to β and the function minimum value ($\lim_{T \to \infty} K(T)$) is equal to C_{noise}. [8]

A different process to compute β_m (see subsection 3.1.4) was proposed by Thompson *et al.* [134] based on an experimental measure. This process is interesting for systems that are not capable of changing their exposure time (single-exposure speckle imaging). The experimental measurement consists in determining the maximum speckle contrast that the system can achieve by using a sample with only static scatterers ($\rho = 1$). In their work [134], the authors used a block of a mixture of silicone and alumina because this material tries to mimic the skin optical properties. Other authors have used simply a paper white sheet to simulate the static scatterers [168]. The value of β_m is then multiplied by the obtained contrast in order to normalize it.

3.2.4 Measuring rho (ρ)

Even if the variable ρ has been presented in many works as the correct way to account for static scatterers, its determination is not yet very clear. However, an experimental and objective method to compute ρ as been presented by Zakharov *et al.* [132].

Typical LSI systems use exposure times (T) longer than the dynamic scatterers decorrelation time (τ_c) and inter-frame times (Δt) longer than the exposure times. The inter-frame time represents the time between the acquisition of one frame and the next one. Considering this, the relation $\Delta t > T >> \tau_c$ can be stated.

Since the decorrelation time is much lower than the inter-frame time, all the dynamic scatterers have been completely decorrelated between consecutive frames ($g_{1d}(\Delta t) \approx 0$).

---

[8] See explanation of subsection 3.1.5 on page 36.

So, the correlation between consecutive frames appear only due to the presence of static scatterers. By substitution this proposition in equation (3.18) we obtained:

$$g_2(\Delta t) = 1 + \beta\rho^2 \tag{3.29}$$

where $g_2(\Delta t)$ is the correlation between two consecutive frames. Since the static scatterers distribution is not homogeneous in the tissues, the ρ values should be computed locally in Regions Of Interest (ROIs) smaller than the image. The computation area can be defined by the researcher.

The initial proposition of this analysis invalidates its use when high speed systems are used like the one proposed in [137, 172]. These type of systems have inter-frames times much lower than the exposure time. In this case, a traditional analysis of the sample should be performed in advance to compute the values of ρ.

3.2.5 Exposure time

The exposure time is another practical key factor that influences the final results of a LSI system. Different exposure times are sensitive to different scatterers velocity. For example shorter exposure times are more suitable to analyze rapid scatterers and *vice versa* [173]. This is a very intuitive notion because at very short exposure times, only rapid movements will cause image blurring.

Some works have been published [128,173] in order to determine the optimal exposure times to use in biomedical applications. Yuan *et al.* proposed that, in case of the use of a single exposure time, its value should be ≈ 5 ms. They showed that the relative sensitivity of speckle contrast is maximum when $T/\tau_c > 1.8$ but also that the SNR decreases with the increasing exposure time. Their experiments were conducted in cerebral blood flow imaging. Single-exposure time systems can be found in literature with many different exposure times. A tendency to use exposure times between 1 ms and 20 ms is noticed [174–179].

Regarding the available commercial devices, the exposure times can be fixed or variable, but so far none have multi-exposure capabilities. For example, the moorFLPI (Moor Instruments - United Kingdom) can be set-up to acquire images with 1, 2, 4 or 8.3 ms [180]. On the other hand, the Pericam PSI (Perimed AB - Sweden) uses a fixed exposure time of 6 ms.

Regarding MESI, Kazmi *et al.* have performed an intensive study on the optimal exposure times and how many they should be to decrease acquisition times. The study started by using 15 exposures times ranging for 50 μs to 80 ms and evaluates the τ_c by a MESI. After that, the redundant exposure times were eliminated and a final optimal set of 6 exposures times was determined as 50 μs, 0.25 ms, 0.75 ms, 5 ms, 25 ms and 80 ms.

This optimal set of exposure times can be plotted as a logarithmic scale, short increases in the shorter exposures times and large increases in larger exposure times. This is an expected result because, for τ_c in the physiological range (up to 2 ms [131]), the $dK(T)/dT$

is higher for lower exposure times. In addition to these intensive studies, several exposure times ranges can be found in the literature, for example from 50 μs to 80 ms [131,133,142], from 50 μs to 30 ms [149], and 200 μs to 20 ms [137].

As the exposure time becomes shorter less photons are detected by the imaging sensor, decreasing the SNR. Adding this to: (1) the fact that to increase the speckle size the imaging iris must be closed (some works reported the use of $f/11$ [169] and $f/6$ [155]) and (2) the polarizer that is often used in front of the imaging sensor reduces the number of detected photons; it is necessary to have a powerful light source in order to perform acquisitions with short exposure times ($<$ 1ms).

A pertinent question arises from the fact that the optimal exposure time can be dependent on the analyzed tissues. Most part of LSI applications are related with highly perfusioned tissues (see section 3.5) like the cerebrum or the cornea. Additionally, most of the studies that try to optimize LSI are performed in this type of tissues. In contrast, the analysis of skin, which is a much less perfused tissue, is also a major application of LSI and the optimization studies should also be performed in this type of tissue.

3.3 Laser speckle imaging techniques

Different LSI techniques have been developed during the last 35 years. LSI started in the analog era using only single-exposure times to assess the blood perfusion. At the time, there was a well established technique for blood perfusion assessment, laser Doppler flowmetry. The research on laser speckle slowed down for many years due to its lack of performance compared with laser Doppler. However, the beginning of the digital era boosted the capabilities of LSI making it an attractive field of investigation.

3.3.1 Single-exposure

Single exposure LSI is based on the computation of the laser speckle contrast (Eq. (3.1)) by using one or more images acquired with a fixed exposure time. The contrast of these images is then related with the decorrelation time by a direct application of the expressions presented in section 3.1.

The pioneer work from Fercher and Briers [126,135] proposed, for the first time, the use of laser speckle effect as a tool for microcirculation assessment. They used a photographic camera to image the retina during laser light illumination. The large exposure time (166 ms) and a completely analog imaging system caused problems to the technique despite their promising results.

The work presented by Fujii *et al.* [181, 182] brought an improvement to the original technique because they used a linear CCD to image blood flow in the hands and fingers. This system required the use of a laser scanning system, composed by a moving mirror, in order to acquire perfusion maps (2D blood flow images). Later, Tamaki *et al.* [183] used a CCD array to produce speckle images of the retina using a blue laser (488 nm). This time, the contrast was not computed spatially, as it was done before, but it was computed temporally.

An important milestone in LSI occurred in 1996 with the work of Briers and Webster [124]. They proposed and used for the first time the acronym Laser Speckle Contrast Analysis (LASCA) to define the analysis of laser speckle images using contrast computation for blood perfusion measurements. Even today, single-exposure LSI is widely used as a research tool because its results, although only qualitative, are conclusive and reliable [100, 141, 174, 184]. Single-exposure LSI has advantages over the traditional blood flow techniques (*e.g.* laser Doppler flowmetry), namely its capacity to perform flow maps (2D images), with good temporal and spatial resolutions, at a fair cost.

3.3.2 Multi-exposure

In a demand for more quantitative LSI an improvement of the original technique emerged more recently [133]. This technique computes the contrast in multiple images, acquired with different exposure times, to perform a most accurate estimation of τ_c. Consequently, several position vectors (K, T) are computed leading to the possibility to represent the $K(T)$ function as a curve. Finally, this curve can be fitted, using for example the least-squares method, and the parameter τ_c extracted as the fitting variable. The obtained τ_c value depends on the initial selected model (Lorentzian, Gaussian or Voigt) as it occurred in single exposure LSI.

The current main line of research in LSI techniques is related to multi-exposure systems [131,134,137,138,142,153,163,185]. These custom systems have been developed by several researcher groups to perform a proof of concept and pre-clinical studies but their results are encouraging. Commercial devices only use single-exposure laser speckle [146]. However the strong commercial interest on this new technique would conduct to a fast update of the existing devices or to the development of new imagers.

3.4 Contrast computation algorithm

The evolution of the theory, instrumentation, and techniques was associated with the development of different ways to compute the laser speckle contrast. These methods can be classified into three categories: spatial contrast (s-K), temporal contrast (t-K) and a combination of both (spatio-temporal (st-K)) [127].

3.4.1 Spatial contrast

The spatial contrast was used in the work of Briers and Webster [124] and consists in the computation of the contrast in small regions (elements) of the laser speckle raw image. Normally, these elements correspond to squares of 3×3 [120], 5×5 [155, 186] or 7×7 [124] pixels. The general equation to compute spatial contrast in raster images can be defined as [127]:

$$\mu^s_{i,j,t} = \frac{1}{n^2} \sum_{x=i-\frac{n-1}{2}}^{i+\frac{n-1}{2}} \sum_{y=j-\frac{n-1}{2}}^{j+\frac{n-1}{2}} I_{x,y,t} \tag{3.30}$$

$$K^s_{i,j,t} = \frac{\sqrt{\frac{1}{n^2} \sum_{x=i-\frac{n-1}{2}}^{i+\frac{n-1}{2}} \sum_{y=j-\frac{n-1}{2}}^{j+\frac{n-1}{2}} (I_{x,y,t} - \mu^s_{i,j,t})^2}}{\mu^s_{i,j,t}}, \tag{3.31}$$

where $\mu^s_{i,j,t}$ is the mean intensity of the element with a central pixel in the coordinates (i, j, t), n is the lateral size of the element and $I_{x,y,t}$ is the raw speckle value in the respective coordinates. Finally, $K^s_{i,j,t}$ is the contrast value associated with the element centered in (i, j, t). Attention must be given to the boundary of the image since it is impossible to evaluate (I) at negative coordinates. Two possible solutions can be applied: (1) exclude the outer borders of the image from the analysis or (2) duplicate the outer borders of the images.

Figure 3.6(a) illustrate an s-K element with size 3×3 pixels (blue square) with a central pixel $(x, y, t) = (i, j, 1)$. The pixels colored in pink represent the image boundary in which the contrast computation can only be computed using padding techniques. This boundary depends of the element size and its typical $(n-1)/2$ rows and columns. The s-K element is then moved along the x and y directions to compute a contrast 2D map. The element displacement is often used without overlapping.

Laser speckle contrast is a statistic measure because it is related with the mean and standard deviation of the speckle image intensity (Eq. (3.1)). Therefore, the larger the element, *i.e.* the processing region, the better contrast estimation is obtained. However, the increase of the element size causes a decrease in the spatial resolution of the contrast images and, consequentially, of the perfusion map. Larger sizes can be used when high resolution laser speckle images are acquired and the spatial resolution is not a key factor.

To select a correct element size it is necessary to take into account the speckle size present in raw images (see subsection 3.2.1). To estimate the contrast in a statistically relevant number of speckles, the element size should be proportional to the speckle size. Consequently, when the value of pixels/speckle is high, larger elements should be used. Duncan *et al.* [187] studied the relation between speckle size and element size but their analysis, in the opinion of the author, is not clear about the relation between speckle size and the optimal element size.

3.4.2 Temporal contrast

Another algorithm was proposed by Cheng *et al.* [186] in order to improve the spatial resolution. The temporal contrast is computed by using a set of statistically independent frames. These frames can only be consecutive when the inter-frame times (Δt) is large

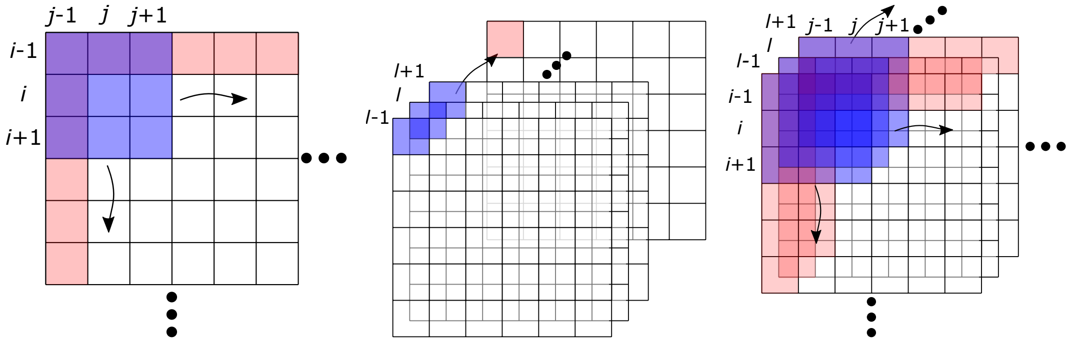

(a) Spatial contrast (b) Temporal contrast (c) Spatiotemporal contrast

Figure 3.6: Ilustration of the elements to compute contrast. The element is represented by blue squares. Pink squares represent the boundaries where the computation of contrast requires padding. Curved arrows were used to indicate the element displacement directions.

enough which, as stated early, does not occur in high speed systems [137, 172].

The minimum number of frames (m) that should be used, in the computation of the temporal contrast, to obtained a valid statistic is 15 [150]. The maximum number of frames only depends on the minimum admissible temporal resolution but references can be found that use up to 49 frames [127]. The t-K can be computed using [127]:

$$\mu^t_{x,y,l} = \frac{1}{m}\sum_{t=l-m/2}^{l+m/2} I(x,y,t) \tag{3.32}$$

$$K^t_{x,y,l} = \frac{\sqrt{\dfrac{1}{m}\displaystyle\sum_{t=l-m/2}^{l+m/2} (I_{x,y,t}-\mu^t_{x,y,l})^2}}{\mu^t_{x,y,l}}, \tag{3.33}$$

where $\mu^t_{x,y,l}$ is the temporal mean of the element with central pixel in (x,y,l) and size m, $K^t_{x,y,l}$ is the temporal contrast within this element.

Figure 3.6(b) illustrate the application of t-K algorithm with an element of size 1×3 and centered in the pixel $(x,y,t) = (1,1,l)$. This element is displaced along the temporal direction (t) until the last frames. Subsequently, this element is moved to another pixel, *i.e.* to another location in the first image.

The t-K reduces the temporal resolution while the s-K reduces the spatial resolution. To select the suitable algorithm, it is important to have in mind which dimension (spatial or time) is more important to preserve. Additionally, t-K proved to accurately estimate contrast in the presence of static scatterers [188]. Ramirez-San-Juan *et al.* [189] recently showed using *in vitro* measurements that the value computed with the t-K algorithm is independent of the static scatterers layer thickness.

The use of t-K has increased due to the advantage of dealing with static scatterers

[133, 190]. In the opinion of the author, temporal laser speckle contrast should be applied in the case of a speckle size equals to pixel size. The use of t-K with larger speckle size (*e.g.* 2 pixels/speckle) will cause a decrease in both the spatial and temporal resolutions without improving the t-K values [133]. Nevertheless, one study [165] suggests that the increase of speckle size causes an increase in speckle contrast for both spatial and temporal algorithms.

We would like to propose the hypothesis that, using fast imaging systems, the t-K can be used for very short exposure times (T≈50 μs). By this method, the t-K information will come from the time variations of a single pixel, and not from the "blurring" of an image region. The shorter the exposure time the better the speckle sampling will be. In the case of slow scatterers, a static speckle will appear with approximately the same intensity along several images, leading to low σ and low contrast. For rapid scatterers, a moving speckle will appear with different intensities along time, due to changes in the interference of the light. This will lead to high σ and high contrast. This is exactly the inverse of the spatial contrast. The inverse value of K could be possibly related with the scatterers decorrelation time.

This hypothesis falls from the Nyquist theorem which states that signals must be sampled with, at least, twice their maximum frequency. Further studies to refute or confirm this hypothesis need to be conducted.

3.4.3 Spatio-temporal contrast

A combination of both spatial and temporal algorithms can be applied to compute laser speckle contrast [191, 192, 192–194]. The used element is usually a cuboide (Fig. 3.6(c)) that can be isotropic or anisotropic. The expression for the st-K computation is not presented because it is too long and its deduction is trivial.

Figure 3.6(c) illustrate the application of the st-K with a cubic element with size $3 \times 3 \times 3$ and centered in the pixel $(x, y, t) = (i, j, l)$. This element is displaced in the spatial and temporal dimensions.

Different sizes of elements can be used to compute st-K, for example, Duncan *et al.* used a element size of $3 \times 3 \times 5$ (N_x, Ny, N_t) pixels. Usually, anisotropic elements are used in which the spatial dimensions are equal and the temporal dimension is different. The temporal dimension of the element is usually larger than the spatial dimensions to ensure good statistical time evaluation.

Qiu *et al.* [193] studied the change in the temporal dimension of the element. They used elements with a spatial dimension of 3×3 and 9×9 pixels and a temporal dimension range from 3 to 30 pixels. This study founds that the mean value of the contrast (μ_{st}) depends on the spatial dimensions and the temporal dimension and, for practical applications a $3 \times 3 \times 15$ pixels (anisotropic) or a $5 \times 5 \times 5$ (isotropic) pixels elements are recommended.

Alternatively, Rege *et al.* [191] have proposed a different approach for anisotropic st-K computation. Their method uses an element with the same orientation of the analysed blood vessel with dimensions of 9×1×3 pixels for N_x, Ny, N_t respectively. The requirement of only 3 temporal frames increases the temporal resolution of this method compared with the standard elements used in st-K.

3.5 Biomedical applications

Multiple biomedical applications can be found for LSI. This section is a short compilation of some practical studies and their conclusions. Other applications can be found in [100, 121, 138, 139, 144, 195].

3.5.1 Microcirculation - Blood perfusion

Historically, LSI was used to assess blood perfusion and blood flow, mainly for retinal and cerebral applications (Cerebral Blood Flow (CBF)). These are the perfect applications for LSI because the blood vessels are close to the tissue surface leading to higher SNR.

LSI was used to study the influence of collateral blood flow during an ischemic stroke in rats [196]. A single-exposure LSI (T = 15 ms) was used and the spatial speckle contrast was computed in local areas of 5×5 pixels. The authors reported that after the vessel occlusion, extensive anastomatic connections were formed to augment the blood blow. Moreover, using single-exposure LSI (T = 20 ms), it has been shown that hyperglycemia worsens the effect of a cerebral stroke in rats [197]. LSI system with fixed exposure time (5 ms) has been used during human neurosurgery in order to monitor the CBF. This system allows to represent online perfusion maps without surgery interference [198]. Additionally, MESI (exposure times 1-100 ms) was used to study the cortical microcirculation of piglets during the application of various vasodilators and asphyxia [199]. Multi-exposure LSI have also been used to assess CBF through a thinned skull in mice [148].

Retinal blood analyses is also a major application of LSI. A single-exposure LSI (T = 40 ms) has been used to image the retinal blood flow [200] during light stimulation. It has been founded that the application of flickering light dilates the retinal arterioles and increases the retinal blood velocity. Furthermore, changes in retinal blood flow according to the position (sitting or supine) were also studied using LSI [201]. Change from a sitting position to a supine position causes an increase in blood flow during 6 minutes. Moreover, Ponticorvo *et al.* [202] have combined single-exposure LSI (T = 5 ms) with an endoscope to analyse retinal blood flow changes in rats. They conclude that the blood flow increases during visual stimulus and hypercapnia while it decreases during hyperoxia.

Skin perfusion assessment represents other of the research fields in which LSI is widely applied. Rege *et al.* [203] used a single-exposure LSI (T = 16 ms) to assess the microvascular remodeling during wound healing. They found that microvessel density increases in the initial tissue inflammation and returns to baseline only during the remodeling stage, 12 days after. Additionally, single-exposure LSI (T = 6 ms) has been used to study the effects of aging in the blood perfusion of the forearm [146]. A correlation between the blood cells velocity and age was founded during post-occlusive reactive hyperaemia. Moreover, lower levels of peripheral blood perfusion were detected in systemic sclerosis patients compared with healthy subjects using single-exposure LSI (T = 6 ms) [204]. Furthermore, LSI has been used to assess the microvascular function in primary Raynaud phenomenon and systemic sclerosis patients [205].

3.5.2 Macrocirculation - Blood pressure

Apart from the original applications of LSI in blood flow measurements, novel applications in the assessment of macrocirculation begin to emerge. LSI has been use to remote estimate blood pulse pressure wave in the radial artery [206]. The two-dimensional correlation was computed between consecutive frames as a measure of artery movement.

Additionally, LSI was used to detect the blood pulsation in presence of motion artifacts [207]. Measurements were performed in the finger and images were processed using contrast and correlation. Finally, CBF in rats was synchronized with cardiac cycle using LSI [175]. This synchronization permits the correction of pulsation-modulated speckle contrast signals.

3.5.3 Others

Beyond the discussed applications, LSI was also used to assess the nephrons blood flow dynamics [208], detect speech at long distance [10], estimate blood glucose levels [209,210] and for microchannels applications [211].

3.6 Limitations and Future trends

Laser speckle has proven to be a simple and very versatile tool that can be applied in many fields of investigation and clinical studies. However, two major limitations of LSI systems need to be addressed: Absolute velocity estimation and deep assessment.

3.6.1 Absolute velocity estimation

Comparison between different studies, using different systems, is very difficult to perform because the absolute velocity of scatterers is extremely hard to measure and depends on several of factors [125, 138]. These factors have been discussed during this chapter and include the non-perfect light polarization, multiple scattering, static scatterers, speckle spatial averaging, approximate velocity models and, the relation between velocity and decorrelation time.

The influence of the blood vessel caliber in the measured decorrelation time is also a major issue in the absolute velocity estimation and it as been studied by some authors [142]. The probability of occurring multiple scattering is higher within large caliber blood vessels compared with small caliber blood vessels [212]. The occurrence of different scattering degrees may cause a poor estimation of the decorrelation time. In this study they suggest that the decorrelation time is proportional to the product between the blood velocity and the blood vessel diameter.

For these reasons, LSI is represented in arbitrary units that can have different definitions. These arbitrary units can be the expressed as the contrast value, the decorrelation time [144], the speckle flow index (SFI) [176], inverse correlation time (ICT) [142], relative flow volume (RFV) [213] and percentage of the baseline [184]. Different techniques to achieve an estimation of red blood cells velocities are accomplished by using calibration with phantoms [214] or other systems [131, 215, 216].

To solve this issue, the future work should be focused in the improvement of theoretical models, namely by accounting the multiple scattering that occurs in biological tissues by approximating the relation between decorrelation time and scatters velocity, and the approximation of the experimental conditions to the theoretical assumptions [100]. Moreover, more experimental work should be performed to infer the effect of static scatterers on laser speckle contrast.

3.6.2 Depth assessment

The second limitation of LSI is related with the maximum depth that produces laser speckle contrast information. According to some authors [98], the penetration of the photons that carry laser speckle information, in LSI standard techniques, is about 300 μm. Alternative techniques like Laser Doppler flowmetry can achieve assessment depths up to about 900 μm [217].

To improve the penetration depth of LSI several studies have been performed recently [174, 212, 218–221]. These studies present novel LSI techniques, in most of the cases with hardware changes. For example, He et *al.* [219] used a linear laser scanning system to collect speckle images. In each image, only the image areas distant from the laser illumination are used to compute the contrast image. The light that is refracted in the tissue areas farther from the penetration zone reaches deeper tissues. This is the so-called "Banana path" [174, 222].

These techniques take advantage of the same principle as diffuse correlation spectroscopy (DCS) [223]. Bi *et al.* [218] have used the same principle but with a point-like laser light source that illuminates the tissue outside the imaging system field of view. The pixels, of the imaging system, farther from the illumination point record photon arising from deeper tissues. Finally, Varma *et al.* [174] proposed a speckle contrast optical tomography that can render 3D volumes of flow information. This techniques is based on the equations of DCS but the autocorrelation function of the scatterers is computed using the speckle contrast (Eq. (3.6)).

This type of techniques work in a complete multi-scattering regime, which, in the opinion of the author, may compromise the use of the theoretical analysis presented in section 3.1 because it assumes a single dynamic scattering regime. More research should be conducted to study if the single scattering approximations performed in the laser speckle contrast theory are valid even in these new LSI techniques.

3.6.3 Future trends

Addressing the limitations present above are clearly two of the future trends in LSI. Additionally, some authors [100] point the possibility to perform blood perfusion measurements in moving subjects as a major advance in LSI because vascular diseases are often displayed during exercise and some diseases cause the patients to move involuntary, *e.g.* Parkinson disease.

Furthermore, the combination of LSI data with other micro/macro-circulation assessment techniques could improve the diagnosis of vascular diseases. The application of automatic classifiers like neural network or Support Vector Machine (SVM) to features extracted from multiple information sources have been applied in other areas [18]. This is an important field to help improving diagnosis which can be explored in LSI.

Moreover, multi-exposure LSI is a recent technique (2008) which is only available in prototypes. Several questions and improvements, which were addressed during this chapter, can be applied for MESI. Equally important is the establishment of standards in order to make possible to obtain comparable results in studies made with different laser speckle systems [100].

3.7 Nomenclature

During the past 35 years many nomenclatures have emerged in LSI works. Many of them are just different names for the same concept. Although the terms Laser Speckle Contrast Imaging (LSCI), Laser Speckle Perfusion Imaging (LSPI), Laser Speckle Flowmetry (LSF), Laser Speckle Flowgraphy (LSFG), LASCA and LSI where proposed together with a specific contrast algorithm [127]. In our opinion, they correspond to equivalent terms that generally define contrast speckle techniques for biomedical applications. More recently, many different acronyms have appeared, mostly related with variations in hardware or/and contrast algorithms compared to the original methods [127].

Chapter 4

Methods and experimental set-up

Stephen Hales (1677 – 1761) was the first to measure blood pressure. He inserted fine tubes into animal arteries and measured the height that the blood rose.

This chapter is divided into three main sections. In the first section, the methods and experimental bench tests developed in order to explore laser speckle applications for macrocirculation assessment are presented. The second main section presents the work and bench tests performed in order to study the effect of static scatterers in laser speckle signals for microcirculation application. The last section describes a computational experiment performed in to optimize the the application of laser speckle spatial contrast algorithm.

4.1 Macrocirculation application

The macrocirculation assessment techniques can be roughly classified in contact and non-contact method. Biological systems, like arteries and skin, are highly sensitive to external pressures and mass variations [118]. So, the application of an external force, or perturbation, leads to an erroneous acquisition of the pulse waveform. For that reason, the truly non-contact nature of LSI, and other optical methods, is a major advantage in pulse waveform extraction over conventional techniques (*e.g.* piezoelectric sensors) [61, 79]. In this work, multiple studies have been performed in order to check the possibility to use laser speckle in macrocirculation assessments.

In the first study, laser speckle measurements have been performed with different wavelengths, ranging from green to infrared, in order to find the most adequate wavelength for pulse waveform extraction. The studies described in this section were performed in a bench test set-up as well as in an *in vivo* situation. The second study has been developed in order to achieve two different goals. The first goal was to extract the pulse pressure waveform using the same processing methods as in microcirculation LSI. The second goal was to validate the results achieved in the first test with a larger population and against the results of a Photoplethysmograph (PPG) logger.

The last study, an image segmentation study, was performed to characterize the longitudinal movements of a phantom. By its nature, laser speckle effect can be used to segment

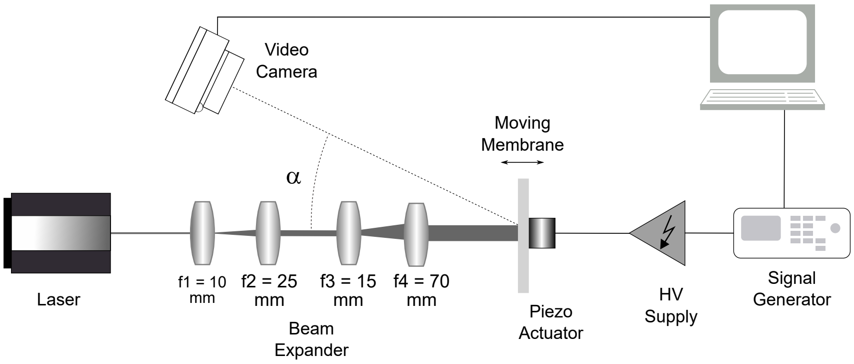

Figure 4.1: Optical scheme of the experimental bench set-up. The angle represented by α is approximately 29°. HV stands for high voltage. Focal distances are expressed in millimetres. Image not to scale.

these movements without the need for stereoscopic vision or other methods. This can be useful in biomedical applications because the arterial movement, and other physiological membranes vibration, can be approximated by a longitudinal movement. To verify this hypothesis, a processing technique, based on entropy, has been applied for two-dimensional image segmentation of surfaces with longitudinal movements.

4.1.1 Experimental bench test

An experimental bench test was designed in order to create a set of controlled conditions. This controlled environment is necessary for the design and evaluation of laser speckle methods for macrocirculation applications. This bench test consisted in a coherent light source and a projection system that conducts the light beam into a skin-like phantom. Moreover, a digital Video Camera (VC) was positioned in order to record the laser speckle patterns.

Figure 4.1 shows a schematic representation of the designed experimental bench test. As light sources, three different lasers have been used: a green laser diode (L_{532}) (from Thorlabs, ref. CPS532) with a wavelength of 532 nm, with an optical power of 4.5 mW, with an output circular beam diameter of 3.5 mm, and with a spectral-width of 0.5 nm; a red laser diode (L_{635}) (from Coherent inc., ref. VHK), with a wavelength of 635 nm, with an optical power of 4.9 mW, with an output circular beam diameter of 1.1 mm, and a spectral-width of 0.5 nm; and a near infra-red laser diode (L_{850}) (from Global Lasers, ref. LDL 175G) with a wavelength of 850 nm, with an optical power of 3 mW, an output focusable elliptical beam diameter of 4×2 mm, and a spectral-width of 0.5 nm.

A tailored beam expander has been used in order to increase the illuminated area. This expander has been built with 4 convergent lenses, making two Keplerian beam expanders. The focal distance of each lens is detailed in figure 4.1. The total magnification (M) of

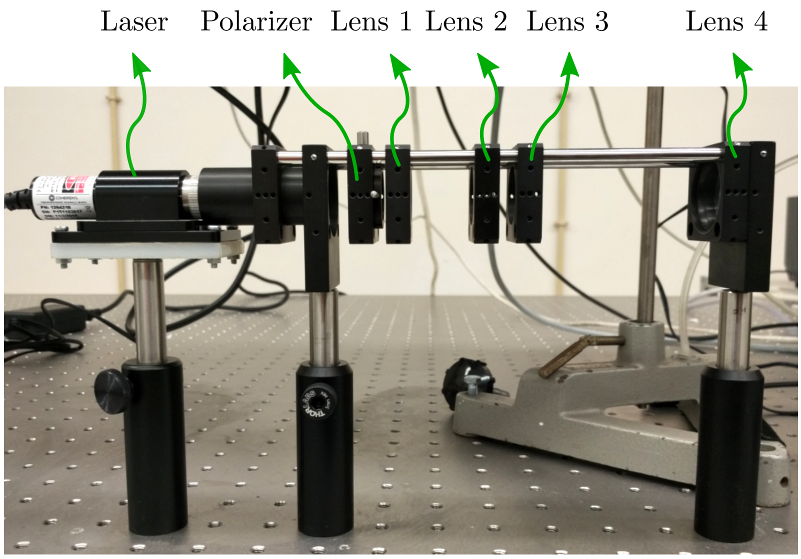

Figure 4.2: Photography of the laser support and beam expander mounted in an optical bench using a cage system.

the beam expander can be determined as:

$$M = \frac{f2}{f1} \times \frac{f4}{f3} = 11.67\,, \tag{4.1}$$

where $f1$, $f2$, $f3$ and $f4$ correspond to the focal distances of the 4 lens that are 10, 25, 15 and 70 mm respectively.

Figure 4.2 depicts the laser-expander coupling, mounted on an optical bench. The optical cage elements allow the attachment or removal of the optical components without changing the system. In this configuration, a polarizer support can be seen. The polarizer was not used in this test but it has been used during microcirculation studies.

The application of the beam expander changes the optical characteristics of the laser light sources, namely the beam diameter and irradiance. The optical parameters of the expanded laser beams are expressed in table 4.1. Moreover, the Maximum Permissible Exposure (MPE) [224] for skin during long exposure times (10 to 30000 seconds) are also presented in table 4.1. All the irradiances are under the MPE and the experiments have been conducted using the appropriate eye protection for class 3R lasers (L_{532}, L_{635}) and class 3B lasers (L_{850}), namely the Thorlabs LG10 and Glendlate GL-310.

Table 4.1: Laser optical characteristics after beam expansion. MPE stands for maximum permissible exposure.

	L_{532}	L_{635}	L_{850}
Expanded diameter (mm)	40.9	12.8	46.6 × 23.3
Illumination area (mm^2)	1313	129	853
Optical power (mW)	4.5	4.9	3
Irradiance (W/m^2)	3.4	38	3.5
MPE (W/m^2)	2000	2000	3990

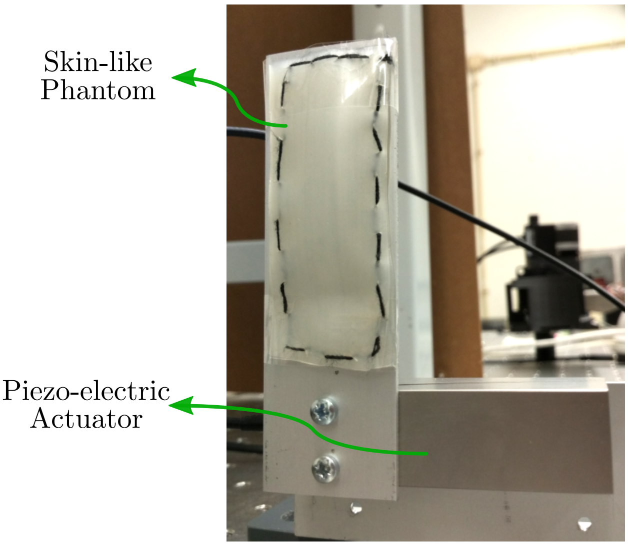

Figure 4.3: Photography of the skin-like phantom connected to the piezo-electric actuator.

The optical cage directs the coherent light into a skin-like phantom composed of 4 white translucent silicone membranes. This diffuse target, with a total thickness of 2 mm, tries to mimic the optical properties of the skin. Similar models have been used in previous works [59, 225]. The target size was 30 mm × 60 mm (W × H). The skin-like phantom can be seen in figure 4.3.

The skin-like phantom was connected to a piezo-electric actuator (Physik Intrumente GmbH P-287) which follows a linear displacement according to the applied voltage. A signal generator, Agilent 33220A, was used to reproduce a pulse waveform that was amplified in an high voltage power supply (Fig. 4.1). The system transfer function can be expressed as [14]:

$$D(t) = \frac{7000}{75} \times V(t)\ (\mu m)\ , \tag{4.2}$$

where $D(t)$ is the displacement of the membrane in micrometers and $V(t)$ is the electric potential in Volts applied by the signal generator. When $V(t)$ is represented by a sinusoidal function, the maximum velocity reached by the skin-like phantom is [17]:

$$v_{max}(V_{pp}, \omega) = \frac{7000}{75} \times \frac{V_{pp}}{2} \times \omega\ (\mu m/s)\ , \tag{4.3}$$

where v_{max} is the maximum velocity achieved by the skin-like phantom in micrometers per second, V_{pp} represents the peak to peak amplitude of the sinusoidal function in Volts and ω corresponds to the sinusoidal wave frequency in radians.

Finally, a monochrome digital VC, Pixelink - B741U [226], connected to a C-mount lens, with a fixed focal length of 50 mm, was used for image acquisition. The camera has been set-up to perform all bench acquisitions with a resolution of 1280 × 1024 pixels, with an exposure time of 15 ms and with a frame rate of 15 frames per second (fps). Each acquisition duration was 7 seconds because it ensures that a complete period of all the movements is recorded. The VC lens possesses an internal diaphragm which has been used to control the lens f-number. This lens supports f-numbers from 2.0 to 22. By using equation (3.26), the optimal f-number to ensure a correct sampling (4 pixels/speckle) was computed.

A Python 2.7 (32 bits) program has been developed as software interface in order to control the VC and save the acquired data. This script takes advantage of the functions provided by openCV library, version 2.4.7 [227]. During the entire project, the Python programming language has been used to performed all the signal acquisition and control, including the VC set-up and Agilent 33220A control. On the other hand, all the mathematical processing steps and algorithm implementations have been performed using MATLAB® programming language [228].

With this set-up, three tests, using different processing methods, have been conducted: the multi-wavelength study, the pulse waveform extraction study and the image segmentation study.

4.1.2 Multi-wavelength study

The experimental apparatus described in subsection 4.1.1 was used to study which wavelength is better to extract the pulse pressure waveform. The recorded laser speckle patterns have been processed using a two-dimensional correlation coefficient. This processing methodology is much more efficient compared with the two-dimensional cross-correlation, used by other authors [10, 206]. The correlation coefficient only requires the computation of one coefficient for each image pair. The cross-correlation requires the computation of $2 \times N - 1$ correlation coefficients, where N is the number of pixels of the image. Nemati *et al.* [177, 207] used this approach but their analysis was applied to a different measuring site and without a multi-wavelength signal source.

4.1.2.1 Vibration frequency determination

The skin-like phantom was actuated with a periodical sinusoidal shape movement with four different values of amplitudes and four distinct values of frequencies. These values are represented in table 4.2. The speckle patterns developed in this target where recorded for offline processing.

In order to identify the vibration frequency, a data analysis based on the computation of a two-dimensional Power Spectral Density (PSD) has been used. The PSD is defined as the modulus of the square Fourier transform of the signal:

$$PSD_{(x,y)}(f_t) = \left| \sum_{t=1}^{K} I(x,y,t) \times e^{\frac{-i2\pi(t-1)(f_t-1)}{K}} \right|^2 , \qquad (4.4)$$

where f_t is the frequency present in the signal, K the total number of frames of the video, I is the three-dimensional structure composed by all images, and x and y represent a pixel position (line, column). In fact, the temporal evolution of the pixel (x, y) intensity is the

Table 4.2: Maximum skin-phantom displacements and maximum velocities according to the excitation signal parameters amplitude and frequency. The velocities are expressed in millimetres per second. Cells with - correspond to configurations not used in this work.

Amplitude	Max. displacement	Frequency (Hz)						
(V_{pp})	(mm)	1/5	1/3	1/2	1	2	3	5
0.5	0.05	-	-	-	0.15	0.29	0.44	0.60
1	0.09	0.06	0.10	0.15	0.29	0.59	0.88	1.47
2	0.19	0.12	0.20	0.29	0.59	1.17	1.76	2.93
4	0.37	0.23	0.39	0.59	1.17	2.34	3.52	5.86
6	0.56	0.35	0.59	0.88	1.76	-	-	-
8	0.75	0.47	0.78	1.17	2.35	-	-	-

raw signal input of the PSD and can be represented as $I_{x,y}(t)$. Before the calculi of the PSD functions, the signal $I_{x,y}(t)$ was filtered with a high-pass filter (4^{th} order Butterworth) with a cut-off frequency of 0.1 Hz in order to remove its DC component.

The PSD was then applied in 9 pre-selected small ROI (W1 to W9) of the speckle image with different sizes. The central pixel of these ROI corresponds to the central points of each zone of the “Rule of thirds” (nine-zone grid). The width of these ROI has taken values of 3, 9, 17 and 81 pixels. To see an example and detailed description of these ROI please see figure 5.1.

Within these ROIs, a PSD was computed for each pixel along the temporal dimension ($I_{x,y}(t)$). The mean of the PSD functions was associated with a ROI position, size, skin-phantom movement and laser wavelength. The PSD predominant frequency was extracted and related with the phantom vibration frequency.

Since all the possible combinations were tested for each movement parameters (9 different ROI positions and 4 different ROI sizes), a total of 36 PSD have been computed for each movement and coherent light source.

4.1.2.2 Velocity profile reconstruction

A velocity profile reconstruction test has been performed using the detailed apparatus. In this study, the skin-like phantom was actuated with a single period of a sinusoidal wave with frequencies of 1, 1/2, 1/3 and 1/5 Hz and amplitudes of 2, 4 and 8 V_{pp}. The acquisition duration, 7 seconds, ensures that the largest sinusoidal period of the phantom movement, 5 seconds, is recorded. Both laser speckle data and electrical actuation signal have been acquired simultaneously.

As explained in Chapter 3, LSI information is related with the velocity of the particles, in the same way as laser Doppler techniques [161]. The algorithm, that has been used to extract the skin-phantom velocity profile, takes advantage of the speckle decorrelation that occurs when the target position changes. We propose the use of a two-dimensional correlation coefficient between consecutive frames. This approach has already been used

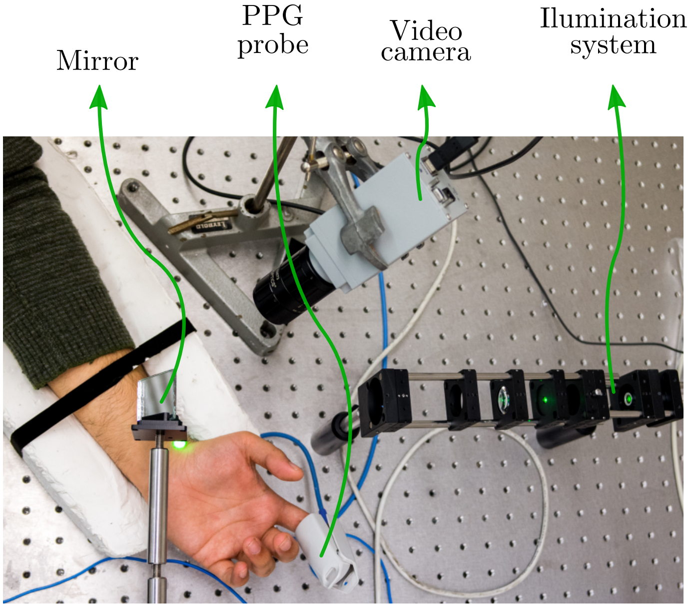

Figure 4.4: Photography of the *in vivo* acquisition scheme.

in LSI but for a different application [229]. The correlation coefficient (r) is defined as:

$$r = \frac{\sum_x \sum_y (A_{xy} - \bar{A})(B_{xy} - \bar{B})}{\sqrt{(\sum_x \sum_y (A_{xy} - \bar{A})^2)(\sum_x \sum_y (B_{xy} - \bar{B})^2)}}\ , \tag{4.5}$$

where A and B are two consecutive images, $\bar{A}$ and $\bar{B}$ represent the average pixel intensity of each image and the indexes x and y the pixel position in the image. When this method is applied to a video with K frames, by using a time sliding window with complete overlapping, $K-1$ coefficients are computed.

When the skin-phantom moves faster, r becomes smaller because the speckle patterns change quickly and become decorrelated. So, an inverse relation between the skin-like phantom velocity and the correlation coefficient exists. To better visualize this relation, the correlation coefficient was normalized between 0 and 1 (r') and inverted ($1 - r'$).

This method has been applied in the center of the laser speckle image. To see an example and detailed description of this area please see figure 5.1.

4.1.2.3 *In vivo* measurements

The skin-like phantom is a much simpler model than the human body and can not be used, *per se*, as a rigorous model. In order to completely show which wavelength is better to extract the pulse pressure waveform an *in vivo* test is essential. This test consisted in the assessment of the radial artery of two distinct subjects using the apparatus presented in figure 4.4. In addition to the LSI system, a custom PPG was used to record the subject HR in the left index finger [230]. Due to synchronization problems, the PPG data were not directly compared with the LSI data.

Two healthy subjects, a female (27 years old) and a male (24 years old), have provided written informed consent prior to participation and the study was carried out in accordance with the Declaration of Helsinki. The test was performed with the subjects in the seated position, after a 5 minutes rest period and with the subject arm fixed to the optical bench with a plaster frame. Nine acquisitions have been performed in each subject (10 seconds each), three for each light source. The acquisitions have been labelled from S1 to S18, where S1-S6 corresponds to L_{532}, S7-S12 corresponds to L_{635} and S13-S18 corresponds to L_{850}.

Since the physiological system consists of a much more complex system, and in order to improve the SNR of the apparatus, the sampling frequency was increased from 15 fps to 50 fps. However, due to hardware limitations, it was necessary to lower the acquisitions image resolution to 320 × 240 pixels.

The PSD processing method was not applied to *in vivo* data because the correlation coefficient methods was able to estimate the HR. Due to the lower resolution of *in vivo* images, the correlation coefficient was computed in the complete frame. In order to improve our results, mainly to cancel some individual tremors, the correlation coefficient signal has been filtered using a 8th order Butterworth with a band-pass frequency between 0.3 Hz and 4 Hz. This frequency band corresponds to HR up to 240 bpm which is an acceptable physiological value.

Besides the application of the signal processing techniques described in 4.1.2.2, two different image pre-processing algorithms have been used as an attempt to increase the SNR. The first pre-processing method consisted of an image binarization that was performed by applying an adaptive threshold. The threshold corresponds to the midpoint of the intensity range of the raw laser speckle image. Pixels with intensity values higher than this threshold were defined as “1”. Contrary, pixels with intensity values lower than the threshold were defined as “0”. The second pre-processing method consists of an histogram equalization. This operation was performed using the MATLAB® function `histeq` from the image processing toolbox. More information about this function can be found in [231].

The flowchart presented in figure 4.5 shows the algorithm that has been applied in this test. The error between the PPG HR and the speckle HR was used as the metric to evaluate the method performance.

4.1.3 Pulse waveform extraction study

After the multi-wavelength study, which has allowed to determine which wavelength is the most suitable for pulse waveform extraction (subsection 4.1.2), further *in vivo* measurements were made to validate the method. For this, the laser speckle prototype has been used to assess the radial artery of 10 healthy volunteers following the Declaration of Helsinki. Simultaneously, a PPG was used to record the pulse waveform [230]. Three acquisitions have been performed for each subject.

The goal of this study was to apply the same methods as the one used in microcirculation LSI for macrocirculation assessment. In order to achieve this goal, the correlation coefficient processing method was replaced by the computation of an overall frame spatial

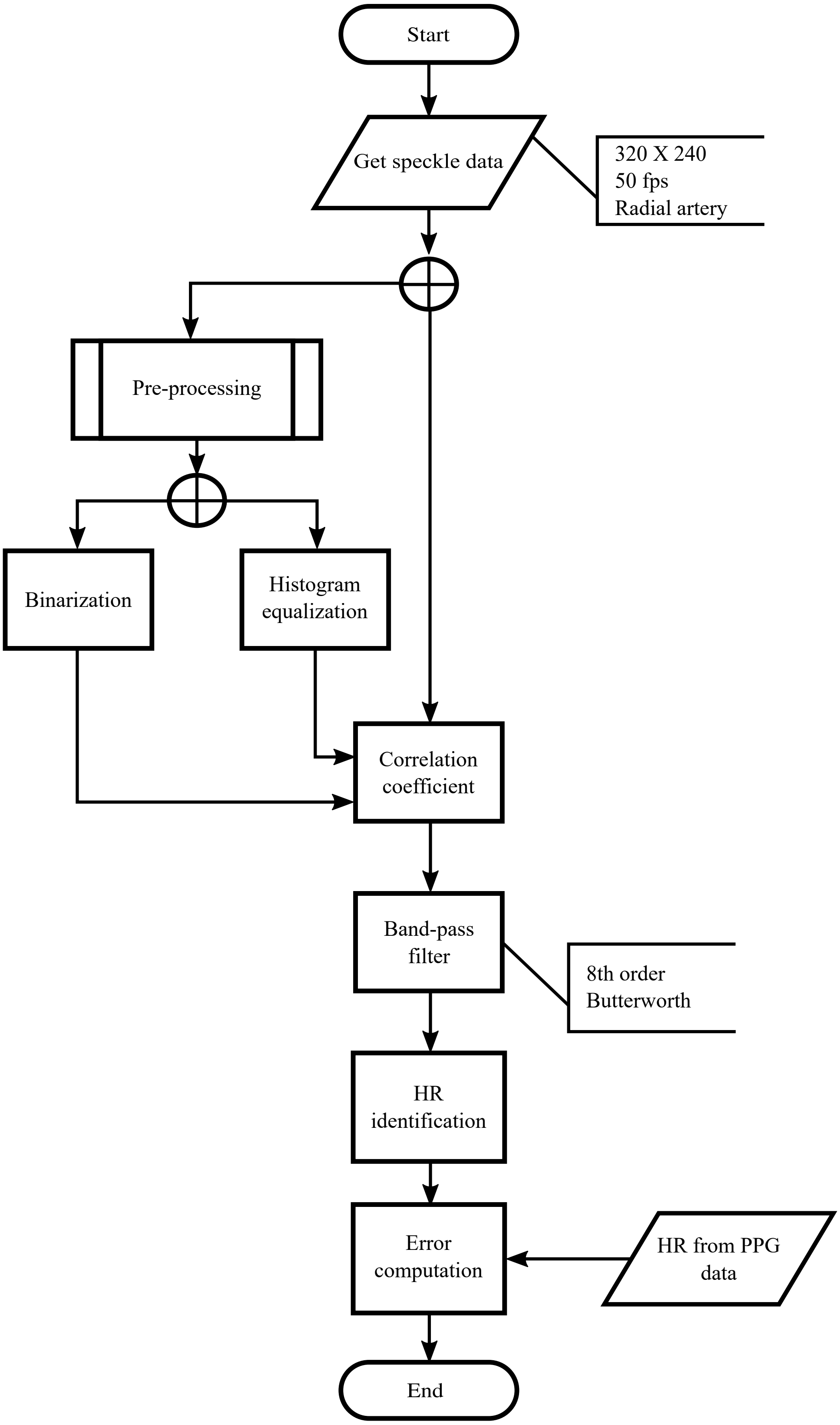

Figure 4.5: Flowchart of the algorithm applied in the *in vivo* measurements of the multi-wavelength study

contrast by using equations (3.30), *i.e.*, with an element of the size of the image.

In this study, the apparatus described in subsection 4.1.1 was slightly modified and only the L_{532} was used, because it achieved the best results in the preliminary study. For this experiments it was only used the first beam expander, which results in a beam magnification of 2.5, resulting in a output beam diameter of 8.75 mm. With an irradiance of 9.4 W/m^2, this exposure is far below the MPE (2000 W/m^2).

The decrease in the laser beam diameter has been used because of the Field Of View (FOV) reduction. Moreover, the increased amount of light density that reaches the VC sensor contribute to higher SNR. The VC acquisition parameters were set as follows: resolution of 320 × 240 pixels, exposure time of 15 ms and frame rate of 50 fps.

4.1.3.1 Heart rate determination

The values of contrast as function of the analysed frame ($K^s(t)$) have been calculated and inverted, due to the inverse relation between contrast and velocity, and normalized ($1 - K^s(t)'$), between -1 and 1. The signal obtained with the PPG ($PPG(t)$) was also normalized between -1 and 1. The speckle contrast has been filtered with a Butterworth low-pass filter with cut-off frequency of 15 Hz. The Fast Fourier Transform (FFT) of both signals have been computed and the dominant frequencies were identified. These frequencies correspond to the subject HR during the acquisition.

4.1.3.2 Spectral similarity

The similarity between both waveforms, ($PPG(t)$ and $K^s(t)$), has been determined using a spectral coherence method which compares the coherence of two signals for a specific frequency. In this work, the magnitude-squared coherence function was computed using the equation:

$$C_{KP}(f) = \frac{|P_{KP}(f)|^2}{P_K(f)P_P(f)}\,, \tag{4.6}$$

where $P_{KP}(f)$ is the cross-spectral power between $K^s(t)$ and $PPG(t)$, while $P_K(f)$ and $P_P(f)$ are the PSD of $K^s(t)$ and $PPG(t)$, respectively. A similarity index (Similarity Index (SI) - equation (4.7)) was then defined as the integral of the magnitude-squared coherence function between 0 and 10 Hz because this band contains the relevant information:

$$SI = \int_0^{10} C_{KP}(f)df\,. \tag{4.7}$$

4.1.4 Image segmentation study

The goal of this pilot study was to use laser speckle methods to segment a longitudinal moving surface without any kind of *a priori* information or stereoscopic data. Longitudinal movements with small amplitude are difficult to identify and segment but laser speckle methods can achieve good results [232,233]. By using the apparatus previously described, this pilot study explores laser speckle methods for two-dimensional segmentation of surfaces with specular reflection, like skin and soft tissues.

Two similar and independent skin-like phantoms have been used. They were positioned side by side, with a 3 mm gap. The moving phantoms (Fig. 4.3) has been actuated with a sinusoidal movement with frequencies of 1, 1/2, 1/3 and 1/5 Hz and amplitudes of 1, 2, 4 and 6 V_{pp}. The velocities and maximum displacement of these movements can be found in table 4.2.

The extra membrane was fixed to the optical table using a rigid structure. A flap was used to prevent rubbing and direct light reflection from one membrane to another. The L_{635} light source was used with full expansion in order to cover a large area (see table 4.1 specifications). The VC has been set-up with the same settings as in subsection 4.1.1, in particular, with an exposure time of 15 ms and an image resolution of 1280 × 1024 pixels.

A temporal backward difference has been applied to the laser speckle data $(I(x,y,t))$ in order to enhance the pattern variations between consecutive frames. This derivative is equivalent to the application of an high-pass temporal filter. Each of the pixels was individually processed as it has been performed in subsection 4.1.2.1. The backward difference was then normalized between 0 and 255 and can be defined as follows:

$$\Delta I(x,y,t) = \frac{I(x,y,t) - I(x,y,t-1) + 255}{2} \,, \tag{4.8}$$

where $\Delta I(x,y,t)$ is the derivative of the pixel with the position (x,y) and time t. This processing step does not reduce the spatial resolution which is essential for an correct image segmentation. The temporal resolution is also maintained, however, the number of speckle frames is reduced from K to $K-1$.

The segmentation was performed by computing the regional entropy (RE) of $\Delta I(x,y,t)$. The RE has been computed in small regions (elements) of the difference image (ΔI), likewise the method used for the speckle spatial contrast (K^s) but with full overlapping. These elements have been defined as ROI of 3×3, 9×9, 27×27, and 81×81 pixels.

For each ROI, its normalized histogram (P) has been computed. This histogram was divided into 256 bins, one for each possible grey scale value. The regional entropy, for each ROI was then computed as:

$$RE = -\sum_{bin=0}^{255} P_{bin} \times log_2(P_{bin}) \,, \tag{4.9}$$

where P_{bin} is the probability of the occurrence of a pixel with value bin in the ROI. bin ranges from 0 to 255.

The entropy map was finally segmented by the application of a threshold. Thresholds varying from 0 to 6 (maximum logged entropy in this experiment), with steps of 0.05, have been applied to the entropy maps. The segmented images have been compared with a mask that has been manually extracted from the raw speckle image. Pixels with entropy

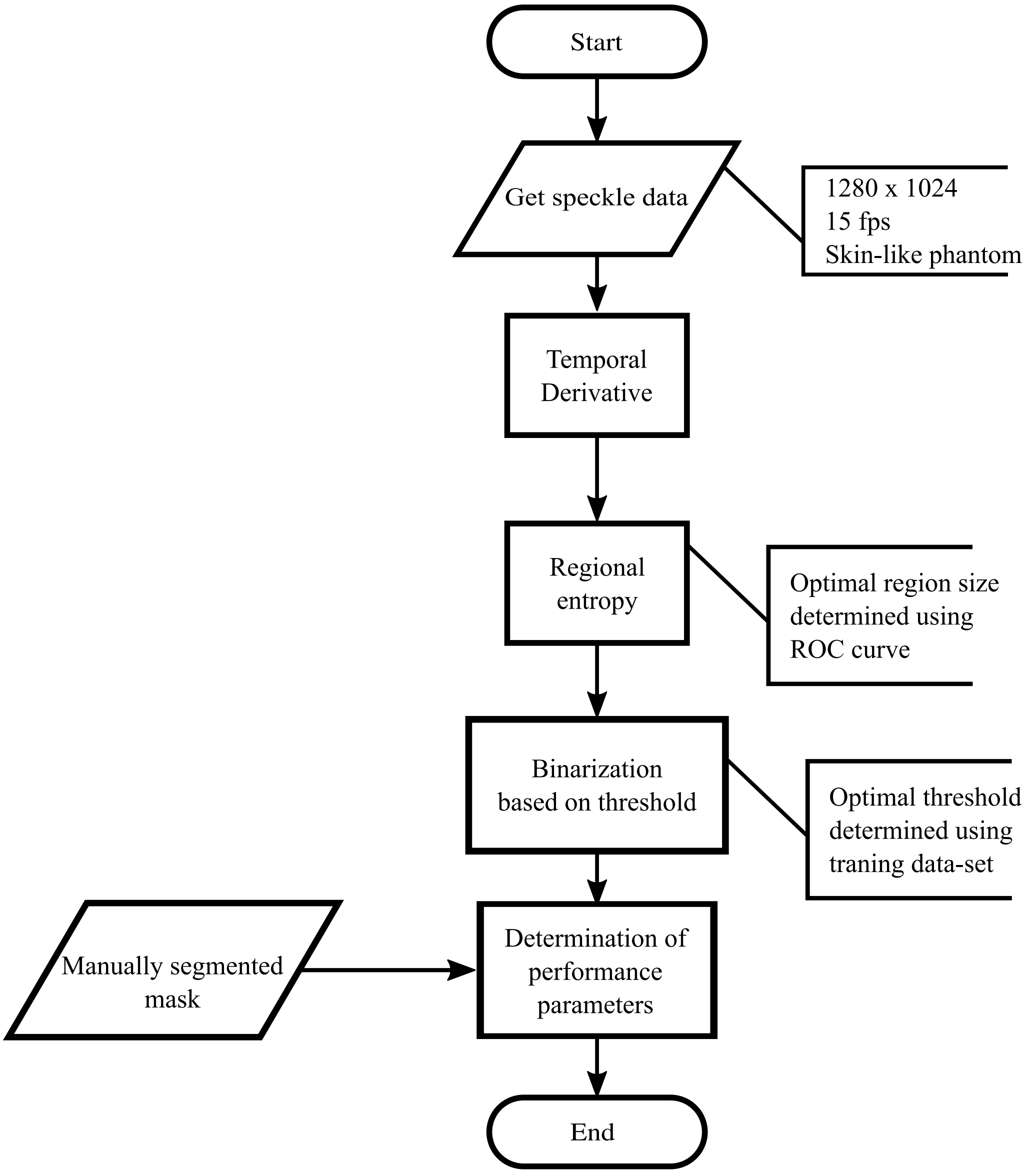

Figure 4.6: Flowchart of the method used to segment the moving skin-like phantoms

above the threshold have been classified as moving pixels (1) and pixels with entropy below the threshold have been classified as non-moving pixels (0). Figure 4.6 presents a flowchart of the algorithm used to process the laser speckle images for this test.

The most suitable element size was also determined by computing the Sensitivity (SE) and Specificity (SP) for each element size, independently of the applied threshold. A receiver operating characteristic (ROC) curve was printed for each element size and its Area Under the Curve (AUC) was computed. Higher values of AUC are related with better sizes. The SE and SP can be computed, by using the classifier True Positives (TP), True Negatives (TN), False Positives (FP) and False Negatives (FN), in order to compare the classifier performance:

$$SE = \frac{TP}{TP + FN}; \tag{4.10}$$

$$SP = \frac{TN}{FP + TN}. \tag{4.11}$$

A data-set of 12 entropy maps was used to determine which threshold can lead to the best results. This data-set contained images of different membrane velocities (0, 59, 98, 117, 147, 195, 235, 293, 352, 586, 880 and 1763 $\mu m\, s^{-1}$). These images have been selected because they cover the complete range of phantom velocities tested in this experiment. The best threshold was defined as the one that maximizes the mean Accuracy (AC) of this training data-set.

The best threshold and element size have been, finally, applied to a validation data-set composed of 5 videos with different maximum velocities that were not used in the training data-set. These data-sets correspond to the movements with the following parameter: 1 Hz-1V_{pp}, 1 Hz-4V_{pp}, 1/2 Hz-6V_{pp}, 1/3 Hz-4V_{pp}, and 1/5 Hz-1V_{pp}. The AC, Positive Predictive Value (PPV), Negative Predictive Value (NPV) and Matthews Correlation Coefficient (MCC) have been used to evaluate the method performance. These metrics can be computed using:

$$AC = \frac{TP + TN}{TP + TN + FP + FN}; \tag{4.12}$$

$$PPV = \frac{TP}{TP + FP}; \tag{4.13}$$

$$NPV = \frac{TN}{TN + FN}; \tag{4.14}$$

$$MCC = \frac{TP \times TN - FP \times FN}{\sqrt{(TP + FP)(TP + FN) \times (TN + FP)(TN + FN)}}. \tag{4.15}$$

4.2 Microcirculation application

As discussed in Chapter 3, one of the major unclear areas of LSI is the influence of static scatterers on LSI. Solving this issue is an essential step in order to developed a fully quantitative LSI technique.

The work presented in this thesis, related with microcirculation, is strongly focused on the study of LSI under different ratios of static/dynamic scatterers. A comparison between the theoretical predictions and experimental results is the main goal of this work. Moreover, the effect of static scatterers concentration on the values of speckle contrast will be discussed.

The bench described in subsection 4.1.1 has been modified, in order to be used for this study, and new phantoms, with different characteristics, have been developed. This test consisted in the acquisition of LSI data using a microchannel phantom that simulates the blood flow inside arterioles. Through this phantom, a fluid (milk) has been pumped with different flows and, consequently, different velocities. The microchannel has been covered with several layers of static scatterers, each one with different scatterers concentrations. The data obtained has been processed according to the methods described in Chapter 3.

4.2.1 Experimental bench test

The LSI prototype detailed in section 4.1.1 has been used to produce LSI data. However, several modifications have been introduced in order to enhance it. A new light source (BioRay, Coherent Inc.), with an optical power of 40 mW, with a light wavelength of 640 nm, and with a beam size of 2.4×1.4 mm has been used in order to increase the irradiance that reaches the sample. This laser is shown in figure 4.2.

The setup is shown in figures 4.7 and 4.8. The cage system has been filled with a vertical polarizer and a beam expander composed of two lenses. The laser light is, by itself, polarized in a preferential direction. However, an external polarizer has been used in order to increase the laser degree of polarization. The beam expander was used to control the laser spot size in the target. This size was controlled by changing the distance between the lenses.

A second polarizer has been coupled with the VC lens. It has been placed in a perpendicular position regarding the one used for the laser. As detailed in subsection 3.2.2, this polarizer removes the light which is directly reflected in the air-sample interface, and direct internal reflection sites, which does not contain any valuable information. The laser beam has been directed to the sample using a 45 degrees mirror.

The sample can be divided in two phases, the static scatterers layer and the microchannel phantom. The scatterers layer consists of a silicone based membrane (Sylgard® 184 silicone elastomer) doped with TiO_2 particles. Figure 4.9 shows a lateral view of the sample, including the microchannel device and the scatterers layer. This sample is supported by a 3D printed part and attached to a motorized rotary stage (Zaber T-RSW60A).

The bottom phase of the sample consists of a microchannel phantom in which semi-skimmed milk is flowing. The milk has been diluted with water in a 1:2 (33%), 1:1 (50%) and, 3:1 (75%) (milk:water) volume proportions. Furthermore, the milk has also been used without dilution (100%) and with the addition of extra static scatterers (200%). The "doped" mixture results from the addition of a 0.1 grams of dried milk for each millilitre of semi-skimmed milk.

This fluid has been used as a blood substitute because its optical properties are suitable for this application [234]. Moreover, milk contains several scatterers, *e.g.* fat globules and proteins, of the same size magnitude of the blood constituents. The advantages of using milk, comparing to blood, are that it does not sediment, its much easier to handle and presents a behaviour similar to the intralipid solution [234, 235]. Finally, this substance has also been used in other optical based studies [87, 236, 237].

The microchannel phantom, constructed in acrylic, contains two holes (inlet and outlet) connected by a fixed depth (0.5 mm) and variable width channel. The channel is narrow

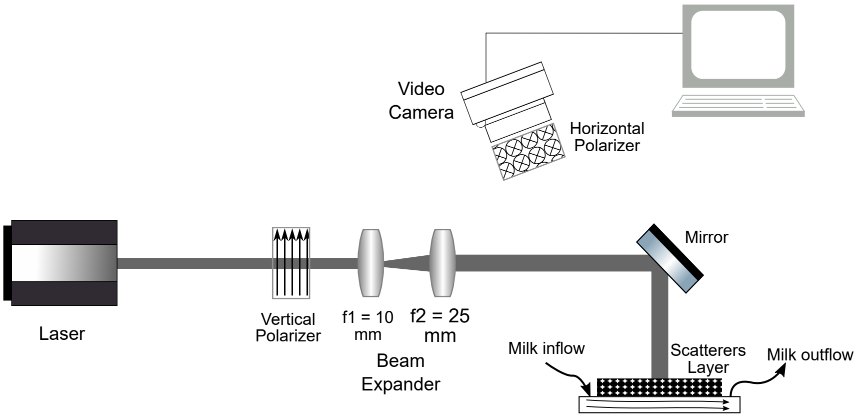

Figure 4.7: Optical scheme of the microcirculation bench set-up.

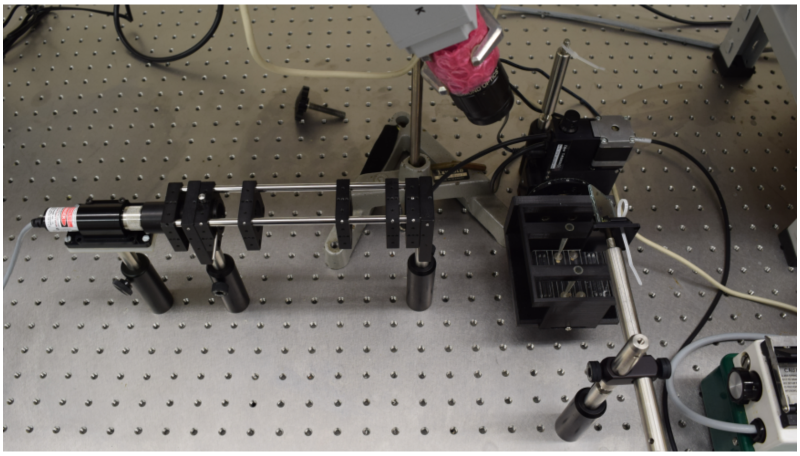

Figure 4.8: Photography of the experimental bench set-up for microcirculation studies.

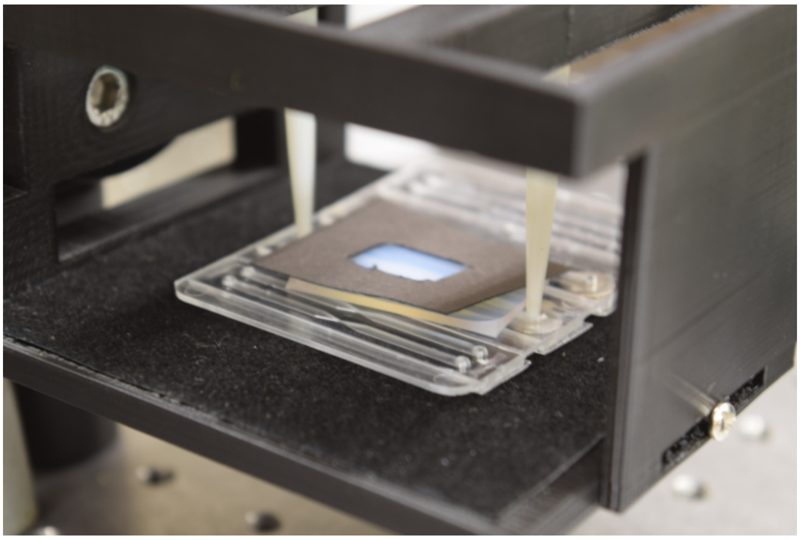

Figure 4.9: Lateral photography of the sample. The microchannel device is visible under the static scatterers layer. Two pipette tips are used to inject and remove the fluid.

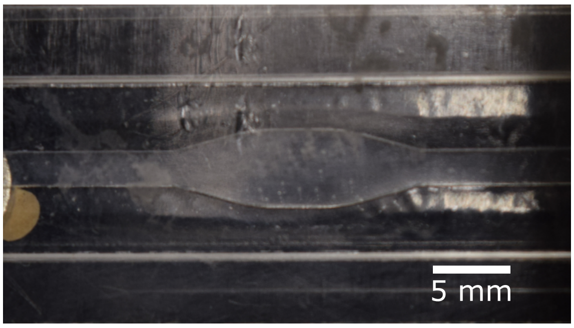

Figure 4.10: Photography of the phantom microchannel.

near the holes, with a width equal to 2 mm, and wider in the middle segment, with a width equal to 5 mm (Fig. 4.10). The microchannel phantom has been kindly provided by the Technical University of Tampere (Finland). A syringe pump, Razel® Scientific Instruments, model R-99, was used to pump the fluid at different flows.

Several modifications have been performed in the VC set-up. The VC image resolution has been fixed to 320 × 240 pixels because the ROI, in this experiment, is restricted (only the phantom microchannel). The other major change was regarding the used exposure time. To match the single-exposure commercial available devices (subsection 3.2.5), the VC exposure time has been set-up to 6 ms and the frame rate to 20 fps.

The ideal lens aperture has been computed using the method described in equation (3.26), subsection 3.2.1, in order to ensure a correct speckle sampling. The imaging system magnification has been determined using an optical resolution target (USAF 1951 1X) and it was $M = 0.2$. Since the pixel size of the imaging sensor is $6.7\mu m \times 6.7\mu m$, the minimum aperture is:

$$f/\# \geq \frac{d}{1.2(1+M)\lambda} \geq \frac{2 \times 6.7\,\mu m}{1.44 \times 640\,nm} \geq 14.5\,. \tag{4.16}$$

Because the used lens only admits discrete values of $f/\#$, the aperture has been fixed to $f/16$ in order to ensure a correct sampling of the speckles.

4.2.2 Microchannel phantom flow simulations

A set of simulations has been performed to study the relationship between the applied inflow at the entrance of the phantom and the fluid velocity inside the channel. COMSOL Multiphysics® 5.0 was used to simulate our system. Both fluid flow and particle tracing studies have been conducted.

4.2.2.1 Fluid flow

The first simulations (Figs. 4.11 and 4.12) have been conducted in order to estimate the fluid velocity inside the microchannel for a specific inflow. Water was selected as the simulation fluid because it presents similar density and viscosity when compared with

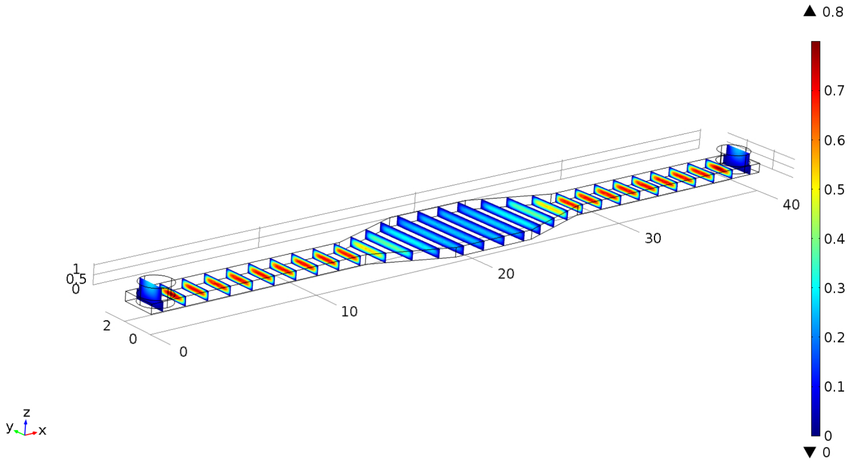

(a) Flow = 1.5 cm^3/h

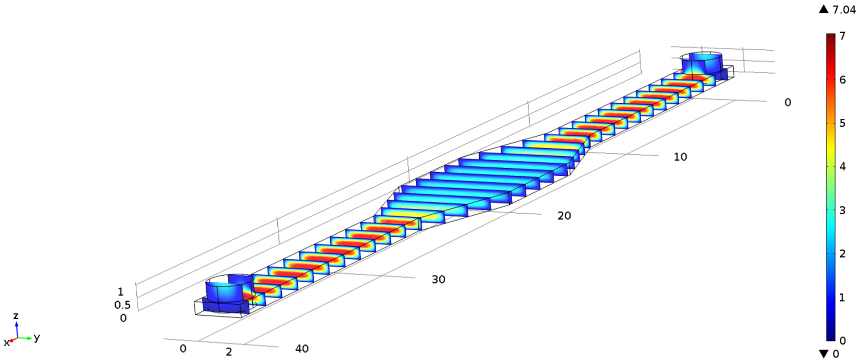

(b) Flow = 14 cm^3/h

Figure 4.11: Fluid velocities along the phantom channel. The two-dimensional slices present the fluid velocity in different channel positions. The values presented in the colour bar are expressed in mm/s. The dimensional values are presented in millimetres.

milk [238, 239]. The water draining has been simulated using different inlet flows (from 1.5 to 14 cm^3/h).

Figure 4.11 shows the results of the simulation regarding the fluid velocity assessment. A set of multiple two-dimensional planes of the microchannel is indicative of the velocity range that can be found inside the phantom. Each plane represents a transversal slice of the channel and its colour encodes the fluid velocity. The values presented in the colour bar are expressed in mm/s. The flow direction is the same as the X-axis. The inlet and outlet holes can be identified near the 0 and 40 x-axis positions and are represented as vertical cylinders.

Figure 4.11(a) presents the case with the minimum inflow (1.5 cm^3/h). The fluid velocity is higher in the narrow parts of the channel, reaching a maximum value of 0.8 mm/s. As expected, the velocity decreases in the wider channel segment. Moreover, the velocity near the channel walls is significantly lower than in the channel core.

The other simulation example (Fig. 4.11(b)) corresponds to the case with maximum inflow (14 cm^3/h). The maximum velocity reached with this flow was 7.04 mm/s. All the

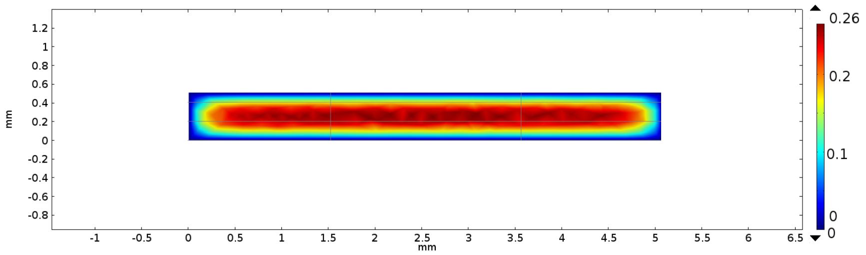

(a) Flow = 1.5 cm^3/h

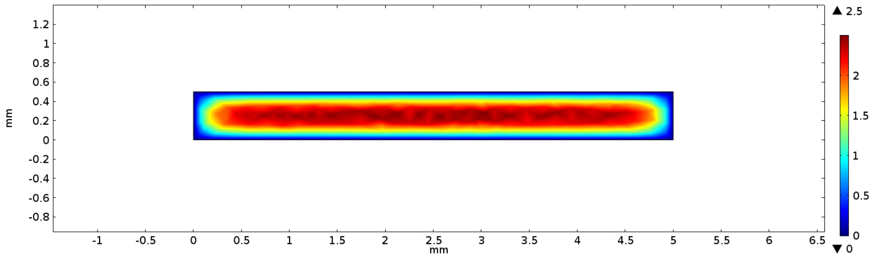

(b) Flow = 14 cm^3/h

Figure 4.12: Fluid velocity inside the wider zone of the channel. Transversal slice. The values presented in the colour bar are expressed in mm/s.

conclusions regarding the first case can also be applied to the highest flow, making both cases to behave as laminar flow.

Figure 4.12 presents a magnification of the central plane of the wider channel segment. This area is the most important for our experiments since the laser light has been directed to the wider channel part.

In this area, the maximum fluid velocities are 0.26 mm/s and 2.5 mm/s respectively for the lowest and highest inflows. These values correspond to a reduction of almost 70% of the velocity compared with the maximum speeds in the narrow channel zone. However, the velocities presented in the wider zone are more appropriate to simulate the physiological case because the blood velocities in capillaries are around 1 mm/s [240].

Table 4.3 summarizes the relation between the inflow (ϕ) and the core velocity of the wider channel zone. The increase of the core velocity is directly proportional to the increase of inflow up to, at least, 14 cm^3/h.

Table 4.3: Relationship between the phantom inflow and the fluid velocity in the core of the wider segment.

Case #	Flow (cm^3/h)	Core velocity (mm/s)
0	0	0
1	1.5	0.26
2	3	0.53
3	7	1.25
4	14	2.50

4.2.2.2 Particle tracing

An additional simulation, taking advantage of the previous results, has also been performed in order to study the behaviour of discrete particles. This situation represents the case where RBC are dragged by the blood plasma. In order to simulate this case, a periodic injection of particles has been added to the previous model. The selected particle diameter was 3 μm which is similar to the fat globules in the cow milk [241].

The results summarized in figure 4.13 show the trajectories followed by the particles under the fluid drag forces. All the particles show clean trajectories without the formation any kind of turbulence. The particles may accumulate near the inflow and outflow holes but this is not critical since the evaluation area is far from this site.

By comparing the images of figures 4.13(a) and 4.13(b), the last one shows a better homogeneity of the particles distribution. This visualization artifact is due to the slower movement of the particles for $\phi = 1.5\ cm^3/h$. Since the particle velocity is lower, their dispersion will take more time. If the simulation had been performed during a longer time, the image would have looked like figure 4.13(b).

4.2.3 Layer fabrication

The static scatterers layers, used in this work, have been custom-made using different concentrations of scatterers. In order to fabricate these layers, a silicone elastomer (Sylgard® 184 DOW Corning) has been used as substrate. Additionally, particles of an optical disperser (Sigma-Aldrich titanium (IV) oxide, 1% Mn doped, nanopowder, particle size <100 nm) have been used to introduce static scatterers in the transparent silicone bulk.

Different quantities of TiO_2 particles have been added in order to produce membranes with multiple static scatterers concentration, leading to layers with different opacity degrees. Table 4.4 summarizes the properties of the fabricated layers. The membranes thickness has been kept constant at approximately 1.3 mm. Figure 4.14 presents a photograph of a scattering layer with intermediate density (Layer IV).

The silicone elastomer was mixed with the TiO_2 using a lab mixer in order to obtain an homogeneous paste. This paste was posteriorly placed in an ultrasonic bath to prevent the formation of clusters of TiO_2 particles. After, a volume proportion of 1:10 (hardener : silicone) of curing agent has been added to the paste and manually mixed. To easily detach the layer after the curing reaction, the final product was poured into a silicon container which does not react with the product. The following protocol details the layers fabrication steps:

Table 4.4: Scatterers concentration of the silicone layers.

Layer	I	II	III	IV	V	VI
Scatterers concentration (mg/ml)	0	0.25	0.5	1	1.5	2

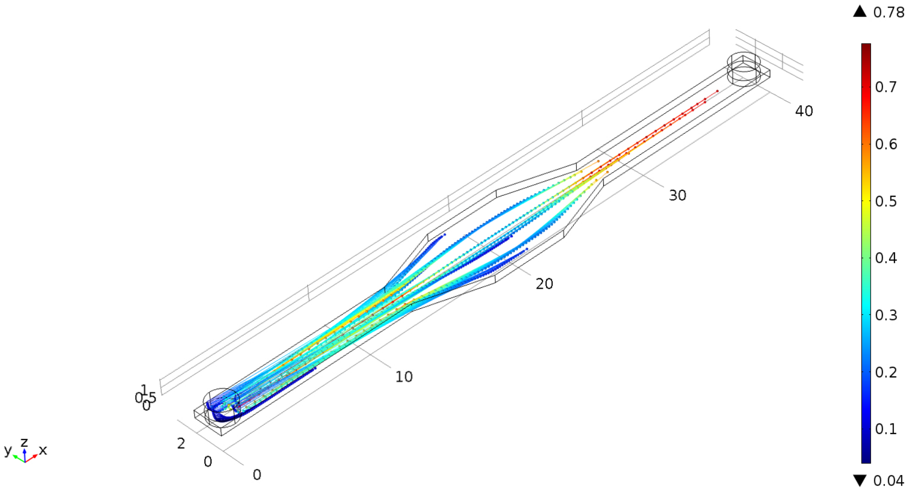

(a) Flow = 1.5 cm^3/h

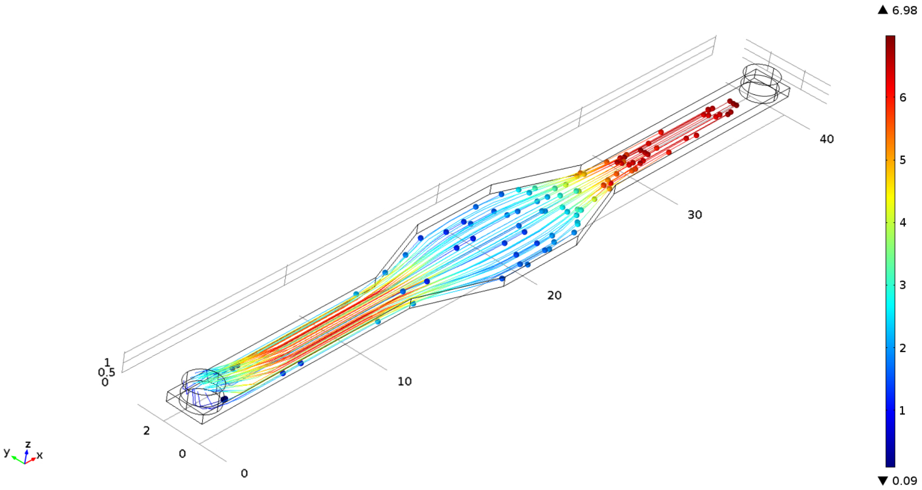

(b) Flow = 14 cm^3/h

Figure 4.13: Particle tracing study results. The values presented in the colour bar are expressed in mm/s.

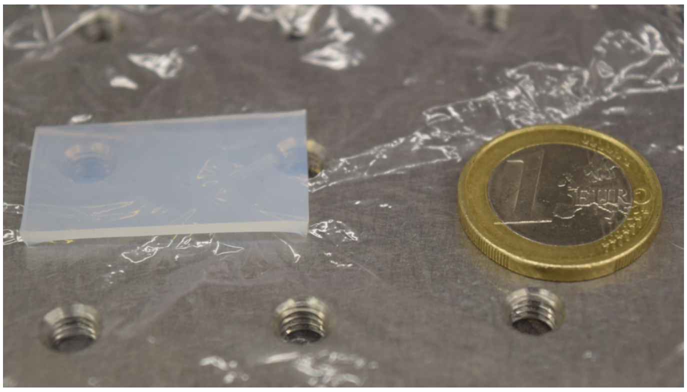

Figure 4.14: Photography of the layer IV.

- Safety
  - Lab coat.
  - No special safety equipment.
- Procedures
  - Measure the required quantity of silicone elastomer.
  - Weight the required quantity of TiO_2.
  - Use a lab mixer to homogenize the paste during 10 minutes.
  - Take the paste to an ultrasonic bath during 45 minutes.
  - Measure the required quantity of hardener.
  - Manually mix the paste with the hardener during 10 minutes.
  - Pour the mixture in a silicon container.
  - Wait 48h to let the cure reactions to occur.
  - Remove the membrane from the container.

Models based in silicone elastomer and TiO_2 are widely used to produce biomedical phantoms due to their optical properties [242–246].

4.2.4 Static scatterers study

The static scatterers study represents the main contribution of this thesis for microcirculation application. The described bench test has been used to clarify the influence of different concentrations of static scatterers in the laser speckle signal. The presented study follows the theory described in subsection 3.1.5 using the methods and approximations described in subsection 3.2.4. The system inter-frame time (1/20 = 50 ms) is larger than the system exposure time (6 ms) making the Zakharov *et al.* [132] approximation valid.

The study aims at testing the equation that relates the ρ value with the correlation between two consecutive frames and the concentration of static scatterers. This equation states that, by computing the correlation between two consecutive frames ($g_2(\Delta t)$), it is possible to determine the ratio between static and total scatterers (ρ). Using the definition of the intensity correlation (Eq. (3.4)) we obtain [132]:

$$g_2(\Delta t) = \frac{\langle A \circ B \rangle_s}{\langle A \rangle_s \langle B \rangle_s}\,, \tag{4.17}$$

where A and B represent two consecutive frames, $\langle ... \rangle_s$ represents the spatial averaging and $\circ$ represents the Hadamard product. This product is defined as a point by point matrix multiplication. By substituting $g_2(\Delta t)$ in equation (3.29) we obtain:

$$\rho = \sqrt{\frac{1}{\beta}\left(\frac{\langle A \circ B \rangle_s}{\langle A \rangle_s \langle B \rangle_s} - 1\right)}\,. \tag{4.18}$$

From this result, we can conclude that $g_2(\Delta t)$ is always positive with a minimum value of 1 and maximum value of $1 + \beta$. This set contains the only possible values that prevent the appearance of imaginary numbers.

Figure 4.15(a) presents the ρ value as function of the theoretically expected correlation ($g_2(\Delta t)$). The increment of static scatters also increases the amount of speckle that does not change in time. These speckles will be presented in all the laser speckle images while speckle originated from moving particles will vary. This is the basic idea behind the use of correlation to quantify the static/dynamic scatterers ratio.

On the other hand, figure 4.15(b) presents the relation between ρ and the static scatterers concentration. This function was computed using ρ definition with a fixed dynamic scatterers concentration:

$$\rho = \frac{\langle I_s \rangle}{\langle I_s \rangle + \langle I_d \rangle} \ . \tag{4.19}$$

The x-axis units are expressed in number of times of dynamic scatterers concentration ($\times\langle I_d \rangle$).

Finally, figure 4.15(c) shows the relation between the correlation and static scatterers concentration. This figure has been computed with the equation that results from the combination of Eq. (3.29) and Eq. (4.19):

$$g_2(\Delta t) = 1 + \beta \Big(\frac{\langle I_s \rangle}{\langle I_s \rangle + \langle I_d \rangle} \Big)^2 \ . \tag{4.20}$$

In this work we propose to use an alternative method to compute the correlation between two consecutive images, the 2D correlation coefficient. The correlation coefficient (r) (Eq. (4.5)) differs from $g_2(\Delta t)$ by including the mean value of each frame. This modification leads to a more standard metric where coefficient values between 0 (no correlation) and 1 (complete correlation) are obtained.

The correlation coefficient, r, by definition, is always a positive value minor than 1, making equation (3.29) impossible to solve using the 2D correlation coefficient. As a way to illustrate this problem, two experimental laser speckle images have been selected. These images correspond to the acquisition using the static layer IV, flow #2 and milk percentage 50%.

Figure 4.16 shows two consecutive images of speckle patterns acquired using layer IV. The r value of this pair is 0.71 while the $g_2(\Delta t)$ is 1.064. When this result is applied to equation (4.18), and assuming $\beta = 0.5964$ (see subsection 5.2.1.1), a ρ value of 0.33 is obtained using $g_2(\Delta t)$ and a ρ value of 0.69i is obtained using r. These results show the impossibility of using the 2D correlation coefficient unless a modification of equation (4.18) is performed or a different interpretation of the imaginary results is empirically determined.

Previously to the study of static scatterers, a first acquisition has been conducted in order to determine β. This constant corresponds to the highest contrast that the developed

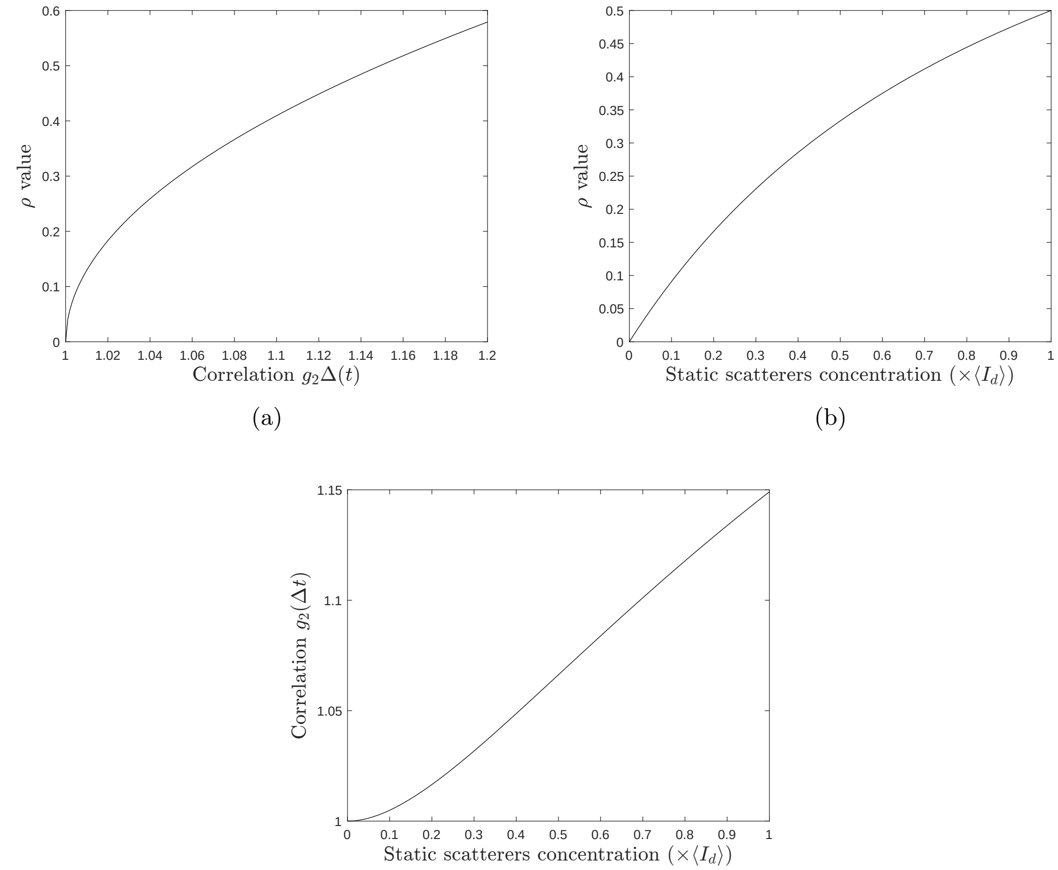

(a)

(b)

(c)

Figure 4.15: Theoretical relations between: correlation and ρ value (a); static scatterers concentration and ρ value (b); and static scatterers concentration and correlation (c). The units of (b) and (c) x-axes $(\times\langle I_d\rangle)$ correspond to number of times of dynamic scatterers concentration.

system can achieve and it is used to compute the ρ value (Eq. (4.18)). The β value has been determined by substituting the sample by a white paper as described in subsection 3.2.3. The image maximum global contrast was then computed spatially and defined as $K_{global} = \beta$.

For the static scatterers study, the prototype and bench test have been used to acquire laser speckle images from the phantom. All the acquisitions have been segmented, to be limited to the wider channel segment. For each configuration (layer, fluid flow, and milk percentage), 600 laser speckle images have been recorded. The correlation metrics ($g_2(\Delta t)$ and r) have been computed in regions of 5×5 pixels, similarly to the contrast algorithm, between two consecutive images. This processing steep results in 599 correlation maps for each configuration (I_{g_2} and I_r).

Finally, a mean correlation map image has been computed for each acquisition configuration ($\overline{I_{g_2}}$ and $\overline{I_r}$). The modified Tompkins-τ algorithm has been used to exclude outliers [247] using a two-tailed distribution with an 95% confidence interval. The exclu-

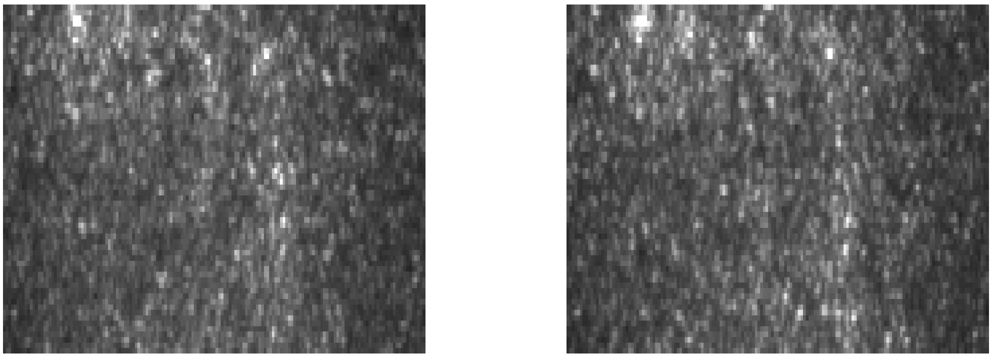

(a) Frame = i

(b) Frame = i+1

Figure 4.16: Consecutive speckle images of membrane IV. Raw data. The correlation and 2D correlation coefficient are respectively: $g_2(\Delta t) = 1.064$ and $r = 0.71$.

sion criterion, in accordance with the table A-3.1 of [247], has been computed as:

$$\tau_{th} = \frac{1}{\sqrt{n}} \frac{t_{\alpha/2}(n-1)}{\sqrt{n-2+t_{\alpha/2}^2}} \,, \tag{4.21}$$

where n is the number of samples and $t_{\alpha/2}$ is the critical value of a Student's t-distribution of $n-2$ samples, with a degree of confidence α. With the remaining points, the mean ($\overline{g_2}$ and $\overline{r}$) and standard deviation (δg_2 and δr) of the correlation have been computed for each configuration. An outliers removal algorithm was applied in order to remove possible areas were the used phantom could present imperfections, like clusters of scatterers in the layers or cracks in the channel.

Additionally, speckle contrast has been computed using spatial, temporal, and spatio-temporal contrast algorithms (section 3.4). The used elements correspond to 5×5 pixels for the s-K, 1×1×15 for the t-K and 3×3×5 for the st-K. The method used to compute the mean and standard deviation contrasts was the same as the one described for the correlation.

4.3 Spatial contrast algorithm optimization

As detailed in subsection 3.4, three families of contrast algorithms are mainly used in LSI. The spatial-based algorithm is the most often used although the results of the temporal-based algorithms are more suited for samples with static scatterers.

Because of the relatively large amount of information on the spatial-based contrast algorithm, compared to the other algorithms, and its importance for commercial devices, we decided to test several implementations of this algorithm in order to find the most optimized. Algorithm optimization is a key factor when online applications are necessary, or large amount of data are analysed.

Many different implementations of the spatial contrast algorithm can be found in the literature [248]. The following implementations have been selected because they take advantage of the MATLAB® matrix operations optimization and can be implemented without using any loop sequence. The MATLAB® version R2016a - 64 bits has been used to perform this evaluation.

Most parts of the implementations presented in the literature correspond to low-level programming language implementations. Contrary, this subsection explores the use of high-level programming tools such as the MATLAB® functions.

In this optimization study, three algorithms have been implemented. Two implementations are already presented in the literature [192, 248, 249] and the last one corresponds to a novel implementation. The state-of-the-art methods include a moving summation based implementation and an image filtering based implementation. Contrary, the novel method is based on two-dimensional convolutions.

These optimized methods take advantage of a modified contrast equation in which the intensity mean and standard deviation have been substituted by intensity sums [249]. This equation can be expressed as:

$$K^s(i,j) = \sqrt{\frac{N^2}{N-1} \times \frac{\sum_x \sum_y I^2(x,y)}{\left(\sum_x \sum_y I(x,y)\right)^2} - \frac{N}{N-1}}\,, \tag{4.22}$$

where $K^s(i,j)$ is the contrast associated with the element in the position (i,j), N is the number of summed points and I is the intensity of the processing element. The summations adopt the same notation as equation (3.30). To compute this equation it is only needed to determine the summation of the pixels inside the element. Apart from this optimized implementations, the analytical solution (equation (3.30)) has been applied as a comparative result.

A set of laser speckle images have been synthesized using the algorithm presented in [250]. The data-set contains 600 images equally divided by 3 different resolutions, 320×240 pixels, 640×480 pixels, and 1024×768 pixels. Within each resolution, 50 images of each speckle size (4, 8, 16 and 32 pixels/speckle) have been included.

Those images have been filtered with two-dimensional average filters in order to simulate different contrasts. Figure 4.17 presents the contrast distribution of the simulated laser speckle images. A wide range of contrast values, from 0.25 to 1.05, is covered by this data-set. The maximum contrast is above the theoretical limit (see section 3.1) because of the nature of the synthesis method [192].

These 4 spatial-contrast implementations have been tested for the most common elements sizes (ROI) which are 3×3, 5×5 and 7×7 pixels. For more details about this algorithm please refer to section 3.4. All the tests have been performed in a computer Toshiba Tecra S11-11G - i7 M620 @ 2.67GHz with 4GB RAM and Windows 10 Pro (64 bits) as operating system.

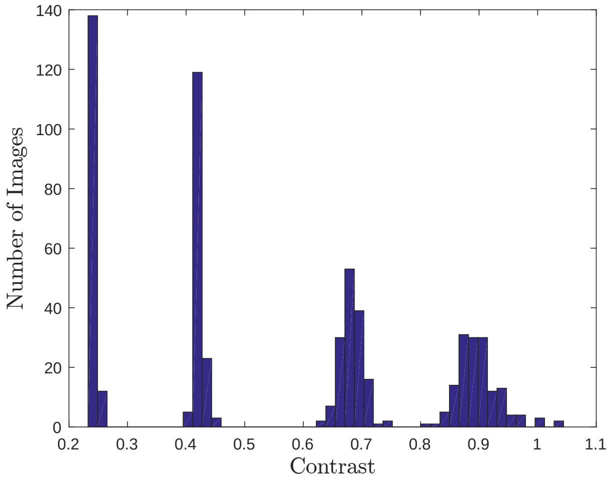

Figure 4.17: Distribution of the global contrast values of all the tested images. Total number of images: 600 frames.

4.3.1 Analytical computation

This implementation has been applied as a reference method and it was not optimized in any way. This method was applied using the MATLAB® functions `std2` and `mean2` within each image element. The element was then translated along the image using two `For` cycles, one for the rows and one for the columns. As discussed earlier, this algorithm implies a reduction of the contrast map resolution because the element displacement is performed without overlapping. This implementation is detailed in pseudo-code in algorithm 1.

Algorithm 1: Analytical computation

```
Input: LS raw image (LSimage) and element size (ROIsize)
Output: Contrast image (cImage)
for ii ← 1 to number of LSimage lines with ROIsize steps;
do
    for jj ← 1 to number of LSimage columns with ROIsize steps;
    do
        ROI ← cut subimage with input size and the pixel center in the position (ii,jj);
        mean ← mean2(ROI);
        std ← std2(ROI);
        contrast ← std/mean;
        cImage ← contrast is stored in the correct position of the cImage
return cImage
```

4.3.2 Filtering implementation

The filtering implementation consists in the application of two image filters in the full resolution speckle image. The MATLAB® function `imfilter` has been used with a all-ones kernel of the same size of the selected element. This filter has been applied to the laser speckle image and its squared in order to compute the two intensity summations of equation (4.22). This implementation does not reduce the resolution of the contrast map. The pseudo-code of this implementation is defined in algorithm 2.

```
Algorithm 2: Filtering
  Input: LS raw image ($LSimage$) and element size ($ROIsize$)
  Output: Contrast image ($cImage$)
  $Kernel \leftarrow$ all-ones matrix with the $ROIsize$;
  $Sum \leftarrow$ imfilter($LSimage$, $Kernel$);
  $Sum2 \leftarrow$ imfilter($LSimage. * LSimage$, $Kernel$));
  $cImage \leftarrow$ application of the sums equation for each point (Eq. (4.22));
  return $cImage$;
```

4.3.3 Moving sum implementation

This algorithm, originally implemented in CUDA [9] and C programming languages, has been described in [248] and [249]. Since the programming language used is MATLAB®, an adaptation of this implementation was used taking advantage of the function `movsum`. This implementation consists in a moving summation, with a length equal to the element lateral size, applied to each line of the laser speckle image. The resultant structure is then summed over the columns, again with the length of the element. This procedure is repeated for the squared image. Finally, the modified contrast equation is applied. The respective pseudo-code is described in algorithm 3.

```
Algorithm 3: Moving sum
  Input: LS raw image ($LSimage$) and element size ($ROIsize$)
  Output: Contrast image ($cImage$)
  $SumLines \leftarrow$ movsum($LSimage$, $ROIsize$) for each line;
  $SumLines2 \leftarrow$ movsum($LSimage. * LSimage$,$ROIsize$) for each line;
  $Sum \leftarrow$ movsum($movSumLines$, $ROIsize$) for each column;
  $Sum2 \leftarrow$ movsum($movSumLines2$, $ROIsize$) for each column;
  $cImage \leftarrow$ application of the sums equation for each point (Eq. (4.22));
  return $cImage$;
```

4.3.4 Convolution implementation

The novel proposed implementation has been applied using the MATLAB® function `conv2`. This function computes the convolution between the laser speckle full resolution image and an all-ones matrix kernel with the same size of the processing element. This procedure is similar to algorithm 2 but using a different function. The convolution is

---

[9] CUDA is a NVIDIA parallel computing platform and application programming interface (API) used to develop general purpose processing in graphics processing units (GPU).

applied to the laser speckle images and its square. The respective pseudo-code is detailed in algorithm 4.

Algorithm 4: Convolution

```
Input: LS raw image ($LSimage$) and element size ($ROIsize$)
Output: Contrast image ($cImage$)
$Kernel$ ← all-ones matrix with size equals to $ROIsize$;
$Sum$ ← conv2($LSimage$, $Kernel$);
$Sum2$ ← conv2($LSimage .* LSimage$, $Kernel$);
$cImage$ ← application of the sums equation for each point (Eq. (4.22));
return $cImage$;
```

Chapter 5

Results

> *Ole Rømer (1644–1710) had proof that the light does not travel instantaneously. He made this discovery by finding changes in the periodicity of the eclipse of a Jupiter moon (Io) when the Earth was close and far from Jupiter.*

This chapter is divided into three main sections. In the first section, the results for macrocirculation applications are presented. The second main section presents the results of microcirculation static scatterers study. The third section shows the results of the contrast algorithm optimization process.

5.1 Macrocirculation application

5.1.1 Multi-wavelength study

This section presents the results obtained for the multi-wavelength study for both bench experiments and *in vivo* studies following the methods described in section 4.1. An example of the laser speckle data extracted from the set-up represented in figure 4.1 can be found in figure 5.1. This figure also contains information of the processing methods used in subsection 4.1.2.1 and subsection 4.1.2.2.

Figure 5.1 shows tree laser speckle images, obtained in the static skin-like phantom with different laser light wavelengths. It can be seen that the speckle pattern obtained with the infrared light (Fig. 5.1(c)) appears blurred compared with the two others. This blurring effect happens because the penetration of the infrared light in the skin-like phantom is higher than the penetration of the other wavelengths [251]. This may happen because the pattern formed by the L_{850} results from light scattered by the internal phantom membranes whereas the L_{532} and L_{635} patterns are formed by light scattered from the superficial layer. The multiple scattering events that occur for the L_{850} could be the cause of this blurring effect.

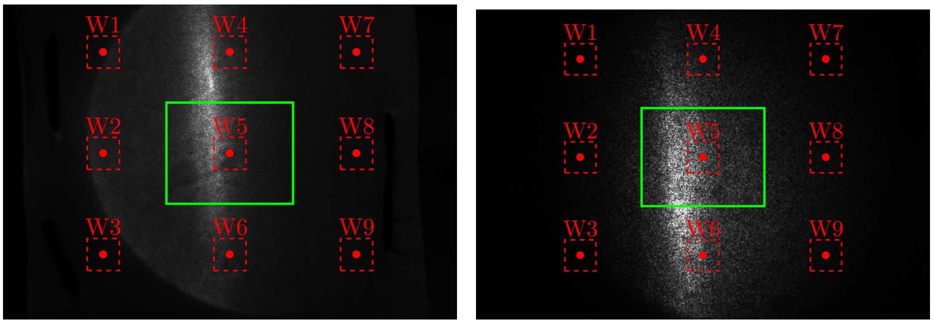

(a) L_{532} - Green (b) L_{635} - Red

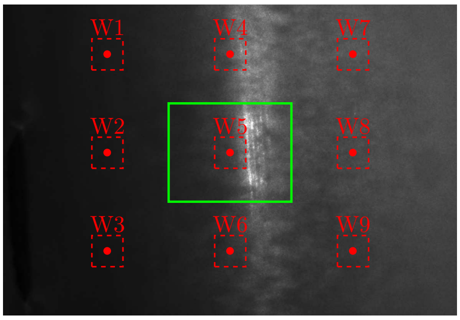

(c) L_{850} - Infra-red

Figure 5.1: Unprocessed speckle images of the skin-like phantom. The images resolution is 1280×1024 pixels and they are displayed in greyscale levels. The red dots represent the windows centres and the red rectangles an example of a 81×81 pixels window. The green squares represent the zone of the image analysed during the velocity profile reconstruction and corresponds to the centre of the image.

5.1.1.1 Vibration frequency determination results

The pre-selected windows where the PSD was computed are represented in figure 5.1 by dashed red squares. These windows were labelled from W1 to W9 from upper left to bottom right. The red squares represent a ROI with size of 81×81 pixels. For each pixel of the ROI, the PSD has been computed and its mean was associated with the window. 36 different combinations between position and size have been obtained resulting in 36 mean PSD. For each one, the most intense frequency and its power were identified and compared with the real vibration frequency.

Figure 5.2(a) shows the temporal variation $(I_{x,y}(t))$ of the central pixel of W5. The skin-like phantom was moving with an amplitude of $1V_{pp}$ and frequency of 3 Hz. This figure corresponds to the grey scale values of the raw laser speckle image recorded with L_{532}. A clear oscillation of the pixel intensity is visible in the graphic.

Figure 5.2(b) corresponds to the mean PSD of all the pixels in W5 with size 81×81 pixels. The most powerful frequency of the PSD is evident at 3 Hz, which is the expected frequency due to the applied movement. A second peak with considerable power is also visible at 6 Hz which corresponds to the second harmonic. This powerful harmonic can be explained by intermediate fluctuations of the pixel intensities (visible in Fig. 5.2(a)). This

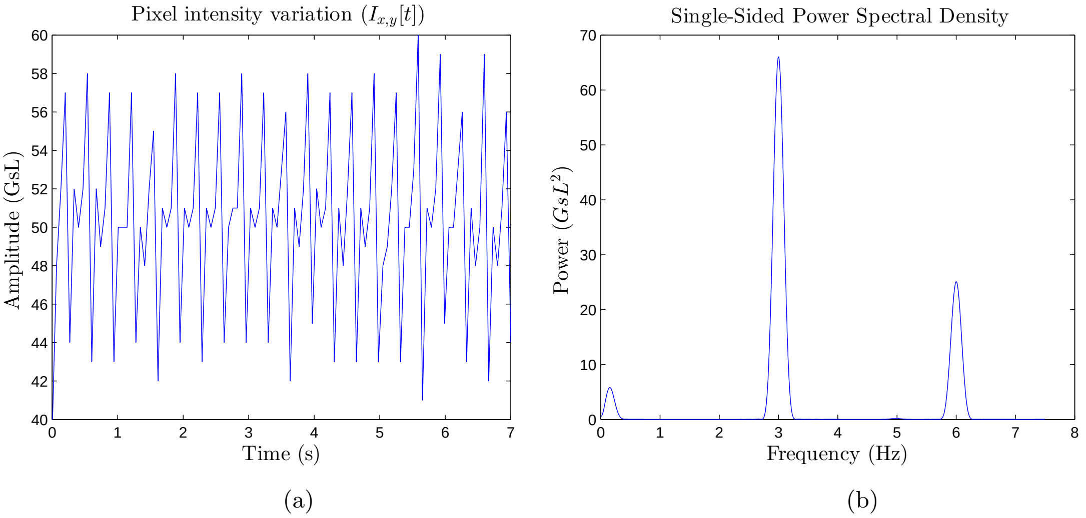

Figure 5.2: (a) - Temporal variation of the central pixel intensity of the acquisition characterized by an amplitude of $1V_{pp}$ and frequency of oscillation of 3 Hz. The amplitude is represented in greyscale levels (GsL). (b) - PSD computed in the ROI W5 with 81 pixels size.

phenomenon can occur when the speckle observation is performed from a non-normal position to the target leading to a pseudo random speckle noise [118]. This second harmonic could be a major problem for the vibration frequency identification if the fundamental and second harmonic frequencies achieve similar spectral power. Moreover, the skin-like phantom is composed of four membranes which can have small independent oscillations.

The most powerful frequency of the mean PSD was then compared with the correct oscillation frequency by computing the root mean square error (ϵ_{rms}). This error was computed using a global analysis where all the possible movement amplitudes and frequencies are considered at once:

$$\epsilon_{rms}^{s,p} = \sqrt{\frac{\sum_{n=1}^{N} (f_{n,s,p}^{estimated} - f_{n,s,p}^{true})^2}{N}}\ , \tag{5.1}$$

where s, p represent the ROI size and position, respectively, and N is the number of analysed phantom movements (16).

The results of this analysis are presented in figure 5.3. The L_{532} case shows lower errors in the central column (W4, W5 and W6), independently of the ROI size. With a minimum error of $10^{-2.9}$ (1.3 mHz), the green light represents the worst result. The membrane curvature causes an anisotropic light diffusion, mainly in the green wavelength, causing the areas along the central column to present higher emittance. Outside these areas, the image quality, in terms of laser speckle information, is weaker. The speckle images of figure 5.1 show the reason for the best results of the central column.

Contrary, for L_{635}, the results evidence that the ROI size is significantly more important than its actual position. By analysing the results obtained for the ROI with 81×81

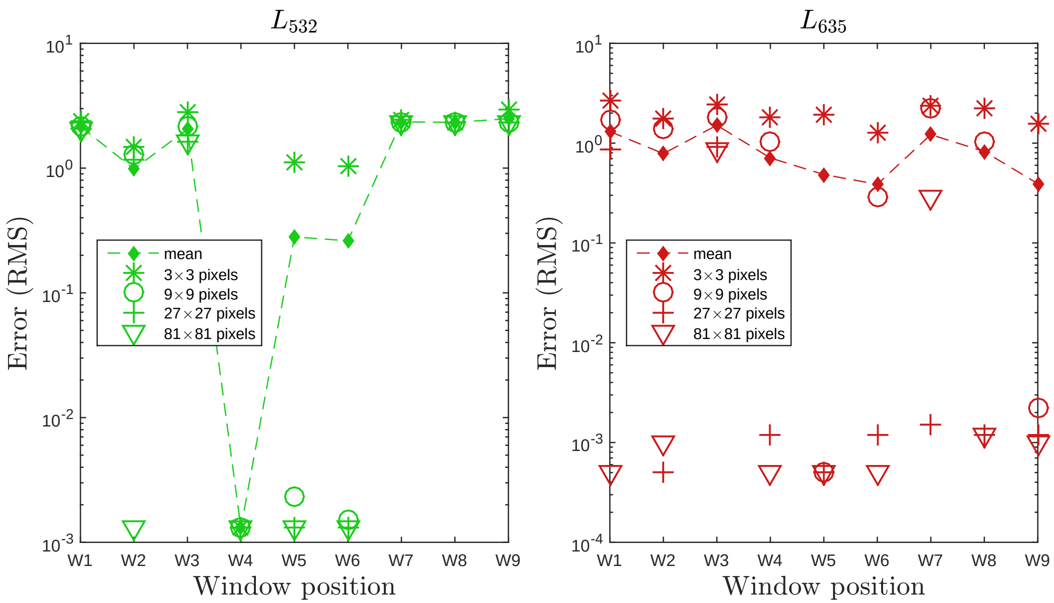

(a) Green laser (b) Red laser

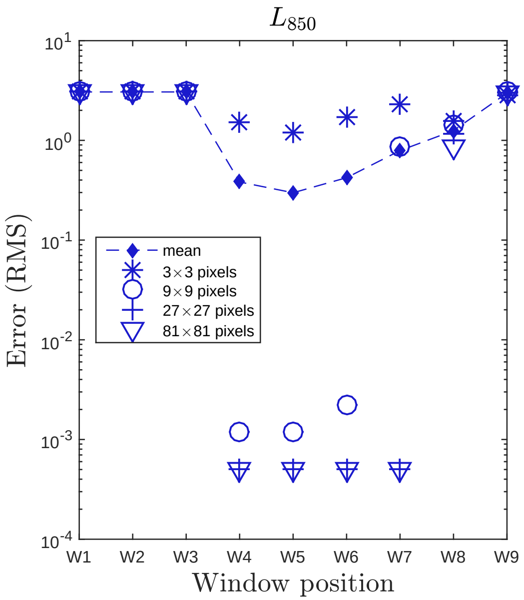

(c) Infra-red laser

Figure 5.3: Results of the root mean square error of the membrane frequency vibration estimation for (a) L_{532}, (b) L_{635} and (c) L_{850}. Different markers indicate different windows sizes (see legend). The y axis is presented in log scale.

pixels, the oscillation frequency is identified, in almost all the cases, with an error close to $10^{-3.3}$ (0.5 mHz). This value, in terms of the analysed frequency range (1 Hz - 3 Hz), represents an error between 0.02% and 0.05%.

Finally, in the L_{850} case, represented in figure 5.3(c), the position of the ROI and its size are relevant parameters for a good vibration frequency identification. The minimum error, obtained with this light source, was 0.5 mHz which is the same as the L_{635} case. This value happens to be related with the FFT resolution. Both the L_{635} and L_{850} achieved similar performances on the identification of the vibration frequency, showing a more isotropic diffraction of the light inside the skin-like phantom. The anisotropic reflection effect is particularly relevant in the L_{532} (Fig. 5.1(a)) because most part of the light is directly reflected by the phantom surface.

5.1.1.2 Velocity profile reconstruction results

For the velocity profile study, the raw laser speckle data have been restricted to the green rectangle represented in figure 5.1 which corresponds to 427×341 pixels (image inner zone). This segmentation has been performed in order to reduce the computational time and because the most relevant information is represented in the centre of the image.

To better compare the reconstructed velocity profile with the real actuation signal, the absolute velocity of the phantom was normalized and compared with the $1 - r'$ signal (equation (4.5)). Figure 5.4 shows the representation of an example of the real (blue line) and reconstructed (red line) velocity profiles. This is an example for the case of a 1/5 Hz frequency and 2 V_{pp} amplitude.

Both profiles are very similar in shape which demonstrates the good reconstruction of the absolute velocity of the skin-like phantom. The method efficiency was analysed by computing the root mean square error between the real profile and reconstructed profile. The error values are presented in table 5.1 and are expressed in percentage.

Regarding the L_{532} case, a clear tendency is observed where movements with larger periods are reconstructed with lower errors. This effect is presented in the mean errors for each period which were, respectively, 17%, 16%, 12% and 11% from high to low frequencies. The lower error was achieved for the movement with amplitude of 8 V_{pp} (0.37 mm maximum displacement) and 1/5 Hz with a value of 9.5%. These results are easily explained because both large periods and small displacements correspond to lower velocities. Due to instrumentation limitations, the low frame rate of the acquisitions (15 fps) is a major obstacle when rapid movements occur. Moreover, the high compliance of the membrane causes it to continue to move even after the piezoelectric actuator stop. This effect is more relevant in rapid movements because the target shows higher linear momentum and takes more time to stop completely.

In the case of the L_{635}, the error decreases for movements with large periods and small displacements. The minor error is 10.3% which occurs for the largest period (5 seconds) and the smallest amplitude ($2V_{pp}$) which is the case presented in figure 5.4. This case corresponds to the lowest maximum velocity (0.12 mm/s) which corresponds, in theory, to the easiest movement to reconstruct. The mean errors for each frequency were respectively 19%, 22%, 19% and 18%, from high to low frequencies. A clear tendency is not observed in this measure but the lowest mean error occurs for the lower frequency (1/5 Hz). Regarding the movement amplitude, the lowest mean occurs for the 2 V_{pp} case with an error of 15.3%.

Finally, the results of the L_{850} present a different situation. The tendency, of this light source, is that movements with large amplitude have smaller error. Nevertheless, the results show poor correlation with the period parameters. For example, the mean errors

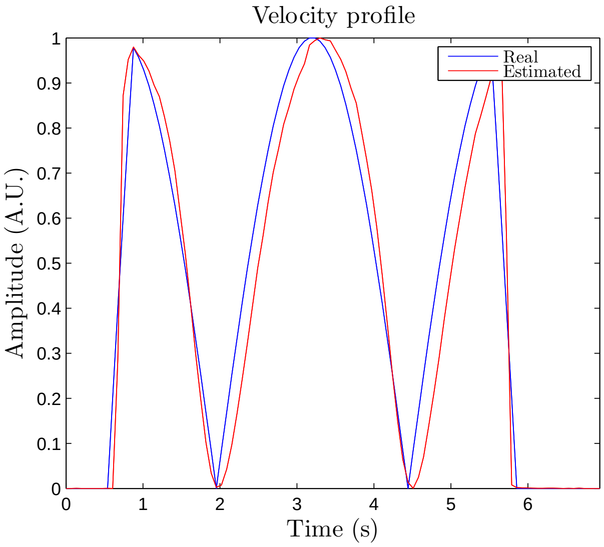

Figure 5.4: Plot of $1 - r'$ along time (red line) and absolute velocity of the phantom (blue line) of the movement with amplitude of 2 V_{pp} and 5 seconds of period.

Table 5.1: Results of the RMS error of the velocity profile reconstruction with L_{532}, L_{635} and L_{850} data. Values are presented in percentage.

		Amplitude (V_{pp})		
	Period (s)	2	4	8
L_{532}	1	20.68	11.87	19.31
	2	18.63	15.08	12.68
	3	15.55	9.92	9.52
	5	12.22	9.45	10.21
L_{635}	1	17.38	18.96	19.58
	2	20.83	21.68	24.91
	3	12.54	20.66	25.11
	5	10.31	16.78	26.64
L_{850}	1	16.27	14.78	13.26
	2	16.11	12.19	13.83
	3	20.42	13.97	9.02
	5	21.62	22.64	14.89

for each frequency were 15%, 14%, 14% and 20% respectively from high to low frequency. Contrary, the error appears to be related with the movement amplitude since the ϵ_{rms} is 19%, 16% and 13% respectively from low to high amplitudes.

The overall result of the three light sources are close to each other, but their mean errors have been 13.8%, 19.6% and 15.8% for L_{532}, L_{635} and L_{850} respectively. The anisotropic reflection of the L_{532} causes most of the light to be reflected within the region of interest leading to a highest SNR.

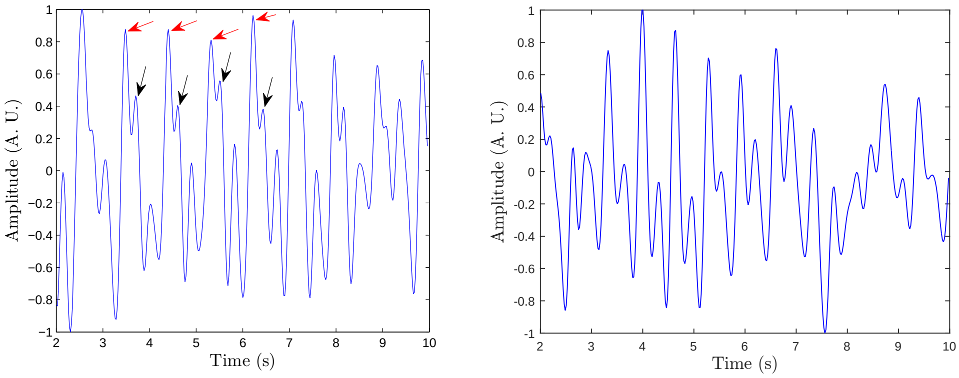

(a) L_{532} (b) L_{635}

Figure 5.5: Output signal of the correlation algorithm with no image pre-processing (including filtering) to the *in vivo* test S4 (a) and S10 (b). Red arrows show the probable systolic peak and black arrows show the probable dicrotic notch.

5.1.1.3 *In vivo* measurements results

The first conclusion of this test was, as expected, that a real *in vivo* application presents a much lower SNR than the posterior bench experiments. Moreover, the light source L_{850} was unable to record reliable data to be used with the described algorithms. The higher penetration of the L_{850} in the bench test (figure 5.1(c)) has been magnified for the living tissues [252]. Higher penetrations cause more scattering events, leading to an output beam less coherent, reducing the speckle effect.

Two examples of extracted pulse waveform signals, after filtering and without any pre-processing method, are presented in figure 5.5, one for each light source. These figures show a periodic movement with the same frequency as the subject HR and some features similar to the pulse waveform (Fig. 2.5). These features are clear in the waveform extracted from L_{535} data. The red and black arrows of figure 5.5 represent the possible location of the systolic peak and dicrotic notch.

The numerical results of the HR identification, for all the data-sets are represented in table 5.2. The subject HR has been determined using the PPG data and compared with the estimated HR. Two errors have been computed, the $d\epsilon_{rms}$, for each acquisition, and the $g\epsilon_{rms}$, for each pre-processing method. The values presented inside the parenthesis for $g\epsilon_{rms}$ correspond to the errors computed including the data-set S3. This data-set was clearly tainted by movement artifacts and constitute an outlier because it shows the highest error for a long margin. The consideration of this data could induce erroneous conclusions.

By analysing the results for the L_{532} light source and excluding the S3, all the $d\epsilon_{rms}$ have been below 0.79 bpm. This is a very good result because it indicates that the skin vibration frequency was identified correctly, with the coefficient correlation method. The minimum error was achieved in data-set S4 with an error of only 0.18 bpm.

The results of the L_{635} light source show a wider range of error, compared with the

Table 5.2: Results of heart rate (HR) estimation with *in vivo* conditions. The values in the table are expressed in bpm. * Data-set tainted by artifacts.

	Data set	S1	S2	S3*	S4	S5	S6	$g\ \epsilon_{rms}$
L_{532}	Subject HR	62.3	62.3	64.1	65.9	67.8	67.8	
	No pre-process	61.4	62.4	69.6	65.7	67.6	67.2	0.50 (2.28)
	Binarization	61.5	61.9	69.5	65.7	67.4	67.4	0.48 (2.24)
	Hist. equal.	61.4	62.3	69.6	65.7	67.6	67.2	0.50 (2.28)
	$d\ \epsilon_{rms}$	0.79	0.22	5.46	0.18	0.26	0.50	
	Data set	S7	S8	S9	S10	S11	S12	$g\ \epsilon_{rms}$
L_{635}	Effective HR	64.1	65.9	67.7	82.4	89.7	60.4	
	No pre-process	66.4	66.0	68.7	82.4	88.6	59.6	1.15
	Binarization	66.7	65.6	68.7	82.5	88.5	59.6	1.26
	Hist. equal.	66.4	65.9	68.7	82.4	88.6	59.6	1.15
	$d\ \epsilon_{rms}$	2.38	0.22	0.92	0.05	1.13	0.82	

L_{532}. The $d\epsilon_{rms}$ ranges from 0.05 bpm (the best result of all data-sets) and 2.38 bpm. Four out of six data-sets (S7, S9, S11, and S12) exceed the maximum L_{532} error which indicates a better performance of the small wavelength.

Regarding the global errors ($g\epsilon_{rms}$), which cover all the data-sets for each pre-processing method, the L_{532} presented the lowest errors (≈ 0.5 bpm). Moreover, no significant performance improvement has been detected for the pre-processing methods. This occurred because laser speckle information is encoded in the image contrast and decorrelation [253]. Concluding, the $g\epsilon_{rms}$ for the L_{635} are more than two times higher than the $g\epsilon_{rms}$ errors of the L_{532}.

Finally, the pre-processing algorithms does not show any type of performance increase in the results. Since the laser speckle information is encoded in the speckles fluctuations, these spatial image processing algorithms do not influence the signal quality.

5.1.1.4 Remarks

The multi-wavelength study has been conducted in order to identify which wavelength is the best for pulse waveform extraction using laser speckle methods. It has been shown that all the selected wavelengths (532 nm, 635 nm and 850 nm) were able to identify the vibration frequency and velocity profile of a skin-like phantom with good reliability and low error. Another remark of this study was that the light dispersion in the skin-like phantom is more isotropic for the L_{850} than for the L_{532} and L_{635}.

The bench experiments, performed with the skin-like phantom, were not conclusive regarding to which wavelength is suitable for this type of assessment. However, the *in vivo* test presented a different situation where the L_{532} achieved the best performance. The lower tissue penetration of L_{532} was the main feature that improved its results in the *in vivo* experiment.

Regarding the biological systems, both the L_{532} and L_{635} have been able to identify the HR of the two subjects. The best result was achieved by the L_{532}. This source has been able to reconstruct the pulse pressure waveform with good detailed allowing the detection of the systolic peak and dicrotic notch. Contrary, the L_{850} was unable to properly reconstruct the pulse waveform.

The instrumentation and methods proposed and used in this test could be used to improve the actual LSI systems in order to combine information from macro and micro-circulation. However, more extensive studies on this type of assessment are required to show the influence of different types of patients (with obesity, hypertension, etc.) on the laser speckle signal. Also, the use of a multi-spectral system capable of simultaneously record data from both sources (macro and micro-circulation) could be of extreme importance for clinical applications.

5.1.2 Pulse waveform extraction study

The study presented in subsections 4.1.2 (where the methods are described) and 5.1.1 (where the results are described) shows that the light source L_{532} achieved the best results. This second study uses this light source in a more extensive *in vivo* study with the goal of analysing the quality of the pulse waveform extraction. Contrary to the previously study, the PPG signal has been recorded simultaneously with the LSI.

Figure 5.6 presents two raw speckle images of the radial artery of one volunteer at different heart cycle stages. These typical speckle images follow the theory discussed in Chapter 3 and are constituted by dark and bright spots. Figure 5.6(a) shows a speckle image of a moment when the radial artery is moving fast (systole). At this moment, the speckle decorrelation is highly visible because of the image blurring. On the other hand, figure 5.6(b) show a case when the radial artery is moving slow or stopped. The contrast of this image is higher because the speckles are much more defined.

After the signal processing (contrast computation), a sequence of laser speckle frames (3D data) is transformed into a one-dimensional data which is a form of information much easier to interpret. This is achieved because the speckle contrast is computed in a window with the same size of the original image. An example of a contrast signal and its correspondent PPG can be seen in figure 5.7. Speckle contrast is plotted in blue and PPG signal is plotted in red.

The speckle contrast and the PPG signals present a very similar periodicity. This fact indicates the good capability of LSI for pulse waveform extraction. Not only the periodicity, but also the waveforms show very similar features between both signal sources. The systolic peak and dicrotic notch are very easy to identify in the speckle contrast signal.

The morphological differences between both wavelengths are expected because the signals are acquired in different location of the arterial tree and by using different techniques. Moreover, the speckle contrast is related with changes in the arterial distension and the PPG is related with changes in the arterial blood volume.

An offset between speckle contrast ($K^s(t)$) and PPG is expected because the signals are acquired in different sites. $K^s(t)$ is acquired in the radial artery while the PPG is

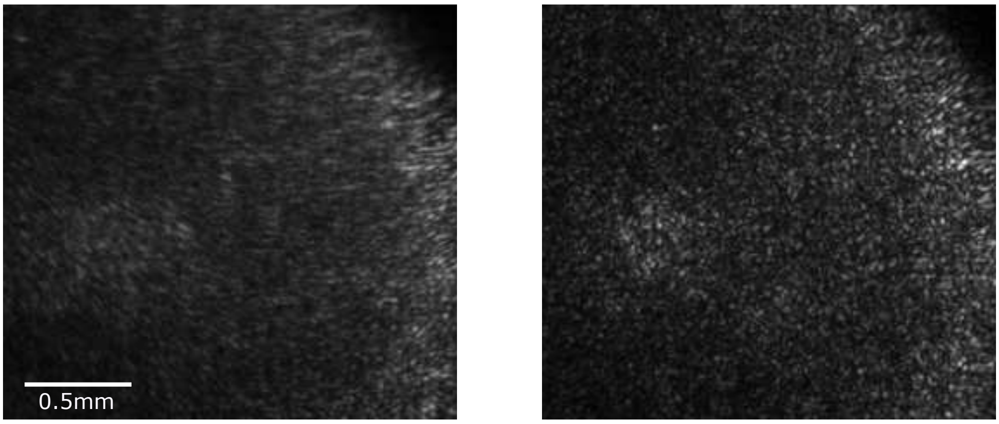

(a) Systole (b) Diastole

Figure 5.6: Laser speckle images from the radial artery at different stages of the cardiac cycle: a) systole, higher skin velocities leading to a blurred speckle image; b) diastole, lower velocities result in a sharper speckle image.

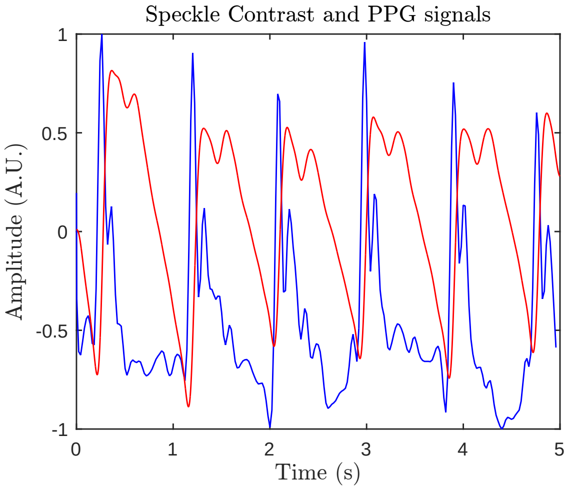

Figure 5.7: Temporal representation of PPG data (red line) and speckle contrast data (blue line).

recorded in the tip of the index finger. This small spatial distance (≈20 cm) adds a small delay between both signals. If we consider a pulse wave velocity of ≈ 5 m/s [60], the delay between both waves should be 40 ms.

According to the temporal resolution of our LSI system (20 ms), the delay between both waves should be 2 samples. In fact, the delays computed from these data range from 30 to 50 ms between the two waves onsets which could lead us to think that this delay is caused by PWV. However, the system low temporal resolution and the impossibility to determine the subjects PWV makes this conclusion highly speculative. Moreover, this delay could be introduced as a systematic error during the synchronization process (software).

The speckle contrast signals have been numerically compared with PPG signals as detailed in subsections 4.1.3.1 and 4.1.3.2. The results of this analysis are presented in

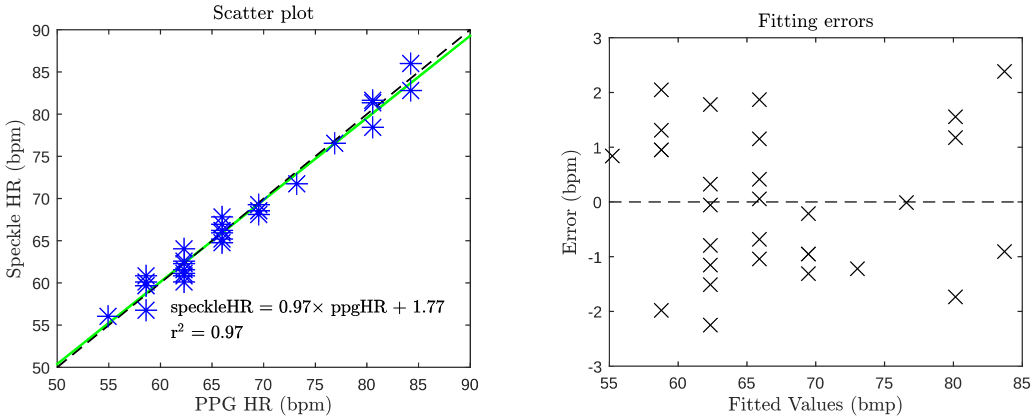

(a) Scatter plot

(b) Fitting errors

Figure 5.8: HR analysis: a) Scatter plot of the PPG HR vs speckle HR. Each star represents one data set. The black line correspond to the fitting equation and the green line to the first quadrant bisector. b) - Fitting errors as function of the HR value.

the next subsections.

5.1.2.1 Hearth rate determination results

Because PPG is a well established technique, the HR identified from this data source has been used as gold-standard. The HR of the 30 data-set were comprised between 55 and 84 bpm with a mean value of 67 bpm which can be considered normal for rest conditions.

Figure 5.8 summarizes the comparative results of the HR computation between both methods. The scatter plot (Fig. 5.8(a)) shows a very good concordance between the data obtained with the two methods. The linear fitting (dashed line) is almost collinear with the first quadrant bisector (green line) which supports the conclusion of a good match between speckle contrast and PPG. The linear fitting equation shows a slope very close to 1 which indicates the direct relation between both measures. Moreover, the coefficient of determination (R^2) was 0.97, which confirms the strong linear correlation between speckle contrast HR and PPG HR.

The errors between the fitting equation and the PPG HR are represented in figure 5.8(b). This figure shows that the error does not increase with the increasing of the fitted values, resulting in an uniform distribution of the errors. Moreover, the differences between the speckle HR and the fitting equation do not exceed 2.5 bpm.

The root mean square error for all the data-sets, between real and estimated HR, was 1.3 bpm which, again, shows a very good result. Finally, the maximum absolute error between the PPG HR and the speckle HR was below 2.2 bpm.

5.1.2.2 Spectral similarity results

As stated in subsection 4.1.3.2, speckle contrast and PPG are signals related with different physical quantities. However, speckle contrast and PPG carry the same information

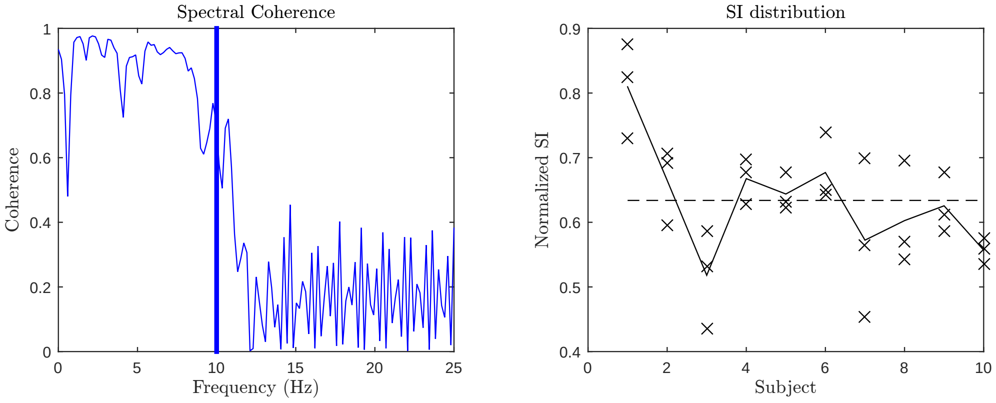

(a) (b)

Figure 5.9: Spectral comparison between speckle contrast and PPG. a) Magnitude-squared coherence function for a given acquisition. The bold vertical line represents the integration limit. b) Scatter plot of the similarity index (SI) for each subject. The dashed line represents the total mean and the solid line the subjects mean.

because they come from the same source. For that reason, the spectral components of the PPG and speckle contrast were analysed using the spectral coherence.

Figure 5.9 summarizes the results obtained for the similarity analysis. Figure 5.9(a) represents the $C_{KP}(f)$ for a specific data-set. Within the range of interest (0-10 Hz), the $C_{KP}(f)$ shows a stable behaviour with a high magnitude value (close to 1). A perfect spectral coherence corresponds to a unitary value of the $C_{KP}(f)$. Above 12 Hz, the spectral coherence value decreases due to the morphological differences and noise, presenting a random behaviour.

Finally, the SI results are expressed in figure 5.9(b). The SI is a numerical quantification of the signals spectral similarity. This quantity ranges form 0 to 1, being 1 a complete similarity in the frequency range of 0 to 10 Hz. This chart shows the SI of all the acquisitions for each subject, resulting in 3 samples (crosses) per subject.

The subject number 1 presents the best results with a maximum SI of 0.87, a minimum of 0.73 and a mean SI of 0.81. All the subjects show balanced values of SI, being the maximum SI range, within the same subject, of 0.24 for subject 7 and the minimum range of 0.04 for subject 10. Moreover, only two of the samples obtained a SI below 0.5 (subjects 3 and 7) while 5 achieved results above 0.75 (subjects 1, and 2 and 6). The SI mean achieved a value of 0.63 with a standard deviation of 0.1.

The results obtained with the SI show that the pulse waveform extraction depends on the analysed subject. Different subjects show different means for the SI (solid line of figure 5.9(b)). This fact can, possibly, be explained by the physiological differences between subjects.

The radial artery movement is affected by the subject blood pressure and by the subject fatty layer. Subjects with low blood pressure will probably show smaller skin vibrations, leading to lower SNR. Moreover, the PPG signal waveform is different from subject to subject. Some types of waveforms could match worst with the laser speckle signal yielding to a decrease of the SI.

5.1.2.3 Remarks

The pulse waveform extraction study has been conducted only with *in vivo* data, the most complex case, with good results. The HR determination for the control signal (PPG) and laser speckle show very good agreement, with low RMS error and good linear relation. In addition, the spectral similarity between both signals presents good global results which are relatively stable but depend on the assessed subject.

The limitations of this study are mainly related with the arm fixation system, the VC sampling frequency and the low number of subjects. The arm support was made in plaster and is not adaptive. Some subjects arm fits better to the support than for other subjects. An adaptive arm support could increase the quality of the results and reduce the subject movements and vibrations. Furthermore, the limited sampling frequency of the VC (50 fps), causes bad reconstruction in the high frequencies of the speckle contrast. An increase of this parameter could improve the spectral coherence in the frequency band above 12 Hz.

In summary, this work demonstrates that laser speckle contrast can be used for pulse waveform extraction with good reliability. The inclusion of these new analysis in the current LSI devices could lead to a multi-parameter assessment that combines information from macro and micro circulation without need to change the processing algorithms.

5.1.3 Image segmentation study

This pilot study aims at spatially segmenting an image where a skin-like phantom presents a longitudinal movement. Figure 5.10 shows two pairs of consecutive raw laser speckle images where both skin-like phantoms are visible. Figures 5.10(a) and 5.10(b) present a case where the left skin-like phantom is moving with a velocity of approximately 59 $\mu m/s$. The other case (figures 5.10(c) and 5.10(d)) presents a moment where both skin-like phantoms are stopped. The black area between both phantoms correspond to the gap that was used in order to prevent rubbing. The surrounding black areas represent zones out of the laser beam.

The speckle pattern that is visible in the left phantom on figures 5.10(a) / 5.10(b) shows small differences that are hard to identify only using the human visual perception. However, these variations can be easily identified after the application of the temporal backward derivative (equation (4.8)).

Figures 5.11(a) and 5.11(b) present the results of the application of the derivative for the moving and stopped cases. The values of the moving case show a much higher range of grey values (80 to 170) than the stopped case (119 to 137), demonstrating that the speckle pattern changes more when the target is moving fast. The pattern variations in the almost stopped case are explained by a non-complete immobilization of the skin-like

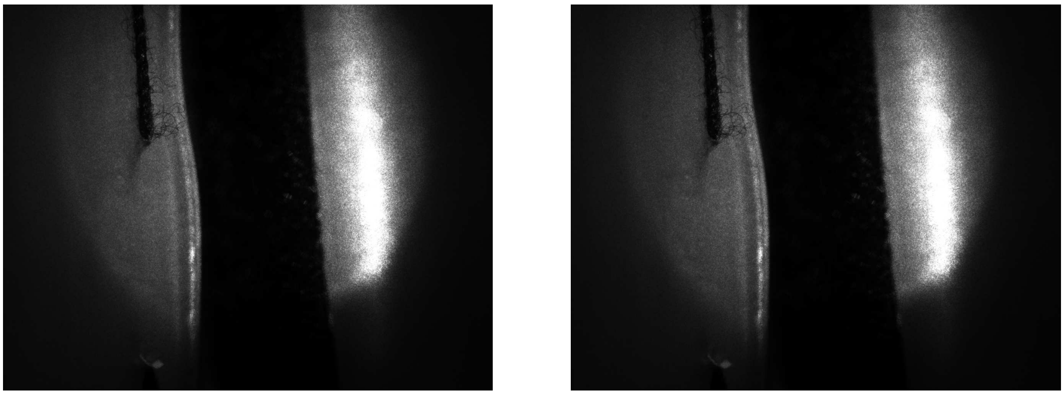

(a) Frame number = i (b) Frame number = i+1

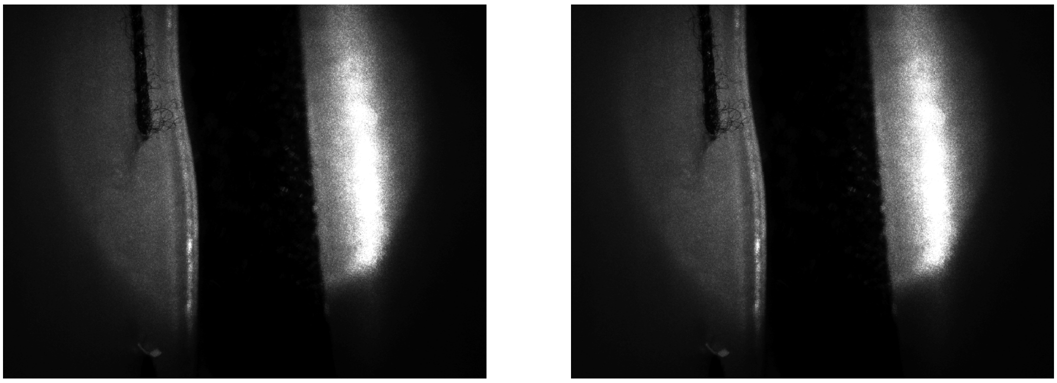

(c) Frame number = i (d) Frame number = i+1

Figure 5.10: Grey scale image of speckle effect corresponding to the acquisition with a sinusoidal movement with a frequency of 1 Hz and a 1 V_{pp} amplitude. (a) and (b) the left membrane was moving with a 59 μm/s velocity. (c) and (d) the left membrane presents very low velocity, almost stopped.

phantom. With an exposure time of 15 ms it is impossible to obtain the exact moment where the membrane stops, causing the derivative value to be different from the mean point (128).

The derivate operation, applied in raw speckle images, results in a two-dimensional matrix with integer values between 0 and 255. The regional entropy algorithm (Eq. (4.9)) was applied in this type of data. Figures 5.11(c) and 5.11(d) present the entropy map computed with a ROI of 27×27 pixels of the corresponding derivatives (figures 5.11(a) and 5.11(b)). The maximum values of the entropy map of the moving phantom are, almost, the double of the values presented in the entropy map of the low velocity phantom. Furthermore, the highlight of the left phantom, comparing to the right phantom and the scene, is much plain in figure 5.11(c) than in figure 5.11(c).

A binary threshold has been applied in these entropy maps in order to segment and identify only the moving targets within the scene. These maps correspond to two-dimensional matrix with positive real numbers. The resultant binary images have been compared with a manual segmented mask.

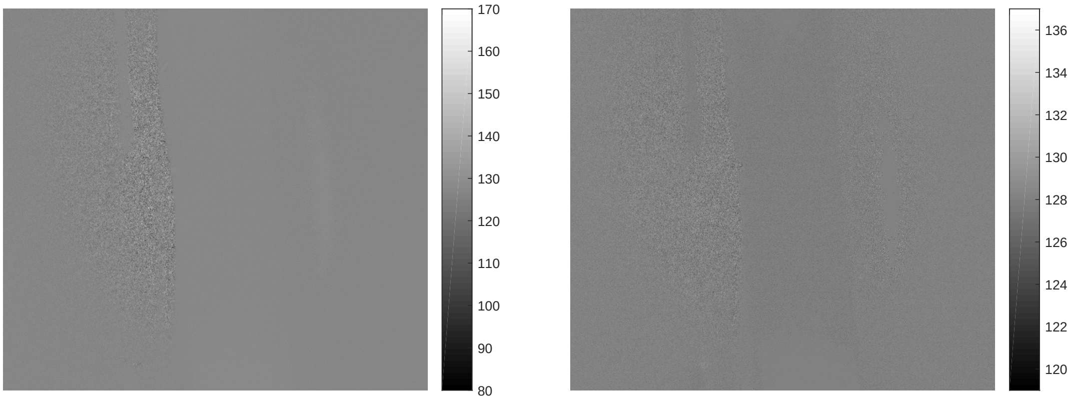

(a) Derivative image - moving

(b) Derivative image - almost stopped

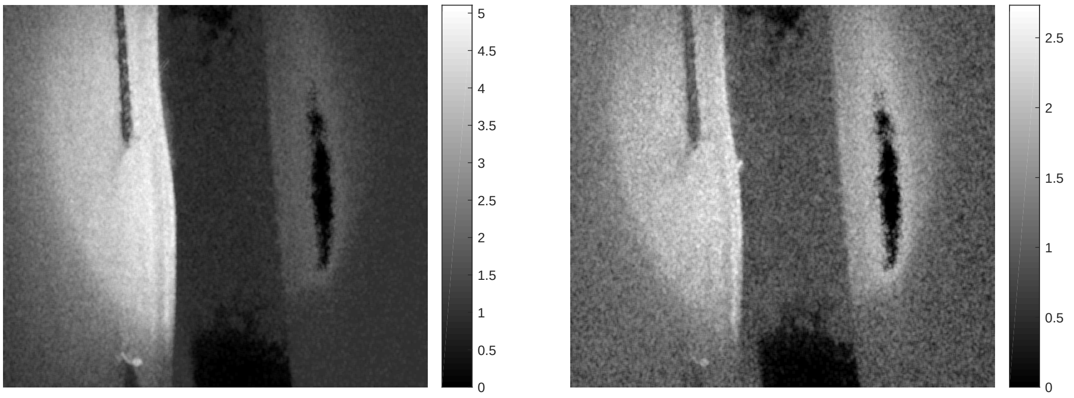

(c) Entropy image - moving

(d) Entropy image - almost stopped

Figure 5.11: Results of the application of the segmentation algorithm. 5.11(a) and 5.11(b) show two derivatives of speckle images. 5.11(c) and 5.11(d) show the correspondent entropy maps computed with regions of 27×27 pixels.

To perform this manual segmentation, the non-uniform illumination of the scene and the black material used to fix the skin-like phantoms have been taken into account. This material, visible as a vertical black line ahead of the left skin-like phantom, can be seen in all the sub-figures of figure 5.10. This fibre absorbs the incident light making the speckle pattern impossible to form.

Figure 5.10 has been used as references for the illumination area. Since the coherent illumination is non-uniform in all the image, only part of the skin-like phantoms show speckle patterns. Considering all these constrains, the moving zone has been manually delimited, resulting in the mask represented in figure 5.12.

Figure 5.13 presents the results obtained for the application of a threshold of 2.95 in the figures 5.11(c) and 5.11(d). These images show a good segmentation of the skin-like phantom when it moves and only a marginal segmentation when it is almost stopped. The segmented zone is larger than the manually determined mask. Therefore, the phantom identification is even wider than the one expected by the observation of the raw images.

Figure 5.12: Manual binary segmentation of the scene.

(a) Moving pahntom

(b) Almost stopped

Figure 5.13: Output of the application a 2.95 threshold (a) to the entropy map of figure 5.11(c); (b) to the entropy map of figure 5.11(d).

Moreover, the moving phantom is highlighted from the background and from the static phantom. These two static surfaces do not produce any effect in the binary classification. This is what is expected since this method is only sensitive to movement, independently of the analysed material.

In the first test, the best ROI size was determined by computing SE (sensitivity) and SP (specificity) for all the possible thresholds (0 to 6). This data is summarized in the ROC curves of figure 5.14. The proposed algorithm, with the 4 element sizes, has been applied in all the recorded data (16 videos). The classification performance was determined by comparing the binary output image for each frame with the manually segmented mask (Fig. 5.12).

The ROC curves show that this method presents a good performance regardless of the element size. All the curves get close to a perfect classifier $(SE, 1 - SP) = (1, 1)$ and distant from the random guess line (black dashed line). However, the curves behave differently near the high accuracy area, making the smaller ROI (3×3 pixels) to perform worst. The intermediate sizes (9×9 pixels and 27×27 pixels) achieved results closer to the

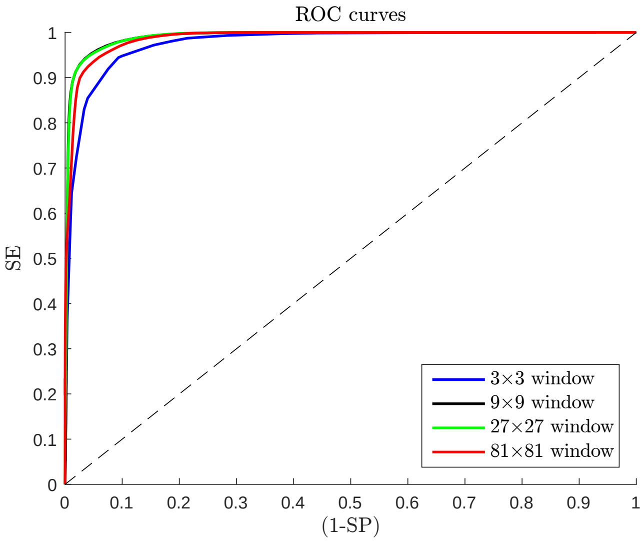

Figure 5.14: Best element size identification using ROC curves. Graphical results. SE stands for sensibility and SP for specificity.

Table 5.3: Results for the Area Under the ROC Curve. This metric quantifies the method performance. Higher values correspond to better methods.

Method	Window Size	AUC
1	3 × 3	0.9760
2	9 × 9	0.9905
3	27 × 27	0.9907
4	81 × 81	0.9873

perfect classifier.

In order to numerically compare the methods, the area under the curve (AUC) has been computed as a metric to evaluate their performance. Its values are presented in table 5.3. As stated before, the smaller ROI, with an AUC of ≈ 0.976, achieved a performance lower than the other sizes. The methods number 2 and 3 achieved the best performances with AUC above 0.99. Contrary, for the ROI with size of 81×81 pixels the performance starts to decrease. According to these results, the method number 2 (size equals to 9×9 pixels) has been considered the most suitable because it achieved a similar performance of the best method (27×27 pixels) and it is faster to compute.

The complete algorithm (Fig. 4.6) was then applied, with an entropy computation region of 9 × 9 pixels, to the 12 image training data-set. The accuracy achieved by each threshold and for each image is summarized in figure 5.15. This figure presents the accuracy as function of the applied threshold for all the images. In addition, the mean accuracy obtained for each threshold has been plotted in bold. The best threshold has been determined as the one that achieved the maximum mean accuracy. The red vertical line of figure 5.15 corresponds to the maximum mean accuracy (0.9767) and occurs for a threshold of 2.95.

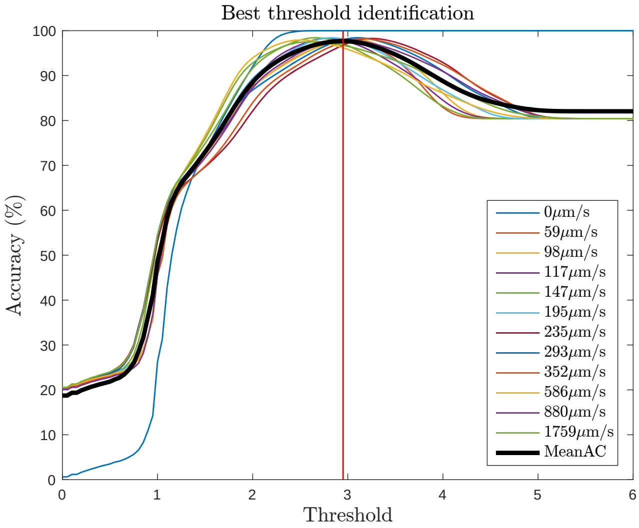

Figure 5.15: Best threshold identification for the 9×9 method using 12 images of the training data-set. The vertical red line represents the best threshold (2.95).

After the determination of the best threshold (2.95) and size (9×9 pixels), the algorithm with these settings was applied to 5 complete videos. These videos constitute the validation data-set. Each video sequence comprises images of skin-like phantoms, with different velocities, up to 1.17 mm/s (see table 4.2 and subsection 4.1.4 for details). Different values of frequencies and amplitudes have been selected for the validation data-set resulting in different maximum velocities for each video. These values, in addiction to the performance metrics described in subsection 4.1.4, are presented in table 5.4.

The best AC was achieved for the 1 Hz - 1V_{pp} movement with a value of 98.73%. This classification rate is confirmed by a high PPV (96.16%) and a very high NPV (99.21%). The worst result has occurred for the fastest movement (1 Hz - 4V_{pp}) although it is still a good performance (AC = 95.15 %). In this case, the PPV presents a value (78.04%) much lower than the other cases (86% - 96%).

The MCC provides a better metric to the performance of classifiers when unbalanced data-sets are used [254]. It is the case of this validation data-set which contains only $\approx$ 30 million of moving pixels (positive class) compared to $\approx$ 150 million stopped pixels (negative class). The MCC values range from -1 to 1, like a Pearson correlation coefficient. An MCC = 1 corresponds to a complete agreement of the classification, -1 to a complete

Table 5.4: Results in the validation data set-for a window of 9 × 9 pixels

Movement	Max. Vel. (mm/s)	AC (%)	PPV(%)	NPV(%)	MCC	No. frames
1/5 Hz - 1V_{pp}	0.06	96.54	86.26	99.03	0.8872	30
1 Hz - 1V_{pp}	0.29	98.73	96.16	99.21	0.9519	15
1/3 Hz - 4V_{pp}	0.59	97.57	94.95	98.13	0.9178	45
1/2 Hz - 6V_{pp}	0.88	95.80	92.96	96.33	0.8512	30
1 Hz - 4V_{pp}	1.17	95.14	78.04	99.34	0.8416	15

disagreement and 0 to a random classifier. The presented data-set achieved values of MCC from 0.84 to 0.95. These results behave similarly to the AC because the NPV does not change significantly between the videos.

All the data-sets achieved NPV above 96%, confirming the existence of a low number of false negatives. A false negative occur when a moving pixels is classified as stopped. Contrary, the PPV only achieved values below 96%. Lower PPV indicate a large number of non-moving pixels that have been classified as moving pixels. This could happen because of the underestimation of the moving zone (Fig. 5.12). The upper left region of the mask and the fixation material are the most problematic areas. A correction and better identification of the binary mask could lead to an improvement of the global accuracy and MCC.

5.1.3.1 Remarks

This pilot test has been based on the idea that longitudinal movements can be detected using laser speckle. An experimental set-up was constructed with two similar skin-like phantoms. One of the phantoms was actuated with longitudinal movements of milimetric and sub-milimetric amplitudes.

An estimation of the image entropy was computed in different region sizes. The regions with 9×9 pixels have been considered more suitable for this application. A training data-set, composed of 12 different images, was used to determine the best binarization threshold. A value of 2.95 achieved the best training performance with an AC of 97.7%.

The algorithm, with this element size and threshold, has been applied in a validation data-set, composed by unused data, with a total of 135 frames. The validation data-set comprises velocities from 0 to 1.17 mm/s with different movement amplitudes and frequencies. A tendency was observed in which the classifier AC is higher for slow moments. Only the movement 1/5Hz-1V_{pp} does not follow this tendency. Finally, all the training data-sets have achieved ACs above 95%.

5.2 Microcirculation application

This section presents the microcirculation studies results. The methods related with the following sections can be found in section 4.2. First, the results of the static scatterers study will be presented. Finally, the results of the contrast algorithm optimization will be analysed and discussed.

5.2.1 Static scatterers study

This section will be focused on the presentation of the results obtained with the bench test detailed in subsection 4.2.1. First, the β determination will be presented. The results of the laser speckle correlation are also discussed in this subsection. The ρ value determination will also be presented and, finally, the speckle contrast results will be detailed.

5.2.1.1 β determination

The first result is related with the determination of beta value. This constant is dependent on the developed apparatus. The LSI system has obtained a normalization constant of $\beta = 0.5964$.

This result corresponds to the maximum achieved spatial contrast and it was determined using a white paper sheet as sample. This value is in accordance with the theory that establishes a maximum contrast below 1.

5.2.1.2 Speckle correlation $g_2(\Delta t)$

For each configuration used in this experiment, the correlation function $g_2(\Delta t)$ and correlation coefficient r have been computed as mean ± standard deviation. These data have been plotted as function of the static scatterers concentration. In this section only a reduced data set is shown in order to increase concision. The results are presented only for flows #0 (0 cm^3/s), #1 (1.5 cm^3/s), #2 (3 cm^3/s), and #4 (14 cm^3/s). The complete data set can be found in appendix B.

Figure 5.16 presents the results obtained for the correlation function $g_2(\Delta t)$. Each subfigure corresponds to a different fluid flow. It is expected an increase of the correlation between two consecutive images with the increase of static scatterers in a range between $1 \leq g_2(\Delta t) \leq 1+\beta$. This range satisfies equation (4.18) resulting in $g_2(\Delta t) = 1 \implies \rho = 0$ (only dynamic scatterers) and $g_2(\Delta t) = 1 + \beta \implies \rho = 1$ (only static scatterers).

The lowest milk concentration (33%) has been excluded from the analysis. This fluid is very poor on dynamic scatterers with an organic compounds concentration (lipids + proteins + carbohydrates) of only 0.033 g/ml. The dynamic speckle signal measured from this fluid is weak and shows large theoretically inconsistencies. However, these data are presented in appendix B.

All the applied flows and used milk concentrations show a consistent behaviour. An initial plateau is visible for small static scatterers concentration (up to 0.5 mg/ml) for all the cases. This zone represents the experimental baseline where almost only dynamic scatterers are present and when the sensitivity of $g_2(\Delta t)$ is low. Theoretically, this plateau is predicted in the mathematical expression that relates the correlation $g_2(\Delta t)$ with the scatterers proportions (Fig. 4.15(c) on page 75). Between $0\times\langle I_d\rangle$ and $0.1\times\langle I_d\rangle$ this function shows a very low slope being almost zero up to $0.05\times\langle I_d\rangle$.

Despite these good results, the absolute values of $g_2(\Delta t)$ in the theoretically plateau are much lower than the experimentally computed ones. A magnification of the region of interest ($1.01 \leq g_2(\Delta t) \leq 1.05$) of figure 4.15(c) (Fig. B.1) reveals that the plateau finishes far below 1.01 while in the experiment it remains up to 1.02. This characteristic indicates that, in an exclusively dynamic scatterers condition, the experimental correlation never reaches the unitary value ($g_2(\Delta t) = 1$) due to experimental imperfections like internal reflections of the microchannel phantom. Moreover, the normalization constant β also changes the function morphology and its erroneous determination could also be the cause

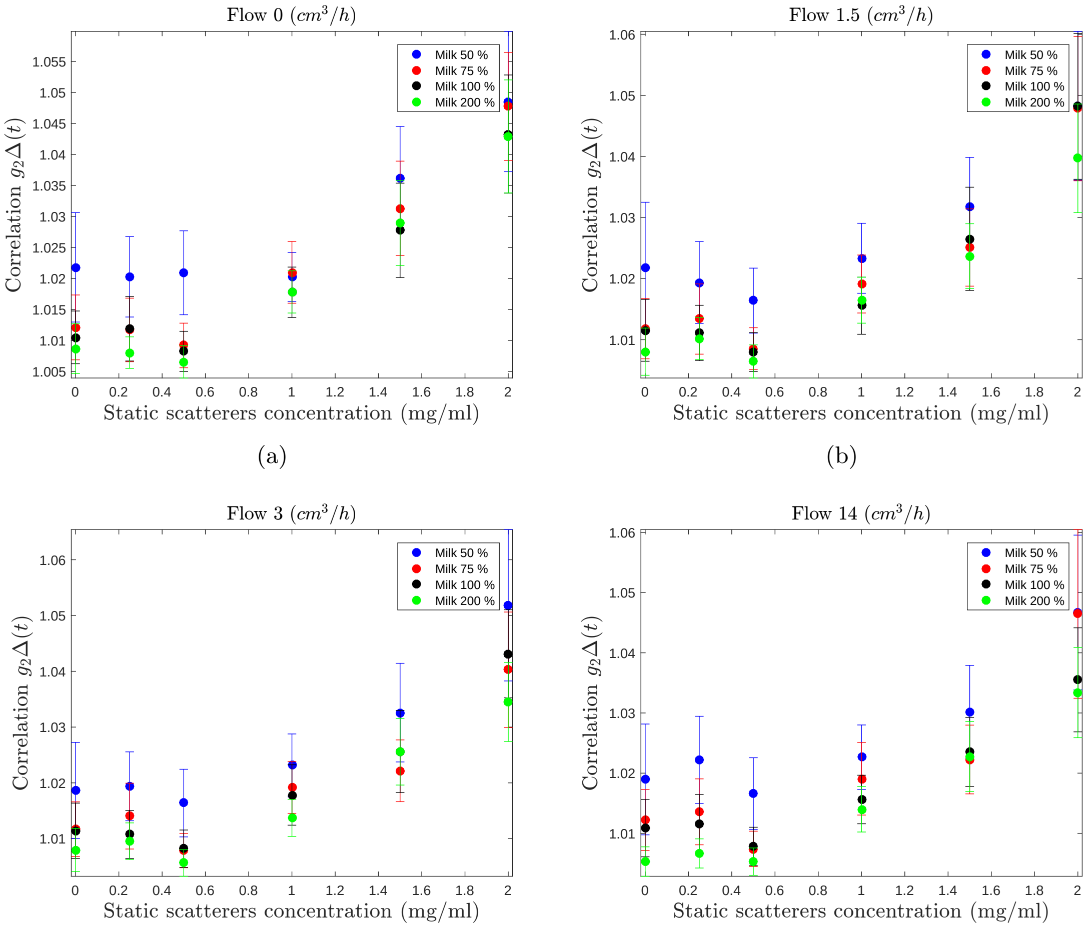

(a) (b) (c) (d)

Figure 5.16: Results obtained for $g_2(\Delta t)$ with the increase of static scatterers concentration. Each sub-figure represents a different fluid flow. The standard deviations have been computed with a minimum of 3165 points. For the other milk concentrations and flows please consult appendix B.

of this situation.

Theoretically, the increase of milk concentration acts like a scale expander because the correlation is sensitive to the ratio static/dynamic scatterers. As an example, a static scatterers concentration of 1 mg/ml at 50% milk should be equivalent to a static scatterers concentration of 2 mg/ml at 100% milk. This effect can be simulated using equation (4.20) (Fig. B.2) where an increase of $\langle I_d \rangle$ corresponds to a horizontal stretch.

The effect of the increment of the dynamic scatterers concentration (milk proportion) is also evident in these results. In our experimental data this is expressed by a gradual downward shifting of the $g_2(\Delta t)$ function from 50% to 200% milk which is a consequence of the theoretically horizontal stretch.

The error bars correspond to the standard deviation of each experimental configuration. Since an adaptive algorithm has been used to remove the outliers, these standard deviations have been computed with a different number of points. The minimum number

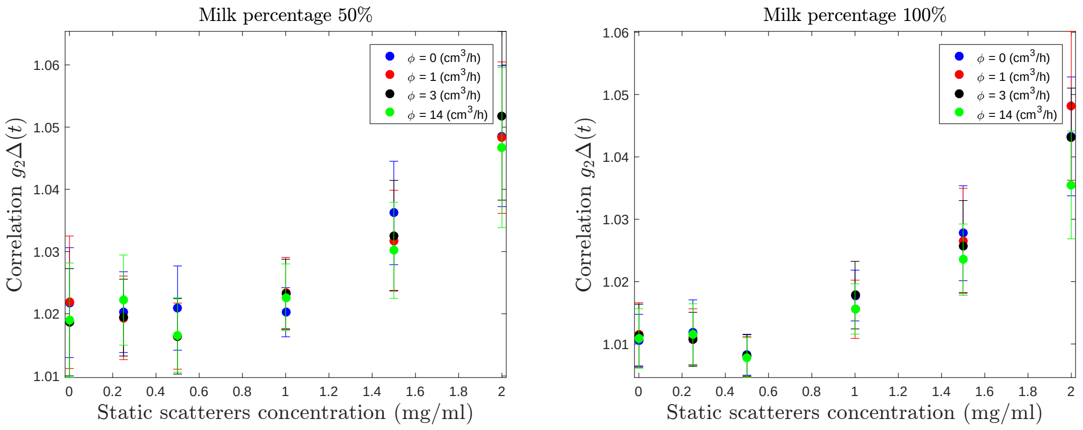

(a) (b)

Figure 5.17: Results obtained for $g_2(\Delta t)$ with the increase of static scatterers concentration. Each sub-figure represents a different milk concentration. The standard deviations have been computed with a minimum of 3165 points. For the other milk concentrations and flows please consult appendix B.

of points was 3165 and the maximum was 6803. The standard deviation of the sample is dependent on the milk concentration; the largest errors are associated with lowest milk concentrations.

Another important outcome of this experiment is that flow changes do not produce significant variations in correlation values. Flow variations are not expressed by a conclusive pattern neither in the correlation values nor in standard deviations, regardless of the static layer used or milk concentration (Fig. 5.17).

The theoretical laser speckle equations predict that $g_2(\Delta t)$ is independent on the scatterers decorrelation time and, thereafter, independent on the scatterers velocity. However, the effect of flow increase results in the decorrelation of the image (blurring) which is the same effect caused by the decrease of $\langle I_s \rangle$ (see subsection 5.2.1.5). This observation could lead us to believe that $g_2(\Delta t)$ will be dependent on the fluid flow. However, this fact has been excluded by the experimental results, in accordance with laser speckle correlation theory.

5.2.1.3 ρ determination

The application of equation (4.18) has been performed for the milk concentrations that show consistent results (milk percentage 33% has been excluded from further analysis for the reasons explained previously). The ρ values, as function of the $\langle I_s \rangle$, are presented in figure 5.18 in the same way as the correlation, one figure for each fluid flow. The error bars shown for ρ determination have been computed using the propagation of uncertainty

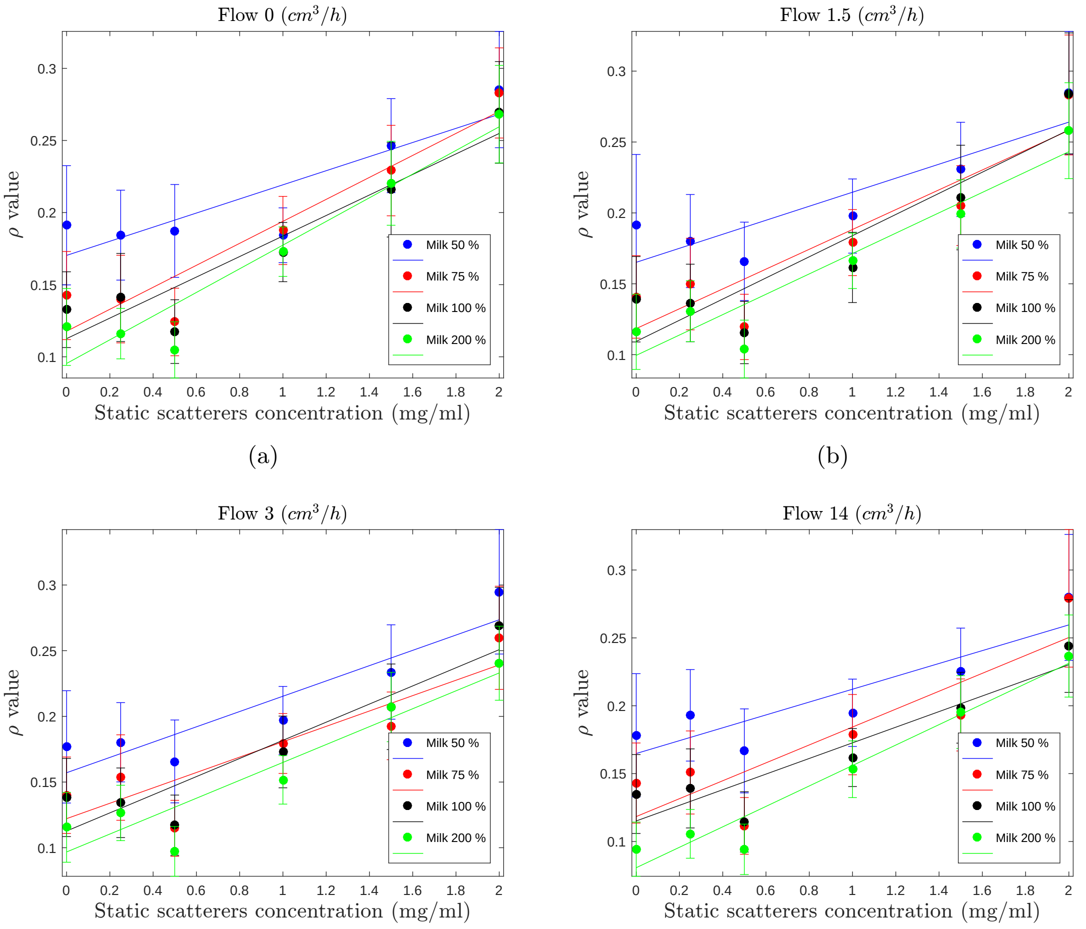

(a) (b)

(c) (d)

Figure 5.18: Results of ρ value determination based on correlation function $g_2(\Delta t)$. Each sub-figure corresponds to a different fluid flow. Solid lines correspond to linear regressions. For the other concentrations and flows please consult appendix B.

from equation 4.18:

$$\sigma_\rho = \left(\frac{1}{\beta}\right)^{1/2} \times \frac{1}{2}(g_2(\Delta t) - 1)^{-1/2} \times \sigma_{g2} \,, \tag{5.2}$$

where σ_{g2} is the error associated with $g_2(\Delta t)$ and σ_ρ is the error associated with ρ determination.

The ρ values have been fitted to a linear model of the type $\rho = m \times \langle I_s \rangle + b$. This model has been chosen because, in the range of experimental ρ values (0.1 to 0.35), the equation (4.19), which relates ρ with $\langle I_s \rangle$, is approximately linear.

Previous conclusions can also be repeated for the ρ values evaluation. Once more, ρ values present a dependency on the milk percentage and static scatterers concentration. The ρ plateau is not eliminated because experimental correlation does not correspond to 1 for $\langle I_s \rangle = 0$. Consequently, the ρ computation does not produce the expected outcome.

Table 5.5: Fitting parameters of the linear regression model. R^2 represents the coefficient of determination.

Milk (%)	Flow (cm^3/h)	m	b	R^2
50	0	0.05	0.17	0.88
	1.5	0.05	0.17	0.88
	3	0.06	0.16	0.92
	14	0.05	0.16	0.89
75	0	0.08	0.12	0.95
	1.5	0.07	0.12	0.91
	3	0.06	0.12	0.89
	14	0.07	0.12	0.88
100	0	0.07	0.11	0.94
	1.5	0.08	0.11	0.92
	3	0.07	0.11	0.93
	14	0.06	0.12	0.92
200	0	0.08	0.10	0.96
	1.5	0.07	0.10	0.95
	3	0.07	0.10	0.94
	14	0.06	0.08	0.98

It was expected that the plateau visible in $g_2(\Delta t)$ for lower $\langle I_s \rangle$ did not appear in the ρ results (Fig. 4.15(b) on page 75), however it still remains.

This wrong behaviour of ρ can be explained with the twisted result of $g_2(\Delta t)$ first three points (0, 0.25 and 0.5 mg/ml). The linear model presented above seems to fit only for high $\langle I_s \rangle$ (1 to 2 mg/ml). Nevertheless, it has been applied to all the data in order to not bias the results. A correction of this 3 points would improve not only the morphology of the function but also the coefficient of determination of the linear regression model.

The fitting parameters are presented in table 5.5. On one hand, the curve slope (m) shows no relation with neither the fluid flow nor the milk concentration. On the other hand, the y-Intercept point (b) decreases with the increase of $\langle I_d \rangle$. The change in b is a direct consequence of the $g_2(\Delta t)$ horizontal stretch caused by the increase of $\langle I_s \rangle$.

Regarding the absolute ρ values, if we look at the relation between ρ and $\langle I_s \rangle$ (Fig. 4.15(c) on page 75) it can be seen that the experimental value for lower static scatterers concentration would not be in accordance with the theory.

5.2.1.4 Correlation coefficient r

As an alternative to the use of the correlation function $g_2(\Delta t)$ (Eq. (4.17)), we propose to test the use of the 2D correlation coefficient (Eq. (4.5)). This metric also quantifies the amount of information that is common in two consecutive images. As a main drawback, the correlation coefficient cannot be applied to compute the ρ value due to the theoretical limitations (Eq. (4.18)).

Figure 5.19 summarizes the results obtained for the correlation coefficient r using the exactly the same data set as the one that has been used to compute $g_2(\Delta t)$. This figure

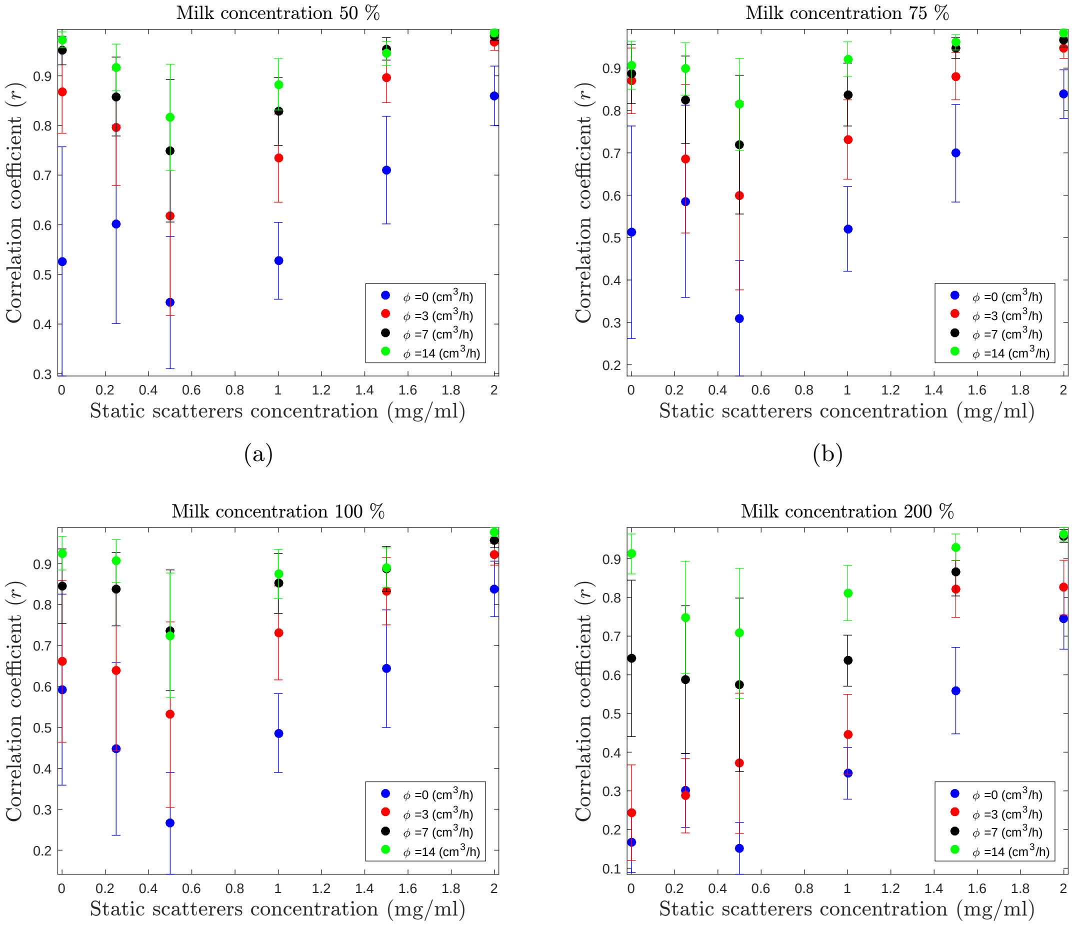

(a) (b)

(c) (d)

Figure 5.19: Results of the correlation coefficient r. Each sub-figure corresponds to different milk concentrations. The standard deviations have been computed with a minimum of 3211 points. For flow #1 please consult appendix B.

shows the milk percentages from 50% to 200% and flows #0, #2, #3 and #4. For flow #1 (1.5 cm^3/h) please consult appendix B. The standard deviations have been computed with a minimum of 3211 points and a maximum of 6121 points.

Almost all the cases (except configuration $\phi = 3$ - 200% milk) present a profile with a negative derivative in the lower static scatterers concentrations and positive derivative for higher static scatterers concentration. The flow variation also shows an interesting effect. A clear tendency is observed where higher flows present higher correlation values. Moreover, the similar distribution of each milk concentration makes this experiment repeatable, since they have been performed at different times.

These results show that the correlation r is sensitive to the velocity of the dynamic scatterers and it is independent on the milk flow used (Fig. 5.20). These conclusions are the contradictory of the original correlation method ($g_2(\Delta t)$), making these two metrics as inequivalent.

Table 5.6 presents the results of a Welch's t-test used in order to compare r distribu-

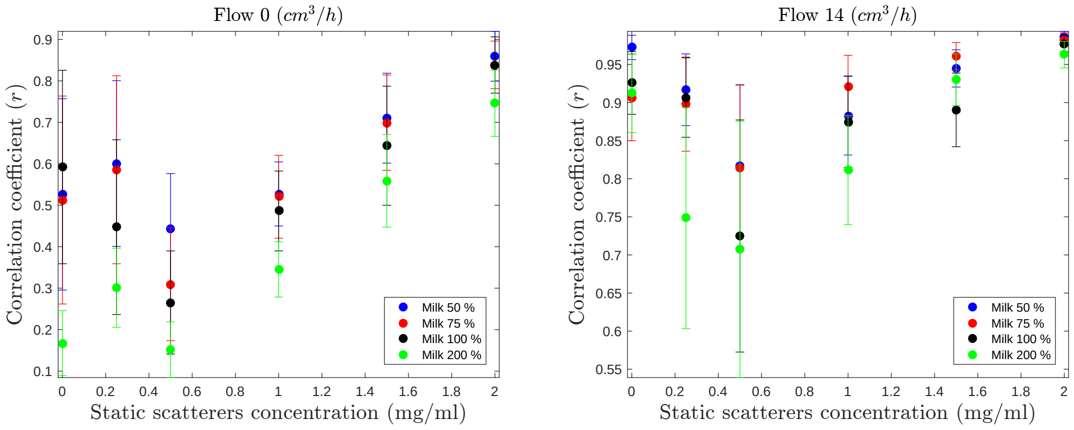

(a) (b)

Figure 5.20: Results of the correlation coefficient r. Each sub-figure corresponds to different fluid flows. The standard deviations have been computed with a minimum of 3211 points. The flows #1, #2 and #3 are presented in appendix B.

Table 5.6: Welch's t-test results (h_0) for correlation coefficient data (r) of borderline configurations with a 95% confidence interval.

			Milk (%)			
			50		200	
		Flow	0	14	0	14
Milk (%)	50	0		1	0	1
		14	1		1	0
	200	0	0	1		1
		14	1	0	1	

tions of the boarder line configurations (max. and min. flow and max. and min. milk concentration).

The Welch's t-test is a two-sample statistical test which is used to test the null hypothesis that both variables come from independent random samples with equal means. When the test achieves a result equal to 1, the null hypothesis is rejected (different means), and when it achieves a result equal to 0, the null hypothesis is not rejected (equal means).

The Welch's t-test shows that correlations extracted from different fluid flows (and same milk concentration) present different means ($h_0 = 1$). On the other hand, correlations extracted from different milk concentrations (and same flow) present equal means ($h_0 = 0$).

The r behaviour shows a dependency on both the scatterers velocity and the amount of static scatterers (but not the static scatterers proportion), while $g_2(\Delta t)$ shows a dependency on the static scatterers proportion. The correlation coefficient presents a dependency similar to the speckle contrast and should be interpreted as a method to estimate flow rather than to estimate ρ .

It was expected for the correlation to be monotonic, *i.e.*, to increase with the increment of static scatterers. However, all the graphics of figure 5.19 show an inflection point and an initial negative slope. This effect contradicts the theory as discussed above. Nevertheless, if we look into the laser speckle raw data a possible explanation for this phenomenon can be detected.

In fact, from this experiment, we can state that two main effects influence the values of r. The first one, as already discussed, is the presence of static scatterers. This type of scatterers induces a constant reflection of light which causes the appearance of static speckles in the LS image. These speckles contribute to the increase of the correlation between consecutive frames.

The second effect is related with the blurring degree of the laser speckle image. When a small portion of, or none, static scatterers are present, all the sample is basically constituted by dynamic scatterers. The system decorrelation time decreases in this condition resulting in a blurred laser speckle image. Two blurred images have higher correlation than its sharp equivalent versions, resulting in an increase of correlation for the cases where the percentage of dynamic scatterers is high. This effect is illustrated in appendix C. Moreover, the effect of flow increment is in accordance with this theory. Rapid dynamic scatterers movements decrease the system decorrelation time, leading to a more blurred and higher correlated images.

The combination of these two effects causes the correlation to be maximum at high dynamic scatterers rates (decorrelation effect), at high static scatterers rates (static speckles), and at high fluid flows. The r curve profile is in accordance with this explanation, with an inflection point on an intermediate static scatterers concentration. Almost all the cases of figure 5.19 exhibit this inflection point and present two distinct slopes, one before and other after this point.

The physical significance of the correlation coefficient r in terms of ρ value determination is limited. Despite its clear relation with the static scatterers concentration, the absence of theoretical model to relate r and ρ completely prevents its use for that application. However, it has been demonstrated that the correlation r encodes important information both in terms of static scatterers concentration and in terms of dynamic scatterers velocity.

5.2.1.5 Contrast results

Laser speckle contrast has been computed in three different ways, using spatial (s-K), temporal (t-K) and spatio-temporal (st-K) contrast. The contrast results have been plotted as function of the static scatterers concentration, in the same way as the correlation results. In this section the fluid flow #1 ($\phi = 1.5cm^3/h$) is not shown. For the complete results please consult appendix B.

It is very clear that all the contrast measurements, for all the algorithms and cases, show a decrease trend with the increase of the fluid flow. This is in accordance with the laser speckle theory because higher scatter velocities produce speckles with faster

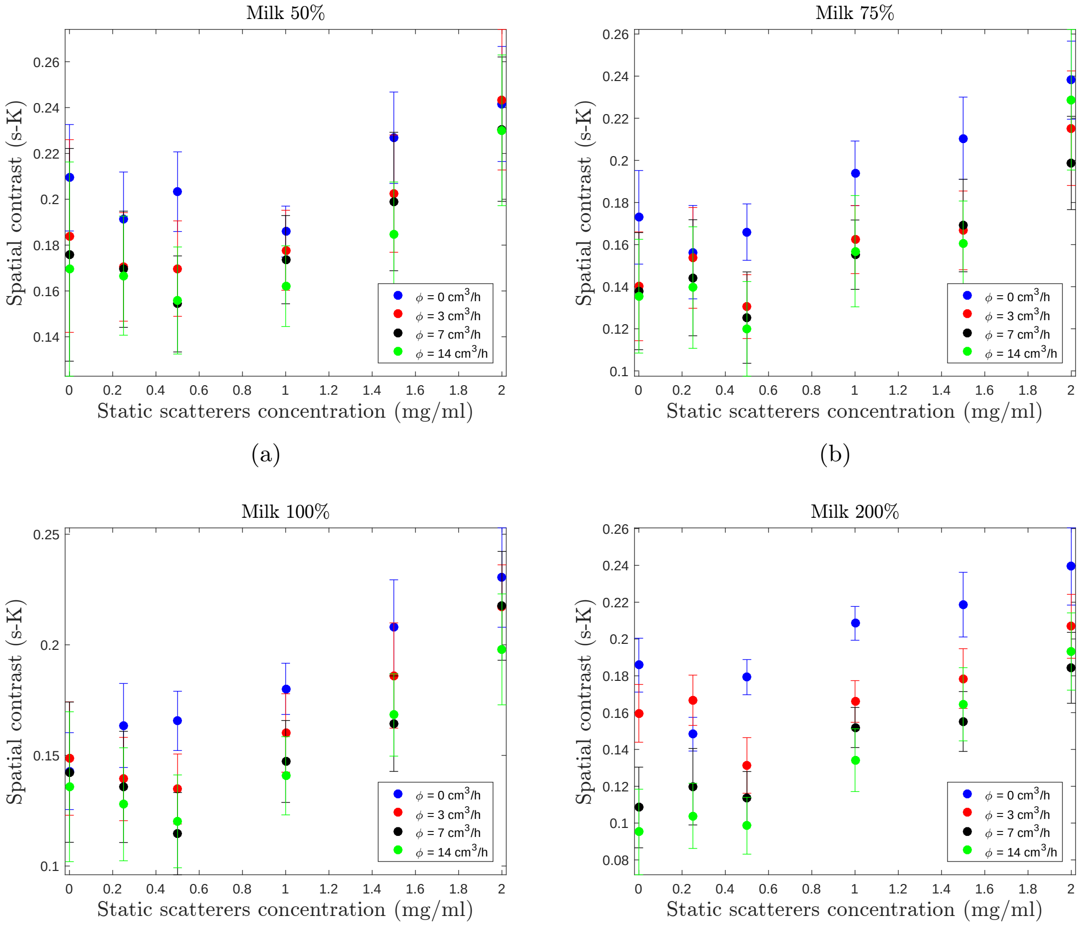

(a) (b) (c) (d)

Figure 5.21: Results of spatial contrast computation. Each figure corresponds to a different milk concentration. The standard deviations have been computed with a minimum of 3602 points. For flow # 1 please consult appendix B.

decorrelation times and, therefore, lower speckle contrasts $(\tau_c \nearrow \Rightarrow K \searrow)$.

The spatial speckle contrast (s-K) is presented in figure 5.21. As for the correlation results, the signal-to-noise ratio of contrast increases with the increase of dynamic scatterers. As stated before, the increment of the fluid flow produces a decrease of the speckle contrast, however this effect is more visible when a large amount of dynamic scatterers are present which could be caused by the decrease in the error bars.

Besides that, the static scatterers concentration has a strong effect in the s-K. The increment of $\langle I_s \rangle$ causes an increase of s-K for all the tested fluid flows and milk percentages. This fact confirms the necessity of estimating both the amount of static and dynamic scatterers (ρ) in order to correct the contrast values.

For example, from figure 5.21(b), it can be seen that s-K $= 0.13$ is associated with a fluid flow of 3 cm^3/h for a $\langle I_s \rangle = 0.5$ mg/ml but it is also associated with a fluid flow of 7 cm^3/h for a $\langle I_s \rangle = 1.5$ mg/ml. Variations on the $\langle I_s \rangle$ results in erroneous contrast determination leading to erroneous τ_c determination, unless a correction is made.

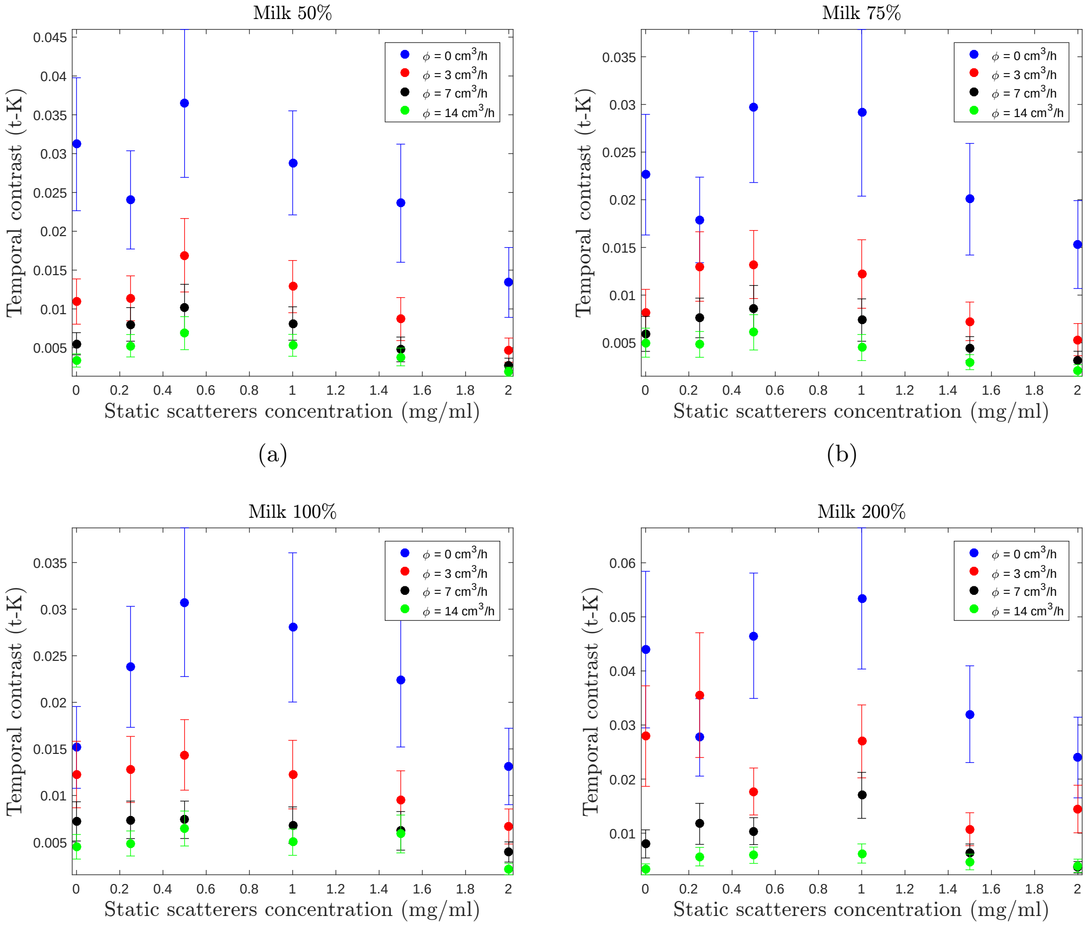

(a) (b) (c) (d)

Figure 5.22: Results of temporal contrast computation. Each figure corresponds to a different milk concentration. The standard deviations have been computed with a minimum of 4017 points. For flow # 1 please consult appendix B

Moreover, in some cases, the spatial contrast varies approximately 64% ($\phi = 14cm^3/h$ - Milk 75%) from lower to higher $\langle I_s \rangle$.

Despite the $\langle I_s \rangle$ and $\langle I_d \rangle$ dependency, s-K shows a capacity to distinguish between multiple scatterers velocities with the same $\langle I_s \rangle / \langle I_d \rangle$ proportion. This ability is more visible in the higher milk concentration (200%) due to the reasons already presented for the correlation cases, *i.e.* more coherent light that contributes to the dynamic speckle signal.

The temporal speckle (Fig. 5.22) shows a different situation. First, the flow discrimination is much more evident in this case than in the spatial contrast. Even in lower $\langle I_d \rangle$ (milk percentage 50%) the t-K is able to differentiate between velocities. The fluid flow change from $\phi = 0\, cm^3/h$ to $\phi = 3\, cm^3/h$ is very visible in almost all the cases of figure 5.22.

Temporal contrast shows a higher degree of independence on the static scatterers concentration. However, t-K presents a fluctuation where it reaches a maximum value in an intermediate $\langle I_s \rangle$ value. This fluctuation is more visible for the Brownian motion case ($\phi = 0$) but it is presented in all the fluid flows and milk concentrations. Even so, the t-K proved to be more suitable in dealing with static scatterers which is in line with other works [188,189].

Regarding the absolute values of t-K, they are very distant from both spatial and spatio-temporal contrast. The decorrelation time represents the physical quantity that can be related with the scatterers velocity. This quantity is computed from contrast values using equation (3.6), which derives from a spatial analysis of the speckle patterns. The application of equation (3.6) with t-K values makes the interpretation of τ_c impracticable due to the large discrepancy between t-K and s-K absolute values.

Lastly, figure 5.23 presents the results of the application of spatio-temporal contrast. Contrary to t-K values, the spatio-temporal algorithm produces contrast values in the same range of the spatial contrast algorithm. The dependency on $\langle I_s \rangle$ is still present in this case, where more static scatterers results in higher contrast values. Compared to s-K, the fluid flow discrimination has been improved with this method.

The spatio-temporal algorithm shows characteristics of both the spatial and temporal methods, having some of their pros and cons. It presents a flow discrimination between the spatial and temporal algorithms but their values are influenced by the presence of static scatterers, like in the spatial contrast. In exchange, this algorithm retains the spatial contrast values which allows the application of equation (3.6) and the computation of a correct decorrelation time.

5.2.1.6 Remarks

The static scatterers study performed in this work has been conducted in order to analyze the influence of different concentrations of static scatterers on laser speckle correlation and laser speckle contrast.

Khaksari and Kirkpatrick [164] showed that the increase of static scatterers concentration linearly changes the medium reduced scattering coefficient (μ_s'). Moreover, the same study claims that the absorption coefficient only influences the speckle contrast in a limited way. This fact makes possible to extrapolate the conclusions here made in terms of tissue scattering and absorption coefficients.

Regarding the correlation results, ρ value fails to follow the theoretical function because the correlation function ($g_2(\Delta t)$) shows values higher than 1 even when only dynamic scatterers are present. This can be explained with the internal phantom reflection and reflection from auxiliary instrumentation like the optical table and fixation poles.

A correction method could be introduced to lower the correlation values to 1 in the case of static scatterers absence (layer I). However, due to the inability to determine the exact relation of static and dynamic scatterers, it was decided not to do it. Even a correction method would be improper since the exact value of ρ , when the silicone layer is not doped, is not known.

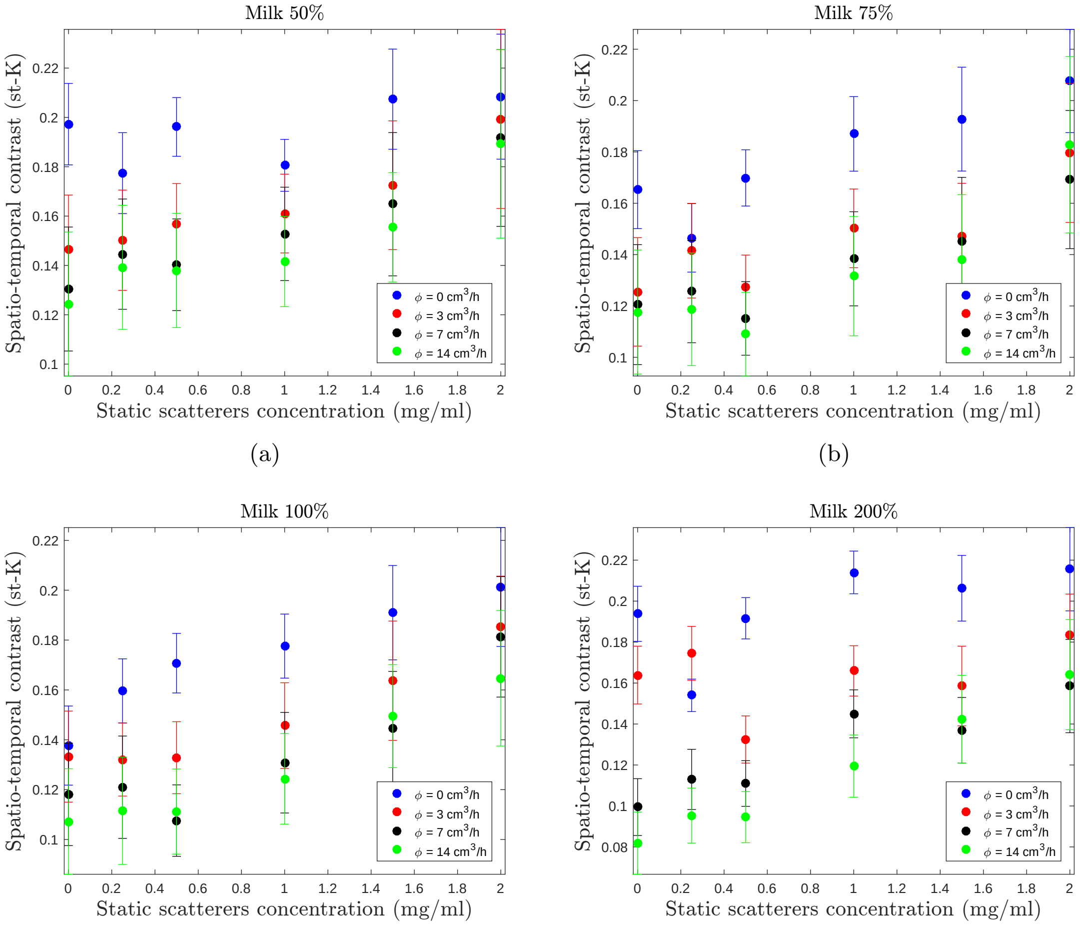

(a) (b)

(c) (d)

Figure 5.23: Results of spatio-temporal contrast computation. Each figure corresponds to a different milk concentration. The standard deviations have been computed with a minimum of 4545 points. For flow # 1 please consult appendix B

The Welch's t-test was also applied to the $g_2(\Delta t)$ results. This test results have not been displayed because it has accepted the null hypothesis (equal means) for both flow and $\langle I_d \rangle$ variations but a visual inspection of the figures 5.16 and 5.17 reveals that the behaviour of $g_2(\Delta t)$ is not the same for flow and $\langle I_d \rangle$ changes.

The interpretation of figure 5.16 reveals that $g_2(\Delta t)$ is sensitive to changes in both the dynamic $\langle I_d \rangle$ and static scatterers $\langle I_s \rangle$. There is a strong correlation between $g_2(\Delta t)$ and $\langle I_s \rangle$ but only from a certain amount of static scatterers. This effect is predicted in theory where variations in regions of small $\langle I_s \rangle$ produce small variations in $g_2(\Delta t)$ (Fig. 4.15(c)). Additionally, the increase of $\langle I_d \rangle$ produces a slightly decrease of $g_2(\Delta t)$ but this effect was not confirmed by the Welch's t-test.

The interpretation figure 5.17, confirmed by Welch's t-test, showed that $g_2(\Delta t)$ is independent on the scatterers velocity. This is a fundamental feature in order to consider $g_2(\Delta t)$ as a possible way to estimate the quantity of static scatterers presented in the analysed tissue.

On the other side, r is strongly dependent on both scatterers velocity and reduced scattering coefficient (proportional to $\langle I_s \rangle$). The velocity dependence excludes the possibility of using r to estimate the amount of static scatterers presented in the sample. Nevertheless this metric showed a very good ability to discern between different dynamic scatterers velocity, mainly for lower velocity values. This important remark leads us to conclude that r could be used in addition to speckle contrast to estimate or correct the decorrelation times.

During the experimental work we came across two major issues of the use of $g_2(\Delta t)$ to estimate the scatterers concentration. The first one is related with the fact that $g_2(\Delta t)$ is not only dependent on the image morphology. This metric (Eq. 4.17) is also dependent on the images absolute values. Take as an example the figure 4.16. If we add a constant value to both images, we will change the value of the correlation $g_2(\Delta t)$ and will not change the value of the correlation coefficient r. For example, if we sum 20 to all the images pixels, we get a new $g_2(\Delta t) = 1.011$ instead of the old $g_2(\Delta t) = 1.064$ while the correlation coefficient remains 0.71.

Another issue has been raised regarding the definition of $\langle I_s \rangle$ and $\langle I_d \rangle$. To recapitulate, the concentration of scatterers is a measure of particles or mass per volume unit. However, in our opinion, the correlation should be sensitive to the amount of static and dynamic scatterers within the light path and not to its absolute concentration. In terms of LSCI, this corresponds to a projection of the amount of scatterers in the sample in the video camera field of view.

In our experiment, the scatterers layers presented a thickness of 1.3 mm while the phantom channel only has a depth of 0.5 mm. Assuming a two-dimensional (x and y) spatial homogeneous distribution, ρ should be sensitive to the multiplication of scatterers concentration by the medium depth (z). This operation leads to a definition of $\langle I_s \rangle$ and $\langle I_d \rangle$ as mass or number of particles per area unit (g/mm^2).

Regarding the speckle contrast results, five main conclusion can be extracted. First, the temporal algorithm (t-K) proved to be more efficient when dealing with different quantities of static scatterers. Second, the temporal contrast presents absolute values that contradict the s-K and st-K, disabling it for the decorrelation time determination (τ_c). Third, the temporal algorithm performing better than the other algorithms in fluid flow discrimination. Fourth, the st-K allows the computation of τ_c while performs better than s-K in fluid flow discrimination. Fifth, and finally, st-K contrast still shows static scatterers dependency.

The used exposure time also plays an important role. The discrimination between fluid flows #3 (7 cm^2/h) and #4 (14 cm^2/h) showed worse overall results than the discrimination between lower flows. This fact is related with the exposure time used because different exposure times produce signals sensitive to different scatterers velocities. In this case, an exposure time of 6 ms showed better sensitivity for scatter velocities from 0 to 0.53 mm/s (Tab. 4.3).

5.3 Contrast algorithm optimization

The optimization of the spatial contrast algorithm is a very important task during on-line applications. Laser speckle data consists of high resolution videos in which the contrast is computed in small regions leading to thousands of contrast values per image. These data can be processed by software or hardware but speed is always a key feature. Four different implementations have been tested in order to find each one is faster in the purposed experimental conditions.

The computational time needed to process a single laser speckle frame has been determined as mean ± standard deviation. The influence of image resolution and element size in the computational time has been investigated. Figure 5.24 summarizes the results of this study. For all the cases, the convolution implementation achieved the best results.

The analytical method presents, as expected, the worst results. The processing time ranges from 11 seconds, for the highest resolution (1024×768 pixels) to 1.8 seconds for the lowest resolution. Moreover, the processing time decreases when the processing element size increases (Fig. 5.24(b)). However, the increment of the element size results in a reduction of the contrast image resolutions.

All the optimized algorithms have obtained much better performances than the reference method. Again, the processing time decreases with the image resolution reduction. The convolution method presents the best results for all the cases, however this improvement is more visible for higher resolutions (Fig. 5.24(a)).

In the case of a 1024×768 pixels image, the performance of the convolution method is approximately 87% better than the moving sum algorithm and 25% better than the filtering algorithm. For the other cases, the results became close but with the convolution implementation achieving always the best performance.

Regarding the processing element size, the larger differences can be seen for the smaller element (Fig. 5.24(b) - 3×3). In this case, the convolution implementation achieves processing times more than two times lower than the moving sum implementation. The time reduction is also significant when compared with the filtering algorithm, with a performance 35% better.

Concluding, all the optimized implementations presented processing times two order of magnitude lower than the analytical method. Among the MATLAB® optimized implementations, the novel proposed method achieved the best results in all the tested cases. Other aspect to empathize is that, all the optimized methods (algorithms 2, 3 and 4) produce contrast maps without spatial resolution reduction. This is equivalent to perform the analytical method with complete overlap of the processing elements.

The convolution method has overcame the two state-of-the-art implementations, moving sum and filtering, for the proposed conditions. It is important to refer that the results achieved in this comparative test are highly depended on the used programming software and can also be implemented by dedicated hardware [255]. For that reasons, these results can only be considered for these very specific conditions.

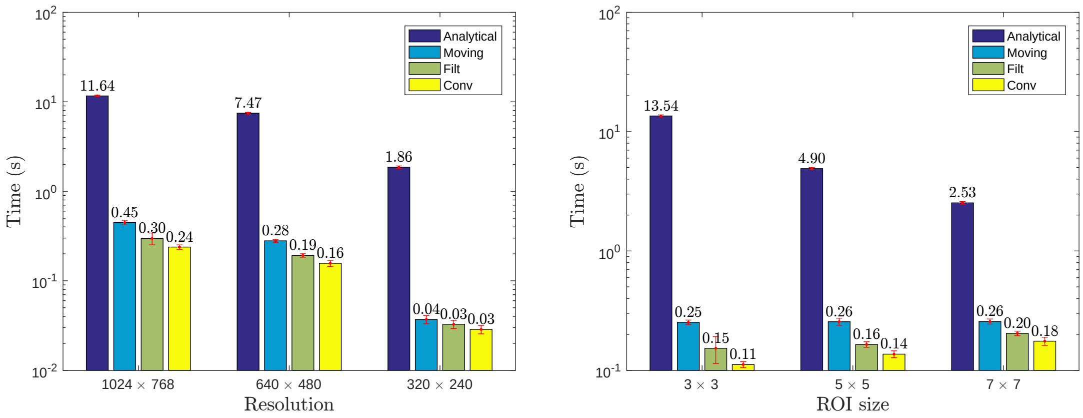

(a) Computation time as function of the LS image resolution.

(b) Computation time as function of the ROI size.

Figure 5.24: Analysis of the time required to process a single speckle image. The error bars represented in red correspond to the standard deviation.

Chapter 6

Conclusions

> *Charles Townes (1915 - 2015) constructed a microwave amplification by stimulated emission of radiation (MASER) device. In 1957, the theory was modified for shorter wavelengths beams and renamed as optical MASER which was the beginning of LASER.*

The final chapter of this thesis contains a summary of the most important conclusions and remarks that can be extracted from this work. Moreover, a brief proposition on future work is made, for the two thesis topics (macrocirculation and microcirculation).

6.1 General conclusions

The goal of this work was to study laser speckle effect as a method for hemodynamic parameters extraction. Two major applications of laser speckle have been explored. The first one, related with the macrocirculation was focused in the pulse pressure waveform extraction. The second one, related with microcirculation, was focused in the study of the effect of static scatterers on the laser speckle signal.

Apart from the core studies of this work, a speckle theory review has been preformed with a strong critical analysis. Finally, the

6.1.1 Speckle theory

An important review of the available laser speckle theory has been performed during this work. This thread was not only focused on the description of the current lines of investigation but also on a critical analysis.

Several laser speckle theoretical issues, such has the different scatterers motion distributions, the effect of static scatterers, and the quantitative velocity estimation have been addressed. Moreover, practical concepts such has the optimal speckle size, how to measure the normalization constant (β) and ρ, the effect of exposure time, and the influence of light polarization have been explored. The two major laser speckle techniques (single and multi exposure) and the contrast algorithms (spatial, temporal and spatio-temporal) have also been detailed.

6.1.2 Macrocirculation

The use of LSI to macrocirculation parameters extraction has been explored in this work with good results. A multi-wavelength laser speckle apparatus has been developed in order to study the influence of each light wavelength. Shorter wavelengths (green light) have presented the best results (subsection 4.1.2).

The green light source was, posteriorly, used to perform an extended study in order to assess the macrocirculation LSI capability. The same method used for laser speckle microcirculation applications, speckle contrast, has been used to extract the pulse pressure waveform of healthy volunteers. This method obtained good results both in the determination of the volunteers heart rate and the spectral similarity between PPG pulse wave. Features like the systolic peak and dicrotic notch have been identified in the laser speckle pulse waveform (subsection 4.1.3).

Finally, the LSI prototype was used to perform a two-dimensional segmentation of an artificial target with longitudinal movement. An algorithm, based on the laser speckle image entropy, has been used to segment a moving silicone membrane and differentiate it from a non-moving target of the same nature with success (subsection 4.1.4). Apart from distance measurements of skin movements, this system could also be important for a specific biomedical application like quantification of vocal folds vibration [256].

6.1.3 Microcirculation

An intensive study on the effect of static scatterers has been conducted in this work. This study has been motivated by the need of understanding how different concentrations of static scatterers affect the laser speckle signal. In our opinion, only by understanding this effect it will be possible to have a quantitative blood perfusion laser speckle imager.

A complex experimental bench test has been constructed for this objective. A microcirculation phantom has been developed by using a microchannel device, kindly provided by the Technical University of Tampere, in conjunction with silicone layer doped with different quantities of static scatterers (subsection 4.2.1).

This experimental work revealed that the correlation between consecutive images can be used to estimate the ratio static/dynamic scatterers presented in the system. In addition, the correlation proved to be independent of the dynamic scatterers velocity which is a very important feature (subsection 5.2.1.2).

These results are in accordance with laser speckle theory which relates the correlation between two consecutive images with the ratio of static and dynamic scatterers (ρ) and the normalization constant (β). The flow independence is of extremely importance because it ensures that tissues with low velocity scatterers, which could be damaged or non-functional, are not simply considered as containing higher concentrations of static scatterers.

An alternative metric (correlation coefficient) has been tested as substitute for the theoretical correlation. However, this new metric showed a strong scatterers velocity dependence which prevents its use to estimate ρ value. Nevertheless, the correlation coefficient showed a good relation with the scatterers velocity and its information could be used as complement to the laser speckle contrast (subsection 5.2.1.4).

The speckle contrast has also been computed using three different algorithms (s-K, t-K, and st-K). The temporal algorithm achieved the best results in dealing with $\langle I_s \rangle$ but, even so, a variation in t-K occurs. The t-K maximum occurs for an intermediate $\langle I_s \rangle$ and decreases for both lower and higher $\langle I_s \rangle$. The interpretation of this effect is not clear for us, however it could be related with the t-K element size (1×1×15) or the camera exposure time. These configurations could have interference in the t-K sensitivity to both fluid flow, $\langle I_s \rangle$ and $\langle I_d \rangle$. These explanations are completely speculative and further studies should be performed to confirm or refute these ideas.

For specific values of ρ and β and for a determined motion model, the contrast is a unequivocal measure. In other words, to a specific value of contrast correspond only one value of velocity. As determined in this work, t-K absolute values shows a one order magnitude discrepancy compared to s-K and st-K values computed for the same conditions. This is a major issue for a fully quantitative system because all the speckle theory is based on a spatial analysis. Based on this results, the st-K proved to be the best algorithm to achieve a quantitative laser speckle system (subsection 5.2.1.5).

6.2 Study limitations and future work

This section describes the probable and necessary future working lines for the methods presented during this thesis. Again, this section is divided into macro and micro circulation items. Most part of the future work is proposed in order to address this work limitations.

6.2.1 Macrocirculation

Laser speckle for macrocirculation assessment is a relatively new idea which enclosure great potential applications. Regarding our system, several technical improvements should be performed in future work. The speed of the acquisition system (VC) must be improved in order to extract the finer details of the pulse pressure waveform. Moreover, the laser light source should be replaced by a new one with more power and collimation. The use of a telephoto lens is also an important modification in order to achieve long distance HR meter.

In this work, we used a plaster support to secure the subject arm. This support has been constructed using the author's arm as model and does not have any adaptation capability. Most part of the errors (vibrations) detected during the acquisitions occurred due to this poor quality support. An adaptive support made from light material, like carbon fibre, would improve all the experimental results of the macrocirculation studies and increase the spectral similarity between PPG pulse wave and speckle pulse wave.

In a general perspective, more studies are necessary to validate this technique in healthy and pathological subjects in order to allow it to compete with other pulse waveform extraction methods [79, 257]. The development of a portable laser speckle system is also of major importance. A portable system will allow to easily reach bigger test groups in medical facilities or outdoor situations.

Other open hypothesis for future work is to miniaturize this technique. The coupling of coherent light source with an endoscope could be used to assess inner body parts that show movement. The speckle pattern formed in the inner tissues should be recorded by the endoscope camera and processed with the methods described above.

6.2.2 Microcirculation

Regarding the microcirculation, a method to determine the exact amount of $\langle I_d \rangle$ and $\langle I_s \rangle$ in each experiment is of extreme importance. Only with this quantification it will be possible to confirm or refute the relation between $g_2(\Delta t)$ and ρ value.

Moreover, the interface between the micro-channel device and static scatterers layer could be improved. Ideally, the micro-channel device should be replaced by a fine tube with a diameter approximately equal to the caterpillars. This tube should be included inside the static scatterers layer during the polymerization in order to minimize secondary reflections.

The layers fabrication process is another important step during this experiment. The necessity of using an outlier exclusion algorithm proved that the layers were not completely uniform. Novel methods to prevent the formation of clusters during the layer polymerization, despite of the used ultrasonic bath, should be studied.

The fluid used (milk) could also be replaced by a more accurate solution. Animal blood or a intralipid solution are two options to replace the milk. However, if a $\langle I_d \rangle$ measuring method is available, the use of milk instead of more reliable fluids is not critical.

Technical improvements could also be introduced to achieved more precise results. An more sensitive VC and a light source with temperature control are important steps to improve the results and reduce the large error bars showed in the results.

6.3 Final remarks

This thesis proved that laser speckle can be used to record macrocirculation parameters with a good reliability. In the future, with technical improvements, the actual laser speckle devices could include this technique in order to record and analyse a wider range of biomedical parameters.

Laser speckle has been used as a microcirculation assessment tool for several decades. However, the technique is still under strong investigation. In our opinion, the absolute quantification of the scatterers velocity is till the major limitation of laser speckle imaging. Several very recent studies confirm this idea [246,258]. This work showed that the influence of static scatterers can be accounted using the variable ρ but only in certain conditions.

In our case, the correlation has been sensitive to change of static scatterers only from a specific value of $\langle I_s \rangle$.

Even with ρ value, laser speckle quantitative systems are very difficult to achieve. Several variables influence the contrast that is obtained. So far, the addition of an external technique, like sidestream darkfield (SDF) imaging [246], seems to be the only way to achieve a quantitative laser speckle system from now. The recent efforts on LSI research lead us to believe that this issue could be solved in a short term (several years) or by theoretical adaptations, or new signal processing methods or calibration methods.

Many LSI studies have been conducted in highly vascularized tissues. Apart from cerebral and ocular applications, this technique could be very important for patients with microcirculatory diseases that affect the skin [100]. Laser speckle could have a great importance for these patients and more studies should be conducted in the application of LSI to less vascularized tissues.

Appendices

Appendix A

Speckle statistical analysis

A.1 Statistics

For the statistical analysis of the speckle pattern, it is assumed that the light source is monochromatic and perfectly polarized. The analytic signal for a representation of the electric field at a observation point (x, y, z) and time (t) is defined as:

$$u(x, y, z; t) = A(x, y, z)e^{i2\pi\nu t}, \tag{A.1}$$

where ν is the optical frequency and $A(x, y, z)$ is the phasor amplitude of the electric field (Eq. (A.2)).

$$A(x, y, z) = |A(x, y, z)|e^{i\theta(x,y,z)}, \tag{A.2}$$

where the $|...|$ operator symbolizes the absolute value and θ the phasor phase. The analytic representation is a generalization of the phasor because it allows for time-variant parameters.

The intensity in a surface point (x, y, z) is a sum of many phasors (N) with different phase. Assuming the contribution of each elementary phasor as $(\sqrt{N})^{-1}$, the resultant phasor amplitude is given by:

$$A(x, y, z) = \frac{1}{\sqrt{N}} \sum_{k=1}^{N} |a_k|e^{i\theta_k}. \tag{A.3}$$

By applying the Euler's formula, the result can be decomposed in real (Eq. (A.4a)) and imaginary part (Eq. (A.4b)).

$$A_{re} = Re(A(x, y, z)) = \frac{1}{\sqrt{N}} \sum_{k=1}^{N} |a_k| \cos\theta_k, \tag{A.4a}$$

$$A_{Im} = Im(A(x, y, z)) = \frac{1}{\sqrt{N}} \sum_{k=1}^{N} |a_k| \sin\theta_k. \tag{A.4b}$$

In order to compute the first order statistic properties of speckle two main assumption are essential. The first one is that each elementary phasor is statistically independent of each other in terms of amplitude and phase. The physical significance of this assumption denotes the independence of each scattering area.

The second main assumption relies on the phases (θ_k) distribution. By assuming that the illuminated surface has a roughness of greater magnitude than the used wavelength, it implies that the phases are uniformly distributed between $-\pi$ and π. The average value of the real and imaginary part of the field phasor are given by:

$$\langle A_{Re}\rangle = \frac{1}{\sqrt{N}}\sum_{k=1}^{N}\langle|a_k|\rangle\langle\cos\theta_k\rangle, \tag{A.5a}$$

$$\langle A_{Im}\rangle = \frac{1}{\sqrt{N}}\sum_{k=1}^{N}\langle|a_k|\rangle\langle\sin\theta_k\rangle. \tag{A.5b}$$

The property of independence is here used to average over amplitude and phase separately. As a consequence of the second assumption, the average values of $\cos\theta$ and $\sin\theta$ between $-\pi$ and π are:

$$\langle\cos\theta_k\rangle = \int_{-\pi}^{\pi}\theta_k\cos\theta_k d\theta_k = 0, \tag{A.6a}$$

$$\langle\sin\theta_k\rangle = \int_{-\pi}^{\pi}\theta_k\sin\theta_k d\theta_k = 0. \tag{A.6b}$$

Replacing the results from equations (A.6) in equations (A.5) we can see that real and imaginary parts of the electric field have an average equal to zero:

$$\langle A_{Re}\rangle = 0, \tag{A.7a}$$

$$\langle A_{Im}\rangle = 0. \tag{A.7b}$$

The second-order central moment is then defined as:

$$\langle[A_{Re}-\langle A_{Re}\rangle]^2\rangle = \langle[A_{Re}]^2\rangle = \frac{1}{N}\sum_{k=1}^{N}\sum_{m=1}^{N}\langle|a_k||a_m|\rangle\langle\cos\theta_k\cos\theta_m\rangle, \tag{A.8a}$$

$$\langle[A_{Im}-\langle A_{Im}\rangle]^2\rangle = \langle[A_{Im}]^2\rangle = \frac{1}{N}\sum_{k=1}^{N}\sum_{m=1}^{N}\langle|a_k||a_m|\rangle\langle\sin\theta_k\sin\theta_m\rangle. \tag{A.8b}$$

In this situation two different cases must be explored. On one hand, when θ_k is independent from θ_m, *i.e.*, $k \neq m$, the average value of the product is simply the product of the average values. On the other hand, when the variables are dependent, *i.e.*, $k = m$ the average value is given by the second subfunction of the piecewise-defined function (A.9). The same relations are applied when the trigonometric function $\cos\theta$ is replaced by $\sin\theta$.

$$\langle\cos\theta_k\cos\theta_m\rangle = \begin{cases}\langle\cos\theta_k\rangle\langle\cos\theta_m\rangle \\ \int_{-\pi}^{\pi} cos^2\theta_k d\theta_k\end{cases} = \begin{cases}0 & \text{If k} \neq \text{m} \\ \dfrac{1}{2} & \text{If k} = \text{m}\end{cases}. \tag{A.9}$$

By using the results from in equation (A.9), the variances of the real and imaginary part of the electric field are:

$$\langle[A_{Re}]^2\rangle = \frac{1}{N}\sum_{k=1}^{N}\frac{\langle|a_k|^2\rangle}{2}, \tag{A.10a}$$

$$\langle[A_{Im}]^2\rangle = \frac{1}{N}\sum_{k=1}^{N}\frac{\langle|a_k|^2\rangle}{2}. \tag{A.10b}$$

From equations (A.7) and (A.10) we conclude that the real and imaginary part of the field have zero mean and equal variances. Assuming a large number of elementary phasors ($N \to \infty$), the probability density function (pdf) is asymptotically Gaussian. Equations (A.11) shows the pdf for real and imaginary part of the field.

$$p(A_{Re}) = \frac{1}{\sigma\sqrt{2\pi}}\, e^{-\dfrac{A_{Re}^2}{2\sigma^2}}, \tag{A.11a}$$

$$p(A_{Im}) = \frac{1}{\sigma\sqrt{2\pi}}\, e^{-\dfrac{A_{Im}^2}{2\sigma^2}}. \tag{A.11b}$$

In this case, the variance (σ) is equivalent to the limit when $N \to \infty$ of the expressions described in (A.10). Having into account the early assumption that the variables are independent, the joint pdf is simply the multiplication of the individual pdf:

$$p(A_{Re}, A_{Im}) = p(A_{Re}) \cdot p(A_{Im}) = \frac{1}{\sigma^2 2\pi}\, e^{-\dfrac{A_{Re}^2 + A_{Im}^2}{2\sigma^2}}. \tag{A.12}$$

A.2 Intensity and Contrast

The statistical moments in terms of the complex electric field are not suitable for the most applications, since it is the intensity of the wave that is measured. Taking into account the relations described in subsection A.1, the statistic of speckle in terms of its intensity will be now explored.

Considering the real and complex field as:

$$A_{Re} = \sqrt{I}\cos\theta, \tag{A.13a}$$

$$A_{Im} = \sqrt{I}\sin\theta, \tag{A.13b}$$

the intensity and the phase of the electric field are obtained as:

$$I = A_{Re}^2 + A_{Im}^2, \tag{A.14a}$$

$$\theta = \tan^{-1} \frac{A_{Im}}{A_{Re}}. \tag{A.14b}$$

Since the joint pdf for the real and imaginary part complex field is known [see equation (A.12)], the relation between the new and the old pdf is given by:

$$p(I, \theta) = p(A_{Re}, A_{Im})||J||, \tag{A.15}$$

in which $||J||$ is the Jacobian of the transformation given by:

$$||J|| = \left\| \begin{matrix} \dfrac{\partial A_{Re}}{\partial I} & \dfrac{\partial A_{Re}}{\partial \theta} \\ \dfrac{\partial A_{Im}}{\partial I} & \dfrac{\partial A_{Im}}{\partial \theta} \end{matrix} \right\| = \left\| \begin{matrix} \dfrac{\cos\theta}{2\sqrt{I}} & -\sqrt{I}\sin\theta \\ \dfrac{\sin\theta}{2\sqrt{I}} & \sqrt{I}\cos\theta \end{matrix} \right\| = \frac{1}{2}. \tag{A.16}$$

Replacing this result in equation (A.15) the new joint pdf is obtained. The use of the joint pdf [equation (A.12)] is mandatory to find the intensity statistics because both real and complex parts depend on the intensity and phase.

$$p(I, \theta) = \frac{1}{\sigma^2 4\pi}\, e^{-\dfrac{I}{2\sigma^2}}. \tag{A.17}$$

After the determination of the joint pdf, and recalling the assumption of independence between intensity and phase, the marginal pdf of the intensity is found:

$$p(I) = \int_{-\pi}^{\pi} p(I, \theta) d\theta = \frac{1}{2\sigma^2}\, e^{-\dfrac{I}{2\sigma^2}}. \tag{A.18}$$

Since the intensity is a positive variable, the first and second order moments are computed applying the mathematical definition:

$$\langle I \rangle = \int_0^\infty I p(I) dI = -e^{-\dfrac{I}{2\sigma^2}} (2\sigma^2 + I) \Bigg|_0^\infty = 2\sigma^2, \tag{A.19a}$$

$$\langle I^2 \rangle = \int_0^\infty I^2 p(I) dI = -e^{-\dfrac{I}{2\sigma^2}} (8\sigma^4 + 4\sigma^2 I + I^2) \Bigg|_0^\infty = 8\sigma^4. \tag{A.19b}$$

In conclusion, there is an evident relation between the first and the second order moments of the intensity of the speckle pattern. This relation is described by equation (A.20a), and it has practical implication when the standard deviation is computed [equation (A.20b)].

$$\langle I^2 \rangle = 2\langle I \rangle, \tag{A.20a}$$

$$\sigma_I^2 = \langle I^2 \rangle - \langle I \rangle^2. \tag{A.20b}$$

Now we are in conditions to stablish a relation between the mean intensity and standard deviation of a speckle pattern in perfect conditions. Several assumptions have to be made, namely, a perfectly coherent and polarized light source is used, the phase and amplitude of each of the scattered beams are independent from each other, and the phase is distributed uniformly in the interval $-\pi$ to π.

In medical applications, speckle images are often processed based in its contrast. The contrast can be defined as:

$$K = \frac{\sigma_I}{\langle I \rangle} \tag{A.21}$$

It is trivial that, from equations (A.20), that if $\sigma_I = I$, the contrast, in perfect conditions, is unitary. In normal conditions, the contrast of speckle ranges from 0 to 1 [124]. This is an important result because it is the base for many algorithms and methods used in LSI for medical applications.

Appendix B

Supplementary data of microcirculation studies

This appendix gather the complete data-set discussed in chapter 5. For details on the analysis of these figures and tables please refer to section 5.2. Some of the figures contain information already displayed in chapter 5.

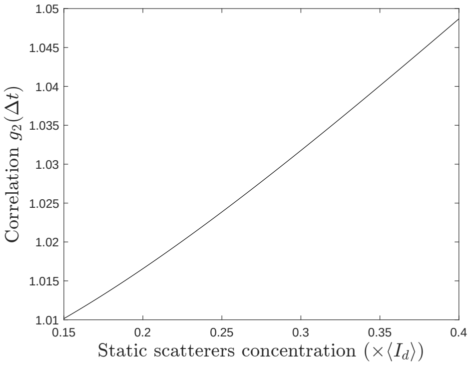

Figure B.1: Correlation value as function of static scatterers concentration. The x-axis units $(\times\langle I_d\rangle)$ corresponds to number of times of dynamic scatterers concentration.

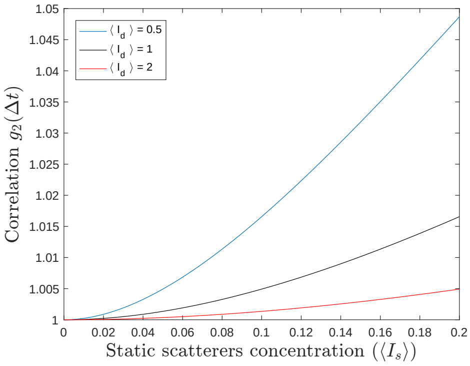

Figure B.2: Correlation value as function of static scatterers concentration for three dynamic scatterers concentrations.

Table B.1: Fitting parameters of the linear regression applied to ρ value data. R^2 represents coefficient of determination.

Milk (%)	Flow (cm^3/h)	m	b	R^2
33	0	-0.015	0.27	-0.31
	1.5	-0.008	0.25	-0.25
	3	-0.007	0.24	-0.33
	7	-0.007	0.24	-0.22
	14	-0.009	0.25	-0.27
50	0	0.05	0.17	0.88
	1.5	0.05	0.17	0.88
	3	0.06	0.16	0.92
	7	0.06	0.16	0.92
	14	0.05	0.16	0.89
75	0	0.08	0.12	0.95
	1.5	0.07	0.12	0.91
	3	0.06	0.12	0.89
	7	0.05	0.12	0.88
	14	0.07	0.12	0.88
100	0	0.07	0.11	0.94
	1.5	0.08	0.11	0.92
	3	0.07	0.11	0.93
	7	0.07	0.11	0.89
	14	0.06	0.12	0.92
200	0	0.08	0.10	0.96
	1.5	0.07	0.10	0.95
	3	0.07	0.10	0.94
	7	0.07	0.09	0.97
	14	0.06	0.08	0.98

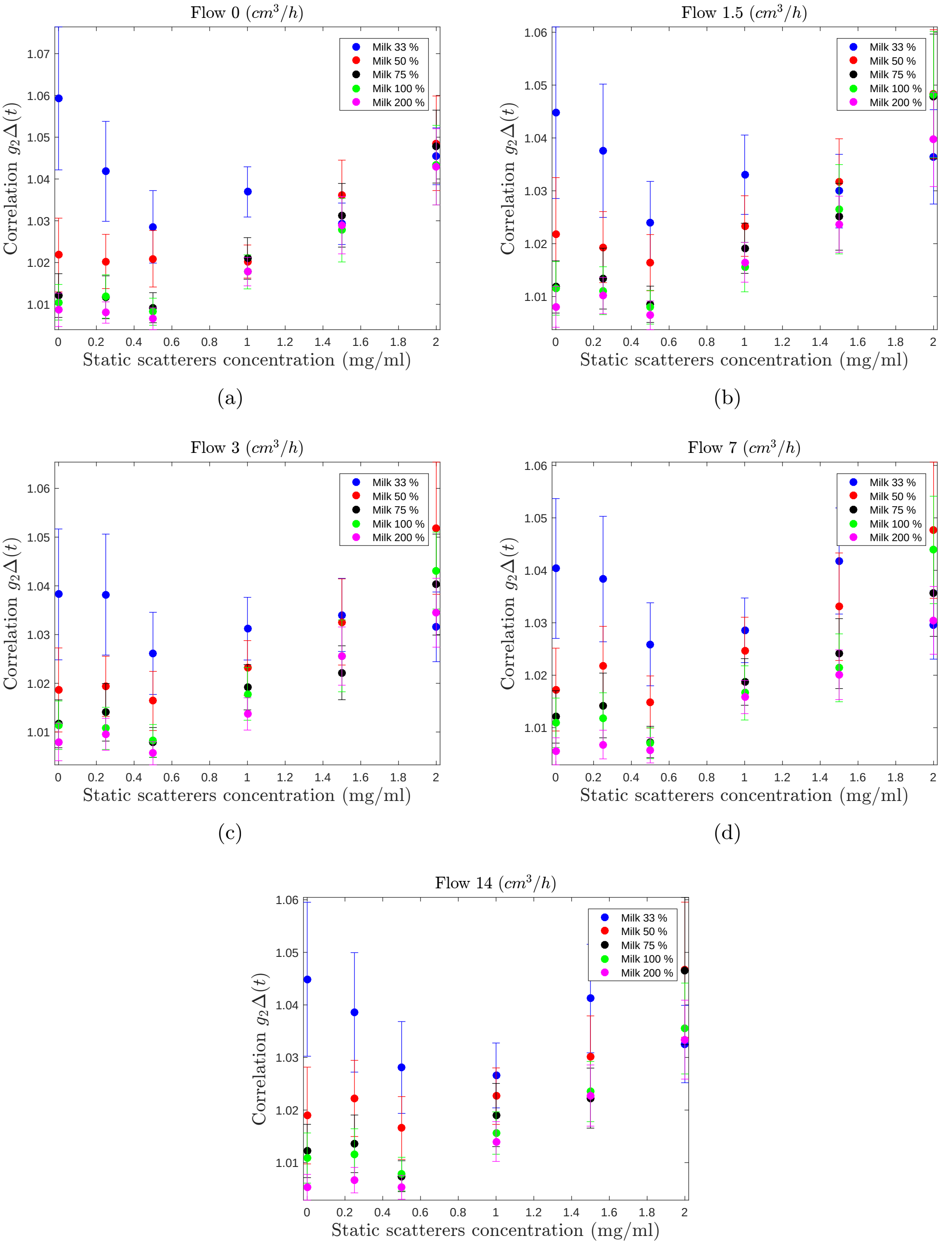

(a)

(b)

(c)

(d)

(e)

Figure B.3: Results obtained for the variation of $g_2(\Delta t)$ with the increase of static scatterers concentration. Each sub-figure represents a fluid flow.

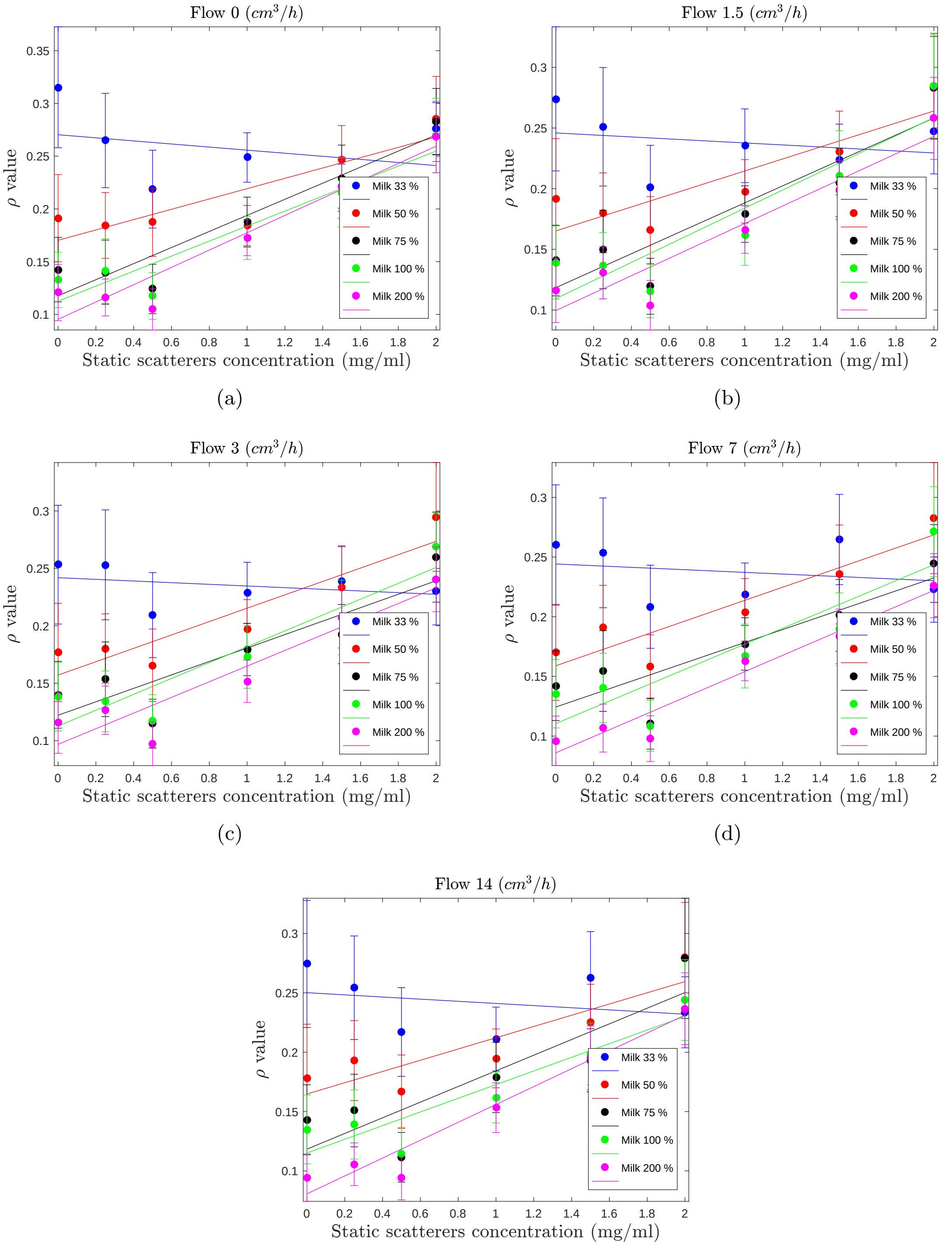

(a) (b) (c) (d) (e)

Figure B.4: Results of ρ value determination based on correlation function $g_2(\Delta t)$. Each sub-figure corresponds to a different fluid flow. Solid lines represent the linear fitting equation.

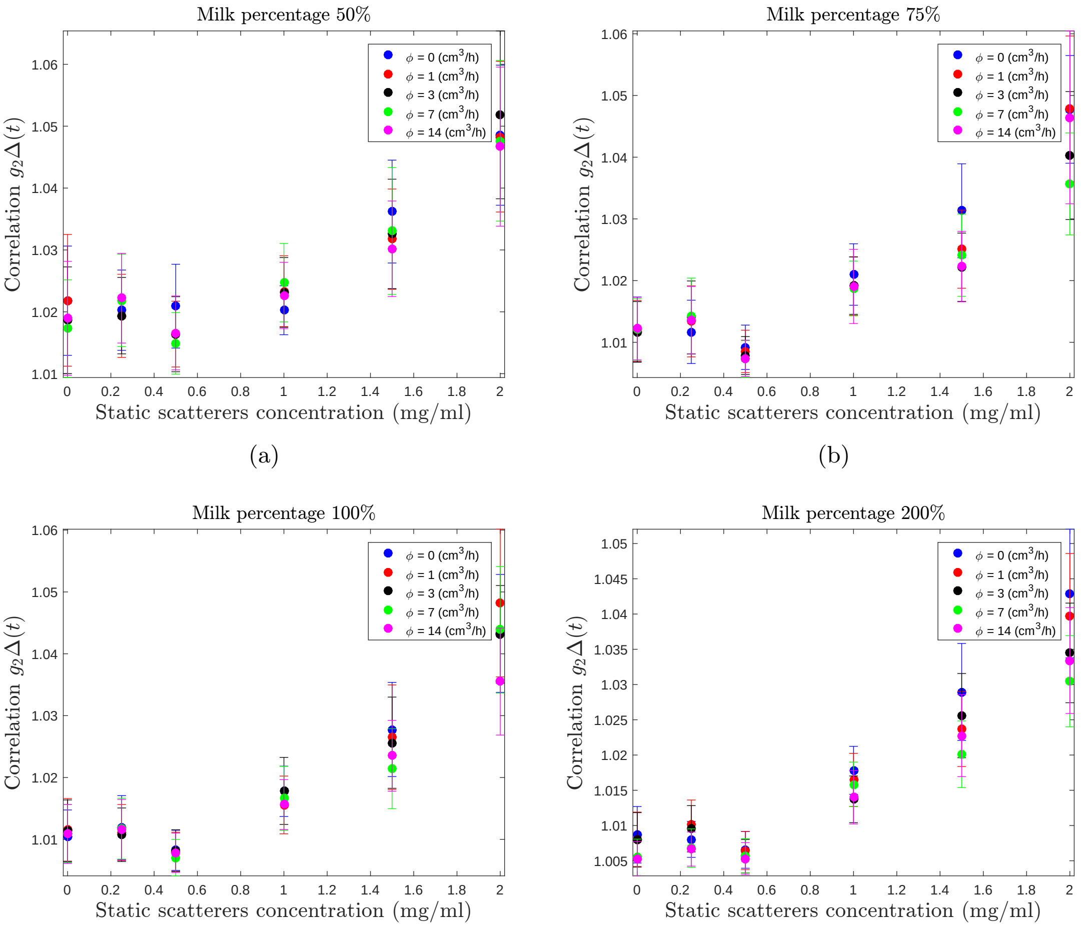

(a)

(b)

(c)

(d)

Figure B.5: Results obtained for the variation of $g_2(\Delta t)$ with the increase of static scatterers concentration. Each sub-figure represents a different milk concentration.

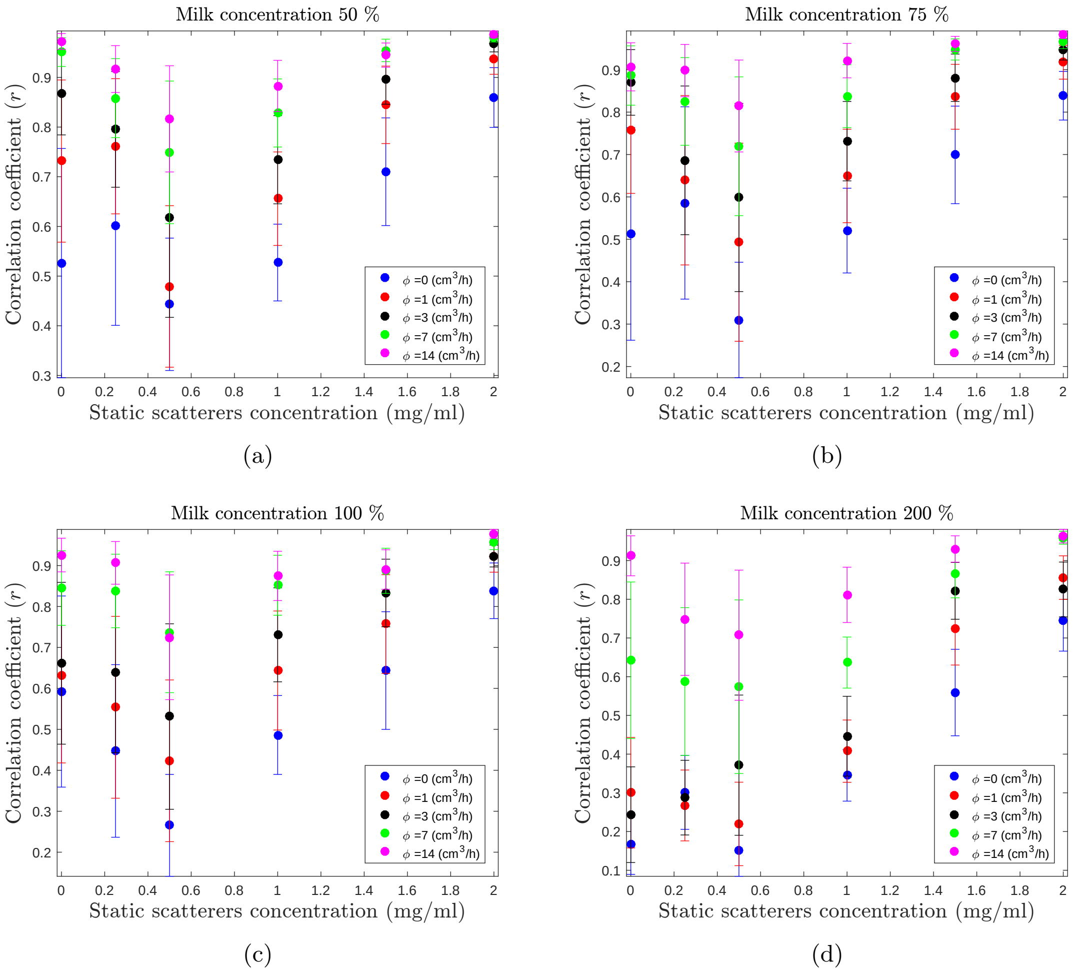

(a) (b)

(c) (d)

Figure B.6: Results of the two-dimensional correlation coefficient r. Each sub-figure corresponds to different milk concentrations.

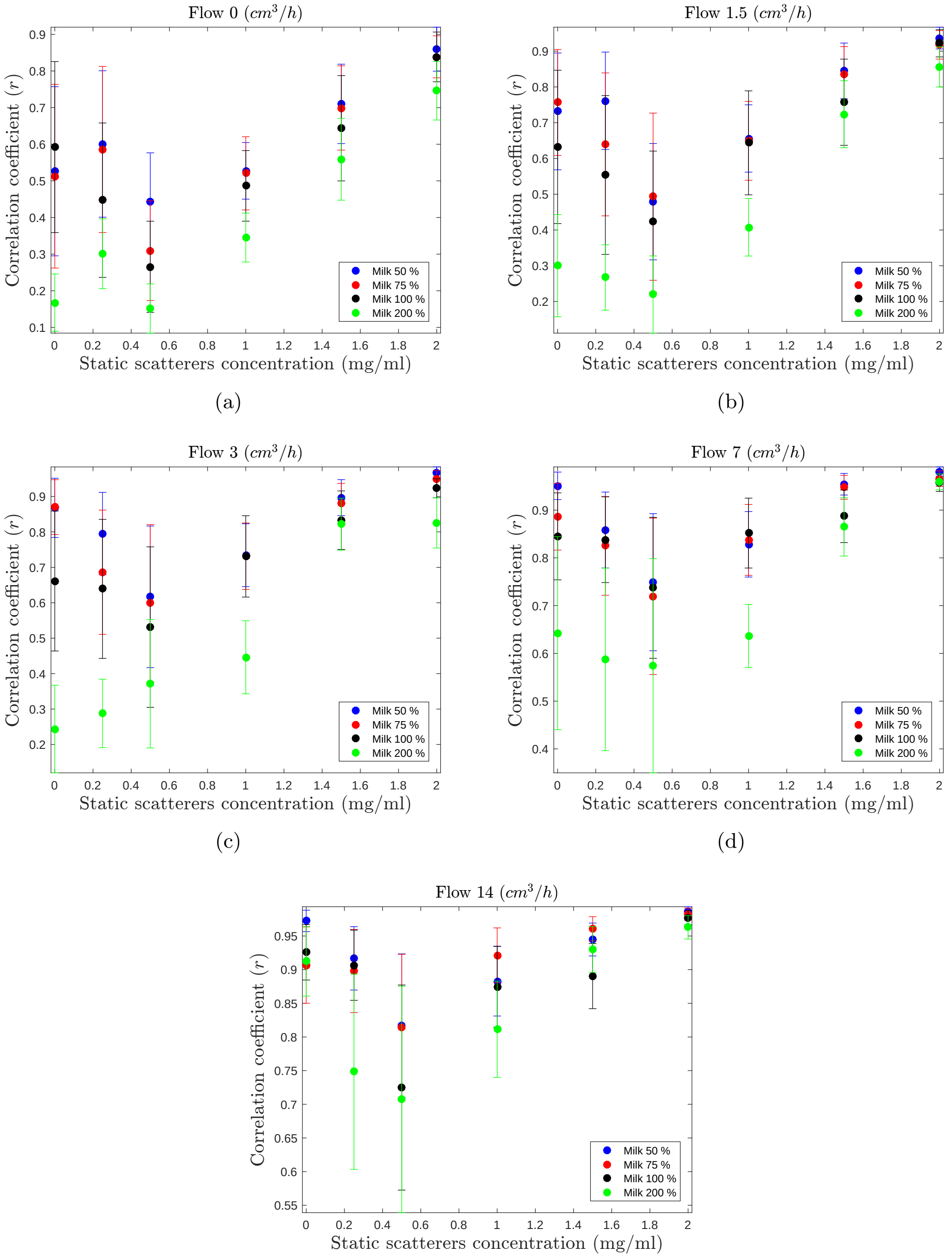

(a) (b) (c) (d) (e)

Figure B.7: Results of the two-dimensional correlation coefficient r. Each sub-figure corresponds to different fluid flow.

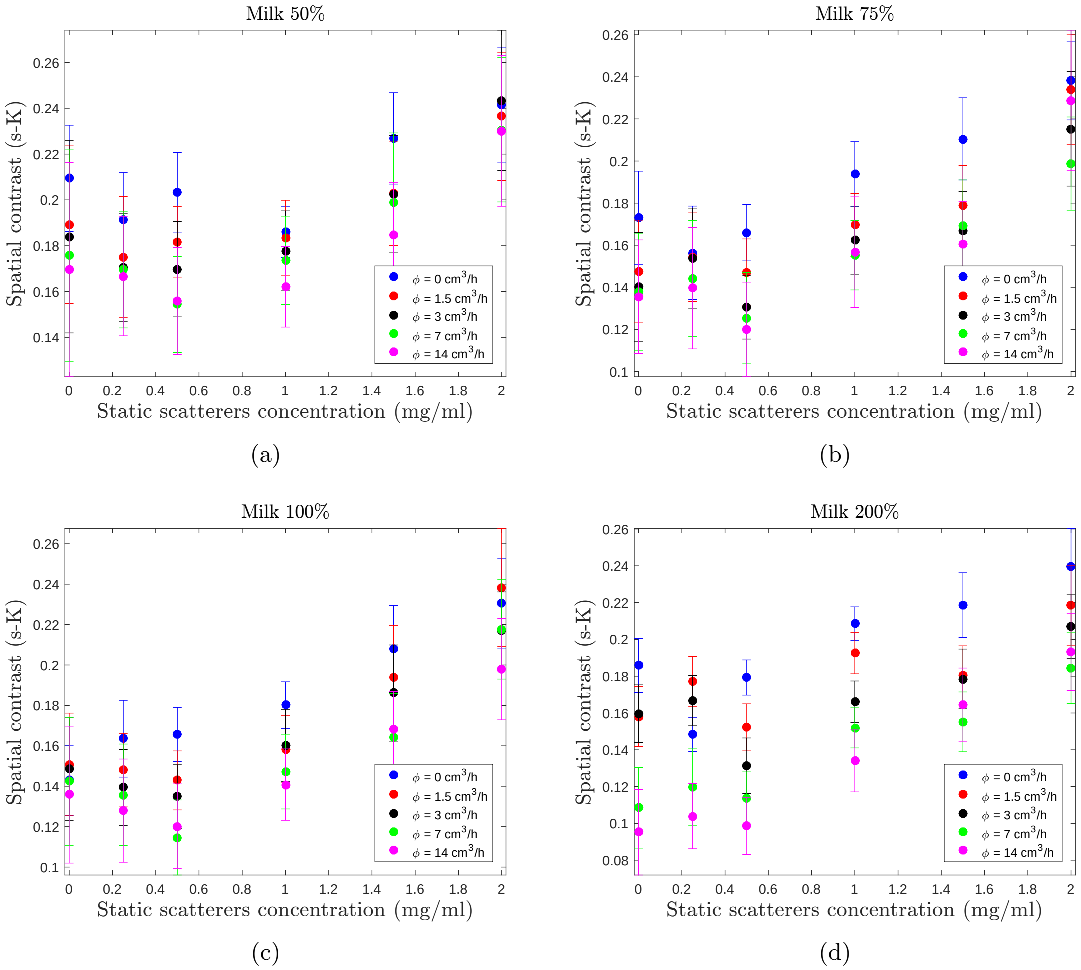

(a) (b)

(c) (d)

Figure B.8: Laser speckle contrast computed with spatial algorithm. Each figure represents a different milk concentration. The standard deviations have been computed with a minimum of 3602 points.

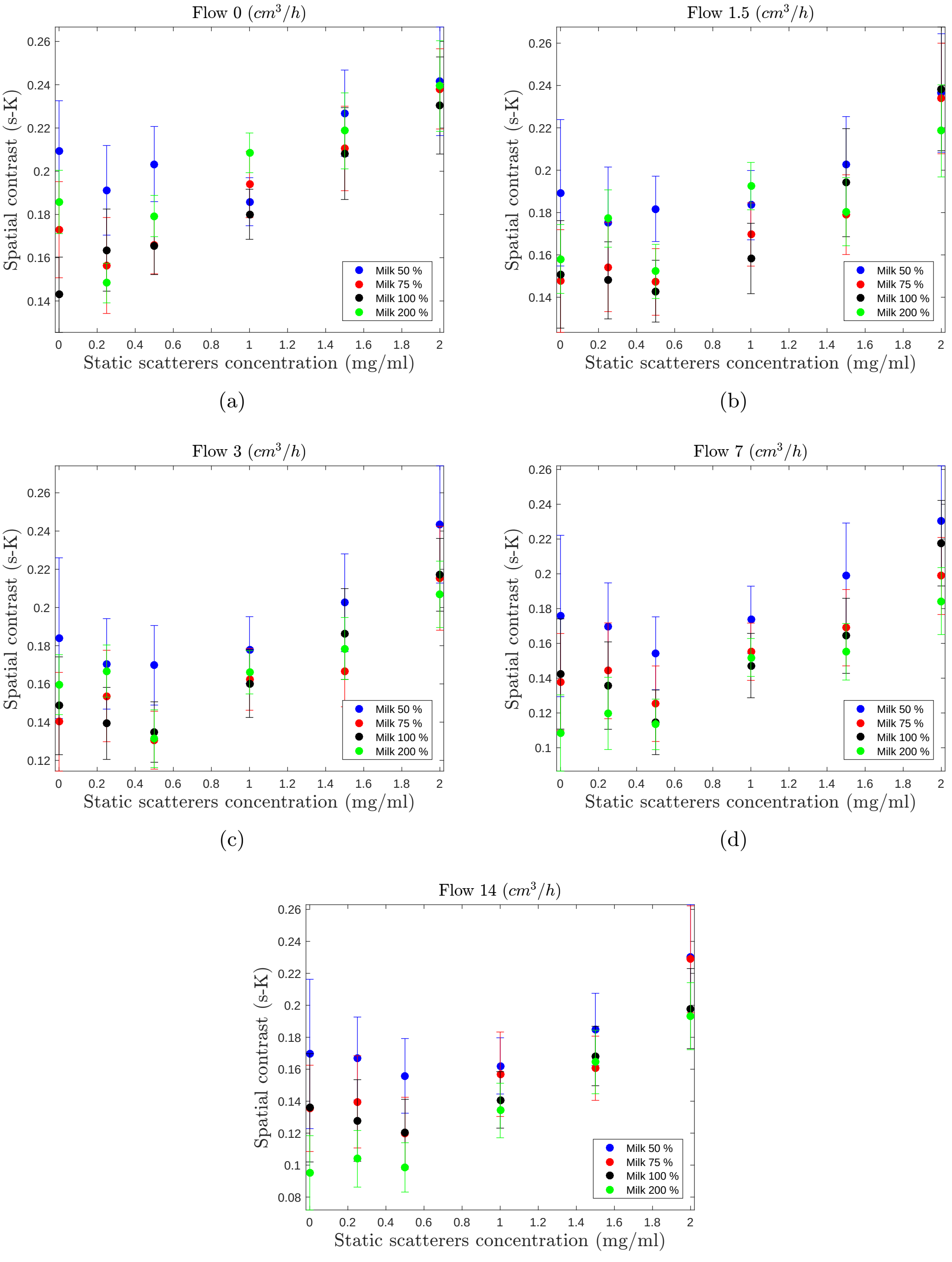

(a) (b) (c) (d) (e)

Figure B.9: Laser speckle contrast computed with spatial algorithm. Each figure represents a different fluid flow. The standard deviations have been computed with a minimum of 3602 points.

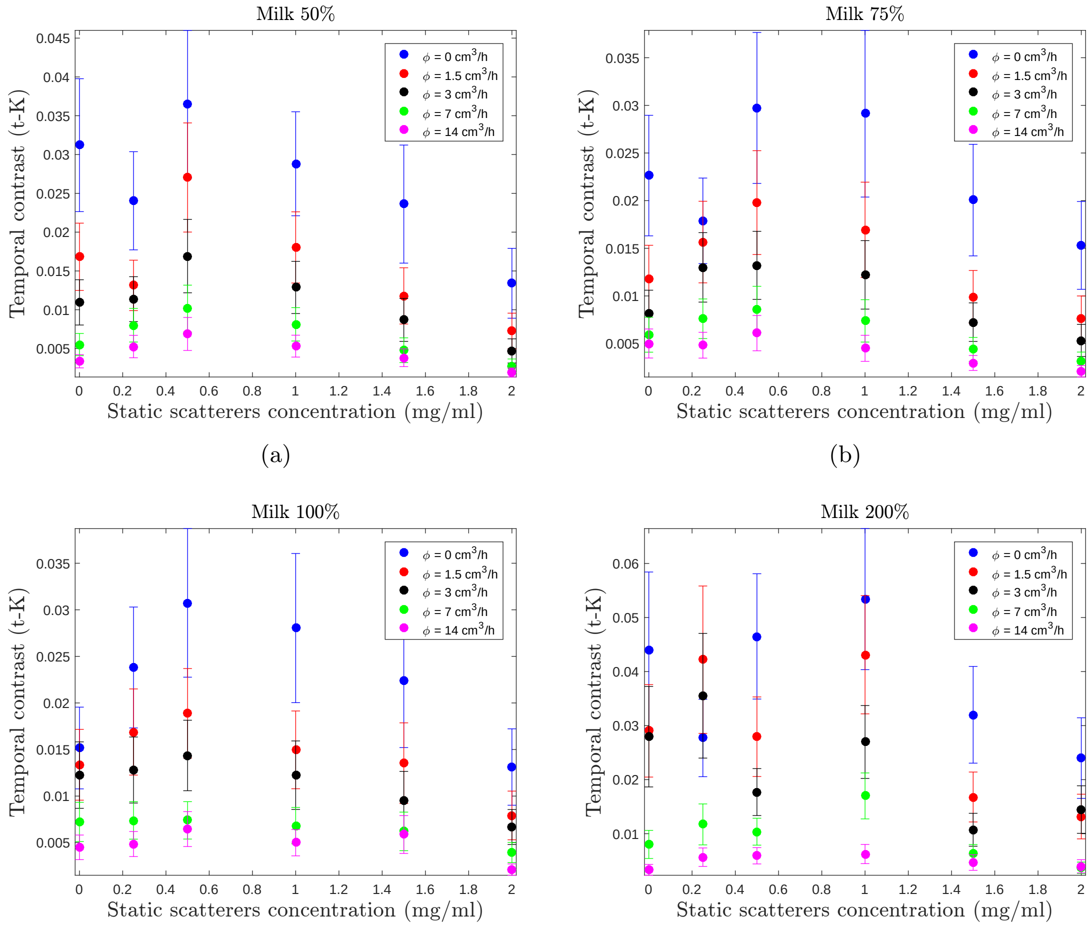

(a)

(b)

(c)

(d)

Figure B.10: Laser speckle contrast computed with temporal algorithm. Each figure represents a different milk concentration. The standard deviations have been computed with a minimum of 4017 points.

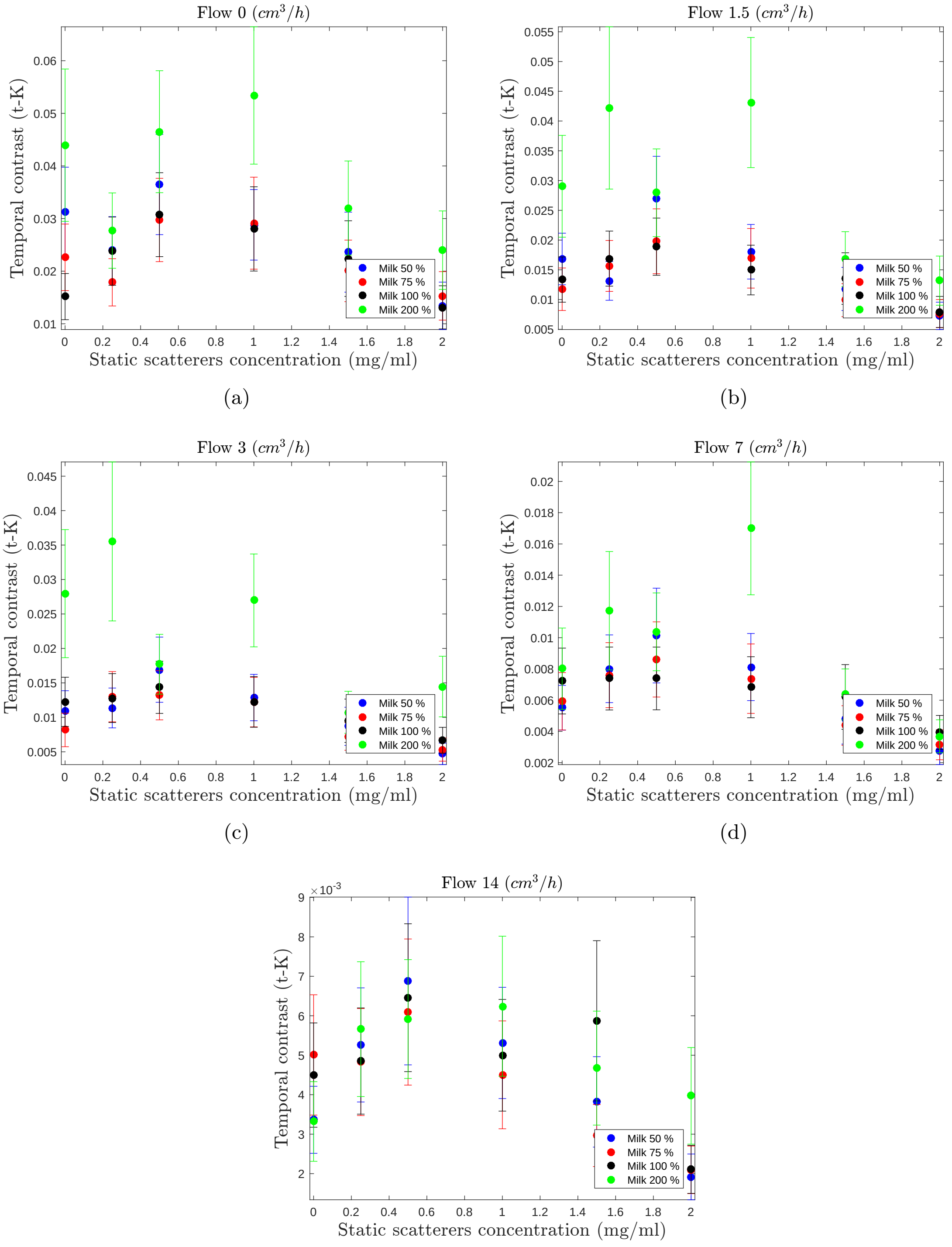

(a)

(b)

(c)

(d)

(e)

Figure B.11: Laser speckle contrast computed with temporal algorithm. Each figure represents a different fluid flow. The standard deviations have been computed with a minimum of 4017 points.

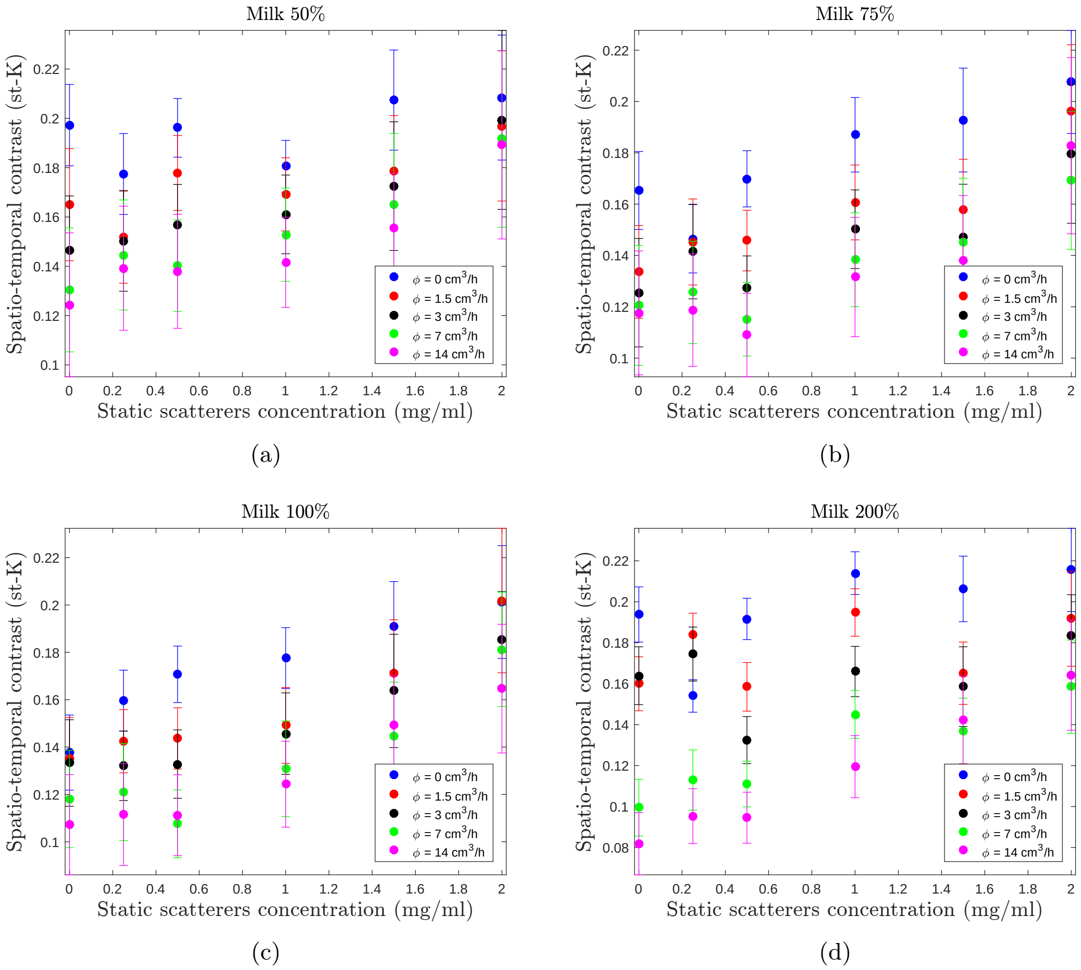

(a) (b)

(c) (d)

Figure B.12: Laser speckle contrast computed with spatio-temporal algorithm. Each figure represents a different milk concentration. The standard deviations have been computed with a minimum of 4545 points.

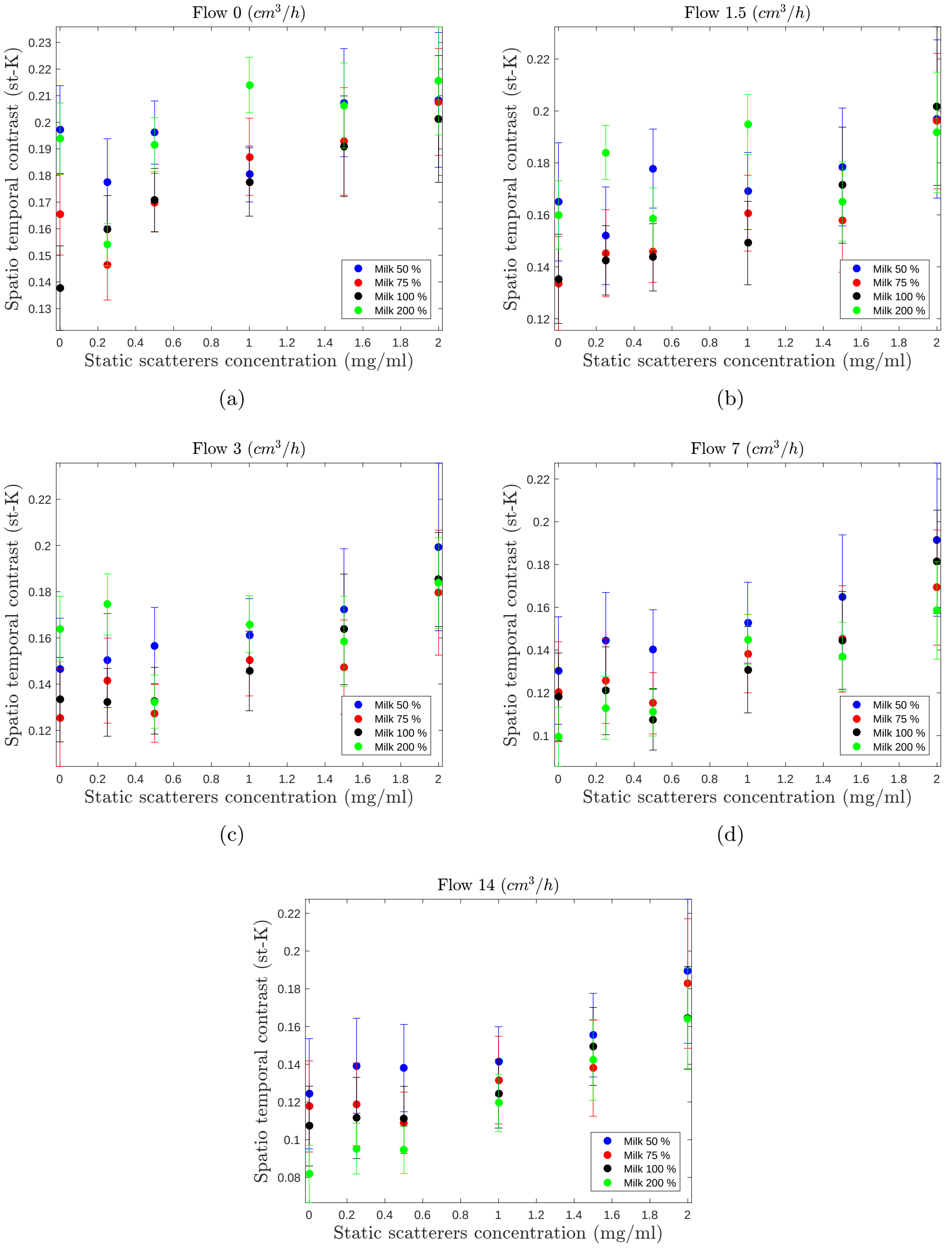

(a)

(b)

(c)

(d)

(e)

Figure B.13: Laser speckle contrast computed with spatio-temporal algorithm. Each figure represents a different fluid flow. The standard deviations have been computed with a minimum of 4545 points.

Appendix C

Contrast effect on correlation - auxiliary data

The correlation between two speckle images is related with its blurring degree. In order to illustrate this effect a set of laser speckle images is represented in this appendix. Figure C.1 is a reproduction of figure 4.16. This figure corresponds to two consecutive images acquired with the static layer IV, flow #3 and milk proportion 1:2.

These two images have been filtered with a Gaussian image filter, with sigma equal 1 and sigma equal 2 in order to simulate the blurring effect. With this data, we want to show that two distinct speckle images become more correlated when the speckles decorrelate.

The values of $g_2(\Delta t)$ and r corroborate this theory. When the Gaussian filter is applied, the correlation coefficient goes from 0.71 to 0.82 ($\sigma = 1$) and to 0.91 ($\sigma = 2$). A r value of 0.91 indicates a very strong correlation between both frames while the original value (0.71) only indicates an average correlation.

Regarding the $g_2(\Delta t)$, this values also changes with the increase of the blurring degree, however it decrease when the blurring effect increases. The value of 1.063 represents the two original images while a $g_2(\Delta t) = 1.037$ is obtained for the higher blurring degree. The evolution of $g_2(\Delta t)$ presents an opposite behaviour regarding the r.

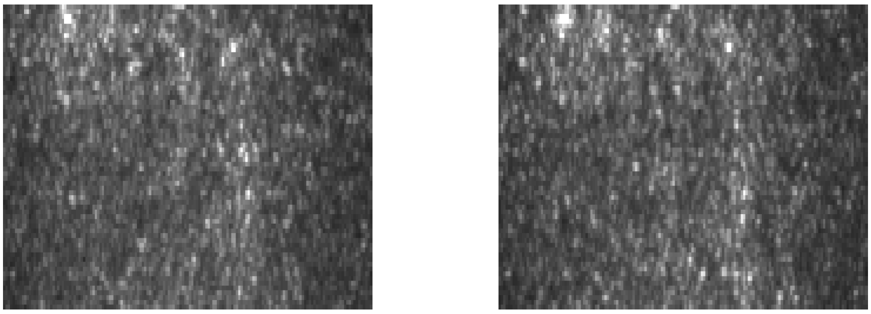

(a) Frame = i (b) Frame = i+1

Figure C.1: Consecutive speckle images of membrane IV. Original data. The correlation and two-dimensional correlation coefficient are respectively: $g_2(\Delta t) = 1.063$ and $r = 0.71$.

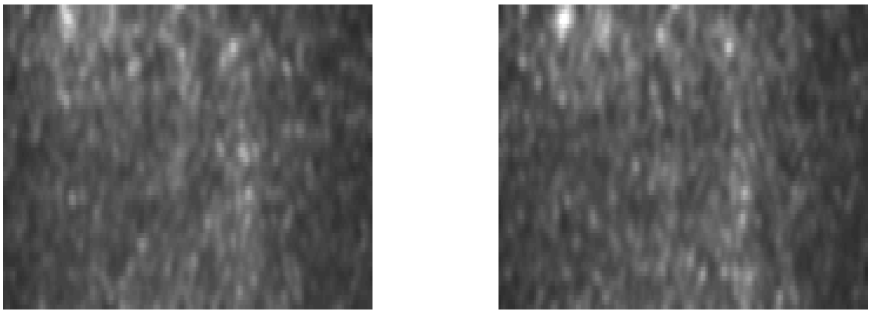

(a) Frame = i (b) Frame = i+1

Figure C.2: Consecutive speckle images of membrane IV. Images filtered with Gaussian filter, sigma 1. The correlation and two-dimensional correlation coefficient are respectively: $g_2(\Delta t) = 1.044$ and $r = 0.82$

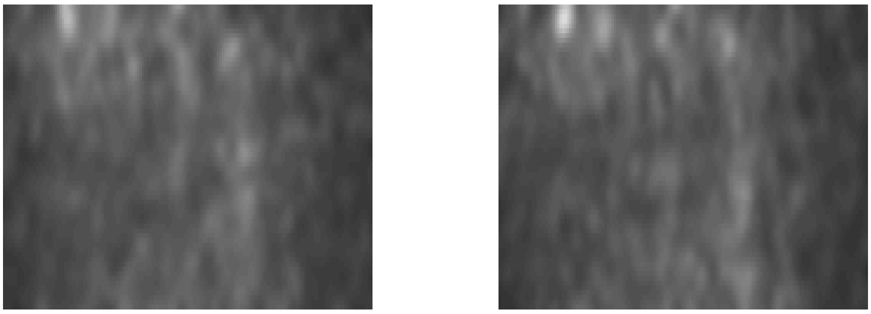

(a) Frame = i (b) Frame = i+1

Figure C.3: Consecutive speckle images of membrane IV. Images filtered with Gaussian filter, sigma 2. The correlation and two-dimensional correlation coefficient are respectively: $g_2(\Delta t) = 1.037$ and $r = 0.91$

Bibliography

[1] M. Bashkansky and J. Reintjes. Statistics and reduction of speckle in optical coherence tomography. *Opt. Lett.*, 25(8):545–547, apr 2000.

[2] M. Kato, Y. Nakayama, and T. Suzuki. Speckle reduction in holography with a spatially incoherent source. *Appl. Opt.*, 14(5):1093–1099, 1975.

[3] L. Wang, T. Tschudi, T. Halldorsson, and P. R. Petursson. Speckle reduction in laser projection systems by diffractive optical elements. *Appl. Opt.*, 37(10):1770–1775, 1998.

[4] L. Novak and M. Burl. Optimal speckle reduction in polarimetric SAR imagery. *IEEE Trans. Aerosp. Electron. Syst.*, 26(2):293–305, 1990.

[5] B. Pan, K. Qian, H. Xie, and A. Asundi. Two-dimensional digital image correlation for in-plane displacement and strain measurement: a review. *Meas. Sci. Technol.*, 20(6):62001, 2009.

[6] M. Grédiac. The use of full-field measurement methods in composite material characterization: interest and limitations. *Compos. Part A Appl. Sci. Manuf.*, 35(7–8):751–761, jul 2004.

[7] C. A. Thompson, K. J. Webb, and A. M. Weiner. Diffusive media characterization with laser speckle. *Appl. Opt.*, 36(16):3726–3734, 1997.

[8] P. Šmíd, P. Horváth, and M. Hrabovský. Speckle correlation method used to measure object's in-plane velocity. *Appl. Opt.*, 46(18):3709–3715, 2007.

[9] D. A. Boas and A. K. Dunn. Laser speckle contrast imaging in biomedical optics. *J. Biomed. Opt.*, 15(1):011109–12, 2010.

[10] Z. Zalevsky, Y. Beiderman, I. Margalit, S. Gingold, M. Teicher, V. Mico, and J. Garcia. Simultaneous remote extraction of multiple speech sources and heart beats from secondary speckles pattern. *Opt. Express*, 17(24):21566–80, nov 2009.

[11] J. Barnes and M. D. Mayes. Epidemiology of systemic sclerosis: incidence, prevalence, survival, risk factors, malignancy, and environmental triggers. *Curr. Opin. Rheumatol.*, 24(2):165–170, 2012.

[12] R. Garner, R. Kumari, P. Lanyon, M. Doherty, and W. Zhang. Prevalence, risk factors and associations of primary Raynaud's phenomenon: systematic review and meta-analysis of observational studies. *BMJ Open*, 5(3):e006389, 2015.

[13] P. G. Vaz, A. Humeau-Heurtier, E. Figueiras, C. Correia, and J. Cardoso. Laser speckle imaging to monitor microvascular blood flow: a Review. *IEEE Rev. Biomed. Eng.*, In press(99):1–1, 2016.

[14] P. Vaz, T. Pereira, E. Figueiras, C. Correia, A. Humeau-Heurtier, and J. Cardoso. Which wavelength is the best for arterial pulse waveform extraction using laser speckle imaging? *Biomed. Signal Process. Control*, 25:188–195, mar 2016.

[15] P. Vaz, V. Almeida, L. R. Ferreira, C. Correia, and J. Cardoso. Signal (Stream) synchronization with White noise sources, in biomedical applications. *Biomed. Signal Process. Control*, 18:394–400, apr 2015.

[16] P. Vaz, P. Santos, E. Figueiras, C. Correia, A. Humeau-Heurtier, and J. Cardoso. Laser speckle contrast analysis for pulse waveform extraction. In *Nov. Biophotonics Tech. Appl. III*, volume 9540, pages 954006–954007, Munich, 2015. SPIE.

[17] P. Vaz, T. Pereira, D. Capela, L. Requicha, C. Correia, A. Humeau-Heuertier, and J. Cardoso. Use of laser speckle and entropy computation to segment images of diffuse objects with longitudinal motion. In *II Int. Conf. Appl. Opt. Photonics*, Aveiro, 2014.

[18] P. Vaz, R. Couceiro, P. Carvalho, and J. Henriques. An Automatic method for motion artifacts detection in photoplethysmographic signals referenced with electrocardiography data. In *Biomed. Eng. Informatics (BMEI), 7th Int. Conf.*, pages 704–708. IEEE, 2014.

[19] B. Lieber. Arterial macrocirculatory hemodynamics. In J. D. Bronzino, editor, *Biomed. Eng. Handb.*, volume 1, chapter 56, page 1. Taylor & Francis Group, 2006.

[20] M. Thiriet. Hemodynamics. In *Biol. Mech. Blood Flows Part II Mech. Med. Asp.*, CRM Series in Mathematical Physics, chapter 5, pages 137–171. Springer New York, 2007.

[21] J. K.-J. Li. Physical concepts and basic fluid mechanics. In *Dyn. Vasc. Syst.*, chapter 3, pages 41–75. World Scientific Publishing Co. Re. Ltd., River Edge, 2004.

[22] E. Merrill. Rheology of blood. *Physiol. Rev.*, 44(4):863–884, 1969.

[23] K. E. Barrett, S. M. Barman, S. Boitano, and H. Brooks. Blood as a circulatory fluid & the dynamics of blood & lymph flow. In *Ganong's Rev. Med. Physiol.*, chapter 32, pages 521–553. McGraw-Hill Education, 23th edition, 2009.

[24] T. Kenner. The measurement of blood density and its meaning. *Basic Res. Cardiol.*, 84(2):111–124, 1989.

[25] G. D. O. Lowe, a. J. Lee, a. Rumley, J. F. Price, and F. G. R. Fowkes. Blood viscosity and risk of cardiovascular events: The Edinburgh Artery Study. *Br. J. Haematol.*, 96(1):168–173, 1997.

[26] G. Pocock and C. D. Richards. The Properties of Blood. In *Hum. Physiol. basis Med.* 3rd edition, 2006.

[27] J. B. Reece, L. A. Urry, M. L. Cain, S. A. Wasserman, P. V. Minorsky, and R. B. Jackson. Circulation and gas exchange. In *Campbell Biol.*, chapter 42, pages 915–928. Pearson, 10 edition, 2013.

[28] M. Thiriet. Blood. In *Biol. Mech. Blood Flows. Part I Biol.*, chapter 6, pages 265–294. Springer-Verlag New York, 1 edition, 2008.

[29] D. E. Goldstein, R. R. Little, R. A. Lorenz, J. I. Malone, D. Nathan, C. M. Peterson, and D. B. Sacks. Tests of glycemia in diabetes. *Diabetes Care*, 27(7):1761–1773, 2004.

[30] G. Késmárky, P. Kenyeres, M. Rábai, and K. Tóth. Plasma viscosity: a forgotten variable. *Clin. Hemorheol. Microcirc.*, 39(1):243–246, 2008.

[31] S. H. Orkin and L. I. Zon. Hematopoiesis: An Evolving Paradigm for Stem Cell Biology. *Cell*, 132(4):631–644, 2008.

[32] V. Kalchenko, Y. Kuznetsov, I. Meglinski, and A. Harmelin. Label free in vivo laser speckle imaging of blood and lymph vessels. *J. Biomed. Opt.*, 17(5):505021–505023, 2012.

[33] J. K.-J. Li. Vascular biology, structure and function. In John, K-J, and Li, editors, *Dyn. Vasc. Syst.*, chapter 2, pages 14–39. World Scientific Publishing Co. Re. Ltd., Danvers, 2004.

[34] G. Pocock and C. D. Richards. Human physiology: the basis of medicine. In *Hum. Physiol. basis Med.*, Oxford core texts, chapter 15, pages 263–277. Oxford University Press, 3rd edition, 2006.

[35] H. Fukuta and W. C. Little. The Cardiac Cycle and the Physiological Basis of Left Ventricular Contraction, Ejection, Relaxation, and Filling. *Heart Fail. Clin.*, 4(1):1–11, jan 2008.

[36] K. E. Barrett, S. M. Barman, S. Boitano, and H. Brooks. The Heart as a Pump. In *Ganong's Rev. Med. Physiol.*, Lange medical book, chapter 31, pages 507–520. McGraw-Hill Education, 23th edition, 2009.

[37] A. C. Guyton and J. E. Hall. Heart Muscle; The Heart as a Pump and Function of the Heart Valves. In *Textb. Med. Physiol.*, chapter 9, pages 103–116. Elsevier Saunders, 11th edition, 2006.

[38] M. Biais, K. Nouette-Gaulain, V. Cottenceau, A. Vallet, J. F. Cochard, P. Revel, and F. Sztark. Cardiac output measurement in patients undergoing liver transplantation: pulmonary artery catheter versus uncalibrated arterial pressure waveform analysis. *Anesth. Analg.*, 106(5):1480–1486, table of contents, 2008.

[39] T. Chan Sin, R. Usubamatov, M. A. Fairuz, M. F. B. M. Amin Hamzas, and L. Kin Wai. Engineering Mathematical Analysis Method for Productivity Rate in Linear Arrangement Serial Structure Automated Flow Assembly Line. *Math. Probl. Eng.*, 2015.

[40] N. Fazeli and J. O. Hahn. Estimation of cardiac output and peripheral resistance using square-wave-approximated aortic flow signal. *Front. Physiol.*, 58, 2012.

[41] R. Mukkamala, A. T. Reisner, H. M. Hojman, R. G. Mark, and R. J. Cohen. Continuous cardiac output monitoring by peripheral blood pressure waveform analysis. *IEEE Trans. Biomed. Eng.*, 53(3):459–467, 2006.

[42] T. Parlikar, T. Heldt, G. V. Ranade, and G. C. Verghese. Model-based estimation of cardiac output and total peripheral resistance. *Comput. Cardiol.*, 34:379–382, 2007.

[43] F. Feihl, L. Liaudet, and B. Waeber. The macrocirculation and microcirculation of hypertension. *Curr Hypertens Rep*, 11(3):182–189, 2009.

[44] M. Thiriet. Vessel Wall. In *Biol. Mech. Blood Flows. Part I Biol.*, chapter 8. Springer-Verlag New York, 1 edition, 2008.

[45] W. R. Milnor. Normal state of the circulation. In *Cardiovasc. Physiol.*, chapter 2, pages 29–61. Oxford University Press, 1990.

[46] M. Thiriet. Anatomy of the Cardiovascular System. In *Biol. Mech. Blood Flows. Part II Mech. Med. Asp.*, chapter 1, pages 9–34. Springer Science + Business Media, LLC, 2008.

[47] Kelvinsong. Diagram of an artery. `https://commons.wikimedia.org/wiki/File:Artery.svg`, 2013.

[48] B. H. Brown, R. H. Smallwood, D. C. Barber, P. V. Lawford, and D. R. Hose. Biofluid mechanics. In *Med. Phys. Biomed. Eng.*, Series in Medical Physics and Biomedical Engineering, chapter 2. Taylor & Francis, 1998.

[49] R. Asmar, A. Benetos, J. Topouchian, P. Laurent, B. Pannier, A.-M. Brisac, R. Target, and B. I. Levy. Assessment of arterial distensibility by automatic pulse wave velocity measurement validation and clinical application studies. *Hypertension*, 26(3):485–490, 1995.

[50] G. F. Mitchell, H. Parise, E. J. Benjamin, M. G. Larson, M. J. Keyes, J. A. Vita, R. S. Vasan, and D. Levy. Changes in arterial stiffness and wave reflection with advancing age in healthy men and women the Framingham Heart Study. *Hypertension*, 43(6):1239–1245, 2004.

[51] K. Sutton-Tyrrell, S. S. Najjar, R. M. Boudreau, L. Venkitachalam, V. Kupelian, E. M. Simonsick, R. Havlik, E. G. Lakatta, H. Spurgeon, and S. Kritchevsky. Elevated aortic pulse wave velocity, a marker of arterial stiffness, predicts cardiovascular events in well-functioning older adults. *Circulation*, 111(25):3384–3390, 2005.

[52] T. W. Hansen, J. A. Staessen, C. Torp-Pedersen, S. Rasmussen, L. Thijs, H. Ibsen, and J. Jeppesen. Prognostic value of aortic pulse wave velocity as index of arterial stiffness in the general population. *Circulation*, 113(5):664–670, 2006.

[53] A. Yamashina, H. Tomiyama, K. Takeda, H. Tsuda, T. Arai, K. Hirose, Y. Koji, S. Hori, and Y. Yamamoto. Validity, Reproducibility, and Clinical Significance of Noninvasive Brachial-Ankle Pulse Wave Velocity Measurement. *Hypertens. Res.*, 25(3):359–364, 2002.

[54] T. Weber, M. Ammer, M. Rammer, A. Adji, M. F. O'Rourke, S. Wassertheurer, S. Rosenkranz, and B. Eber. Noninvasive determination of carotid–femoral pulse wave velocity depends critically on assessment of travel distance: a comparison with invasive measurement. *J. Hypertens.*, 27(8):1624–1630, 2009.

[55] P. Salvi, G. Lio, C. Labat, E. Ricci, B. Pannier, and A. Benetos. Validation of a new non-invasive portable tonometer for determining arterial pressure wave and pulse wave velocity: the PulsePen device. *J. Hypertens.*, 22(12):2285–93, dec 2004.

[56] H. Tomiyama, A. Yamashina, T. Arai, K. Hirose, Y. Koji, T. Chikamori, S. Hori, Y. Yamamoto, N. Doba, and S. Hinohara. Influences of age and gender on results of noninvasive brachial–ankle pulse wave velocity measurement—a survey of 12 517 subjects. *Atherosclerosis*, 166(2):303–309, 2003.

[57] E. Hermeling, K. D. Reesink, R. S. Reneman, and A. P. G. Hoeks. Measurement of Local Pulse Wave Velocity: Effects of Signal Processing on Precision. *Ultrasound Med. Biol.*, 33(5):774–781, may 2007.

[58] H. C. Pereira, T. Pereira, V. Almeida, E. Borges, E. Figueiras, J. B. Simões, J. L. Malaquias, J. M. R. Cardoso, and C. M. B. Correia. Characterization of a double probe for local pulse wave velocity assessment. *Physiol. Meas.*, 31(11):1449–65, 2010.

[59] T. Pereira, P. Vaz, T. Oliveira, I. Santos, H. Pereira, V. Almeida, C. Correia, and J. Cardoso. Empirical mode decomposition for self-mixing Doppler signals of hemodynamic optical probes. *Physiol. Meas.*, 34(3):377–390, mar 2013.

[60] T. Pereira, I. Santos, T. Oliveira, P. Vaz, T. Correia, T. Pereira, H. Santos, H. Pereira, V. Almeida, and J. Cardoso. Characterization of optical system for hemodynamic multi-parameter assessment. *Cardiovasc. Eng. Technol.*, 4(1):87–97, 2013.

[61] T. Pereira, C. Correia, and J. Cardoso. Novel Methods for Pulse Wave Velocity Measurement. *J. Med. Biol. Eng.*, pages 1–11, 2014.

[62] W. R. Milnor. Arterial impedance as ventricular afterload. *Circ. Res.*, 36(5):565–570, 1975.

[63] W. W. Nichols, C. R. Conti, W. E. Walker, and W. R. Milnor. Input impedance of the systemic circulation in man. *Circ. Res.*, 40(5):451–458, 1977.

[64] M. F. O'Rourke, A. Pauca, and X.-J. Jiang. Pulse wave analysis. *Br. J. Clin. Pharmacol.*, 51(6):507–522, 2001.

[65] J. K.-J. Li. Hemodynamics of large arteries. In *Dyn. Vasc. Syst.*, chapter 4, pages 76–136. World Scientific Publishing Co. Re. Ltd., River Edge, 2004.

[66] G. M. London and a. P. Guerin. Influence of arterial pulse and reflected waves on blood pressure and cardiac function. *Am. Heart J.*, 138(3 Pt 2):220–224, sep 1999.

[67] B. Williams, P. S. Lacy, S. M. Thom, K. Cruickshank, A. Stanton, D. Collier, A. D. Hughes, H. Thurston, and M. O'Rourke. Differential impact of blood pressure-lowering drugs on central aortic pressure and clinical outcomes: Principal results of the Conduit Artery Function Evaluation (CAFE) study. *Circulation*, 113(9):1213–1225, 2006.

[68] A. C. Guyton and J. E. Hall. Overview of the circulation; Medical physics of pressure, flow, and resistance. In *Textb. Med. Physiol.*, Guyton Physiology Series, pages 161–170. Elsevier Saunders, 2006.

[69] S. P. Sutera and R. Skalak. The history of Poiseuille's law. *Annu. Rev. Fluid Mech.*, 25(1):1–20, 1993.

[70] A. Popel and R. Pittman. Mechanics, molecular transport, and regulation in the microcirculation. In J. D. Bronzino, editor, *Biomed. Eng. Handb.*, chapter 59, pages 1–10. Taylor & Francis Group, 3rd edition, 2006.

[71] M. Thiriet. Cardiovascular physiology. In *Biol. Mech. Blood Flows Part II Mech. Med. Asp.*, CRM Series in Mathematical Physics, chapter 2, pages 35–80. Springer New York, 2007.

[72] Y. Fung. Blood flow in heart, lungs, arteries, and veins. In *Biomech. motion, flow, Stress. growth*, Biomechanics / Y. C. Fung, chapter 5, pages 155–194. Springer-Verlag, 1990.

[73] A. C. Guyton and J. E. Hall. Vascular distensibility and functions of arterial and venous systems. In *Textb. Med. Physiol.*, Guyton Physiology Series, chapter 15, pages 171–179. Elsevier Saunders, 2006.

[74] H. Miyashita. Clinical Assessment of Central Blood Pressure. *Curr. Hypertens. Rev.*, 8(2):80–90, 2012.

[75] F. Ding, W. Fan, R. Zhang, Q. Zhang, Y. Li, and J. Wang. Validation of the non-invasive assessment of central blood pressure by the SphygmoCor and Omron devices against the invasive catheter measurement. *Int. J. Cardiol.*, 152(12):S7–S8, 2011.

[76] I. G. Horváth, Á. Németh, Z. Lenkey, N. Alessandri, F. Tufano, P. Kis, B. Gaszner, and A. Cziráki. Invasive validation of a new oscillometric device (Arteriograph) for measuring augmentation index, central blood pressure and aortic pulse wave velocity. *J. Hypertens.*, 28(10):2068–2075, 2010.

[77] B. Sztrymf, F. Jacobs, D. Chemla, C. Richard, and S. C. Millasseau. Validation of the new Complior sensor to record pressure signals non-invasively. *J. Clin. Monit. Comput.*, 27(6):613–619, 2013.

[78] K. Takazawa, H. Kobayashi, N. Shindo, N. Tanaka, and A. Yamashina. Relationship between radial and central arterial pulse wave and evaluation of central aortic pressure using the radial arterial pulse wave. *Hypertens. Res.*, 30(3):219–228, 2007.

[79] T. Pereira, I. Santos, T. Oliveira, P. Vaz, T. Pereira, H. Santos, H. Pereira, C. Correia, and J. Cardoso. Pulse pressure waveform estimation using distension profiling with contactless optical probe. *Med. Eng. Phys.*, 36(11):1515–1520, 2014.

[80] M. Collette, A. Lalande, S. Willoteaux, G. Leftheriotis, and A. Humeau. Measurement of the local aortic stiffness by a non-invasive bioelectrical impedance technique. *Med. Biol. Eng. Comput.*, 49(4):431–439, 2011.

[81] A. C. Guyton and J. E. Hall. The microcirculation and the lymphatic system: capillary fluid exchange, interstitial fluid, and lymph flow. In *Textb. Med. Physiol.*, chapter 16, pages 181–193. Elsevier Saunders, 2006.

[82] A. C. Guyton and J. E. Hall. Cardiac output, Venous return, and their regulation. In *Textb. Med. Physiol.*, chapter 20, pages 232–244. Elsevier Saunders, 2006.

[83] A. C. Guyton and J. E. Hall. Cardiac Failure. In *Textb. Med. Physiol.*, chapter 22, pages 258–265. Elsevier Saunders, 2006.

[84] L. W. Henderson. The problem of peritoneal membrane area and permeability. *Kidney Int*, 3(6):409–410, 1973.

[85] I. M. Braverman. The cutaneous microcirculation. *J. Investig. Dermatology Symp. Proc.*, 5(1):3–9, 2000.

[86] K. E. Barrett, S. M. Barman, S. Boitano, and H. Brooks. Circulation through special regions. In *Ganong's Rev. Med. Physiol.*, LANGE Basic Science Series, pages 489–506. Mcgraw-hill, 23 edition, 2009.

[87] E. Figueiras. *Métodos e instrumentação para fluxometria laser : aplicações à microcirculação sanguínea.* PhD thesis, University of Coimbra, 2012.

[88] I. M. Braverman. The cutaneous microcirculation: ultrastructure and microanatomical organization. *Microcirculation*, 4(3):329–340, 1997.

[89] A. C. Guyton and J. E. Hall. Body temperature, temperature regulation, and fever. In *Textb. Med. Physiol.*, chapter 73, pages 889–900. Elsevier Saunders, 11th edition, 2006.

[90] Madhero88 and M.Komorniczak. Layers of the skin. `https://commons.wikimedia.org/wiki/File:Skin{_}layers.svg`, 2012.

[91] R. Zhang, W. Verkruysse, B. Choi, J. A. Viator, B. Jung, L. O. Svaasand, G. Aguilar, and J. S. Nelson. Determination of human skin optical properties from spectrophotometric measurements based on optimization by genetic algorithms. *J. Biomed. Opt.*, 10(2):024030, 2005.

[92] A. N. Bashkatov, E. A. Genina, V. I. Kochubey, and V. V. Tuchin. Optical properties of human skin, subcutaneous and mucous tissues in the wavelength range from 400 to 2000 nm. *J. Phys. D. Appl. Phys.*, 38(15):2543–2555, 2005.

[93] H. Kolárová, D. Ditrichová, and J. Wagner. Penetration of the laser light into the skin in vitro. *Lasers Surg. Med.*, 24(3):231–235, 1999.

[94] G. J. Tortora and B. H. Derrickson. The integumentary system. In *Princ. Anat. Physiol.*, chapter 5, pages 142–162. Wiley Global Education, 14 edition, 2014.

[95] I. V. Meglinski and S. J. Matcher. Quantitative assessment of skin layers absorption and skin reflectance spectra simulation in the visible and near-infrared spectral regions. *Physiol. Meas.*, 23(4):741–753, 2002.

[96] S. Eriksson, J. Nilsson, and C. Sturesson. Non-invasive imaging of microcirculation: a technology review. *Med. Devices (Auckl).*, 7:445–52, 2014.

[97] P. M. McNamara, J. O'Doherty, M. L. O'Connell, B. W. Fitzgerald, C. D. Anderson, G. E. Nilsson, R. Toll, and M. J. Leahy. Tissue viability (TiVi) imaging: Temporal effects of local occlusion studies in the volar forearm. *J. Biophotonics*, 3(1):66–74, 2010.

[98] J. O'Doherty, P. McNamara, N. Clancy, J. Enfield, and M. Leahy. Comparison of instruments for investigation of microcirculatory blood flow and red blood cell concentration. *J. Biomed. Opt.*, 14(3):034025–034025, 2009.

[99] E. Figueiras, R. Campos, S. Semedo, R. Oliveira, L. F. Requicha Ferreira, and A. Humeau-Heurtier. A new laser Doppler flowmeter prototype for depth dependent monitoring of skin microcirculation. *Rev. Sci. Instrum.*, 83(3):034302, mar 2012.

[100] A. Humeau-Heurtier, E. Guerreschi, P. Abraham, and G. Mahé. Relevance of laser Doppler and laser speckle techniques for assessing vascular function: State of the art and future trends. *IEEE Trans. Biomed. Eng.*, 60(3):659–666, 2013.

[101] M. Roustit and J.-L. Cracowski. Assessment of endothelial and neurovascular function in human skin microcirculation. *Trends Pharmacol. Sci.*, 34(7):373–384, 2013.

[102] E. Figueiras, R. Oliveira, C. Lourenço, R. Campos, A. Humeau-Heurtier, R. Barbosa, J. Laranjinha, L. Requicha Ferreira, and F. de Mul. Self-mixing microprobe for monitoring microvascular perfusion in rat brain. *Med. Biol. Eng. Comput.*, 51(1-2):103–112, 2013.

[103] M. Leutenegger, E. Martin-Williams, P. Harbi, T. Thacher, W. Raffoul, M. André, A. Lopez, P. Lasser, and T. Lasser. Real-time full field laser Doppler imaging. *Biomed. Opt. Express*, 2(6):1470–1477, jun 2011.

[104] Perimed AB. Periflux system 5000. `https://www.perimed-instruments.com/products/periflux-system-5000-tcpo2`.

[105] Moor Instruments. moorVMS-LDF. `http://gb.moor.co.uk/product/moorvms-ldf-laser-doppler-monitor/1`.

[106] Moor Instruments. High resolution laser Doppler imager. `http://gb.moor.co.uk/product/moorldi2-hir-high-resolution-laser-doppler-imager/242`.

[107] Perimed AB. Pericam PSI sytem. `https://www.perimed-instruments.com/products/pericam-psi`.

[108] Moor Instruments. Laser speckle contrast imager. `http://gb.moor.co.uk/product/moorflpi-2-laser-speckle-contrast-imager/291`.

[109] S. Laurent, P. Boutouyrie, R. Asmar, I. Gautier, B. Laloux, L. Guize, P. Ducimetiere, and a. Benetos. Aortic stiffness is an independent predictor of all-cause and cardiovascular mortality in hypertensive patients. *Hypertension*, 37(5):1236–41, may 2001.

[110] J. Blacher, R. Asmar, S. Djane, G. M. London, and M. E. Safar. Aortic pulse wave velocity as a marker of cardiovascular risk in hypertensive patients. *Hypertension*, 33(5):1111–1117, 1999.

[111] R. Asmar, A. Rudnichi, J. Blacher, G. M. London, and M. E. Safar. Pulse pressure and aortic pulse wave are markers of cardiovascular risk in hypertensive populations. *Am. J. Hypertens.*, 14(2):91–97, 2001.

[112] F. M. Wigley. Clinical practice. Raynaud's Phenomenon. *N. Engl. J. Med.*, 347(13):1001–8, 2002.

[113] T. Asakura and N. Takai. Dynamic laser speckles and their application to velocity measurements of the diffuse object. *Appl. Phys.*, 194:179–194, 1981.

[114] H. Hirabayashi, T. Matsuo, H. Ishizawa, H. Kanai, and T. Nishimatsu. Surface Roughness Evaluation by Laser Speckle. In *2006 SICE-ICASE Int. Jt. Conf.*, pages 5809–5812, 2006.

[115] A. M. Hamed, H. El-Ghandoor, F. El-Diasty, and M. Saudy. Analysis of speckle images to assess surface roughness. *Opt. Laser Technol.*, 36(3):249–253, apr 2004.

[116] T. Yoshimura, K. Kato, and K. Nakagawa. Surface-roughness dependence of the intensity correlation function under speckle-pattern illumination. *J. Opt. Soc. Am. A*, 7(12):2254–2259, 1990.

[117] S. Rothberg and B. Halkon. Laser Vibrometry meets laser speckle. In *Proc. SPIE - Int. Soc. Opt. Eng.*, volume 5503, pages 280–291, 2004.

[118] P. Martin and S. Rothberg. Introducing speckle noise maps for Laser Vibrometry. *Opt. Lasers Eng.*, 47(3-4):431–442, 2009.

[119] A. A. Veber, A. Lyashedko, E. Sholokhov, A. Trikshev, A. Kurkov, Y. Pyrkov, A. E. Veber, V. Seregin, and V. Tsvetkov. Laser vibrometry based on analysis of the speckle pattern from a remote object. *Appl. Phys. B*, 105(3):613–617, jun 2011.

[120] A. Humeau-Heurtier, P. Abraham, and G. Mahe. Linguistic analysis of laser speckle contrast images recorded at rest and during biological zero: Comparison with laser doppler flowmetry data. *IEEE Trans. Med. Imaging*, 32(12):2311–2321, 2013.

[121] D. Briers, D. Duncan, S. Kirkpatrick, M. Larsson, T. Stromberg, and O. Thompson. Laser speckle contrast imaging : theoretical and practical limitations. *J. Bomedical Opt.*, 18(6):1–9, 2013.

[122] R. Bandyopadhyay, A. S. Gittings, S. S. Suh, P. K. Dixon, and D. J. Durian. Speckle-visibility spectroscopy: A tool to study time-varying dynamics. *Rev. Sci. Instrum.*, 76(9):93110, 2005.

[123] J. Goodman. Statistical properties of laser speckle patterns. In *Laser Speckle Relat. Phenom.*, volume 9 of *Topics in Applied Physics*, pages 9–75. Springer Berlin Heidelberg, 1975.

[124] J. Briers and S. Webster. Laser speckle contrast analysis (LASCA): A nonscanning, full-field technique for monitoring capillary blood flow. *J. Biomed. Opt.*, 1(2):174–179, 1996.

[125] D. D. Duncan and S. J. Kirkpatrick. Can laser speckle flowmetry be made a quantitative tool? *J. Opt. Soc. Am. A. Opt. Image Sci. Vis.*, 25(8):2088–2094, aug 2008.

[126] J. D. Briers and A. F. Fercher. Retinal blood-flow visualization by means of laser speckle photography. *Invest. Ophthalmol. Vis. Sci.*, 22(2):255–259, 1982.

[127] M. Draijer, E. Hondebrink, T. van Leeuwen, and W. Steenbergen. Review of laser speckle contrast techniques for visualizing tissue perfusion. *Lasers Med. Sci.*, 24(4):639–651, 2009.

[128] S. M. Kazmi, S. Balial, and A. K. Dunn. Optimization of camera exposure durations for multi-exposure speckle imaging of the microcirculation. *Biomed. Opt. Express*, 5(7):2157–2171, 2014.

[129] D. Boas and A. G. Yodh. Spatially varying dynamical properties of turbid media probed with diffusing temporal light correlation. *J. Opt. Soc. Am. A*, 14(1):192–215, 1997.

[130] G. Yu, T. Durduran, C. Zhou, R. Cheng, and A. G. Yodh. Near-Infrared Diffuse Correlation Spectroscopy for Assessment of Tissue Blood Flow. In *Handb. Biomed. Opt.*, chapter 10, pages 195–216. CRC Press, 1st edition, 2011.

[131] A. Nadort, R. G. Woolthuis, T. G. van Leeuwen, and D. J. Faber. Quantitative laser speckle flowmetry of the in vivo microcirculation using sidestream dark field microscopy. *Biomed. Opt. Express*, 4(11):2347–61, 2013.

[132] P. Zakharov, A. C. Völker, M. T. Wyss, F. Haiss, N. Calcinaghi, C. Zunzunegui, A. Buck, F. Scheffold, and B. Weber. Dynamic laser speckle imaging of cerebral blood flow. *Opt. Express*, 17(16):13904–13917, 2009.

[133] A. B. Parthasarathy, W. J. Tom, A. Gopal, X. Zhang, and A. K. Dunn. Robust flow measurement with multi-exposure speckle imaging. *Opt. Express*, 16(3):1975–89, feb 2008.

[134] O. Thompson, M. Andrews, and E. Hirst. Correction for spatial averaging in laser speckle contrast analysis. *Biomed. Opt. Express*, 2(4):1021–1029, apr 2011.

[135] A. Fercher and J. Briers. Flow visualization by means of single-exposure speckle photography. *Opt. Commun.*, 37(5):326–330, 1981.

[136] N. C. Santos and M. a. Castanho. Teaching light scattering spectroscopy: the dimension and shape of tobacco mosaic virus. *Biophys. J.*, 71(3):1641–1650, 1996.

[137] T. Dragojević, D. Bronzi, H. Varma, C. Valdes, C. Castellvi, F. Villa, A. Tosi, C. Justicia, F. Zappa, and T. Durduran. High-speed multi-exposure laser speckle contrast imaging with a single-photon counting camera. *Biomed. Opt. Express*, 6(8):2865–2876, 2015.

[138] S. M. S. Kazmi, L. M. Richards, C. J. Schrandt, M. a. Davis, and A. K. Dunn. Expanding applications, accuracy, and interpretation of laser speckle contrast imaging of cerebral blood flow. *J. Cereb. Blood Flow Metab.*, 35(7):1076–1084, 2015.

[139] J. Senarathna, S. Member, A. Rege, N. Li, and N. V. Thakor. Laser Speckle Contrast Imaging : Theory , Instrumentation and Applications. *Biomed. Eng. IEEE Rev.*, 6(1):99–110, 2013.

[140] D. D. Duncan, S. J. Kirkpatrick, and J. C. Gladish. What is the proper statistical model for laser speckle flowmetry? In *Complex Dyn. Fluctuations Biomed. Photonics V*, volume 6855, pages 685502–7. International Society for Optics and Photonics, 2008.

[141] K. Basak, G. Dey, M. Mahadevappa, M. Mandal, and P. Dutta. In vivo laser speckle imaging by adaptive contrast computation for microvasculature assessment. *Opt. Lasers Eng.*, 62:87–94, 2014.

[142] S. Kazmi, E. Faraji, M. Davis, Y.-Y. Huang, X. Zhang, and A. Dunn. Flux or speed? Examining speckle contrast imaging of vascular flows. *Biomed. Opt. Express*, 6(7):2588–2608, 2015.

[143] J. C. Ramirez-San-Juan, R. Ramos-García, I. Guizar-Iturbide, G. Martínez-Niconoff, and B. Choi. Impact of velocity distribution assumption on simplified laser speckle imaging equation. *Opt. Express*, 16(5):3197–3203, 2008.

[144] A. K. Dunn. Laser Speckle Contrast Imaging of Cerebral Blood Flow. *Ann. Biomed. Eng.*, 40(2):367–377, 2012.

[145] R. Bi, J. Dong, C. L. Poh, and K. Lee. Optical methods for blood perfusion measurement—theoretical comparison among four different modalities. *JOSA A*, 32(5):860–866, 2015.

[146] A. Khalil, A. Humeau-Heurtier, G. Mahé, and P. Abraham. Laser speckle contrast imaging: age-related changes in microvascular blood flow and correlation with pulse-wave velocity in healthy subjects. *J. Biomed. Opt.*, 20(5):051010, 2015.

[147] S. M. S. Kazmi, R. K. Wu, and A. K. Dunn. Evaluating multi-exposure speckle imaging estimates of absolute autocorrelation times. *Opt. Lett.*, 40(15):3643–3646, 2015.

[148] A. Parthasarathy, S. Kazmi, and A. Dunn. Quantitative imaging of ischemic stroke through thinned skull in mice with Multi Exposure Speckle Imaging. *Biomed. Opt. Express*, 1(1):246–259, 2010.

[149] Y. Atchia, H. Levy, S. Dufour, and O. Levi. Rapid multiexposure in vivo brain imaging system using vertical cavity surface emitting lasers as a light source. *Appl. Opt.*, 52(7):C64–C71, 2013.

[150] H. Cheng and T. Q. Duong. Simplified laser-speckle-imaging analysis method and its application to retinal blood flow imaging. *Opt. Lett.*, 32(15):2188–2190, 2007.

[151] T. Smausz, D. Zölei, and B. Hopp. Real correlation time measurement in laser speckle contrast analysis using wide exposure time range images. *Appl. Opt.*, 48(8):1425–1429, 2009.

[152] O. B. Thompson and M. K. Andrews. Spectral density and tissue perfusion from speckle contrast measurements. *Proc. SPIE*, 6847:68472D–68472D–7, 2008.

[153] D. Zölei, T. Smausz, B. Hopp, and F. Bari. Self-tuning laser speckle contrast analysis based on multiple exposure times with enhanced temporal resolution. *J. Eur. Opt. Soc.*, 8, 2013.

[154] P.-A. Lemieux and D. J. Durian. Investigating non-Gaussian scattering processes by using nth-order intensity correlation functions. *J. Opt. Soc. Am. A*, 16(7):1651–1664, 1999.

[155] A. K. Dunn, H. Bolay, M. A. Moskowitz, and D. A. Boas. Dynamic imaging of cerebral blood flow using laser speckle. *J. Cereb. Blood Flow Metab.*, 21(3):195–201, 2001.

[156] P. Zakharov, A. Völker, A. Buck, B. Weber, and F. Scheffold. Quantitative modeling of laser speckle imaging. *Opt. Lett.*, 31(23):3465–3467, 2006.

[157] H. Li, Q. Liu, H. Lu, Y. Li, H. F. Zhang, and S. Tong. Directly measuring absolute flow speed by frequency-domain laser speckle imaging. *Opt. Express*, 22(17):21079–21087, 2014.

[158] A. Mazhar, D. Cuccia, T. Rice, S. Carp, A. Durkin, D. Boas, B. Choi, and B. Tromberg. Laser speckle imaging in the spatial frequency domain. *Biomed. Opt. Express*, 2(6):1553–1563, 2011.

[159] A. E. Ennos. Speckle interferometry. In *Laser Speckle Relat. Phenom.*, volume 9 of *Topics in Applied Physics*, chapter 6, pages 203–253. Springer Berlin Heidelberg, 1975.

[160] K. Basak, M. Manjunatha, and P. Dutta. Review of laser speckle-based analysis in medical imaging. *Med. Bol. Eng. Comput.*, 50(6):547–58, jun 2012.

[161] J. D. Briers. Laser Doppler and time-varying speckle: a reconciliation. *J. Opt. Soc. Am. A*, 13(2):345–350, 1996.

[162] D. Magatti, A. Gatti, and F. Ferri. Three-dimensional coherence of light speckles: Experiment. *Phys. Rev. A - At. Mol. Opt. Phys.*, 79(December):1–11, 2009.

[163] O. B. Thompson and M. K. Andrews. Tissue perfusion measurements: multiple-exposure laser speckle analysis generates laser Doppler-like spectra. *J. Biomed. Opt.*, 15(2):027015–027015–7, 2010.

[164] K. Khaksari and S. J. Kirkpatrick. Combined effects of scattering and absorption on laser speckle contrast imaging. *J. Biomed. Opt.*, 21(7):76002, 2016.

[165] J. C. Ramirez-San-Juan, E. Mendez-Aguilar, N. Salazar-Hermenegildo, A. Fuentes-Garcia, R. Ramos-Garcia, and B. Choi. Effects of speckle/pixel size ratio on temporal and spatial speckle-contrast analysis of dynamic scattering systems: Implications for measurements of blood-flow dynamics. *Biomed. Opt. Express*, 4(10):1883–1889, 2013.

[166] S. J. Kirkpatrick, D. D. Duncan, and E. M. Wells-Gray. Detrimental effects of speckle-pixel size matching in laser speckle contrast imaging. *Opt. Lett.*, 33(22):2886–2888, 2008.

[167] C. P. Valdes, H. M. Varma, A. K. Kristoffersen, T. Dragojevic, J. P. Culver, and T. Durduran. Speckle contrast optical spectroscopy, a non-invasive, diffuse optical method for measuring microvascular blood flow in tissue. *Biomed. Opt. Express*, 5(8):2769–2784, 2014.

[168] J. Qiu, Y. Li, Q. Huang, Y. Wang, and P. Li. Correcting speckle contrast at small speckle size to enhance signal to noise ratio for laser speckle contrast imaging. *Opt. Express*, 21(23):255–265, 2013.

[169] R. A. Braga and R. J. González-peña. Accuracy in dynamic laser speckle: optimum size of speckles for temporal and frequency analyses. *Opt. Eng.*, 55(12):121702–1–6, 2016.

[170] J. Bennett. Polarization. In M. Bass, editor, *Handb. Opt.*, chapter 12, pages 12.3–12.30. McGraw-Hill, 3rd edition, 2001.

[171] D. Brewster. On the Laws Which Regulate the Polarisation of Light by Reflexion from Transparent Bodies. *Philos. Trans. R. Soc. London*, 105:125–159, jan 1815.

[172] S. Sun, B. R. Hayes-Gill, D. He, Y. Zhu, and S. P. Morgan. Multi-exposure laser speckle contrast imaging using a high frame rate CMOS sensor with a field programmable gate array. *Opt. Lett.*, 40(20):4587–4590, 2015.

[173] S. Yuan, A. Devor, D. Boas, and A. Dunn. Determination of optimal exposure time for imaging of blood flow changes with laser speckle contrast imaging. *Appl. Opt.*, 44(10):1823–1830, 2005.

[174] H. M. Varma, C. P. Valdes, A. K. Kristoffersen, J. P. Culver, and T. Durduran. Speckle contrast optical tomography: A new method for deep tissue three-dimensional tomography of blood flow. *Biomed. Opt. Express*, 5(4):1275–1289, 2014.

[175] P. Zakharov, F. Scheffold, and B. Weber. Laser speckle analysis synchronised with cardiac cycle. In *Eur. Conf. Biomed. Opt.*, pages 954008–954008–9. International Society for Optics and Photonics, 2015.

[176] O. Yang, D. Cuccia, and B. Choi. Real-time blood flow visualization using the graphics processing unit. *J. Biomed. Opt.*, 16(1):016009–016009–14, 2011.

[177] M. Nemati, L. G. Paroni, N. Bhattacharya, and H. P. Urbach. Fluid pulsation detection in presence of induced motion artifacts using speckle techniques. *AIP Conf. Proc.*, 1600:215–222, 2014.

[178] L. M. Richards, S. M. S. Kazmi, J. L. Davis, K. E. Olin, and A. K. Dunn. Low-cost laser speckle contrast imaging of blood flow using a webcam. *Biomed. Opt. Express*, 4(10):2269–2283, jan 2013.

[179] K. R. Forrester, C. Stewart, J. Tulip, C. Leonard, and R. C. Bray. Comparison of laser speckle and laser Doppler perfusion imaging: measurement in human skin and rabbit articular tissue. *Med. Biol. Eng. Comput.*, 40(6):687–97, nov 2002.

[180] C. Scully. *Detection of Spatial and Temporal Interactions in Renal Autoregulation Dynamics.* PhD thesis, 2013.

[181] H. Fujii, T. Asakura, K. Nohira, Y. Shintomi, and T. Ohura. Blood flow observed by time-varying laser speckle. *Opt. Lett.*, 10(3):104–106, 1985.

[182] H. Fujii, K. Nohira, Y. Yamamoto, H. Ikawa, and T. Ohura. Evaluation of blood flow by laser speckle image sensing. Part 1. *Appl. Opt.*, 26(24):5321–5325, 1987.

[183] Y. Tamaki, M. Araie, E. Kawamoto, S. Eguchi, and H. Fujii. Noncontact, two-dimensional measurement of retinal microcirculation using laser speckle phenomenon. *Invest. Ophthalmol. Vis. Sci.*, 35(11):3825–34, oct 1994.

[184] G. Mahé, A. Humeau-Heurtier, S. Durand, G. Leftheriotis, and P. Abraham. Assessment of skin microvascular function and dysfunction with laser speckle contrast imaging. *Circ. Cardiovasc. Imaging*, 5(1):155–63, jan 2012.

[185] O. Thompson, J. Bakker, C. Kloeze, E. Hondebrink, and W. Steenbergen. Experimental comparison of perfusion imaging systems using multi-exposure laser speckle, single-exposure laser speckle, and full-field laser Doppler. *Dyn. Fluctuations Biomed. Photonics IX*, 8222:822204–822204–8, 2012.

[186] H. Cheng, Q. Luo, S. Zeng, S. Chen, J. Cen, and H. Gong. Modified laser speckle imaging method with improved spatial resolution. *J. Biomed. Opt.*, 8(3):559–564, 2003.

[187] D. D. Duncan, S. J. Kirkpatrick, and R. K. Wang. Statistics of local speckle contrast. *J. Opt. Soc. Am. A. Opt. Image Sci. Vis.*, 25(1):9–15, 2008.

[188] H. Cheng, Y. Yan, and T. Q. Duong. Temporal statistical analysis of laser speckle images and its application to retinal blood-flow imaging. *Opt. Express*, 16(14):10214–9, 2008.

[189] J. Ramirez-San-Juan, C. Regan, B. Coyotl-Ocelotl, and B. Choi. Spatial versus temporal laser speckle contrast analyses in the presence of static optical scatterers. *J. Biomed. Opt.*, 19(10):106009–106009, 2014.

[190] P. Li, Y. Li, H. He, Y. Tang, and M. Chen. Methods on Improving Sampling Depth of Laser Speckle Contrast Imaging of Blood Flow. In *Asia Commun. Photonics Conf. 2013*, OSA Technical Digest (online), page AF1J.4, Beijing, 2013. Optical Society of America.

[191] A. Rege, J. Senarathna, N. Li, and N. V. Thakor. Anisotropic processing of laser speckle images improves spatiotemporal resolution. *IEEE Trans. Biomed. Eng.*, 59(5):1272–1280, 2012.

[192] D. Duncan and S. Kirkpatrick. Spatio-temporal algorithms for processing laser speckle imaging data. In *Opt. Tissue Eng. Regen. Med. II*, number February, pages 685802–685802–6. International Society for Optics and Photonics, 2008.

[193] J. Qiu. Spatiotemporal laser speckle contrast analysis for blood flow imaging with maximized speckle contrast. *J. Biomed. Opt.*, 15(1):016003–016003–5, 2010.

[194] N. Li, X. Jia, K. Murari, R. Parlapalli, A. Rege, and N. V. Thakor. High spatiotemporal resolution imaging of the neurovascular response to electrical stimulation of rat peripheral trigeminal nerve as revealed by in vivo temporal laser speckle contrast. *J. Neurosci. Methods*, 176(2):230–236, 2009.

[195] J. Allen and K. Howell. Microvascular imaging: techniques and opportunities for clinical physiological measurements. *Physiol. Meas.*, 35:R91–R141, 2014.

[196] G. Armitage, K. Todd, A. Shuaib, and I. Winship. Laser speckle contrast imaging of collateral blood flow during acute ischemic stroke. *J Cereb Blood Flow Metab*, 30(8):1432–1436, aug 2010.

[197] Z. Wang, W. Luo, P. Li, J. Qiu, and Q. Luo. Acute hyperglycemia compromises cerebral blood flow following cortical spreading depression in rats monitored by laser speckle imaging. *J. Biomed. Opt.*, 13(6):64023–64026, 2008.

[198] A. B. Parthasarathy, E. L. Weber, L. M. Richards, D. J. Fox, and A. K. Dunn. Laser speckle contrast imaging of cerebral blood flow in humans during neurosurgery: a pilot clinical study. *J. Biomed. Opt.*, 15(6):66030–66038, 2010.

[199] F. Domoki, D. Zölei, O. Oláh, V. Tóth-Szűki, B. Hopp, F. Bari, and T. Smausz. Evaluation of laser-speckle contrast image analysis techniques in the cortical microcirculation of piglets. *Microvasc. Res.*, 83(3):311–317, 2012.

[200] A. I. Srienc, Z. L. Kurth-Nelson, and E. a. Newman. Imaging retinal blood flow with laser speckle flowmetry. *Front. Neuroenergetics*, 2(September):1–10, 2010.

[201] Y. Shiga, M. Shimura, T. Asano, S. Tsuda, Y. Yokoyama, N. Aizawa, K. Omodaka, M. Ryu, S. Yokokura, T. Takeshita, and T. Nakazawa. The Influence of Posture Change on Ocular Blood Flow in Normal Subjects, Measured by Laser Speckle Flowgraphy. *Curr. Eye Res.*, 38(6):691–698, may 2013.

[202] A. Ponticorvo, D. Cardenas, A. K. Dunn, D. Ts'o, and T. Q. Duong. Laser speckle contrast imaging of blood flow in rat retinas using an endoscope. *J. Biomed. Opt.*, 18(9):90501–90501, 2013.

[203] A. Rege, N. Thakor, K. Rhie, and A. Pathak. In vivo laser speckle imaging reveals microvascular remodeling and hemodynamic changes during wound healing angiogenesis. *Angiogenesis*, 15(1):87–98, 2012.

[204] B. Ruaro, A. Sulli, E. Alessandri, C. Pizzorni, G. Ferrari, and M. Cutolo. Laser speckle contrast analysis: a new method to evaluate peripheral blood perfusion in systemic sclerosis patients. *Ann. Rheum. Dis.*, pages annrheumdis–2013, 2013.

[205] J. D. Pauling, J. A. Shipley, D. J. Hart, A. McGrogan, and N. J. McHugh. Use of Laser Speckle Contrast Imaging to Assess Digital Microvascular Function in Primary Raynaud Phenomenon and Systemic Sclerosis: A Comparison Using the Raynaud Condition Score Diary. *J. Rheumatol.*, 42(7):1163–1168, 2015.

[206] Y. Beiderman, I. Horovitz, N. Burshtein, M. Teicher, J. Garcia, V. Mico, and Z. Zalevsky. Remote estimation of blood pulse pressure via temporal tracking of reflected secondary speckles pattern. *J. Biomed. Opt.*, 15(6):61707–61707–7, 2010.

[207] M. Nemati, C. Presura, H. Urbach, and N. Bhattacharya. Dynamic light scattering from pulsatile flow in the presence of induced motion artifacts. *Biomed. Opt. Express*, 5(7):2145–2156, 2014.

[208] N.-H. Holstein-Rathlou, O. V. Sosnovtseva, A. N. Pavlov, W. A. Cupples, C. M. Sorensen, and D. J. Marsh. Nephron blood flow dynamics measured by laser speckle contrast imaging. *Am. J. Physiol. Physiol.*, 300(2):F319–F329, 2011.

[209] Y. Beiderman, R. Blumenberg, N. Rabani, M. Teicher, J. Garcia, V. Mico, and Z. Zalevsky. Demonstration of remote optical measurement configuration that correlates to glucose concentration in blood. *Biomed. Opt. Express*, 2(4):858–870, apr 2011.

[210] N. Ozana, Y. Beiderman, A. Anand, B. Javidi, S. Polani, A. Schwarz, A. Shemer, J. Garcia, and Z. Zalevsky. Noncontact speckle-based optical sensor for detection of glucose concentration using magneto-optic effect. *J. Biomed. Opt.*, 21(6):65001, 2016.

[211] L. Campagnolo. *Optical Feedback Interferometry sensing technique for flow measurements in microchannels.* PhD thesis, Université de Toulouse, 2013.

[212] M. Davis, S. M. S. Kazmi, and A. K. Dunn. Imaging depth and multiple scattering in laser speckle contrast imaging. *J. Biomed. Opt.*, 19(8):086001–086001, 2014.

[213] Y. Shiga, T. Asano, H. Kunikata, F. Nitta, H. Sato, T. Nakazawa, and M. Shimura. Relative Flow Volume, a Novel Blood Flow Index in the Human Retina Derived From Laser Speckle Flowgraphy. *Investig. Opthalmology Vis. Sci.*, 55(6):3899–3904, 2014.

[214] K. R. Forrester, J. Tulip, C. Leonard, C. Stewart, and R. C. Bray. A Laser Speckle Imaging Technique for Measuring Tissue Perfusion. *IEEE Trans. Biomed. Eng.*, 51(11):2074–2084, 2004.

[215] S. M. S. Kazmi, A. B. Parthasarthy, N. E. Song, T. a. Jones, and A. K. Dunn. Chronic imaging of cortical blood flow using Multi-Exposure Speckle Imaging. *J. Cereb. Blood Flow Metab.*, 33(6):798–808, 2013.

[216] Z. Luo, Z. Wang, Z. Yuan, C. Du, and Y. Pan. Optical coherence Doppler tomography quantifies laser speckle contrast imaging for blood flow imaging in the rat cerebral cortex. *Opt. Lett.*, 33(10):1156–1158, 2008.

[217] I. Fredriksson, M. Larsson, and T. Strömberg. Measurement depth and volume in laser Doppler flowmetry. *Microvasc. Res.*, 78(1):4–13, 2009.

[218] R. Bi, J. Dong, and K. Lee. Deep tissue flowmetry based on diffuse speckle contrast analysis. *Opt. Lett.*, 38(9):1401–3, 2013.

[219] H. He, Y. Tang, F. Zhou, J. Wang, Q. Luo, and P. Li. Lateral laser speckle contrast analysis combined with line beam scanning illumination to improve the sampling depth of blood flow imaging. *Opt. Lett.*, 37(18):3774–6, sep 2012.

[220] I. Sigal, R. Gad, A. M. Caravaca-Aguirre, Y. Atchia, D. B. Conkey, R. Piestun, and O. Levi. Laser speckle contrast imaging with extended depth of field for in-vivo tissue imaging. *Biomed. Opt. Express*, 5(1):123–135, 2014.

[221] R. Bi, J. Dong, and K. Lee. Multi-channel deep tissue flowmetry based on temporal diffuse speckle contrast analysis. *Opt. Express*, 21(19):22854–22861, 2013.

[222] M. M. Gonik, A. B. Mishin, and D. a. Zimnyakov. Visualization of Blood Microcirculation Parameters in Human Tissues by Time-Integrated Dynamic Speckles Analysis. *Ann. N. Y. Acad. Sci.*, 972(1):325–330, oct 2002.

[223] T. Durduran and A. G. Yodh. Diffuse correlation spectroscopy for non-invasive, micro-vascular cerebral blood flow measurement. *Neuroimage*, 85:51–63, 2014.

[224] R. Matthes. Revision of guidelines on limits of exposure to laser radiation of wavelengths between 400 nm and 1.4 microm. International Commission on Non-Ionizing Radiation Protection. *Health Phys.*, 79(4):431–440, 2000.

[225] T. Pereira, T. Oliveira, M. Cabeleira, V. Almeida, E. Borges, J. Cardoso, C. Correia, and H. C. Pereira. Visible and infrared optical probes for hemodynamic parameters assessment. In *IEEE sensors*, pages 1796–1799. Ieee, oct 2011.

[226] Pixelink. PL-B741U. `http://pixelink.com/product/pl-b741u-on-semi-ibis-5b/`.

[227] Open source computer vision library. `http://opencv.org/`.

[228] Mathwork. Matlab. `http://www.mathworks.com/products/matlab/`.

[229] Y. N. Kul'chin, O. B. Vitrik, A. D. Lantsov, and N. P. Kraeva. Correlation method for processing speckle patterns of dynamic light scattering by small particles based on spatial averaging of data. *Optoelectron. Instrum. Data Process.*, 46(3):282–286, jul 2010.

[230] P. Santos, V. Almeida, J. Cardoso, and C. Correia. Photoplethysmographic logger with contact force and hydrostatic pressure monitoring. In *Bioeng. (ENBENG), 2013 IEEE 3rd Port. Meet.*, pages 1–6. IEEE, 2013.

[231] Histeq documentation. `http://www.mathworks.com/help/images/ref/histeq.html?s{_}tid=gn{_}loc{_}drop`, 2016.

[232] A. Lohmann and G. Weigelt. The measurement of depth motion by speckle photography. *Opt. Commun.*, 17(1):47–51, 1976.

[233] C. Narayanamurthy and C. Joenathan. Speckle pattern fringes produced by longitudinal motion of the diffuse object—sensitivity dependence and multiple exposures. *Opt. Commun.*, 65(3):179–184, 1988.

[234] M. D. Waterworth, B. J. Tarte, A. J. Joblin, T. Van Doorn, and H. E. Niesler. Optical transmission properties of homogenised milk used as a phantom material in visible wavelength imaging. *Australas. Phys. Eng. Sci. Med. by Australas. Coll. Phys. Sci. Med. Australas. Assoc. Phys. Sci. Med.*, 18(1):39–44, 1995.

[235] R. Cubeddu, A. Pifferi, P. Taroni, and A. Torricelli. A solid tissue phantom for photon migration studies. *Phys. Med. Biol.*, 42(10):1971–1979, 1997.

[236] S. Wojtkiewicz, A. Liebert, H. Rix, N. Żołek, and R. Maniewski. Laser-Doppler spectrum decomposition applied for the estimation of speed distribution of particles moving in a multiple scattering medium. *Phys. Med. Biol.*, 54(3):679, 2009.

[237] E. Figueiras, L.-F. R. Ferreira, and A. Humeau. Phantom validation for depth assessment in laser Doppler flowmetry technique. In *EOS Top. Meet. Diffractive Opt.*, Koli, 2010.

[238] F. M. White. *Fluid Mechanics.* McGraw-Hill international editions. McGraw-Hill, 7th edition, 2009.

[239] P. Walstra. *Dairy Technology: Principles of Milk Properties and Processes.* Food Science and Technology. CRC Press, 1999.

[240] P. Vennemann, R. Lindken, and J. Westerweel. In vivo whole-field blood velocity measurement techniques. *Exp. Fluids*, 42(4):495–511, 2007.

[241] O. Ménard, S. Ahmad, F. Rousseau, V. Briard-Bion, F. Gaucheron, and C. Lopez. Buffalo vs. cow milk fat globules: Size distribution, zeta-potential, compositions in total fatty acids and in polar lipids from the milk fat globule membrane. *Food Chem.*, 120(2):544–551, may 2010.

[242] D. M. de Bruin, R. H. Bremmer, V. M. Kodach, R. de Kinkelder, J. van Marle, T. G. van Leeuwen, and D. J. Faber. Optical phantoms of varying geometry based on thin building blocks with controlled optical properties. *J. Biomed. Opt.*, 15(2):025001, 2010.

[243] D. Y. Diao, L. Tchvialeva, G. Dhadwal, H. Lui, D. I. McLean, and T. K. Lee. Durable rough skin phantoms for optical modeling. *Phys. Med. Biol.*, 59:485–92, 2014.

[244] C.-E. Bisaillon, G. Lamouche, R. Maciejko, M. Dufour, and J.-P. Monchalin. Deformable and durable phantoms with controlled density of scatterers. *Phys. Med. Biol.*, 53:N237–N247, 2008.

[245] L. Tchvialeva, G. Dhadwal, D. Diao, H. Lui, D. I. McLean, and T. K. Lee. Laser speckle contrast vs. depolarization: a solid skin phantom study. *Techniques*, 8090:809018–809018–6, 2011.

[246] A. Nadort, K. Kalkman, T. G. van Leeuwen, and D. J. Faber. Quantitative blood flow velocity imaging using laser speckle flowmetry. *Sci. Rep.*, 6, 2016.

[247] R. H. Dieck, W. G. Steele, and G. Osolsobe. Test Uncertainty. ASME PTC 19.1-2005. Technical report, New York, 2005.

[248] W. J. Tom, A. Ponticorvo, and A. K. Dunn. Efficient processing of laser speckle contrast images. *Med. Imaging, IEEE Trans.*, 27(12):1728–1738, 2008.

[249] A. Steimers, W. Farnung, and M. Kohl-Bareis. Improvement of Speckle Contrast Image Processing by an Efficient Algorithm BT - Oxygen Transport to Tissue XXXVII. pages 419–425. Springer New York, New York, NY, 2016.

[250] S. Kirkpatrick, D. Duncan, R. Wang, and M. Hinds. Quantitative temporal speckle contrast imaging for tissue mechanics. *J. Opt. Soc. Am. A. Opt. Image Sci. Vis.*, 24(12):3728–3734, 2007.

[251] K. R. Byrnes, R. W. Waynant, I. K. Ilev, X. Wu, L. Barna, K. Smith, R. Heckert, H. Gerst, and J. J. Anders. Light promotes regeneration and functional recovery and alters the immune response after spinal cord injury. *Lasers Surg. Med.*, 36(3):171–185, 2005.

[252] M. Niemz. *Laser-tissue interactions. Fundamentals and Applications.* Springer, 3rd edition, 1996.

[253] N. Yokoi and Y. Aizu. Depth measurement of a blood flow region based on speckle decorrelation. *Opt. Rev.*, 22(2):365–373, 2015.

[254] P. Baldi, S. Brunak, Y. Chauvin, C. a. Andersen, and H. Nielsen. Assessing the accuracy of prediction algorithms for classification: an overview. *Bioinformatics*, 16(5):412–424, 2000.

[255] S. Liu, P. Li, and Q. Luo. Fast blood flow visualization of high-resolution laser speckle imaging data using graphics processing unit. *Opt. Express*, 16(19):2188–2190, 2008.

[256] G. M. Gardner, M. Conerty, J. Castracane, and S. M. Parnes. Electronic Speckle Pattern Interferometry of the Vibrating Larynx. *Ann. Otol. Rhinol. Laryngol.*, 104(1):5–12, jan 1995.

[257] V. Almeida, H. Pereira, T. Pereira, E. Figueiras, E. Borges, J. Cardoso, and C. Correia. Piezoelectric probe for pressure waveform estimation in flexible tubes and its application to the cardiovascular system. *Sensors Actuators A Phys.*, 169(1):217–226, sep 2011.

[258] M. A. Kirby, K. Khaksari, and S. J. Kirkpatrick. Assessment of incident intensity on laser speckle contrast imaging using a nematic liquid crystal spatial light modulator. *J. Biomed. Opt.*, 21(3):36001, 2016.